



Technische Universität München

Fakultät für Medizin

**Effects of cellular aging in human and murine MSCs on their
DNA double-strand break repair and telomere stability**

Xuanwen Bao

Vollständiger Abdruck der von der Fakultät für Medizin der Technischen Universität
München zur Erlangung des akademischen Grades eines

Doctor of Philosophy (Ph.D.)

genehmigten Dissertation.

Vorsitzender: Prof. Dr. Agnes Görlach

Betreuer/in: Prof. Dr. Michael J. Atkinson

Prüfer der Dissertation:

1. Prof. Dr. Harry Scherthan
2. Prof. Dr. Karima Djabali

Die Dissertation wurde am 23.07.2020 bei der Technischen Universität München
eingereicht und durch die Fakultät für Medizin am 31.08.2020 angenommen.

Table of Contents

Abstract	1
1 Introduction	3
1.1 Adult stem cells	3
1.2 Mesenchymal stem cells (MSCs)	4
1.2.1 History and origin.....	5
1.2.2 The definition of MSCs in normal physiology	6
1.2.3 Functional assays for characterizing MSCs in labs	7
1.2.4 The properties of MSCs.....	9
1.2.5 MSCs in preclinical models.....	11
1.3 Telomeres and DNA repair	13
1.3.1 Telomere structure.....	13
1.3.2 Telomerase-dependent pathway for elongation of telomeres	15
1.3.3 Alternative lengthening of telomeres (ALT) pathway for elongation of telomeres.....	16
1.3.4 Alternative lengthening of telomeres in normal cells	18
1.4 The relationship between telomere maintenance and radiation	19
1.4.1 Cellular effects of ionizing radiation.....	19
1.4.2 DNA repair pathways for ionizing radiation-induced double strand breaks.....	20
1.4.3 Telomeric DNA damage by radiation.....	21
1.4.4 Telomere length changes by radiation damage	21
1.4.5 Telomerase activity changes by radiation damage	22
1.4.6 Radiation and the ALT mechanism	23
1.5 Ageing in MSC and the transformation potential	24
1.5.1 Aging of MSCs <i>in vivo</i>	24
1.5.2 Aging of MSCs <i>in vitro</i>	25
1.5.3 Malignant transformation of <i>in-vitro</i> aged MSCs	26
1.6 Aim of the project	26
2 Materials	27
2.1 Mice	27
2.2 Cell lines	27

2.3	Medium and serum mixtures for cell culture	27
2.4	Enzyme.....	27
2.5	Antibodies	28
2.6	Solutions and buffers	28
2.7	Chemicals.....	29
2.8	Consumables	31
2.9	Technical Equipment.....	32
2.10	Software	33
2.11	Primers	33
3	Methods.....	35
3.1	Cell culture	35
3.1.1	Isolation and culture of primary murine mesenchymal stem cells	35
3.1.2	Isolation and culture of primary human mesenchymal stem cells	36
3.1.3	Cell counting	36
3.1.4	Freezing and thawing of human and mouse MSCs.....	37
3.1.5	Colony analysis.....	37
3.2	Irradiation	38
3.2.1	Gama-irradiation	38
3.2.2	X-ray irradiation.....	38
3.3	Real-Time Polymerase Chain Reaction (RT-PCR)	38
3.3.1	RNA extraction and reverse transcription	38
3.3.2	RNA concentration measurement	39
3.3.3	Reverse transcription.....	39
3.3.4	RT-PCR reaction.....	40
3.3.5	Analysis of Real-Time RT-PCR	42
3.4	The pipeline for RNA-seq analysis in our project.....	43
3.5	Alkaline phosphatase	46
3.6	Oil red O double-staining	46
3.7	Immunofluorescent staining	46

3.8 Analyzing of foci	47
3.9 Chromosome orientation fluorescence in situ hybridization (CO-FISH) staining	48
3.9.1 BrdU-incorporation in S-phase cells and fixation.....	48
3.9.2 Digestion of BrdU-substituted DNA strand	49
3.9.3 CO-FISH – First Hybridization	50
3.9.4 CO-FISH – Second Hybridization	50
3.9.5 Types of structural alterations observed at telomeres of murine.....	51
3.9.6 Analysis of radiation-induced T-SCE	53
3.10 Immunofluorescence-fluorescence in situ hybridization (IF-FISH) for detection the telomere dysfunction induced foci (TIF) in mouse MSCs	54
3.11 Quantification-fluorescence in situ hybridization (Q-FISH) of mouse MSCs... 54	54
3.12 Cell cycle analysis	55
3.12.1 Cell preparation	55
3.12.2 Propidium iodide (PI) staining.....	56
3.13 Bromodeoxyuridine incorporation and Hoechst 33342 staining.....	56
4 Results.....	58
4.1 Extended <i>in-vitro</i> culture of primary human mesenchymal stem cells downregulates Brca1-related genes and impairs recognition of DNA breaks	58
4.1.1 Transcriptome analysis for young and <i>in vitro</i> aged human MSCs	58
4.1.2 Gene ontology analysis	61
4.1.3 KEGG pathway analysis	63
4.1.4 GSEA analysis	64
4.1.5 Altered DNA repair-related profile.....	65
4.1.6 IPA analysis revealed altered DNA replication, recombination and repair coupled with change in cellular assembly and organization.....	67
4.1.7 Downregulation of genes involved in homologous recombination repair	68
4.1.8 Validation of downregulation of key components in homologous recombination	70
4.1.9 Gene network and IPA analysis confirmed the alteration in BRCA-mediated DNA damage response	71
4.1.10 Cell cycle analysis for young and aged human MSCs	73

4.1.11	Impaired DNA damage response during hMSC aging <i>ex vivo</i>	76
4.1.12	Changes in DNA repair foci involved in homologous recombination in human MSCs..	79
4.2	Characterizing of the stemness and autologous differentiation of mouse MSC.	82
4.3	Telomere instability post IR in murine MSCs	85
4.3.1	Q-FISH quantifies the telomere length in MSCs.....	85
4.3.2	Telomere losses and signal interruptions associate with greater donor age and with exposure to γ -irradiation	87
4.3.3	Higher donor age of MSCs increases level of T-SCE after exposure to γ -irradiation	90
4.3.4	ALT associated PML bodies are not found in mMSCs after IR	92
4.3.5	Irreparable DNA repair/telomere foci are existed in irradiated MSCs	93
5	Discussion	95
5.1	ATM-dependent recognition of DNA breaks and chromosomal instability in <i>ex vivo</i> aging human MSCs	95
5.2	Downregulated Brca1-related homologues recombination and impaired DNA double-strand break recognition in aging MSCs.....	96
5.3	Telomere instability is increased following IR in MSCs from aging donors.....	99
6	Conclusion.....	103
7	Appendix	105
	Declaration.....	105
7.1	Abbreviations.....	105
7.2	Bioinformatics for transcriptome data analysis	106
7.2.1	RNA-seq quality check by FASTQC	106
7.2.2	Aligning reads to a reference.....	107
7.2.3	Counting reads in genes.....	108
7.2.4	DESeq2 for differently expressed gene analysis.....	110
7.2.5	Design formula to perform DEG analysis.	111
7.2.6	Relevel of experimental condition.....	112
7.2.7	Pipeline running	112
7.2.8	Inspection of the result from DESeq2 analysis.....	112
7.2.9	Gene symbol annotation.....	114

7.2.10	Diagnostic plots	114
7.2.11	Sample distances and Principal components analysis (PCA)	116
7.3	List of significant genes in transcriptome analysis	124
7.4	List of DNA repair-related DEGs	136
7.5	List of Figures	138
7.6	List of Tables	147
8	Reference	149
9	Bibliography.....	166
10	Acknowledgement.....	170

Abstract

Mesenchymal stem cells (MSCs) have a lifelong proliferation capacity *in vivo*. They retain their potential to differentiate into cells of the different mesenchymal lineages to replace cells lost by attrition from mesenchymal tissues. This regenerative capacity has prompted the idea that autologous or allogenic MSCs could serve as cell reservoirs for the treatment of chronic degenerative diseases and acute injuries. Importantly, harvested MSCs may have been exposed to genotoxic stress during the lifetime of the donor. Moreover, after successful transplantation the engrafted MSCs will be - as any other cell of the body - subjected to further genotoxic stress. The DNA damage accumulated from exposure to ionizing radiation in the form of natural background irradiation or from medical exposures prior to and following transplantation poses a risk of malignant transformation. Therefore, understanding the biological principles and consequences behind the effects of radiation exposure is necessary for the safe application of MSC therapies. This risk may be greatly increased during the required massive *in vitro* expansion of MSCs prior to transplantation.

This project focuses on understanding the molecular changes in the capacity for DNA repair in MSCs of murine and human origin during *in-vivo* (physiological) ageing. This is compared with changes during the *in-vitro* ageing in the course of massive stem cell expansion. Because of the importance of telomere stability for the maintenance of the long-term repopulation potential and stemness of MSCs, the DNA repair capacity was studied with a special interest for the telomeric regions of MSCs.

We have found that *in vitro* expanded murine MSCs gradually lost the capacity to recognize double strand breaks (DSBs) and form γ H2AX/53BP1 foci with increasing cell divisions. A reduction of ATM-dependent foci with increased age *in vitro* implied that ATM signaling of DSBs became impaired during the extended *in vitro* expansion. Through analysis on transcriptome data we identified BRCA1-mediated homologous recombination (HR) to be the major repair process affected during *in vitro* aging of human MSCs. Low expression of genes participating in the repair of DSBs by homologous recombination (BRCA1, RAD51, and RAD54) and a higher fraction of residual pBRCA1+ γ -H2AX foci in *ex vivo* aged versus young MSCs, indicated that the recognition of DNA DSBs and the efficiency of homologous recombination-mediated DSB repair were both impaired during *in vitro* aging.

Finally, we compared the effect of irradiation on the stability of the telomeres in murine MSCs from young and aged mice. Telomere integrity and the maintenance of a minimal length are both instrumental for the preservation of the proliferation capacity of adult stem cells. In contrast to the large body of knowledge about the mechanisms of DNA damage repair in coding regions of the genome, the pathways involved in the repair of radiation-induced DNA DSBs at telomeric regions are only poorly understood. Our studies on the age effects investigated the role of Atm and Brca1 in telomere damage signalling and repair following *in-vitro* gamma-irradiation in MSCs harvested from mice with different donor ages. It was found that 16 months of *in vivo* aging and 2 Gy of γ -irradiation independently both increased the percentage of cells showing telomere losses or telomere splitting signal. However, age and radiation acted synergistically in sister telomere exchange (T-SCE) in the MSCs of older donor mice. An increase of non-uniform telomere length in individual cells with T-SCE, but an absence of concomitant PML-body staining, suggest that ionizing radiation can trigger an incomplete alternative lengthening of telomere (ALT) mechanism in aged donor MSCs. MSCs are stem cell populations with low telomerase activity. One potential explanation for the characteristics is the repression of telomerase genes at the chromatin level, similar to the situation in ALT cell lines of mesenchymal origin, indicating the potential link between ALT mechanism and mesenchymal stem cells. The results obtained in this project will contribute to understand the effect of cellular aging on DNA double-strand break recognition, repair, and telomere stability of human and murine MSCs, which might contribute to solve the possible concerns on the therapeutic efficiency of the stress exposed MSCs.

1 Introduction

1.1 Adult stem cells

Stem cells have the ability to perpetuate themselves through self-renewal and to generate lineage-committed precursor cells such as osteoblasts, chondroblasts and neural precursor cells. The self-renewal property of stem cells is required to maintain the stem cell population. Stem cells may either divide symmetrically or asymmetrically. In symmetrical division two daughter stem cells are generated, each with the same stem cell potential as the parental cell (1). Asymmetric division generates one daughter stem cell and one precursor cell (1).

Committed precursor cells are lineage restricted cells generated by asymmetric division of stem cells. One daughter cell retains the same potential and properties of the original stem cell, while the other daughter is a committed precursor cell (Figure 1.1). A second property of stem cells is their pluripotency, which is the ability of a given stem cell to differentiate into different lineages of cells (1).

Stem cells can be divided into two categories based on the source and function: embryonic stem cells (ESCs) and adult stem cells (ASCs).

i). Embryonic Stem Cells (ESCs):

ESCs are located in the inner cell mass during the blastocyst phase of embryonic development (2). They are totipotent and this can be maintained in vitro under appropriate culture conditions. Cells of the three germ layers can be produced by ESCs and the daughter cells can proliferate continuously and produce various kinds of tissue cells, for instance neurons from ectoderm, pulmonary epithelial cells from endoderm or cardiomyocytes from mesoderm.

ii). Adult stem cells (ASCs)

ASCs exist in many organs and tissues, including brain, bone marrow, peripheral blood, blood vessels, skeletal muscle, skin, teeth, heart, gut, liver, ovarian epithelium, and testis. ASCs can differentiate into several predetermined types of terminal cells such as neural cells, skeletal muscular cells, cardiac cells, liver cells and stomach cells, depending on the origin and type of the parental ASC. The ASCs divide and

1.2.1 History and origin

With guinea pigs as a model organism, Friedenstein and colleagues transplanted bone marrow cells from a donor animal into the kidney capsule of a recipient animal. They found that the de-novo formation of bone in the transplant was due to the presence of a subpopulation of non-haematopoietic cells within the bone marrow (4). This subpopulation was subsequently characterized by their ability to adhere to the plastic surface of a cell culture flask forming low-density colonies when these adherent cells were culturing *in vitro*. The cells were named colony-forming unit-fibroblastic (CFU-F) cells because of the fibroblast-like shape of the cells in these colonies (5). The CFU-F cells have the potential to give rise to a number of different cell lines including the osteogenic line. *In vivo* assays of CFU-F have demonstrated that some CFU-F have a high ability for self-renewal and multipotentiality, which led to the hypothesis that non-haematopoietic cells with stem cell properties exist in bone marrow (6). These cells were renamed “stromal stem cells”. In 1991, Arnold Caplan again renamed these cells as “mesenchymal stem cells” (7), after he successfully differentiated these cells isolated from embryonic chick limbs into terminally differentiated cells (chondrocytes and osteoblasts). Pittenger later isolated MSCs from bone marrow aspirates of healthy human donors (8) and induced their differentiation into osteocytes, chondrocytes and adipocytes, thereby proving the multipotency of MSCs under appropriate *in vitro* conditions.

Bone marrow is not the only tissue of origin for MSCs. Studies have revealed that MSCs can be isolated from a range of tissues (9), including bone marrow, adipose tissues, umbilical cord blood and all adult connective tissues. The wide distribution of MSCs throughout the body makes obtaining MSCs easier via non-invasive or invasive procedures.

The set of features that characterize mesenchymal stem cells remains controversial. To date, single-cell level studies establishing the multilineage differentiation potential of MSCs have not been established *in vitro* (10). Whilst a subpopulation of CD271 positive cells with the highest capacity for tri-potency *in vitro* could be enriched by FACS from human bone marrow aspirates, this subset of CD271 positive MSCs has not yet been found in mice (11, 12). Moreover, the sources of postnatal MSCs, which develop into differentiated tissues, are heterogeneous; that is, these MSCs are derived from a mixed population of distinct progenitors (10). In a

previous study and my own experiments, cells with fibroblast-like adherence to plastic exhibited heterogeneous properties (13). The International Society for Cellular Therapy has suggested using the term multipotent mesenchymal stromal cells, regardless of the tissue from which they are isolated, to refer to fibroblast-like plastic-adhering cells, while reserving the term mesenchymal stem cells to indicate cells that meet the standard criteria (14).

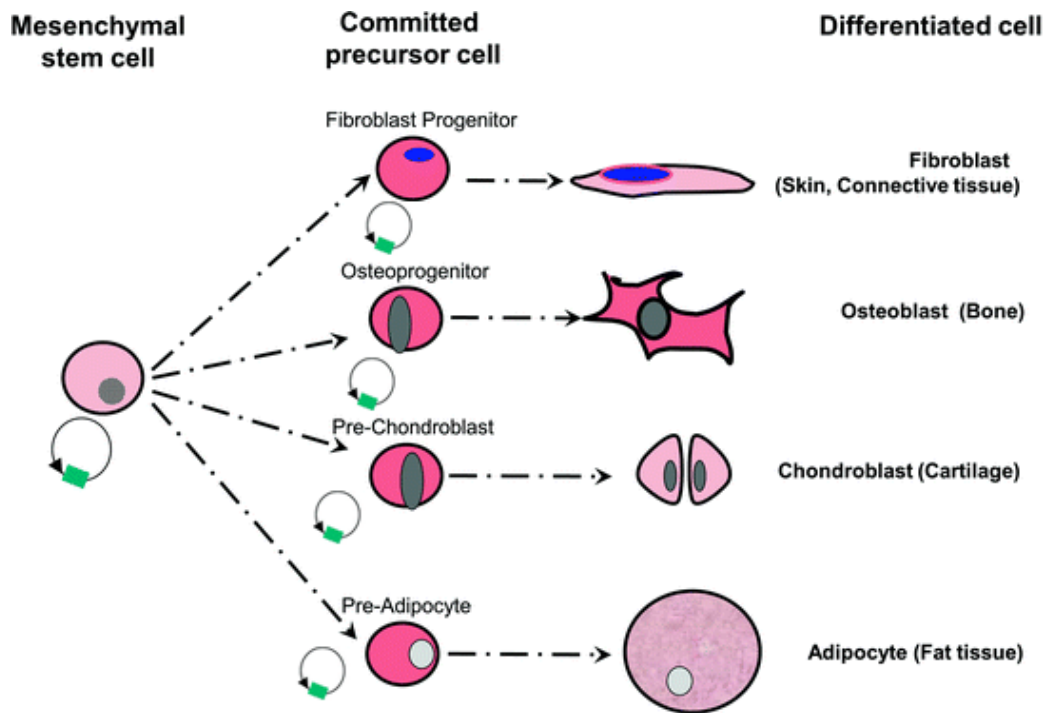


Figure 1.2: The differential potential of mesenchymal stem cells. Mesenchymal stem cells are self-renewing cells that can differentiate into several cell lineages, e.g. chondrocytes, adipocytes, osteocytes, fibroblasts, and other lineages. (modified from Michael Rosemann (1))

1.2.2 The definition of MSCs in normal physiology

The method selected for the isolation and expansion of MSCs, and the characteristics used to define these MSCs, differs between laboratories. To address and resolve this problem, the International Society for Cellular Therapy has proposed several criteria for the definition of MSCs (15):

- i) *The ability to adhere to plastic surfaces,*
- ii) *Special surface markers for MSCs (e.g., CD73, CD90, CD105 and other markers):*

These markers are suitable for characterising MSCs from humans and other species. The antigen expression on the surface of MSCs is one key piece of information for the identification of MSCs, and for distinguishing them from endothelial cells and haematopoietic cells which are also located in the bone marrow niche. For instance, CD73, CD105, and CD90 are commonly expressed on the surface of all species of MSCs (15). However, very few MSCs may also have low expression of haematopoietic and endothelial markers such as CD34, CD45 and HLA-DR (16).

Some surface markers are the same amongst the MSCs obtained from different tissues. Thus, CD73, CD105, and CD90 are commonly expressed on human MSCs obtained from bone marrow and adipose tissue (17). The surface markers for MSCs differ not only according to the tissue source of the MSCs but also by the species from which they come. Therefore, CD105 and CD90 are highly expressed on the surface of human and murine MSCs, whereas they are absent from the MSCs from goats, sheep, and dogs (18). Moreover, the expression of CD73 differs between the surface of human MSCs and murine MSCs. Lower expression levels of CD73 are observed on the surface of murine MSCs than are found on human MSCs (18).

iii) Pluripotency differentiation:

Multipotency is one key ability necessary for MSCs in regenerative medicine based clinical trials. MSCs are not only able to differentiate into osteocytes, chondrocytes, and adipocytes, but are also reported to be able to produce chromocytes, neurons, and smooth muscle cells under special conditions *in vitro* (19, 20).

1.2.3 Functional assays for characterizing MSCs in labs

Functional assays may be used to characterize the properties of MSCs, and these are listed as follows:

i) Clonogenic assay

Primary MSCs harvested from bone marrow and other tissue sources are able to adhere to plastic surfaces *in vitro* (10). When primary MSC cells are seeded at a limiting dilution they form individual colonies. As each colony is initiated from a single primary MSC the number of colonies formed can provide information about the number of original stem cells present in the primary MSC stock (21).

ii) The population doubling time analysis

Active proliferating MSCs have a high proliferation rate and can grow *in vitro* for a considerable time. This potential for long-term growth may be established by observing the constancy of the population doubling times over several weeks *in vitro*.

iii) Assay for testing the tri-potent differentiation potential

There are several assays that can test the tri-potent differentiation potential of MSCs *in vitro* (15). Oil Red O assay is used for the detection of lipid droplets in the adipocytes, while osteogenic differentiation is established by von Kossa, Alizarin Red, or alkaline phosphatase (ALP) staining (22). Chondrogenic differentiation may be validated with Alcian Blue or by immunohistochemical staining for collagen type II (23).

iv) Assay of cellular senescence

Actively proliferating MSCs should produce a very low fraction of senescent cells (24). Senescence can have different reasons, such as cellular stress by ROS, replicative exhaustion, unrepaired DNA damage, structural chromosomal aberrations or activated oncogenes (25, 26). An increased proportion of senescent MSCs would impair the quality of a clinical therapy that uses these cells. Senescent MSCs were also found to secrete pro-inflammatory cytokines (27-29) as a constituent of the so-called "senescence associated secretory program" (SASP). This SASP plays an important role in age-associated tissue degeneration and carcinogenesis. Firstly, IL- α is produced in the senescent cells, which triggers a signalling cascade that ultimately activates the NF- κ B pathway (30). NF- κ B transcribes genes (e.g. IL-6 and IL-8) that involve in producing the pro-inflammatory components of SASP (31). SASP components such as IL-6 and IL-8 reinforce the senescence growth arrest by autocrine signaling. Finally, SASP components affect the behavior of neighboring cells by paracrine signaling (31). In such a case, senescent cells may promote both the degenerative and neoplastic diseases of aging by the SASP program. The optimal function of normal cells within the tissues is impaired due to the SASP of senescent cells, leading to tissue degeneration (32). Thus, it is important to assess the extent of the senescence of MSCs *in vitro*. Senescence-associated beta-galactosidase staining (SA- β -gal staining) is the staining method commonly used to assay the proportion of senescent MSCs in culture.

v) Assay of telomere length

Telomere shortening is observed in MSCs that have become senescent (33). External stressors, such as radiation and chemical agents, may accelerate the onset

of senescence of MSCs and cause the shortening of telomeres (34, 35). Thus, telomere-related functional assays, such as a telomere length analysis by genomic PCR, quantitative fluorescence in situ hybridization (Q-FISH), and telomere-FISH, may all inform on the status of telomeres in long-term cultured MSCs (36). It is also suggested that telomere lengths be measured at regular intervals during long-term MSC culture (36). Because of the difficulties of standardisation, inter-individual variation as well as cell- and tissue heterogeneity have prevented telomere length measurements and assays of telomere status from becoming established in clinical practise.

vi) Chromosomal stability

Potential chromosomal instability must be excluded prior to the clinical application of MSCs, in particular after their expansion *in vitro*. This is usually done by whole chromosomal painting and karyotyping and allows a very sensitive and specific evaluation of the genomic status of MSC clones.

1.2.4 The properties of MSCs

i) Immunoregulatory Properties of MSCs

MSCs are able to suppress the immune response through numerous processes. They may interfere with immune-related pathways that require cell-to-cell interactions by secretion of interleukins 6 and 10, matrix metalloproteinases (MMPs), nitric oxide and indoleamine 2,3 deoxygenase (IDO). Other soluble factors with the ability to regulate other cells have been identified as being produced by MSCs such as Prostaglandin E2 (37). MSCs may express co-inhibitory molecules such as B7-H1 on their surface upon IFN- γ treatment (38), thus inhibiting the proliferation of T cells. In addition the maturation and function of dendritic cells and the differentiation and chemotaxis of B cells can also be impaired by MSCs (39-41).

ii) Secretions from MSCs

Besides the release of immunomodulating factors, MSCs can also produce extracellular vesicles such as exosomes. By characterizing the content of bone marrow MSC-derived vesicles, one study has identified 730 proteins, among which were regulators controlling self-renewal and differentiation (42). A number of surface markers (EGFR, PLAUR, and PDGFRB), signalling molecules (RAS-MAPK pathway, RHO pathways and CDC42 pathways), and cell adhesion molecules were identified in

the MSC-derived vesicles. This observation supports a possible role of MSC-derived vesicles in tissue repair (42). Senescent MSCs acquire a senescence-associated secretory phenotype (SASP). These proteins play several functions, such as sensitizing surrounding cells to senesce; immunoregulatory activity, and either impairing or fostering cancer growth (32). One study revealed extracellular matrix/cytoskeleton/cell junctions; metabolic processes; ox-redox factors; and regulators of gene expression was all enriched in the SASP protein secretome of MSCs, implying potential roles in the induction of senescence in neighbouring cells and may confer apoptosis resistance to senescent cells (43).

iii) MSCs in cancer

Since tumours share characteristics with sites of chronic inflammation, MSCs are frequently recruited to tumours and by the migratory capacity invade tumour (44). Their role here is a multifacet one, with some studies showing a tumour-inhibitory effect from their presence, whilst others show a tumour growth-promoting action. Because MSCs have the capacity to home specifically to tumour sites in humans (44), they could be designed as specialized delivery vehicles for targeted anti-cancer drugs or gene-therapy (45). Possible pro-tumorigenic properties are indicated by the expression of growth factors and pro-angiogenic molecules that can induce the formation of cancer stem cell niches and suppress the immune response (46).

There are indications that once recruited to the tumour, MSCs generate local fibroblasts (TAFs for “tumour associated fibroblasts”) that are responsible for building the tumour stroma. MSCs respond to chemokines secreted by the tumour (CXCR4/SDF1) and undergo chemotaxis (47). The binding partners for these molecules are CXCL12 and MIF respectively, both of which are expressed by MSCs (47).

iv) MSCs support haematopoietic stem cells in the perivascular niche of bone marrow

MSCs frequently reside on the outside of micro-vessels (arterioles and sinusoids). There are histologically identified there as perivascular cells (48). The sinusoids and arterioles that make up the dense network of blood vessels in the bone marrow stroma constitute the perivascular niche. This is a protective and supportive structure for the maintenance of haematopoietic stem cells (HSCs). It has been shown that in patients

who undergo HSCs transplantation, the risk for a graft-versus-host disease can be significantly reduced by co-injecting donor-derived MSCs (49).

1.2.5 MSCs in preclinical models

MSCs serve as promising cell sources for the therapy of different diseases due to their multilineage differentiation potential, tissue regenerative ability, and the secretion of immunoregulatory molecules.

Several animal models have been constructed to study MSC-based cell therapy. The tyrosine hydroxylase level in the substantia nigra pars compacta was increased following the injection of murine MSCs into the femoral vein in a mouse model of Parkinson's disease (50). The secretion of neurotrophin-3, vascular endothelial growth factor, epidermal growth factor, brain-derived neurotrophic factor and hepatocyte growth factor by MSCs are all suggested to prevent the direct differentiation of neurons into neurocytes (51, 52). The intranasal delivery of MSCs led to their distribution into different brain regions (the cerebral cortex, hippocampus, olfactory lobe, and brain stem) in a Parkinson's disease mouse model, which increases the level of tyrosine hydroxylase and decreased the level of toxic 6-hydroxydopamine in the lesions of the substantia nigra and ipsilateral striatum (53).

Alzheimer disease (AD) is one of the most common neurodegenerative disease, which shares common symptoms such as memory loss, dementia, and intellectual disabilities (54). No effective treatment has been established to stop the progression of AD (54). Stem cell therapy has shown promising results in terms of reducing the neuropathological deficits in an AD animal model (55). One study has demonstrated that human MSCs activate the microglia by increasing the expression of the enzymes responsible for A β -degradation and decreasing the expression of pro-inflammatory cytokines (55). Moreover, MSCs show the ability to regulate the inflammatory environment of AD by inadequacy of regulatory T-cells (Treg) and modulation of microglia activation (56). More recently, it was observed that human MSCs activate Tregs that in turn regulated microglia activation and increased the neuronal survival in AD mice model (57).

Rheumatoid arthritis (RA) is a an autoimmune disease affecting the joints that is caused by the loss of immunological self-tolerance (58). MSCs showed the capacity to attenuate RA progression in preclinical mouse models (59). The intraperitoneal

injection of human MSCs into an RA mouse model facilitated the reduction of inflammatory chemokines and cytokines in paws, thus leading to the expansion of Th1/Th17 antigen-specific cells in the damaged area (60). Moreover, the increased level of IL 10 after MSC injection intraperitoneally into RA mouse model further increased Tregs activities, which control self-active T-cells and instigate peripheral tolerance (59).

Type 1 diabetes is a serious autoimmune disease characterized by the destruction of insulin-producing β -cells of the pancreas due to the production of auto antibodies directed against them. Some studies has demonstrated that MSCs have the ability to differentiate into insulin producing cells and to modulate the immune response (38, 61). Human bone marrow MSCs were found to be effective in differentiating into glucose competent pancreatic endocrine cells both *in vitro* and *in vivo* (62). Furthermore, Human umbilical cord blood-derived MSCs (UCB-MSCs) is an alternative for differentiation into insulin producing cells (63). Unsal et al showed that the co-transplantation of MSCs and islets cells into streptozocin-treated diabetic rats enhance the survival rate of the engrafted islets and was beneficial for treating non-insulin-dependent patients in type 1 diabetes (64).

The multilineage differentiation potential of MSCs makes them good sources for cell-based repair. Cardiomyocyte differentiation *in vivo* is very rare, and *in vitro* differentiation is effective with cells from immature sources e.g. MSCs derived from embryonic stem cells (65, 66). MSC differentiation into cardiomyocytes was reportedly induced by a cocktail of growth factors and was used for the treatment of myocardial infarction and heart failure secondary to left ventricular injury in a pig model (67). The injection of bone marrow-derived-MSCs into infarcted diseased rodent models partially recompensed the infarcted myocardium (68, 69). The co-transplantation of autologous MSCs and endothelial progenitor cells improved the contractibility of myocardium. UCB-MSCs showed their retention in heart for several weeks in acute myocardial infarction mice. UCB-MSCs proliferated early and then differentiated into the endothelial lineage at the sites of the acute myocardial infarction (70, 71).

A large number of MSC-related clinical trials have been conducted and is trending gradually upwards (Figure 1.3). Most of these trails are phase I/II or combined phase II/III studies whereas only a small numbers are phase IV or phase III/IV (72).

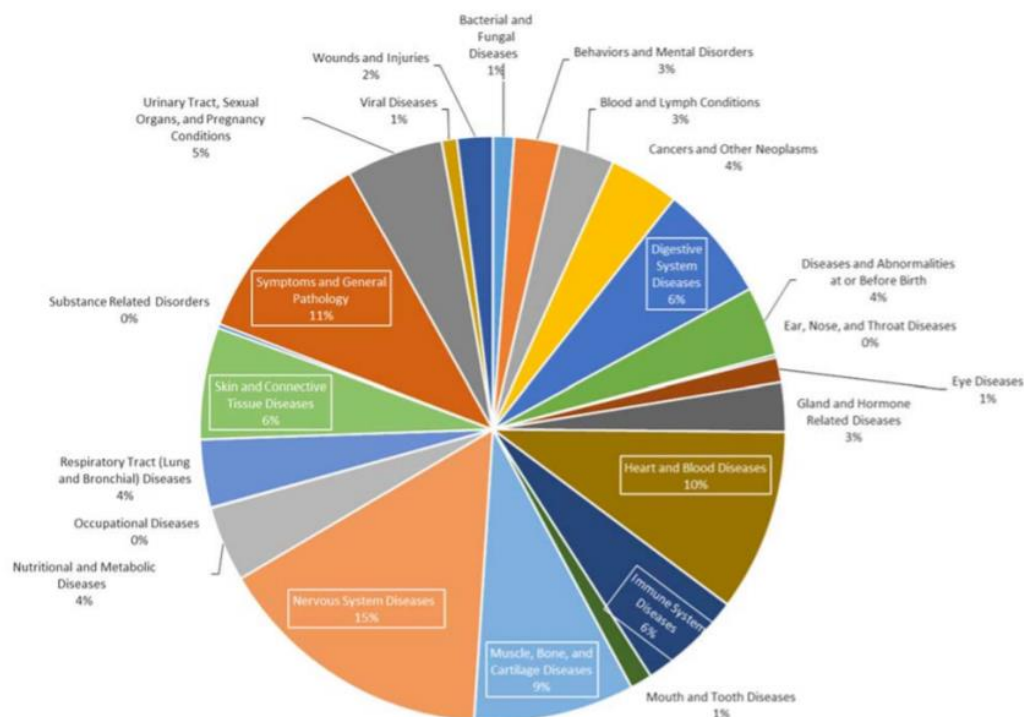


Figure 1.3: Current MSC-based clinical trials. The pie chart shows the proportion of MSC-based clinical trials classified by disease category (from Najjar et al (73)).

1.3 Telomeres and DNA repair

In accordance with the fact that adult stem cells express a low level of telomerase activity their telomeres slowly shorten. Indeed, MSCs are affected by telomere shortening during long-term culture and *in vivo* aging (74, 75). Loss of telomere length facilitate some kind of internal clock to assess the state of cellular aging (36). Therefore, it is important to track telomere status of MSCs during *in vivo* and *in vitro* aging.

1.3.1 Telomere structure

Telomeres are guanine-rich tandem DNA repeats located at the chromosomal ends. They are composed of multiple tandem repeats of the TTAGGG DNA sequence. The length of normal telomeres varies from 10 to 15 kb in human cells and from 20 to 50 kb in mouse cells (76). Specific proteins (e.g., RAP1, TRF1, TRF2, and TIN2) bind to the telomeres and form a stable DNA-protein complexes, termed shelterin complexes (77). The sheltering complex proteins protects chromosome ends from being recognised as DNA double strand breaks, thereby preventing initiation of repair processes that would lead to attrition, degradation, recombination, and end-to-end

ligation events that would lead to telomere fusion (77). As an additional protective feature of the telomere is the 3' single-stranded G-rich overhang at each telomere end. This DNA is folded back and inserted into adjacent double-stranded regions, forming a lasso-like telomere loop (T-loop) that also protects telomeres from being recognized as double-stranded breaks (DSBs) (78). The 3' G strand extension invades the duplex telomeric repeats and forms a D-loop. In the D loop the TTAGGG G strand overhang is base paired to the internal CCCTAA tracts, protecting the terminus and creating a structure that is distinct from a broken DNA end (79).

Every replication of the chromosomal DNA during cellular division reduces the level of stability as the ends of the telomeric regions are truncated (80). After each cell division the telomeres become progressively shortened because of incomplete replication at the lagging strand. In embryonic and primordial germ cells telomerase, a ribonucleoprotein enzyme complex consisting of reverse transcriptase (RT) and an RNA template, reextends the telomeric lagging strand maintaining the full length after each division. However, in somatic cells, including adult stem cells, telomerase activity is not high enough or is even absent, rendering the cells unable to compensate for replicative telomere loss. Moreover, rescue processes that may extend critically short telomeres are lacking in most somatic cells. When too many "uncapped" telomeres accumulate this may trigger apoptosis or cellular senescence (81, 82). Therefore, telomere length serves as an internal clock useful for the estimation of cell and tissue status (36). The progressive loss of telomeric DNA *in vivo* is considered to act as a tumour suppressor mechanism. This will lead to the removal of aged, possibly damaged, cells as well as preventing clonal dominance, limit clonal proliferation, and ensure the poly-clonal composition of cells in tissues and organisms. For instance, in human nucleated blood cells, the average telomere length shows a highly significant decline with individual age (82). In terms of MSCs, the telomere length in young donors was significantly longer than that of MSCs from older donors when the cells were cultured for the same number of population doublings (75). The difference in telomere length between cells of young and older donors, in terms of the length of the mean telomere restriction fragments, can be estimated to be about 17 bp/year (83). Telomeres that become too short fail to form the protective T-loop, with the overhanging single strand not able to insert to create the D-loop. This destabilises the binding of the protecting shelterin complex proteins, leading to recognition of the open chromosome end as DNA damage and the initiation of a repair response. The unprotected end of chromosomes tends to

have end-to-end fusions and then induce the breakage-fusion-bridge (BFB) cycles. With the propagation of BFB cycles, the genetic aberrations were introduced into the genome of cells (Figure 1.4). In most cancer cells the telomere shortening, and therefore apoptosis and senescence, is bypassed through an acquired high activity of telomerase activity or by the alternative lengthening of telomeres (ALT) mechanism (84, 85).

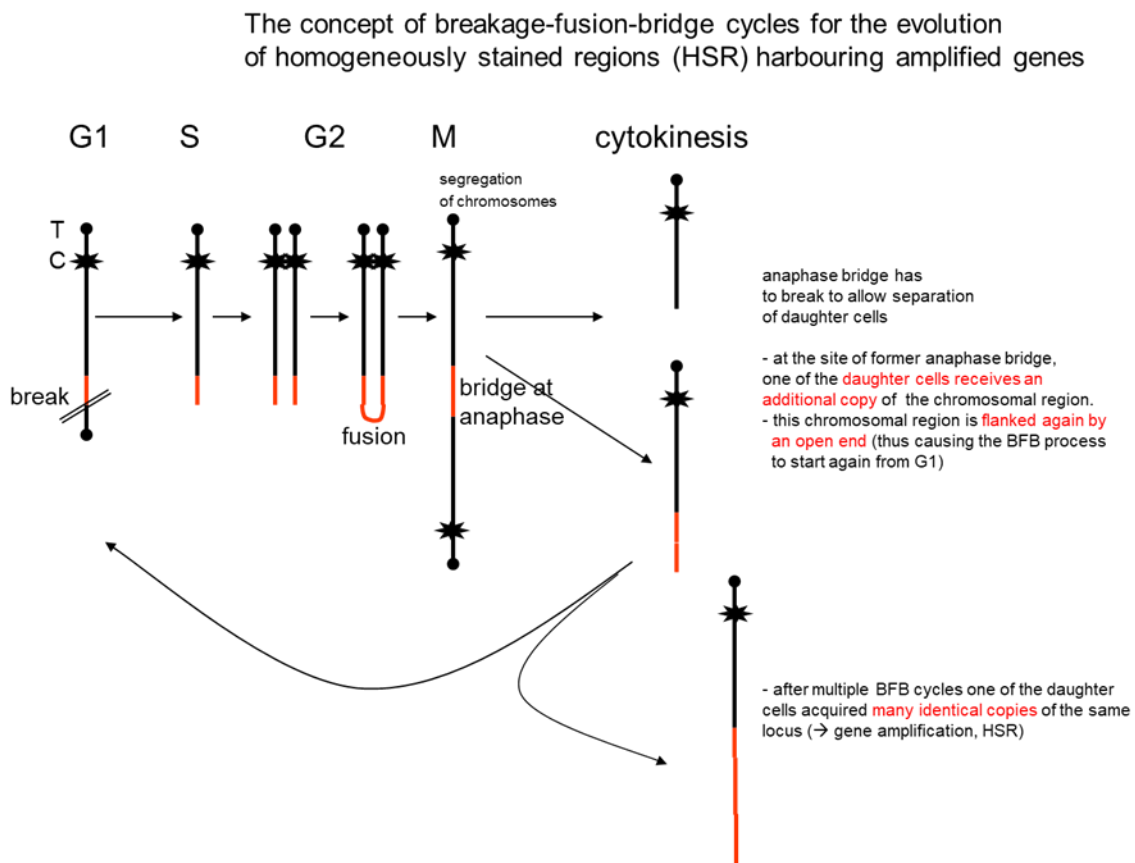


Figure 1.4: Bridge-fusion-bridge cycle. A bridge will be formed by the sister chromatids during anaphase. The fusion breaks apart from each other by pulling in opposite directions, which results in the two daughter cells receiving an uneven chromatid. The BFB cycle will continue in every subsequent cell division since the lack of telomeres on the two resulting chromatids, and stop until those chromatids receive a telomere, usually from a different chromatid through the process of translocation.

1.3.2 Telomerase-dependent pathway for elongation of telomeres

There are two pathways for the elongation of telomeres: 1) The telomerase-dependent pathway and 2) the alternative lengthening of telomeres (ALT) pathway.

The telomere elongation by telomerase pathway requires several steps (86-88). First, the telomeric DNA is recognized by the telomerase ribonucleoprotein, which consists of the telomerase reverse transcriptase (TERT) protein, including the RNA subunit and the anchor sites. The 3' end of the telomeric DNA forms a hybrid structure with the RNA subunit, whereas the 5' region of the telomeric DNA interacts with the proximal and distal anchor sites. Then, elongation of the 3' end of the DNA substrate by nucleotide addition using RNA as template and 5' template boundary recognition occurs. The template adds nucleotides to the 3' end of the telomeric DNA sequentially until the 5' end of the template is reached. The DNA substrate and the telomerase enzyme translocate and reposition to the 3' end of the telomeric DNA, which is in concert with recognition of the 3' template boundary. Lastly, another round of nucleotide addition is initiated.

1.3.3 Alternative lengthening of telomeres (ALT) pathway for elongation of telomeres

The ALT pathway is a telomerase-independent mechanism that extends telomere length in several tumour types (e.g., osteosarcoma (89), astrocytoma (90), glioblastoma (91), undifferentiated pleomorphic sarcoma (92), chondrosarcoma (92). An homologous recombination DNA repair process is activated at the telomeres with the sister chromatid strands serving as the templates to extend the length of the telomeres (93, 94). There are several unique features of ALT-positive cells (94):

- 1) The telomere length is heterogeneous with some cells exhibiting extremely long telomeres, whilst others have relatively short telomeres;

- 2) telomere sister chromatid exchanges take place (T-SCE); T-SCE represents the sister chromatid exchange events that occur at the telomeric region of the genome. T-SCE frequency is increased in ALT-positive cells and is widely used as an important assay for identifying the ALT mechanism (93). ALT-positive cells that have lost other characteristic ALT markers (APBs, T-circles and heterogeneous telomere lengths) still retain a high frequency of T-SCE, showing the value of T-SCE in ALT activity detection (95).

- 3) the presence of ALT-associated promyelocytic leukaemia protein bodies (APBs) that contain telomere-binding proteins (e.g. TRF1, TRF2 and proteins involved in DNA recombination and replication, including Mre11-Rad50-Nbs1 complex proteins MRE11,

RAD51 and NBS), and telomeric DNA in addition to the PML protein. Promyelocytic leukaemia nuclear bodies (PML-NBs) consist of proteins found in the cell nucleus. PML-NBs do not contain nucleic acids in normal cells. However, in ALT-positive cells, a subset of PML-NBs co-localizes with telomeric DNA (96). The name of promyelocytic leukaemia nuclear bodies comes from the overexpression of this protein in promyelocytic leukaemia cells (97). The structures of the PML-NBs are heterogeneous and dynamic, and more than 40 proteins involved in essential cellular processes such as DNA damage response and repair, apoptosis, and transcriptional regulation, telomere stability have been found to colocalize with PML in the PML-NBs (98). For instance, PML-NBs and their components (HIPK2, CBP, hSir2, HAUSP, Chk2) regulate extrinsic and intrinsic apoptosis pathways, in particular those elicited by ligation of death-inducing cell surface receptors or those resulting in p53 activation (99). The ATRX syndrome protein forms a chromatin-remodelling complex with death domain associated protein (DAXX) and localizes in PML-NBs, therefore displaying ATP-dependent activities that resemble those of other chromatin-remodelling complexes, including triple-helix DNA displacement and alteration of mononucleosome disruption patterns (100). Moreover, PML may localize at mitochondria-associated membranes and controls autophagosome formation. Stress conditions such as starvation or cancer control the regulation of PML-NBs on AMPK/mTOR/autophagy signalling (101, 102). PML-NBs are also found to be involved in the ALT mechanism (103). The subset of PML bodies that contain DNA homology-directed repair and replication proteins and telomeres is an indication of the activation of the ALT mechanism (104). SMC5/6 complex, formed by Smc5 and Smc6, together with the Nse4, SUMOylated the telomeric chromatin, together with action of PML3, one of PML isoforms, lead to the colocalization of telomeres and PML bodies (105). ALT-associated PML bodies (APBs) are specialized PML-NBs found exclusively in telomerase-negative tumours in which telomeres are maintained by ALT mechanisms (106). APBs that involve telomeres exhibit enlarged structures in ALT-positive cells (96, 106). The aggregation of telomeres with PML bodies causes the strong telomeric signals of APBs, which can be identified by fluorescence in situ hybridization (FISH) (107). Moreover, telomere binding proteins such as TRF1 and TRF2 have been found in APBs (108). APBs also contain telomere-associated proteins (Rad51, Rad52 and BRCA1) (109). It is still not clear whether APBs are directly involved in the ALT mechanism or are a response to the presence of abnormal telomeres (telomere

recombination, telomere uncapped events) in ALT-positive cells. APBs are characterized by active DNA synthesis (110). Inappropriate replication of the telomeres in APBs may facilitate telomere extension by HR-mediated replication in ALT-positive cells (111). SMC5/6 complexes and MRN, which are involved in the ALT mechanism, are found in APBs (112, 113). Moreover, knocking down MRN and the SMC5/6 complex inhibits the ALT mechanism and leads to the disappearance of APBs (113). APBs are found after activation of the ALT mechanism. However, APBs are not detected in two ALT-positive cell lines. AG11395 cells have aggregated telomeres and T-circles (T-circles refer to double stranded DNA telomeric circles that are not supercoiled due to nicks in both strands (78)) but not APBs (114). Another ALT-positive cell line without APBs also lacks T-circles and long heterogeneous telomeres (95).

1.3.4 Alternative lengthening of telomeres in normal cells

As described before, the ALT pathway is a telomerase-independent mechanism that extends telomere length in several tumour types. However, the role of the ALT pathway in normal cells has been debated and accumulated evidences reveal that HR-mediated telomere maintenance is not exclusive to cancer cells (115-117). Telomere recombination is stimulated in yeast short telomeres due to the loss of telomere capping (118). Normal primary murine cells also harbor very short telomeres (116). Human fibroblasts are able to repair telomeric DSBs by HR and the inhibition of RAD51 by siRNA or chemical inhibitors impairs telomeric recombination (119). CRISPR-Cas9 modified fibroblasts with induced telomeric DSBs displayed significantly higher frequency of T-SCE than the control group, suggesting an ALT-like phenotype in telomeres with DSBs (119). Some studies also report telomere DSB and the followed HR-mediated telomere recombination (ALT telomere phenotype shown by the appearance of T-SCE) in human fibroblasts after X-ray or LET irradiation (115, 120). One recent study demonstrates that IR-induced damage at telomeres activates telomeric recombination as telomeric DDR and the process is sustained if the telomeric DNA damage persists (120). A strong similarity has been raised between such DNA repair in normal cells and ALT (120).

1.4 The relationship between telomere maintenance and radiation

1.4.1 Cellular effects of ionizing radiation

There are several effects of IR on cells such as cell killing (either immediately or after cell division) leading to loss of clonogenic cell capacity, induction of apoptosis, necrosis), genetic changes (mutations or stable chromosomal aberrations in surviving cells), radiation-induced senescence, autophagy, and damage of cell membranes and mitochondria (121).

Spontaneous damage to the DNA occurs very frequently due to oxidative processes in the cell. Mutations in the genomic DNA would occur if damaged DNA were to be transmitted during cell division. However, the extensive DNA damage detection and repair capacity ensures that damage is rapidly repaired, ensuring that mutations occur very infrequently in normal cells (122). IR induces the DSB and SSB throughout the whole genome of cells, which increase the mutation rate of cells upon irradiation. This increase in mutation frequency may arise from the direct effects of radiation or indirectly via the effects of decreased level of antioxidants on levels of mutations (123). The accumulated mutation may lead to cell cycle arrest, apoptosis, or IR-induced malignant transformation (124, 125).

The biological effects of ionizing radiation (IR) were long held to be the result of DNA damage caused by ionization of molecules along the tracks of radiation through the cell nucleus. X-rays and γ -rays interact with atoms and molecules after being absorbed by cells and tissues. Free radicals such as superoxide radicals and hydroxyl are produced by the interaction of low-LET radiation and molecules and cause DNA and chromosome damage in cells (126). In contrast, high-LET radiation such as protons, α -particles, and neutrons display concentrated energy that is limited to the region of the radiation track (127). This non-uniform distribution pattern leads to direct damage along the radiation track and results in chromosomal lesions and DNA damage (127). Heterochromatin is the name for tightly packed DNA structure that forms structural functions and usually characterized by the repetitive DNA sequence. The effect of IR and the DSB pathway on euchromatin and heterochromatin varied. γ H2AX accumulation was unremarkable at sites of constitutive heterochromatin and in accordance with the lack of histone acetylation (128). Also, heterochromatin exhibited highly resistance to IR treatment than euchromatin (128). In MSCs, γ -irradiation activated the DNA damage response through induction of p53 and p21, and activation

of PI3 kinase-related protein kinase (PIKK)-dependent phosphorylation of histone H2AX on serine 139, and replication protein A2 on serine4/serine8. Inhibition of ATM or DNA-PK reduced DNA damage-induced phosphorylation of H2AX, indicating a role for both PIKKs in the response of hMSCs to DNA damage (129).

Thoughts about this process have changed based on the finding that genomic instability is initiated by cytoplasmic irradiation without any direct nuclear exposure to IR (130), and that cellular damage can occur in non-proliferating tissues (131, 132). In the previous decades, DNA double helix has been considered as the main target of IR either by direct energy deposition or indirectly by ROS generation. Nevertheless, cellular membranes are then identified as important target by IR, too. ROS was generated through IR, inducing the modification of proteins and lipids in cellular membrane (133). Oxidized bases and single-strand breaks (SSBs) are oxidative DNA lesions that are generated by excess ROS. Base excision repair is critical for their repair (134). What's more, studies also revealed that spatial and temporal re-localization of proteins and/or lipids generate new cell signals and cause the alterations and damage of cellular membrane upon IR (135).

Senescence is an irreversible growth arrest that halts the proliferation of cells. In the case of cells with DNA damage, especially with telomeric changes, senescence prevents the transmission of genetic instability to the daughter cells. Senescent cells are characterized by cell cycle arrest, loss of proliferation potential and expression of senescence-related biomarkers (136). IR causes chromosomal aberrations in a dose-dependent manner, therefore inducing senescence of cells (137). IR triggers telomere instability including end-end fusions and induces senescence in a p53 dependent manner (138).

1.4.2 DNA repair pathways for ionizing radiation-induced double strand breaks

Cell division and normal cellular processes require a stable genome, and the ability to repair DNA lesions is critical for long-term survival and normal division of cells. DSBs in the genome caused by DNA damage agents or radiation induce a DNA damage response (DDR) resulting in cell senescence, cell cycle arrest and apoptosis (139). Two main pathways have been found in DSB repair: non-homologous end joining (NHEJ) and homologous recombination (HR). NHEJ is an error-prone method that involves minimal processing of the damaged DNA by nucleases and direct re-ligation of the DNA ends. Small deletions may be introduced into the genome by NHEJ and

cause intrinsic mutations (140). In contrast, HR is a DNA metabolic process that provides high-fidelity, template-dependent repair or tolerance of complex DNA damages (141).

1.4.3 Telomeric DNA damage by radiation

IR-induced damage affects telomeres, both from direct hits from particles or indirect physiological changes, which include those to changes in telomere maintenance mechanisms and telomere uncapping events (142). Telomeres are constitutive heterochromatin structure which include repetitive sequence. In such cases, the effect of IR on telomeres may differ from the effect on genome. Moreover, telomeres constitute only 0.02% of the total genome in humans. The likelihood that a radiation particle traverses directly or close to a telomere is very low (143). Thus, direct telomere damage by IR is more likely the result of the indirect effects of IR that alter telomere maintenance mechanisms.

Guanine nucleotides are especially susceptible to oxidative stress, and the G-rich repeats (5'-TTAGGG-3') in telomeres are particularly sensitive to oxidative DNA damage such as from UV light and agents of oxidative DNA damage agents. Oxidative stress induced base damage also inhibits the binding of shelterin proteins TRF1 and TRF2 (144, 145). Taking together, this damage interferes with DNA replication and results in telomere shortening and loss in cells undergoing oxidative stress (146). Antioxidant treatment rescues the loss of telomere length after IR exposure in directly irradiated cells and bystander cells, which illustrates the roles of oxidative stress and antioxidants in the control of telomere length (147, 148). However, DNA lesions are repaired less efficiently in telomeres than in the rest of the genome due to the heterochromatic nature of telomeres and the inhibition of NHEJ by TRF2 (149, 150). One study revealed that telomeric DNA damage is persistent due to low rate of repair (143). In contrast, another study suggested that telomeric DSBs are repaired albeit slowly, within 48 h (151). The different and conflicting results may be due to the use of different experimental conditions and DNA damage methods for assessing residual (radiation doses or agents of oxidative DNA damage).

1.4.4 Telomere length changes by radiation damage

The influence of radiation exposure on telomere length in normal cells is still under debate. Radiation type and dose and cell types, cell culturing time may have influenced

the IR effect on telomere length in several different studies. One study revealed that 4 Gy of X-ray exposure did not change the telomere length in human HFFF2 fibroblasts, whereas high-LET proton irradiation triggered the elongation of telomeres in the same cells (152). However, another study demonstrated that no changes in telomere length were found after either low- or high-LET irradiation (24 h and 48 h) at low doses (0.1-1 Gy) in normal human fibroblasts (153). Moreover, a very high (therapeutic) dose of γ -irradiation (>40 Gy) was found to induce the loss of telomere length in fibroblasts and lymphocytes 24 h after irradiation (154). Another study demonstrated that, while the average telomere length is not affected by *in vivo* irradiation (52 Gy), there was a significant decrease in the fraction of cells with short telomeres (155). The effect of irradiation on telomere length is based on a dynamic process influenced by time. Some studies have revealed that normal fibroblasts showed different telomere lengths at different time points post-irradiation with 4 Gy of X-rays (152, 156). While radiation did not change the telomere length at 24 hours, telomere shortening was found 72 hours post-radiation, followed by delayed telomere extension 15 days post-radiation. Taken together, the changes in telomere length were only found after irradiation with high doses (>4 Gy). As the shelterin protein complex is directly involved in modulating the length of telomeres, as discussed in previous chapter, changes in telomere length after IR can be due to IR-induced changes in the shelterin proteins. One study revealed that there was a slight decrease in TRF1 and TRF2 and a significant decrease in TPP1 and POT1 were found in normal human T lymphocytes and fibroblasts cells after irradiation (154).

1.4.5 Telomerase activity changes by radiation damage

The influence of IR on telomerase activity is still under debate due to many conflicting results. Previous studies suggested that upregulation of telomerase activity and the elongation of telomere length after the IR of cancer cells enhances the radio-resistance of cancer cells e.g. Ewing sarcoma, breast cancer, chronic myelogenous leukemia during radiotherapy (157, 158). Inhibition of telomerase activity by telomerase inhibitors (e.g. GRN163L) in cancer cells has been found to improve the effect of radiation treatment and prohibit the growth of tumour cells (159). However, one recent study showed that low-dose IR had limited influence on telomerase activity in human fibroblasts (120).

1.4.6 Radiation and the ALT mechanism

As described in the previous chapter, ALT pathway in normal cells may not be exclusive to cancer cells (115, 117, 120). In addition, radiation exposure may induce alterations in ALT-phenotype telomere combinations and telomere length in human primary fibroblast cells (115, 120). The appearance of hallmarks of ALT (e.g. T-SCE, heterogeneous telomere length, APBs) validates the supposition that ALT mechanism is activated in primary cells after irradiation (120).

Some studies have demonstrated that telomeres resist DNA repair, and the proportion of foci resisting DDR in telomeres increases in a time-dependent manner after IR, while most DNA damage in the chromosome is repaired (143, 160). As explained above, oxidative stress target specifically on G-rich regions, inducing the development of 8-oxo-guanine, which increases the rate of replication forks stall on telomeres (161, 162). A radioprotective compound, NAC, decreased oxidative stress and totally abrogated telomere length change caused by IR, indicating that telomere damage by IR may be induced through an oxidative stress-dependent pathway (120). The colocalization of the telomeric protein TRF1 with γ -H2AX and 53BP1 after IR confirmed the IR-induced telomeric damage (120), which is also in agreement with the previous findings in which IR induces telomere erosion and telomere-positive anaphase bridges (152, 163). Marco De Vitis et al (120) found the amount of telomeric damage was significantly higher than control at days 3 and 6 post-IR with highest yield of telomere shortening and highest frequency of T-SCE, indicating that activated ALT-phenotypic telomeric recombination by IR-induced DNA damage. Increased evidence shows that damage at telomeres might favor ALT activation in either telomerase-positive cancer cells or in primary cells promoting telomere recombination (116, 164, 165).

The molecular mechanism for ALT activation in response to irradiation is still not clear. One explanation is the chromatin assembly alterations due to the loss of ATRX expression after IR (120). A significant reduction of ATRX expression was observed in response to X-ray irradiation (120). Another possibility is the disruption of TRF2, the shelterin component, following X-ray irradiation (161, 166, 167). One study indicated that ATRX was downregulated in response to IR in a dose-dependent manner (168). ATRX serves as a critical regulator of chromatin states, exerting multiple effects on chromatin-mediated activities, including mitosis, meiosis, gene regulation, telomere

protection, DNA replication, and X chromosome inactivation (169). ATRX target telomeres via a direct interaction with structured DNA, such as G-quadruplexes, and recruit DAXX to deposit (H3.3/H4)₂ tetramers (169). Thus, normal ATRX expression levels are important for the maintenance of chromatin assembly and telomere structure (169). ATRX inhibition of replication protein A (RPA) loading on telomeres and maintenance of a compact chromatin status at telomeres by the ATRX-DAXX complex repress HR in telomere regions (170). ATRX downregulation is commonly found in ALT-positive cells (170, 171), and the depletion of ATRX may be caused by epigenetic changes (reduction of trimethylation of H3K9 and H4K20) on telomeres, which favour a relaxed chromatin structure, and onset of HR in telomere regions (172). The reintroduction of ATRX into ALT-positive cells suppresses T-SCE, APB, and increase the heterogeneity of telomere length, indicating that the activation of HR of telomeres may associate with alterations in chromatin status (171, 173). The reduction in ATRX expression after irradiation may cause chromatin reconstruction and abnormal chromatin remodelling, thereby activating the ALT pathway in telomeres.

Taken together, these results imply that IR-induced telomere damage lead to ALT-like pathway activation. The HR-based DNA damage repair of telomere regions in primary normal cells shares similar features (e.g. the appearance of T-SCE, heterogeneous telomere length, APBs) with that in ALT-positive cancer cells. Understanding the HR-mediated ALT like pathway to repair telomeric DNA damage in normal cells may advance therapeutic targeting of the telomere maintenance mechanism.

1.5 Ageing in MSC and the transformation potential

1.5.1 Aging of MSCs *in vivo*

The exact definition of aging of cells is daunting. Aging can be divided into normal physiological ageing of cells *in vivo* and the ageing during prolonged *in vitro* culture of cells, which might or might not simulate 'true' aging.

The proliferation, differentiation, gene expression pattern, and the immunophenotype of MSCs are changed as a consequence of the *in vivo* aging (174). Thus, the number of colony forming unit-fibroblast (CFU-F) cells is decreased in MSC preparations from both human and murine sources (175). MSC aging may contribute to organismal aging/age-related diseases. The deficiency of bone-marrow MSC

osteogenesis can in part be responsible for the occurrence of age-dependent bone loss (osteoporosis) (176), as shown by a gradual MSC loss in mice with bone aging (177).

Accelerated aging has been found to associate with metabolic syndrome. It may be partly due to the disruption of MSC function. Lipodystrophies, the diseases of adipose tissue degeneration, are observed in patients with metabolic syndrome (178). Thus, high level of adipogenesis is found in metabolic syndrome, which cause the exhaustion of stem cells (179).

1.5.2 Aging of MSCs *in vitro*

It is still under debate that whether long-term culture reproduces the physiological change associated with MSC aging *in vivo*. Nevertheless, the relatively small amount of starting materials is one of the major limitations to the application of MSCs. Thus, the utilization of MSCs in clinical treatment requires *in vitro* expansion prior to transplantation (180, 181), in which cellular aging of MSCs might be an issue.

MSCs subjected to extended culture time display changes that include decreased expression of specific stem cell surface markers, enlarged morphology, and disrupted differentiation potential (174). The accumulation of mutations (182), declining self-renewal capacity (183), telomere length loss and uncapping (75) may cause the long-term culture-related change. Any form of cellular stress, including oxidative stress induced by the *in vitro* expansion time itself, may impair the potency and stability of the MSCs during long-term culture (184).

Declined migratory capacity of MSCs during *in vitro* aging has been reported (185). Given the fact that the cytoskeleton and focal adhesion machinery of MSC are impaired during passage (185), it is not surprising to see the alterations in migratory capacity (186).

Epigenetic dysregulation is another important change for MSC *in vitro* aging. The genes that are involved in self-renewal capacity of MSCs (e.g. Oct4, Sox2) are silenced as a result of epigenetic change (187). Moreover, the expression of histone deacetylases is observed to increase upon *in vitro* aging of MSCs (188), which declines MSC self-renewal by downregulating polycomb group genes and upregulation of jumonji domain containing 3 expression. In terms of DNA methylation regulation, it has been shown that whilst MSCs maintain the overall level of DNA methylation there are

significant changes in specific promoters, including the promoter regions of the homeobox genes (e.g. DLX5, ALX4) and genes that are involved in stem cell differentiation (e.g. RUNX3, BMP10/15) (189).

Collectively, therapeutic benefits are attenuated as aging phenotype, senescence, telomere loss, and decrease of stemness by the decreased growth factor production of senescent MSCs (190).

1.5.3 Malignant transformation of *in-vitro* aged MSCs

Abrogation of the function of DNA repair genes as MSCs age may increase damage in the genome (36), with aged MSCs developing tetraploid and aneuploid karyotypes with significant changes in gene expression (191). Malignant transformation may result from such inadequate DNA repair if this lead to mutation of oncogenes or tumor suppressor genes (192). Passaged murine MSCs have the potential to evolve into sarcoma and fibrosarcoma after *in vivo* transplantation (193, 194). Interestingly, in the mouse *in vitro* tumorigenic transformation seems to be a unique property of MSCs since it is absent in all other stem cells, including hematopoietic stem cells and embryonic stem cells (195). Notably, human MSCs do not show spontaneous transformation into malignant cells after long-term *in vitro* culture (196).

1.6 Aim of the project

Understand the molecular changes of DNA repair in MSCs of murine and human origin, which take place during *in-vivo* (physiological) ageing and during *in-vitro* ageing in the course of massive stem cell expansion. Particular focus is put on ageing related changes affecting the different DNA repair pathways, in particular the mechanisms of HR repair.

Considering the importance of telomere stability for the maintenance of MSCs long-term repopulation potential and stemness, the DNA repair capacity was studied with a special interest for the telomere regions of MSCs.

2 Materials

2.1 Mice

FVB/N mice - - Helmholtz Zentrum Muenchen, Germany. The mouse facility of the Helmholtz Zentrum Muenchen maintained C3H/He mouse stocks in a breeding colony in a controlled environment (22 °C, 55% relative humidity and 12 h day/night cycle). Up to 4 mice of the same gender were housed per cage. A normal diet and water were provided ad libitum (197).

2.2 Cell lines

A human U2OS (198) and a murine osteosarcoma cell line (199) were kindly provided by Dr. Michael Roseman, Institute of Radiation Biology, Helmholtz Zentrum Muenchen.

2.3 Medium and serum mixtures for cell culture

The media and foetal bovine serum (FBS) for cell culture were all bought from Gibco Thermo Fisher Scientific, Darmstadt, Germany. Media were supplemented with 10% FBS before usage (Table 2.1).

Table 2.1: Medium for cell culture

Cells	Basal medium	serum
Human mesenchymal stem cells	α DMEM, GlutaMAX™	Qualified Fetal Bovine Serum (FBS)
Mouse mesenchymal stem cells	DMEM/F-12, GlutaMAX™	MSC Qualified Fetal Bovine Serum (FBS)
Osteoblasts	DMEM, GlutaMAX™	Qualified Fetal Bovine Serum (FBS)
Mouse Osteosarcoma cell line	DMEM, GlutaMAX™	Qualified Fetal Bovine Serum (FBS)

2.4 Enzyme

The enzymes used in this thesis are listed in Table 2.2.

Table 2.2: Enzyme

Enzyme	Catalogue No.	Producer
--------	---------------	----------

Exonuclease III	M1811	Promega, Mannheim, Germany
Proteinase K	03115879001	Roche, Basel, Switzerland
RNaseOUT Ribonuclease Inhibitor	10777019	Thermo Fisher, Darmstadt, Germany
StemPro® Accutase	A1110501	Gibco, Darmstadt, Germany
SuperScript® II Reverse Transcriptase	18064-022	Thermo Fisher, Darmstadt, Germany
Trypsin-EDTA 0.05%	25300-054	Gibco, Darmstadt, Germany

2.5 Antibodies

The antibodies used in this thesis were showed as Table 2.3.

Table 2.3: Enzyme

Antibody	Company	Dilution	Catalogue No.
Primary antibodies			
Anti- γ H2AX, monoclonal, mouse	Merck Millipore Schwalbach, Germany	1:500	Lot. 2064512
Anti-53BP1, polyclonal, rabbit	Novus Biological Littleton, USA	1:500	NB 100-305
Anti-pBRCA1, polyclonal, rabbit	Abcam, England	1:500	ab90528
PML clone, polyclonal, mouse	Upstate, NY, United States	1:500	36.1-104
Secondary antibodies			
Cy3-conjugated sheep anti mouse	Jackson ImmunoResearch, California, United States	1:500	No. 515-165-003
Alexa 488-conjugated goat anti rabbit, goat	Invitrogen, Oregon, United States	1:200	Lot. 659082

2.6 Solutions and buffers

The solutions and buffers used in this thesis were shown in Table 2.4.

Table 2.4: Solutions and buffers

Solution or buffers	Reagents and preparation methods
10 mM Tris-HCl	Dissolve 1.211 g of Trizma Base in 800 ml of ddH ₂ O. Adjust pH to 7.2 with HCl and adjust volume to 1 l with ddH ₂ O. Sterilize by autoclaving.
0.075 M KCl	Dissolve 5.591 g potassium chloride in 1 l of ddH ₂ O. Sterilize by autoclaving.
1 M Tris-HCl	Dissolve 12.11 g Trizma Base in 100 ml ddH ₂ O. Adjust to pH 7.4 with HCl. Sterilize by autoclaving.

20× SSC buffer	Dissolve 175.3 g NaCl and 88.2 g sodium citrate in 800 ml ddH ₂ O. Adjust pH to 7.0 with HCl and adjust volume to 1 l. Sterilize by autoclaving.
5 M NaCl	Add 14.6 g NaCl and ddH ₂ O up to 50 ml.
70% Formamide	Mix 20 ml 20× SSC buffer and 10 ml ddH ₂ O with 70 ml deionized formamide.
De-staining solution	60 ml 100% Ethanol + 40 ml 96% Acetic acid
Blocking solution for immunocytochemistry	100 ml PBS + 1 g BSA + 2.5 ml 20% Triton X-100
Exonuclease Mix	In 88.5 µl H ₂ O, add 10 µl Exo III 10× Buffer and 1.5 µl Exo III (final concentration of 3U/µl)
Fixative solution for CO-FISH	Mix 300 ml Methanol with 100 ml Acetic Acid, keep mixture on ice.
Oil Red O stock solution	0.5 g Oil Red O + 100 ml 2-Propanol
Oil Red O working solution	60 ml Stock solution + 40 ml Distilled water
PBS+	BSA 1 g + Glycine 0.15 g + PBS 100 ml
PNA Probe mix	200 µl Herring sperm DNA, 100 µl 10 mM Tris HCl pH 7.2, 100 µl BSA (concentration 10 µg/ml) and 4.8 µl PNA-Probe (Cy3 or Alexa488; final concentration 1.2 µg/ml), followed by 700 µl 70% formamide. Warm working solutions of PNA probes (20-50 µg/ml) at 80 °C while shaking
Senescence staining solution (pH 6)	1.42 g di-Sodium hydrogen phosphate dehydrate (40 mM) + 200 ml Distilled water + 1.75 g NaCl (150 mM) + 81.32 mg MgCl ₂ (2 mM) + 400 mg II Hexacyanoferrate (5 mM) + 320 mg Hexacyanoferrate III (5 mM) + 100 µl X-gal (50 mg/ml) to 5 ml of Buffer
Substrate solution for alkaline phosphatase staining	1 sigma fast BCIP®/NBT tablet + 10 ml ddH ₂ O
TNT solution	For 150 ml, mix 129.3 ml ddH ₂ O, 15 ml 1M Tris-HCl (pH 7.4, 100 mM final), 4.5 ml 5 M NaCl (150 mM final) and 1.2 ml of Tween-20.
Washing buffer for alkaline phosphatase staining	0.05% TWEEN® 20 in DPBS without calcium and magnesium
Propidium iodide /Trion X-100 solution	10 ml of 0.1% (v/v) Trion X-100 (prepared in PBS) add: 200 µl of 1 mg/ml Propidium iodide stock, 2 mg DNase-free RNase A

2.7 Chemicals

The chemicals used in this thesis were listed in Table 2.5.

Table 2.5: Chemicals

Chemicals	Company
3% Formaline (3% PFA)	Sigma-Aldrich, Taufkirchen, Germany
5-Brom-2-desoxyuridin (BrdU)	Sigma-Aldrich, Taufkirchen, Germany

5-Bromo-4chloro-3-indolyl β galactopyranoside	MP Biomedicals, Germany
Acetic Acid	Merck, Schwabach, Germany
Albumin from bovine serum (BSA)	Sigma-Aldrich, Taufkirchen, Germany
Alexa488-labeled G-rich telomere probe	Panagene, Daejeon, South-Korea
Chloroform	Merck, Schwabach, Germany
Citric Acid	Sigma-Aldrich, Taufkirchen, Germany
Colcemid	Gibco, Life Technologies, Darmstadt, Germany
Concentrated hydrochloric acid	Merck, Schwabach, Germany
Cys3-labeled C-Rich telomere probe	Panagene, Daejeon, South-Korea
Cytochalasin B, 0.5 μ g/ml	AppliChem, Darmstadt, Germany
DAPI nuclei staining, 150 ng/ml	Merck, Schwabach, Germany
Deionized Formamide	AppliChem, Darmstadt, Germany
DI-Sodiumhydrogen phosphate dihydrate	Merck, Schwabach, Germany
DMEM	Gibco, Life Technologies, Darmstadt, Germany
DMSO	Sigma-Aldrich, Taufkirchen, Germany
Ethanol	Merck, Schwabach, Germany
Exonuclease III	Promega, Germany
Fetal Bovine Serum for MSCs	Gibco, Life Technologies, Darmstadt, Germany
Formalin deonised	AppliChem, Darmstadt, Germany
Giemsa	Merck, Schwabach, Germany
Glycine	Cal Biochem, EMD Millipore, Germany
HCl	Merck, Schwabach, Germany
Hering sperm DNA	Invitrogene, Darmstadt, Germany
Hoechst 33342	Merck, Schwabach, Germany
Isopropanol	Merck, Schwabach, Germany
Magnesium Chloride	Sigma-Aldrich, Taufkirchen, Germany
MAXWELL miRNA kit	Promega, Mannheim, Germany
Methanol	Merck, Schwabach, Germany
Mounting Medium with DAPI (Hoechst)	Sigma-Aldrich, Taufkirchen, Germany
NaCl	Merck, Schwabach, Germany
Oligo(dT)	Promega, Mannheim, Germany
Opti-MEM	Gibco, Life Technologies, Darmstadt, Germany
Paraformaldehyde	Merck, Schwabach, Germany
Phosphate buffer saline (PBS)	Gibco, Life Technologies, Darmstadt, Germany
Potassium chloride	Merck, Schwabach, Germany
Potassium Hexacyanoferrate II	Sigma-Aldrich, Taufkirchen, Germany
Potassium hexacyanoferrate III	Sigma-Aldrich, Taufkirchen, Germany
Propidium iodide (PI)	Sigma-Aldrich, Taufkirchen, Germany

Proteinase K	Roche, Basel, Switzerland
Random primers	Promega, Mannheim, Germany
Reverse transcriptase SuperScript® II	Invitrogene, Darmstadt, Germany
Reverse transcriptase SuperScript® III	Invitrogene, Darmstadt, Germany
RNase OUT	Invitrogene, Darmstadt, Germany
Rock inhibitor Y-27632	Tocris Bioscience, Bristol, UK
Sodium chloride	Merck, Schwalbach, Germany
Stem pro Accutase	Gibco, Darmstadt, Germany
Triton-X-100	AppliChem, Darmstadt, Germany
Trypsin	Invitrogene, Darmstadt, Germany
Tween 20	Sigma-Aldrich, Taufkirchen, Germany

2.8 Consumables

The consumables used in this thesis are listed in Table 2.6.

Table 2.6: Consumables

Components	Company
100 ml/200ml Glass Bottles	Schott, Mainz, Germany
96-well plates black	Neolab, Heidelberg, Germany
Adhesive PCR foil seals	Thermo Fisher Scientific, Germany
Aluminium 1.5 ml Eppendorf holder	Eppendorf, Hamburg, Germany
Cell culture Flasks (T25, T75)	Greiner Bio-One GmbH, Frickenhausen, Germany
Cell scraper (25 cm)	Sarstedt, Nuembrecht, Germany
Coverslips	Thermo Fisher Scientific, Darmstadt, Germany
Eppendorf Tubes	Eppendorf, Hamburg, Germany
Falcon tubes (50 ml, 15 ml)	Greiner, Frickenhausen, Germany
Filter paper Whatman 595 125 mm	Whatman GmbH, Dassel, Germany
Filter tips TipOne®	STARLAB GmbH, Hamburg, Germany
Injection needle 0.3 × 12 mm	B.Braun, Melsungen, Germany
MicroAmp® Optical adhesive film	Thermo Fisher Scientific, Darmstadt, Germany
Microscope slide	Thermo Fisher Scientific, Darmstadt, Germany
Needle 20 G, 27 G 0.4 mm	Terumo, Eschborn, Germany
Parafilm®	Sigma-Aldrich, Taufkirchen, Germany
Petri plates (10 cm)	Thermo Fisher Scientific, Darmstadt, Germany
Pipette tips 10, 20, 100, 200, 1000 µl	Eppendorf, Hamburg, Germany
Reaction tubes 1.5 ml, 2 ml	Eppendorf, Hamburg, Germany
Slides, 76 × 26 mm	Carl Roth, Karlsruhe, Germany
Syringe, single-use 1, 5, 10, 50 ml	Henke-Sass Wolf, Tuttlingen, Germany

Vertical staining jar with cover, 50 ml	Ted Pella, California, United States
Wheaton staining dishes	Ted Pella, California, United States

2.9 Technical Equipment

The technical equipment used in this thesis are documented in Table 2.7.

Table 2.7: Technical equipment

Technical Equipment	Company
137 Cs-γ radiation source HWM-D-2000	Walschmiller ENgeneering, Germany
Analytical balance	Kern&Sohn GmbH, Balingen, Germany
Apotome Microscope	Carl Zeiss, Jena, Germany
Axio imager M1 microscope	Carl Zeiss, Jena, Germany
Cell Counter	BeckmanCoulter, Krefeld germany
Centrifuge 3k15	Sigma, Darmstadt, Germany
Dispenser Multipette® plus	Eppendorf, Hamburg, Germany
Electric pipet controller	Thermo Fisher Scientific, Germany
Electronic pH meter	Thermo Fisher Scientific, Germany
Function line incubator with O ₂ regulation	Heraeus, Osterode, Germany
Heating block Thermomixer compact	Eppendorf, Hamburg, Germany
Heating plate	Thermostat, Frankfurt, Germany
Keyence BZ 9000 Microscope	Keyence, Frankfurt, Germany
Magnetic stirrer	IKA-Werke, Staufen, Germany
Microscope Axiovert 25	Carl Zeiss, Jena, Germany
Microscope Laser-Scanning IX81	Olympus, Hamburg, Germany
O ₂ / CO ₂ incubator	Sanyo, ETTEN-LEUR, The Netherlands
Olympus CK ₂ Microscope	Olympus, Hamburg, Germany
Oven for sterilization	Memmert, Büchenbach, Germany
pH meter Lab850	SI Analytics GmbH, Mainz, Germany
Shaker	Rotatest, Essex, UK
StepOnePlus Real-Time PCR System	Applied Biosystems, Darmstadt, Germany
Sterile working bench	Thermo Fischer Scientific, Frankfurt, Germany
TECAN Infinity M200 Microplate Reader	Tecan, Mnnedorf, Switzerland
Thermal Cycler Veriti® (PCR cycler)	Applied Biosystems, Darmstadt, Germany
UV Oven	Vilber, Eberhardzell, Germany
Vortexer Reax top	Heidolph Instruments, Schwabach, Germany
Z Series Coulter Counter - Z1	Beckman Coulter, Krefeld, Germany
XStrahl RS225 device	XStrahl Ltd., Surrey UK
Maxwell 16 AS2000 extraction machine	Promega, Mannheim, Germany

2.10 Software

Software used in this thesis are shown in Table 2.8.

Table 2.8: Software

Software	Company
Axiovert imager	Zeiss Axiovert, Frankfurt, Germany
BZ-II-Analyzer	Keyence, Frankfurt, Germany
clusterProfiler (Version 3.16.0)	Institute of Life and Health Engineering, Jinan University, China
Cytoscape (Version 3.78)	Institute of Systems Biology, Seattle, United States
DEseq2 (Version 1.28.1)	Dana Farber Cancer Institute and Department of Biostatistics, Harvard School of Public Health, Cambridge, United States
edgeR (Version 3.30.3)	The Walter and Eliza Hall Institute of Medical Research, Parkville, Austria
FASTQC (Version 0.11.8)	Babraham Bioinformatics, Cambridge, UK
Genefilter (Version 1.70.0)	Dana-Farber Cancer Institute, Cambridge, United States
GenomicAlignments (Version 1.24.0)	Genentech, Inc. California, United States
GenomicFeatures (Version 1.40.0)	Genentech, Inc. California, United States
ggplot2 (Version 2.2.1)	RStudio, Inc. Boston, United States
GSEA (Version 4.03)	Broad Institute, Cambridge, United States
org.Hs.eg.db (Version 3.11.4)	Fred Hutchinson Cancer Research Center, Seattle, United States
Pheatmap (Version 1.0.12)	University of Tartu, Tartu, Estonia
R (Version 3.4)	R Foundation for Statistical Computing
RColorBrewer (Version 1.1.2)	University of Vienna, Vienna, Austria
reshape2 (Version 1.4.4)	Iowa State University, Iowa, United States
hisat2 (Version 2.1.0)	Johns Hopkins University School of Medicine, Baltimore, United States
TxDb.Hsapiens.UCSC.hg19.knownGene (Version 3.2.2)	Fred Hutchinson Cancer Research Center, Seattle, United States

2.11 Primers

Oligonucleotides were obtained from Genscript Corporation (NJ, USA) as a stock of 100 pmol/μl. The primer sequencing was shown in Table 2.9.

Table 2.9: Primer sequences

Primer	Forward	Reverse
BRCA1 (human)	CTGCTCAGGGCTATCCTCTC	TGGCTCCCATGCTGTTCTAA

RAD51 (human)	CCACAACCCATTTACGGTT	GCAACAGCCTCCACAGTATG
RAD54L (human)	GTAGAGCGCCACTTCTCTCT	GTGCAACCTGTCATGTGTGT
RAD54B (human)	GCACCTACACTGGCAACATT	AGAACAGCATCACCTTCCCA
KIF4 (mouse)	GAACTCACACAGGCGAGAAA	AAAGGCCCTGTCACACTTCT
BMI1 (mouse)	GTCAGCTGATGCTGCCAAT	CCTCTTCTCCTCATCTGCAA
NESTIN (mouse)	CAACTGGCACACCTCAAGAT	GTGTCTGCAAGCGAGAGTTC
TBP (mouse)	ACTTCGTGCAAGAAATGCTG	CTTCACTCTTGGCTCCTGTG

3 Methods

3.1 Cell culture

3.1.1 Isolation and culture of primary murine mesenchymal stem cells

Murine bone marrow was isolated from female C3H/He mice of 3 or 18 month of age. Mice were sacrificed by CO₂ asphyxiation to obtain bone marrow. Both hind and fore limbs of mice were dissected to harvest the whole bone marrow. Adherent soft tissues were scraped from femur, tibia and humerus. The ends of the bone were removed. The bone marrow was aspirated by flushing each bone cavity with 1 ml ice-cold DPBS through a 27-gauge needle, and the aspirates from all bones of a mice were collected in a 15 ml Falcon tubes.

After gently passing the bone marrow suspension 5 times through a 1ml Eppendorf pipette, the resulting single cell solution was cooled on ice. The cell suspension was centrifuged for 5 min at 300g and the resulting cell pellet resuspended in 1 ml DMEM/F12, GlutaMAX medium supplemented with 10% MSC qualified FBS. Cell numbers were determined using a coulter counter and the suspended cells were plated at the density of 3.5×10^5 cells per cm² in T25 flasks. The cell cultures were maintained in the incubator at 37 °C in a water-humidified atmosphere under low (2%) O₂. The supernatant was replaced with fresh medium after 4 hours to remove non-adherent cells. The floating cells removed with the medium were incubated in a fresh T25 flask to increase the yield of mMSCs by allowing any remaining cells to contact plastic surface. The medium was changed after a further 7 days incubation for both the first batch and second batch of MSCs (the floating cells). The cells were maintained in the incubator and medium was changed once per week. All the procedures were performed under aseptic conditions.

The cells were passaged at around 70%-80% confluency. For this, medium was aspirated and the adherent cells rinsed twice with pre-warmed DPBS to remove traces of serum. 1 ml StemPro Accutase was pipetted onto the cells followed by a 5 min incubation at 37°C. 1 ml of fresh medium with PBS was added to detach the cells. The cells were re-plated with 1:3 split ratio.

3.1.2 Isolation and culture of primary human mesenchymal stem cells

Human MSCs were isolated and firstly cultured by department of Trauma and Reconstructive Surgery of the Ludwig-Maximillian University. Bone marrow derived human MSCs were isolated from the femoral heads of donors recruited at the Clinic for General, Trauma and Reconstructive Surgery of the Ludwig-Maximillian University. Cells were isolated by washing the surplus bone graft material with phosphate buffered saline (PBS, pH 7.4). The fragmented bone material was incubated with 250 U/ml collagenase II (Worthington) in DMEM (Life Technologies) three times for 10 min at 37°C and the supernatant containing released bone marrow cells collected. To remove bone fragments the pooled suspensions were filtered with a 100 µm cell strainer. After centrifugation at 500×g for 5 min, the cell pellet was resuspended in culture media of αMEM (Thermo Fisher Scientific) supplemented with 10% fetal bovine serum (FBS, Life Technology) and 40 IU/ml penicillin/streptomycin (Life Technology). Cells were kept growing at 37 °C in a humidified incubator at 5% CO₂ and ambient oxygen. After three days cultivation, non-adherent cells were removed by washing with PBS for three times.

For *in vitro* expansion and aging of the hBM-MSCs, cells were passaged every 7 days over a period of 10 weeks in antibiotic-free growth medium (see above). From week 2 till week 6, cells were split in a 1:3 ratio, and from week 7 till week 10 in a 1:2 ratio. The entire aging protocol therefore covered 8 passages, and from the splitting ratios it can be estimated to be equivalent to approximately 10.9 cell divisions ($\log_2(3) * 4 + 3 = 10.9$).

3.1.3 Cell counting

Z1 Series COULTER COUNTER (Beckman Coulter, USA) was used to determine the cell numbers (Figure 3.1). Cell suspension was diluted with 0.9 % NaCl solution (200 µl into 7.8 ml). The diluted cell suspension was subjected to Z1 Series COULTER COUNTER for three times to obtain the average cell numbers. The final cell number was calculated by multiplying the measured cell concentration with the total volume of the cell suspension.

3.1.4 Freezing and thawing of human and mouse MSCs

StemPro Accutase reagent was used to detach mouse/human MSCs from plastic surfaces. In each T75 flask 1 ml StemPro accutase was added and incubated for 3 min at room temperature. Cell fraction was collected in 15 ml Falcon tube for 5 min centrifugation at 300 g. Following centrifugation, cells were counted and resuspended at 2×10^6 cells/ml in STEM-CELLBANKER reagent. The cell suspension was transferred into 1 ml cryo tubes and transferred to a -80 °C freezer. Later cells were moved to liquid nitrogen for long time storage.

For thawing the cryo tube was rapidly warmed in a 37 °C water bath for 2 min with gentle rotation to thaw the frozen cells. The cell supernatant was then transferred into a 15 ml Falcon tube. 10 ml medium was added to dilute the cell supernatant. After gentle mixing the suspension was centrifuged at 300 g for 5 min. The supernatant was discarded and the cell pellet was resuspended with 4 ml fresh medium into a fresh T25 flask. The medium was replaced with pre-warm fresh medium 24 hours later to remove residual stem cell banker reagent.

3.1.5 Colony analysis

Giemsa staining was used to detect colonies of murine MSCs during the colony formation assay. The medium was removed from the flasks and the colonies were washed with DPBS for twice. 100% ethanol was used to fix the cells for 15 min. The ethanol was aspirated and the flask was air-dried for 1 h. A 5% Giemsa solution (5% Giemsa in PBS) was added to stain the cells. The Giemsa solution was removed after 15 min and the cells were washed with water. A bright-field microscope was used to observe the colonies after overnight drying.

The colony forming ability of mMSCs was assessed by the colony formation assay. After isolation of mMSCs from one murine bone marrow, the whole cell supernatants were suspended in 5 ml cold PBS. The 5 ml cell suspension were separated into 1 ml per Eppendorf tube into 5 groups. Each group of cell suspension were irradiated with 0 Gy, 0.5 Gy, 1 Gy, 2 Gy, 4 Gy at room temperature. Cells were then seeded into wells. The cultures were continued for 14 days to obtain colonies large enough for counting at 10x magnification. 100% ethanol was used to fix the cells, followed by staining with Giemsa stain. The number of colonies was counted under the Olympus SZX12

microscope to assess the clonogenicity of MSCs. A group of cells with a minimum 25 cells was considered as a colony.

3.2 Irradiation

3.2.1 Gama-irradiation

Gamma-irradiation was performed with a ^{137}Cs gamma-source HWM D-2000 irradiator. The dose rate was 0.5Gy/min. Control cells were taken into the radiation room without exposing them to gamma-irradiation. The whole irradiation process was performed at room temperature. After irradiation the cells were returned to the incubator in 2% O_2 at 37 °C.

3.2.2 X-ray irradiation

X-ray irradiation was performed in a closed cabinet XStrahl RS225 device operating at 195 kVp, 1.14 Gy/min dose rate and 3 mm Al filter. Cells were kept at ambient temperature during irradiation, and control cells were treated identically apart from not placing them inside the radiation source.

3.3 Real-Time Polymerase Chain Reaction (RT-PCR)

3.3.1 RNA extraction and reverse transcription

The cultured human/mouse MSCs were washed twice with cold PBS. MSCs were collected using a cell scraper and centrifuged for 5 min at 300g to obtain cell pellets. MAXWELL miRNA kit was used to automatically purify RNA using a Maxwell 16 AS2000 extraction machine (following the manufacturers recommended protocol. 200 μL of prechilled homogenization buffer was added to the cell pellet and the tube gently vortexed. 200 μL of lysis buffer and 15 μL of proteinase K solution (20mg/ml) from this Kit were added in the tube followed by gently vertexing. DNase I (from the kit) was added Elution tubes filled with 50 μL RNA-free water were inserted in the collection rack of the MAXWELL machine. The program “microRNA extraction” was selected to obtain the whole RNA from cell samples.

3.3.2 RNA concentration measurement

A Tecan infinite M200 microplate reader was used to determine the RNA concentration by absorbance. Two μl of RNA solution was placed on the NanoQuant plate to measure the absorbance of each sample. RNA-free water was used as the blank control. A_{260nm} was taken to determine the concentration and A_{280nm} was taken to assess the quality. The ideal A₂₆₀/A₂₈₀ ratio for RNA is 2. The A₂₆₀/A₂₈₀ ratio between 1.8-2.0 is acceptable. Other ratios may indicate contamination in RNA solutions.

3.3.3 Reverse transcription

Reverse transcription was performed using RNA as a template and synthesizing the cDNA. The newly synthesized cDNA can be used to perform Real-Time PCR reaction and quantify expression of various transcript. A 20- μL final reaction volume was used as listed in Table 3.1. 100 ng of each RNA sample were transferred into a 1 ml nuclease-free microcentrifuge tube. Vacuum was used to evaporate the water from the samples. 0.5 μl random primers and 0.5 μl Oligo(dT), 1 μl dNTP Mix (10 mM each) and 10 μl RNA-free water were added into each tube. Samples were denatured at 65 °C for 10 min and quickly chilled on ice. The contents of the tube were collected by brief centrifugation and 5 \times First-Strand Buffer 4 μl , 0.1 M DTT 2 μl and RNaseOUT (40 units/ μL) 1 μl added. Contents were mixed gently and incubated at 42 °C for 2 min. 1 μl (200 units) of SuperScript II RT was added and samples were mixed by pipetting gently. The incubation for reverse transcription was run at 42 °C for 50 min, and the reaction inactivated by heating at 70 °C for 15 min.

Table 3.1: Reverse transcription reaction mixture

Reagent	Quantity (μl)
FS Buffer	4
dNTPs (10 μM)	1
DTT (0.1 M)	2
SuperScript® II Reverse Transcriptase	1
RNaseOUT	1
Random primers	0.5
Oligo(dT)	0.5
Nuclease-free water	10
Total volume	20

3.3.4 RT-PCR reaction

qRT-PCR was applied to measure the relative amount of the mRNA transcripts of a particular gene. The cDNA derived from the mRNA by reverse transcription was added as template. Sequence-specific primers were used to amplify each gene of interest. A 20 μ L reaction system was used for all experiments. The reaction components are described in Table 3.2 below:

Table 3.2: RT-PCR reaction mixture

Reagent	Quantity (μ l)
Forward primer (5pmol/ μ l)	1
Reverse primer (5pmol/ μ l)	1
Nuclease free water	8
Template cDNA (100ng)	2
2 x SYBR-GREEN master mix	10
Total volume	20

20 μ L of qRT-PCR mixture that contains the template and reaction reagents was added into 96-well StepOnePlus plate. A MicroAmp Optical Adhesive film was used to cover the plate to avoid the evaporation of samples. Following a brief centrifugation, the samples were located at the bottom of the wells. The StepOnePlus Real-Time PCR System machine detected the threshold cycle (C_T) values during the reaction. A pre-designed PCR cycle program was applied to run the reaction. The detailed cycle time and temperature was listed in Table 3.3.

The C_T value was defined as the cycle value at which the amplification reaching a set threshold. cDNA template amplified in 40 \times cycling step. In each cycle, the PCR product was quantified and recorded to obtain the C_T curve. To determine the specificity and quality of RT-PCR reaction, A melting curve analysis was performed following the cycling program. Normally, a single peak for an amplified product of gene of interest is present in the melting curve (Figure 3.1). However, if primer-dimers or non-specific amplifications exist, multiple peaks are visual in melting curves of both sample and No Template Control (NTC). The data were collected from StepOnePlus instrument once the program was finished. Three technical replicates were used to obtain the average C_T value of samples. The data (C_T value and melting curve) was collected from StepOnePlus instrument and analysed using StepOne software v2.3.

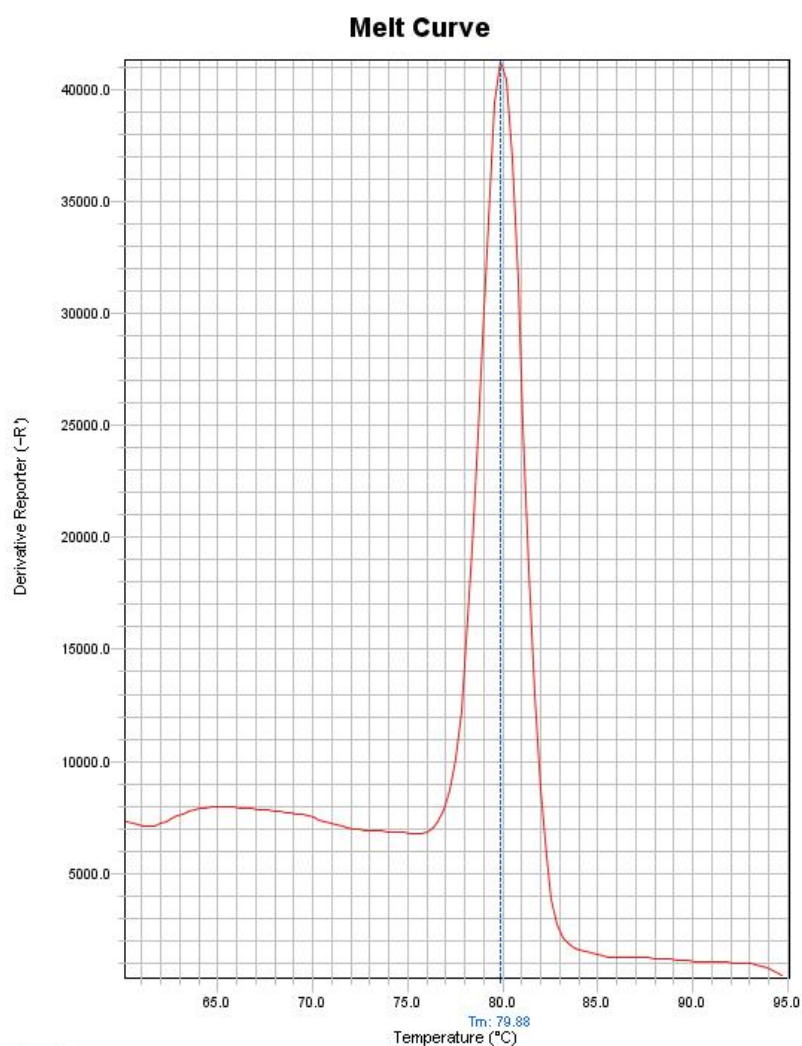


Figure 3.1: Real-Time PCR melting curve.

The positive quality control was performed with pooled embryonic cDNA. The housekeeping genes TBP and GAPDH were employed as control amplifications to quantify differences in the content of cDNA. A negative control (as the NTC) (RNase-free water) was used to detect unspecific amplification.

Table 3.3: RT-PCR reaction program

Steps	Temperature	Time
Initial denaturation (holding stage)	95 °C	10 min
40× Cycling stage: Cycling stage-denaturation	95 °C	15 sec
40× Cycling stage: Cycling stage-annealing and elongation	60 °C	1 min
Melting curve Stage I	95 °C	15 sec
Melting curve Stage II	60 °C	1 min
Melting curve Stage III	95 °C	15 sec

3.3.5 Analysis of Real-Time RT-PCR

The DNS binding dye, SYBR green only binds to the double-stranded DNA amplification product and emits a fluorescence signal upon binding. After each amplification cycle, the fluorescence signal in each tube was detected after excitation by a blue laser by the StepOnePlus qRT-PCR machine. The green fluorescence signal is proportional to the amount of double stranded PCR product. StepOne software v2.3 was used to load and analysis the raw data. Each gene was adjusted for the baseline and threshold.

The threshold was set above the background fluorescence signal and below the plateau of the reaction within a linear region of the curve (Figure 3.2). The threshold cycle (C_T) value was defined as the cycle value at which the amplification reaching a set threshold. The ΔC_T method was applied to calculate the relative quantification of the target template between all samples. The formula is described as follows:

$$\Delta C_{T \text{ sample}} = \Delta C_{T \text{ Target gene}} - \Delta C_{T \text{ Housekeeping gene}}$$

Target gene: The target DNA template expression to be measured. $\Delta C_{T \text{ sample}}$ is used to normalize for the amount of nucleic acid that is used in each sample. Then, $\Delta \Delta C_{T \text{ sample}}$ is calculated as follows: $\Delta \Delta C_{T \text{ sample}}$ describes the difference between the average $\Delta C_{T \text{ sample}}$ value of the replicates from samples in the two groups.

$$\Delta \Delta C_T = \Delta \Delta C_{T \text{ sample1}} - \Delta \Delta C_{T \text{ sample2}}$$

Lastly, the fold change of target gene was calculated by:

$$\text{Fold change} = 2^{\Delta \Delta C_T}$$

Hence, the fold change in the gene expression level of the sample was normalized to the housekeeping gene (by the step of $\Delta C_{T \text{ sample}}$) and was relative to the control group (by the step of $\Delta \Delta C_T$).

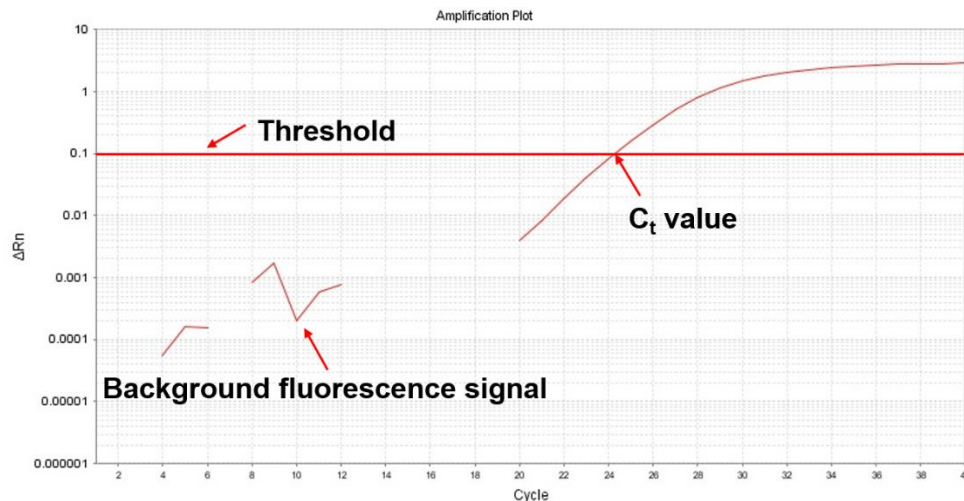


Figure 3.2: Real-Time PCR amplification plot. A graph showing a set threshold, background fluorescence and a baseline start for the sample after the Real-Time PCR reaction.

3.4 The pipeline for RNA-seq analysis in our project

The FASTQ files were downloaded from GEO database (GSE59966). Each biological replicate involved young and old samples from one donor (Figure 3.3).

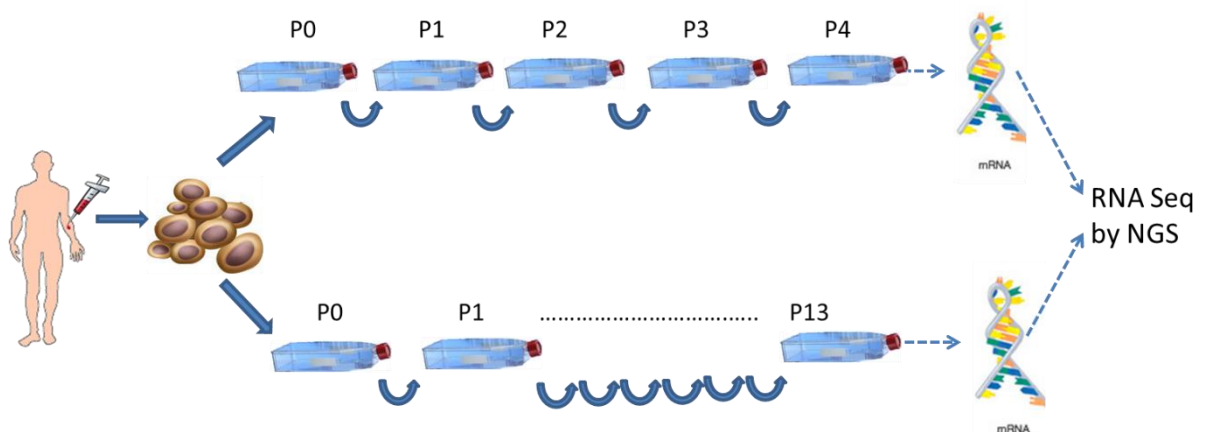


Figure 3.3: Experimental design for transcriptome analysis. Human MSCs from passage 4 (young) and passage 13 (aging) were used to analyze differential mRNA expression by NGS transcriptome profiling.

The detailed pipeline for the RNA-seq analysis in our project is shown below (Figure 3.4): The obtained sequencing data was stored as FASTQ files. “FASTQC”

software was applied to perform the quality control step (200). A quality control plot was plotted by FASTQC, showing the average quality score across all bases in the library that used in the project (Figure 3.5). The FASTQ files contain millions of short reads with the nucleotide sequence information and a quality score at each nucleotide sequence position. A reference genome (here we applied hg19 human genome) was used to align these reads. Paired FASTQ files were used to perform “hisat2” alignment for paired FASTQ files (201). BAM files were obtained after the alignment step. Following mapping of reads to genome by “hisat2”, the gene count matrix (with the row names indicate the gene ID and the column names represent the sample information) was created by the “GenomeAlignments” package in R (202). The differently expressed gene (DEG) analysis was performed with the “DESeq2” package (203). For our project, we specified “~*Donor* + *Passage*”, which means that the test was applied for the effect of “*Passage*”, controlling for the effect of “*Donor*”. The estimation of size factor that control for differences in the library size of each files, the estimation of dispersion of each gene and a generalized linear model are shown during the analysis. Functional pathway analysis included several kinds of methods such as Gene ontology (GO) analysis, KEGG (Kyoto Encyclopedia of Genes and Genomes) pathway analysis, Gene set enrichment analysis (GSEA) and others. Gene ontology enrichment is applied for interpreting sets of genes making use of the GO classification, in which genes are assigned to a set of predefined gene sets depending on their functional characteristics. The GO terms have three categories: biological process (BP), molecular function (MF), and the cellular component (CC). Gene ontology (GO) and KEGG analysis were done with the “clusterProfiler” package (204). GSEA analysis was performed with the whole transcriptome with the hallmark of *h.all.v7.0.entrez.gmt* by the GSEA software from Broad institute (<https://www.gsea-msigdb.org/gsea/index.jsp>). The detailed workflow and codes are in the supplementary section.

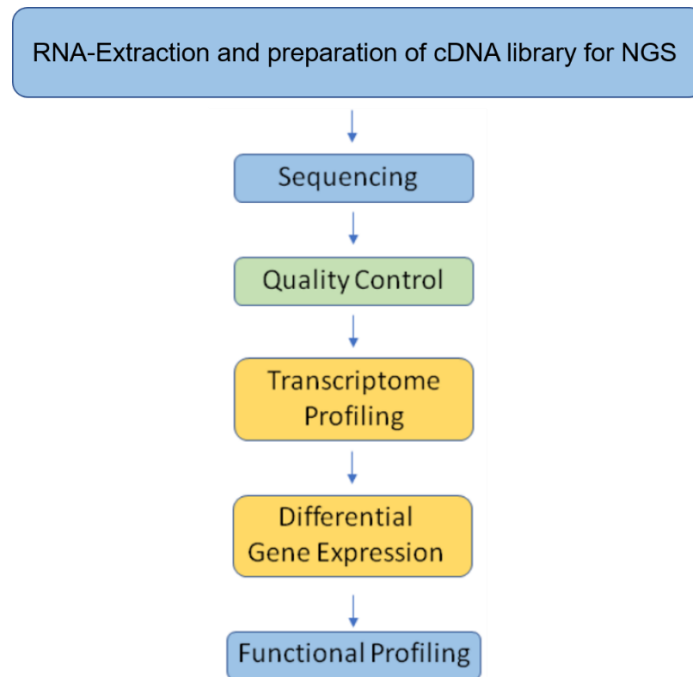


Figure 3.4: The pipline of RNA-seq for our project.

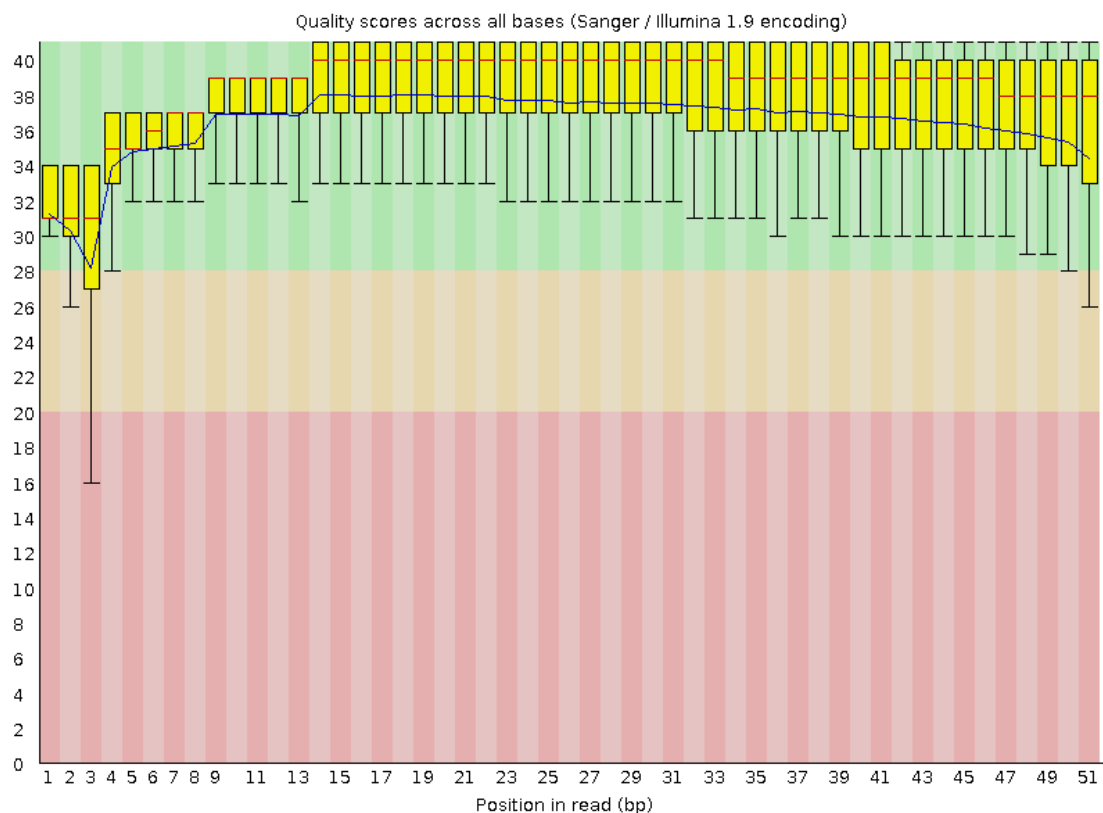


Figure 3.5: An output plot from FASTQC software showing the quality of the FASTQ file used in the project. Green bar means the bp position pass through the quality while red bar represents the bp position does not pass through the quality check. Yellow means the intermediate potential between pass and not pass.

3.5 Alkaline phosphatase

Weak alkaline phosphatase (AP) enzyme activity is found in undifferentiated MSCs, whereas differentiated osteoblasts show high alkaline phosphatase activity. Therefore, AP activity is an indicator of differentiation into osteoblasts. The enzymatic reaction of BCIP/NBT tablet stains the cells dark blue when AP is active, thus is an easy way to confirm and visualize the AP activity in cells. The presence of the enzyme alkaline phosphatase during osteoblastic differentiation reacts with BCIP/NBT and produces an insoluble violet blue coloured precipitate. This can be used to detect MSCs that have produced differentiated daughter cells. The mouse cells were incubated for 10 days to allow the growth of colonies. On day 10, the alkaline phosphatase staining was performed. Following a wash with DPBS, the cells were fixed with 500 μ L of 4% paraformaldehyde for 2 min. Fixed cells were washed with 1 ml of washing buffer (0.05% TWEEN® 20 in DPBS w/o calcium and magnesium) and incubated with BCIP®/NBT substrate at RT for 10 min.

3.6 Oil red O double-staining

The mouse cells were incubated for 21 days. On day 10 and day 21, oil red O double-staining was performed. Following a wash with DPBS, the cells were fixed with 500 μ L of 4% paraformaldehyde for 2 min. Oil Red O staining can stain lipid vacuoles with a bright red colour. In our analysis, we developed oil red O double-staining to check the spontaneous differentiation of a single colony.

After a wash 2 ml of Oil Red O staining solution was used to stain the cells. The working solution was discarded and the cells were washed with still water after 45 min incubation at RT. In this study cells were subjected to a double staining by combining Oil red O and alkaline phosphatase staining. Cells with osteoblast differentiation exhibit blue color for alkaline phosphatase activity. Bright red lipid vacuoles appear in adipocytes due to staining with Oil Red O.

3.7 Immunofluorescent staining

Immunofluorescent staining (IF) was used to check the presence of promyelocytic leukemia (PML) bodies and DNA repair foci. The cells were cultured on sterile Superfrost microscope slide (Carl Roth GmbH, Germany) for at least 1 day in the incubator to allow attachment and proliferation. After different timepoint of irradiation for each experiment, the medium was discarded and cells were washed with DPBS for

twice. After washing cells were fixed with histo-fix for 10 min at RT. 3 × 5 min wash with PBS was done after the aspiration of 4% Paraformaldehyde (PFA) (histo-fix). The PFA-fixed cells were covered with 1% blocking buffer for one hour in a humidified chamber. After blocking, 100 µl of a diluted solution of the primary antibody was used and the slides were incubated in the cold room at 4 °C. The primary antibodies were diluted in 1% blocking buffer (dilution ratio: 53BP1: 1: 200, pBRCA1: 1: 200, and γH2AX: 1: 400) to prepare the primary antibody solution. Double staining was performed with 53BP1 + γH2AX antibodies and γH2AX + pBRCA1 antibodies. After an overnight incubation with the primary antibody cells were washed with PBS twice to remove residual primary antibody. Secondary antibody was diluted 1:500 in 1% blocking buffer and 100µl of this solution added to the cells for 2 hours at RT. Finally, the slides were washed with DPBS twice. The cells were counterstained with 200 µl of DAPI solution for 5 min at room temperature to visualize the nuclei. After 10-min incubation at RT, the DAPI solution was removed, and slides were rinsed 2x with PBS and covered with Vectashield (Vector Labs, Burlingame, CA, USA) and glass coverslips. A Laser Scanning Microscope (Keyence, Itasca, IL, USA) was used to capture the pictures for IF staining (Figure 3.8). The analysis of the stained pictures was performed with Keyence analyzer software.

3.8 Analyzing of foci

Co-localized γH2AX and 53BP1 foci or pBRCA1 and 53BP1 foci were counted automatically using the Keyence BZ-9000 fluorescence microscope software. Images of stained cells were taken with an exposure time of 1/3 sec for the green and red channel and 1/10 sec for the blue channel. The images were imported into the BZ-II Analyser software for further analysis. Haze reduction was performed and a black balance was used to minimize the unspecific background signal (Figure 3.6). For the analysis of co-localized foci, only foci with co-localized signal were counted. For each experiment at least 50 cells were counted for each group. For the analysis with the Keyence analyzer software only foci with co-localized γH2AX and 53BP1 signals were scored automatically by a threshold (of 60) correlated to the size of the foci (Figure 3.9).

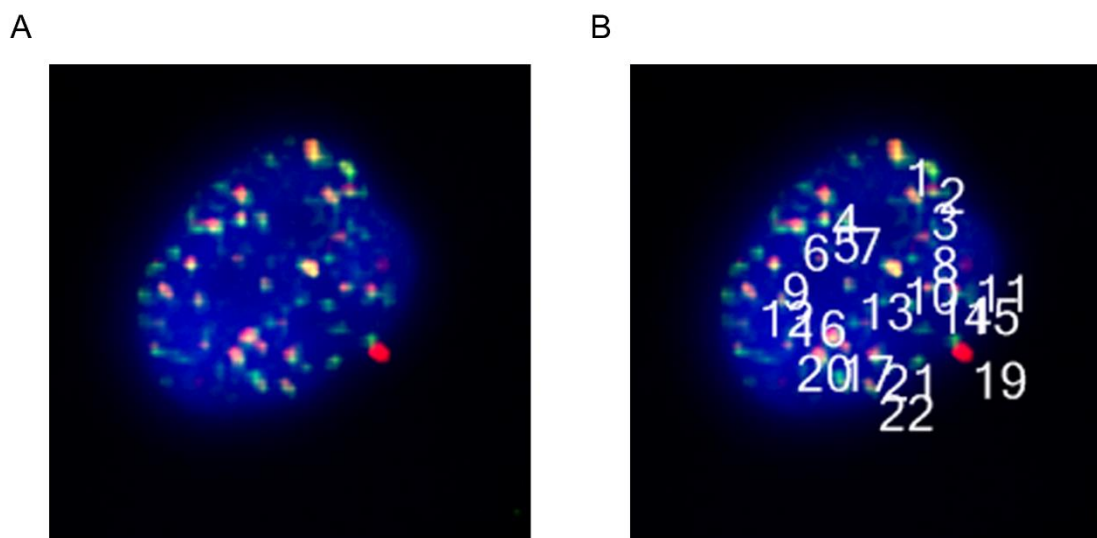


Figure 3.6: Quantification of γ H2AX and 53BP1 co-localized foci. Single nuclei were defined and DNA repair foci were automatically scored by a threshold (Extraction setting by brightness) with the Keyence counting software. Left: The original plot. Right: The co-localized γ H2AX and 53BP1 signals were scored automatically by Keyence analyzer software.

3.9 Chromosome orientation fluorescence in situ hybridization (CO-FISH) staining

3.9.1 BrdU-incorporation in S-phase cells and fixation

The telomeres were visualized by chromosome orientation fluorescence in situ hybridization (CO-FISH) staining. Mouse MSCs were cultured for a single round of replication in the presence of BrdU to incorporate BrdU into the newly synthesized strands. Nuclease digestion was then performed to specifically remove the daughter strands, thus creating a single-strand for hybridization of single-stranded probes. In our project, two separate probes (C-rich probe: repeats of CCCTAA and G-rich probe: repeats of TTAGGG) were used to detect 3'-telomeres and 5'-telomeres respectively, thus allowing to assay sister chromatid segregation patterns directly and allow for easy T-SCE quantification. The mouse cells were cultured on 14nm glass slides for at least 2 days in the incubator to allow them to attach and proliferation. BrdU was added to each slide chamber (final concentration 10 μ g/ml) and cells were placed in the incubator for 24 h. The BrdU nucleotide analog is incorporated into each cell passing S phase during this incubation, labelling newly formed DNA strands. This is crucial to

differentially labeling sister chromatids. For murine MSCs, incubation times of 24h were found to correspond to a full cell cycle. Independent on the cell cycle stage at start of the experiment with this protocol, all cells that entered S phase during a 24 hour period can be determined.

Following the incubation with BrdU, colcemid was added to each slide chamber for 4 hours. Colcemid arrests cells during metaphase and thus allows visual recognition of the condensed M-phase chromosomes, but the number of metaphases on each slide can vary depending on cell lineage and number of passages. Medium was removed from each slide chamber and cells were washed twice with warm PBS. Following this the cells were ruptured by 30min osmotic shock in 0.075 M KCl solution, leading to spreading of the metaphase chromosomes for each cell on the slide. Thereafter 3-4 ml fixative (3:1 methanol and acetic acid, ice-cold) was added dropwise to each slide chamber (ratio of KCl solution and fixative 1:1) and cells were incubated at RT for 20 min. Liquid was discarded from the slide chambers. 1 ml 0.075 M KCl and 3 ml fixative (ratio of KCl solution and fixative 1:3) was added to the cells for incubation at RT for 20 min. Liquid was removed from slide chambers, 4 ml fixative was added and cells were incubated at room temperature for 20 min. Liquid was removed from slide chambers, slides were air-dried and stored in a dark, dry slide box.

3.9.2 Digestion of BrdU-substituted DNA strand

Slides with more than 20 metaphases were selected for analysis. Slides were put on a heating block at 65 °C for 1 h or at 55 °C overnight. This treatment hardens the chromatin scaffold and prevents a loss of morphology during subsequent DNA denaturation. Slides were flooded with PBS for 15 min at RT on a shaker (Rotatest). Slides were placed in a light-sealed vertical staining jar with 50 ml 2× SSC and 2.5 µl Hoechst 33258 stock of 10 µg/ml (final concentration 0.5 µg/ml) for 15 min at RT. Hoechst 33258 is a dye that increases photosensitivity in the newly synthesized DNA strands where BrdU was incorporated. Slides were removed and covered with 2× SSC solution and exposed to 365 nm ultraviolet light for 30 min at 0.12 J (Calculated dose $5.4 \times 10^3 \text{ J m}^2$) in Viber Lourmat UV-Exposure chamber. Exposing the cells to UV light in the presence of Hoechst results in numerous strand breaks that preferably occur at the sites of BrdU incorporation. These single strand breaks serve as substrate for digestion by exonuclease III. Excess 2× SSC solution was shaken from the slides and the BrdU-substituted DNA strands were digested with by pipetting 100 µl Exonuclease

III-Mix (3 U/ μ l final concentration) onto each slide. They were covered with parafilm and incubated at room temperature for 10 min.

This results in degeneration of the newly replicated strands, while the parental strands are left largely intact; therefore, rendering the 2 sister chromatids of a chromosome single stranded and complementary to each other for subsequent hybridization reactions. The parafilm was removed and slides were washed twice in PBS for 5 min at room temperature with gentle shaking.

3.9.3 CO-FISH – First Hybridization

Cys3-labeled C-Rich PNA probe mixture was added per slide and was covered with a glass coverslip and placed on a heating block for 5 min at 80°C for hybridization. Slides were hybridized for 2 hours at room temperature in a dark, wet container. Coverslip were removed and the slides were washed twice in 70% formamide for 15 min on the shaker at room temperature to remove the un-incorporated probes. Following formamide washing, slides were washed in PBS three times for 5 min on a shaking table at room temperature.

3.9.4 CO-FISH – Second Hybridization

Peptide nucleic acid (PNA) probes are able to hybridize with their target DNA with high sensitivity and specificity (205). The PNA probe is an alternate to a DNA probe, except the phosphate backbone is instead a pseudo-peptide polymer (205). DNA are not repealed as the pseudo-peptide polymer has no charge (205). This allows the PNA probe to bind to a complimentary sequence of DNA with a higher affinity than the DNA would have when binding with itself (206). In our project, Cy3 -labeled C Rich Telomeric PNA probe and Alexa488-labeled G-rich PNA probe were used. Alexa488-labeled G-rich PNA mixture was preheated to 80°C. 20 μ l of the G-rich PNA Mixture was dropped quickly onto the slide, followed by a glass coverslip and the reaction placing for 5 sec on a cooled aluminum block, which helps the binding of G-rich PNA mixture. Place slides into dark, wet container, keep at room temperature for 2 hours. Coverslips were removed and slides were washed twice in 70% formamide on a shaker. TNT wash solution were used to cover the slide three times for 5 min on the shaker at RT to remove all the un-incorporated probes. PBS was used for 3x 5 min washes on the shaker at RT. Slides were placed in PBS for 10 min followed by DAPI staining. The cells were counterstained with 200 μ l of DAPI solution for 5 min at room temperature

to visualize the nuclei. After 5 min incubation of DAPI solution, slides were rinsed 2x with PBS. After a 10-min incubation at RT, the DAPI solution was removed, and slides were rinsed 2x with PBS and covered with Vectashield (Vector Labs, Burlingame, CA, USA) and glass coverslips. Visualization and image acquisition were done on a Keyence BZ9000 microscope using 40x plan fluorescence lenses. The metaphases were identified on the basis of their DAPI staining. Wilcoxon-Mann-Whitney-Test was used to analysis the difference between groups from young and old donors.

3.9.5 Types of structural alterations observed at telomeres of murine

The typical metaphase of a murine MSC labeled by CO-FISH is shown in Figure 3.7, with each chromosome carrying two G-rich (Cy5, red) and two C-rich (Alexa 488, green) signals, respectively, and with the two sister chromatids normally showing a reverse orientation (contralateral orientation of the leading and lagging strand).

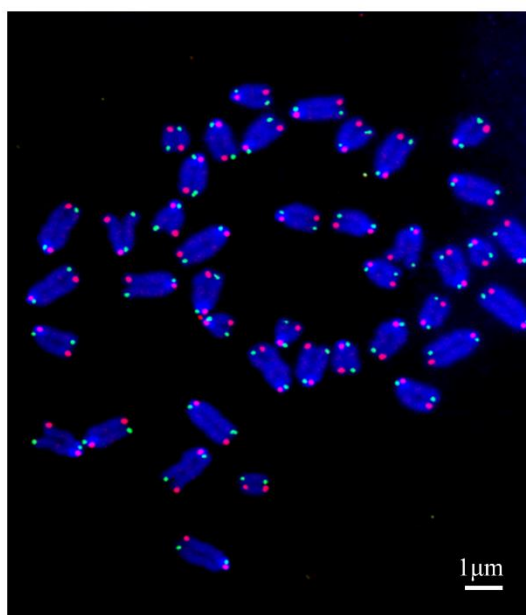


Figure 3.7: Typical picture of metaphase. Representative metaphase spreads of primary mouse MSCs showing DAPI counterstaining (blue), leading strand (G-rich) telomere fluorescence signals (red) and lagging strand (C-rich) telomere fluorescence signals (green).

Several kinds of abnormal telomeric phenotypes in the MSc cells were observed following exposure to IR (Figure 3.8). The frequencies of the various abnormalities were examined in cells derived from young and old mice. Telomere signal free ends

(SFEs), indicating losses or critically shortened telomere sequences as well as telomeres with discontinues or multiple signals (MTS), as indicated by the splitting of one telomere signal into two separate ones were both found with higher frequencies in MSCs after *in-vitro* 2Gy γ -irradiation (Figure 3.8, b-c). Sister chromatid fusion produces telomeres with differentially colored overlapping G-rich and C-rich signals (Figure 3.8, d), but this aberration appeared infrequently and was independent of the age of donor mice or to *in vitro* irradiation. Also, it is not clear if this represents a real covalent fusion of the DNA strands of two sister telomeres, or is simply a late or non-segregating part of the chromatin. Chromosomes without a telomeric signal were found after IR (Figure 3.8, e-f). In some rare cases, a fusion of different chromosomes at their telomere regions was observed (Figure 3.8, g), but because of its very low frequency this was not further evaluated. T-SCE in sister chromatids is shown in Figure 3.8, h.

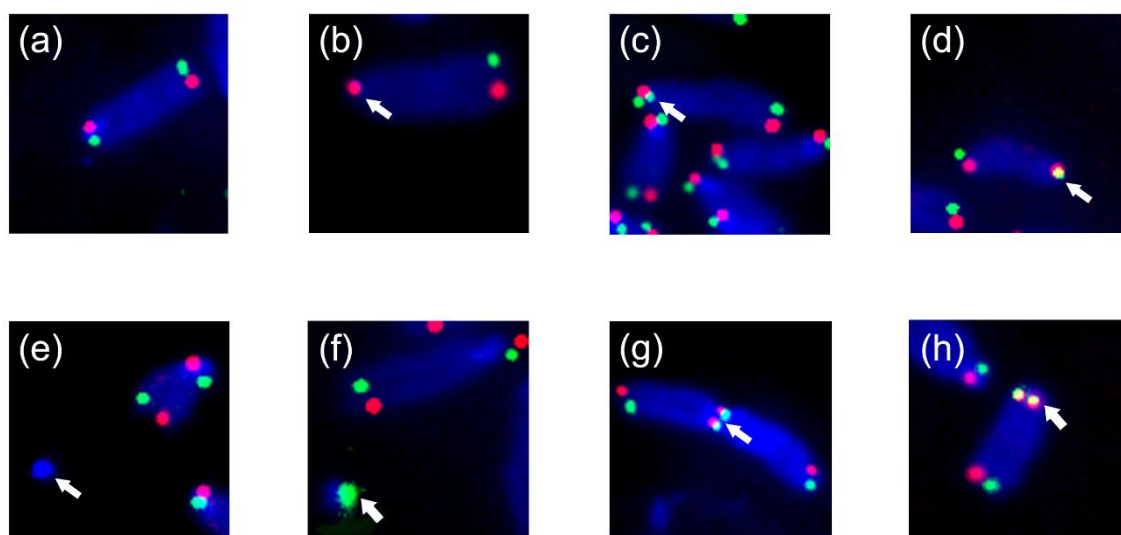


Figure 3.8: Dysfunctional telomeric phenotype in MSCs after IR. Examples of chromosomal abnormalities observed after 2Gy γ -irradiation *in vitro*. Metaphase spreads were stained with orientation dependent CO-FISH. (a) normal telomere; (b-h) aberrant chromosomes from MSCs after IR; (b) telomeric signal missing from chromatid; (c) multiple telomeric signal in one chromatid end; (d) Sister telomere fusion in one end of a chromatid pair; (e) fragment of chromosome without a telomeric signal; (f) fragment with a telomeric signal; (g) chromosome fusion; (h) T-SCE in sister chromatids.

3.9.6 Analysis of radiation-induced T-SCE

To investigate effects of IR and ageing process on recombination at telomeres, we examined T-SCE frequencies in MSCs which came from young and old mice. The mechanism of T-SCE is shown below in Figure 9.

A



B

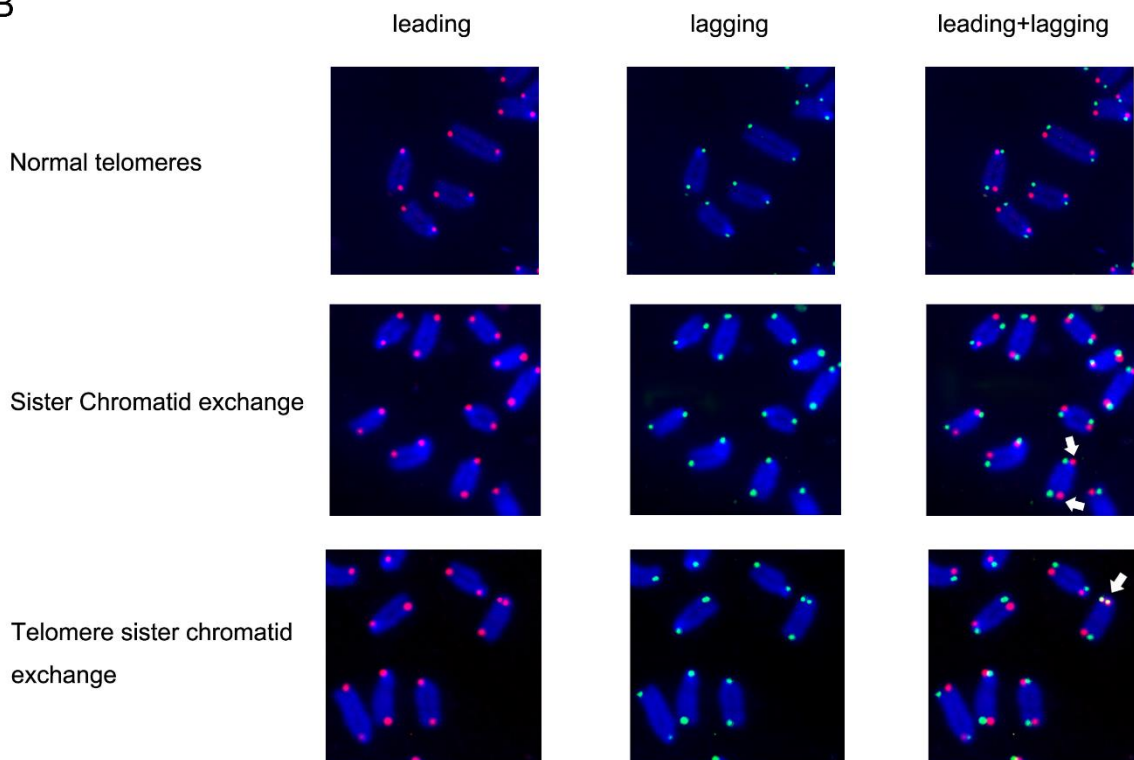


Figure 3.9: T-SCE and sister chromatid exchange after IR in MSCs. (A) A schematic presentation of CO-FISH. (A) A schematic presentation of CO-FISH. In brief, BrdU incorporated strands are removed, leaving parental strands of the telomeres to be detected by Cy5-(TTAGGG)₃ PNA probe (red color) and Alexa488-(CCCTAA)₃ PNA probe (green color). In an event of T-SCE, one chromatid end shows telomere signals in both green and red. (B) Representative metaphase spreads of normal telomere, sister chromatid exchange and T-SCE event showing DAPI staining (blue) and telomere fluorescence signals (red for leading strand, green for lagging strand).

3.10 Immunofluorescence-fluorescence in situ hybridization (IF-FISH) for detection the telomere dysfunction induced foci (TIF) in mouse MSCs

The mouse MSCs were cultured on a 14 mm slide for at least 1 day in the incubator to allow them to attach and proliferate. After 30 hours after irradiation, the medium was removed and cells were washed with DPBS for twice. After washing cells were fixed with histo-fix for 5 min at RT. The histo-fix was discarded followed by 3 washes with PBS. The cells were incubated with 1% blocking buffer for one hour in a humidified chamber. After blocking, 100 μ L of the primary antibody (anti-gamma-H2AX) in 1% blocking buffer was used to cover the cells and the reaction was placed in a cold room at 4 °C. After an overnight incubation the cells were washed with PBS twice to remove residual primary antibody. Secondary antibody was diluted in 1% blocking buffer (1:500 dilution) and 100 μ l of this solution added to the cells for 2 hours at RT in a dark room. After 2 hours at RT, the cells were washed with PBS twice. Cys3-labeled C-Rich PNA probe mixture was added per slide and was covered with a glass coverslip and place on the heating block for 5 min at 80°C for hybridization. Slides were hybridized for 2 hours at room temperature in a dark, wet container. Coverslip were carefully removed and the slides were washed in 70% formamide twice for 15 min on the shaker at room temperature. Following formamide washing, slides were washed in PBS for 5 min three times on the shaker at room temperature. The cells were counterstained with 200 μ L of DAPI solution to visualize the nuclei. After 5 min incubation of DAPI solution, slides were rinsed 2x with PBS. After a 10-min incubation at RT, the DAPI solution was removed, and slides were rinsed 2x with PBS and covered with Vectashield (Vector Labs, Burlingame, CA, USA) and glass coverslips. The metaphases were identified by the DAPI staining. Visualization and image acquisition were done on a Keyence BZ9000 microscope using 40x plan fluorescence lenses.

3.11 Quantification-fluorescence in situ hybridization (Q-FISH) of mouse MSCs

The cells were cultured on a 14 mm slide for at least 1 day to allow attachment and proliferation. The medium was removed and cells were washed with DPBS for twice. After washing cells were fixed with histo-fix for 5 min at RT. The histo-fix was removed and cells were washed 3x with PBS. Cys3-labeled C-Rich PNA probe mixture was added per slide and was covered with a glass coverslip and place on the heating

block for 5 min at 80 °C for hybridization. Slides were hybridized for 2 hours at room temperature in a dark, wet container. Coverslip were removed and slides were washed in 70% formamide twice for 15 min on the shaker at room temperature. Following formamide washing, slides were washed three times in PBS for 5 min on the shaker at room temperature. The cells were stained with 200 μ L of DAPI solution to visualize the nuclei. After 5 min incubation of DAPI solution, slides were rinsed 2x with PBS. After a 10-min incubation at RT, the DAPI solution was removed, and slides were rinsed 2x with PBS and covered with Vectashield (Vector Labs, Burlingame, CA, USA) and glass coverslips. The metaphases were identified by the DAPI staining. Visualization and image acquisition were done on a Keyence BZ9000 microscope using 40x plan fluorescence lenses. Two-way ANOVA analysis was performed to analysis the signal intensity difference between each group.

3.12 Cell cycle analysis

Cell cycle progression can be investigated by Propidium iodide (PI) staining of cells, followed by flow cytometry. After fixation and permeabilization of cells, PI binds to the nuclear DNA in a stoichiometric manner and its red fluorescence signal is therefore a direct measure of the cellular DNA content. The fluorescent signal in G2 phase-cells is almost exactly 2 times higher than the signal of G1 phase-cells. Cells in S phase during DNA replication have a fluorescent signal that is intermediate between the signal of G1 and G2 cells.

3.12.1 Cell preparation

For cell cycle analysis of MSC populations at different passages 50 000 cells were seeded in 2 ml per well in a 6-well-plate. The cells were incubated for 2 days before the cell cycle analysis. 2x PBS washing for 10 min was performed followed by detaching from the surfaces with trypsin-EDTA 0.05% treatment for 5 min at RT. The enzymatic reaction was stopped with an equal amount of serum containing culture medium. The cell suspension was transferred into 15 ml falcon tube, followed with centrifugation. The supernatant was discarded and cells were fixed with icecold 70% ethanol for 4 hours. The fixed cells can be stored at 4 °C for several days or be used for cell cycle analysis immediately.

3.12.2 Propidium iodide (PI) staining

Fixed cell suspensions were centrifuged at 1400 rpm for 5 minutes to obtain cell pellets. Following removal of the supernatant, cells were resuspended in 4 ml of ice-cold 70% ethanol for 3 hours. The fixed cells were spun down at 1,400 rpm for 5 minutes and resuspended in 475 μ l PBS, plus 3.3 μ l RNaseA (30 mg/ml) and 25 μ l propidium iodide (1 mg/ml). The samples were mixed gently and subjected to flow cytometry. The DNA content of each cell was measured with the flow cytometer LSR II (Beckton Dickinson, USA) (PI-A channel) Analysis of cytometric data was performed using Flowjo. The percentage of cells in each phase of the cycle were calculated and plotted with ggplot2.

3.13 Bromodeoxyuridine incorporation and Hoechst 33342 staining

To analysis whether the aged human MSCs can enter S phase, the Bromodeoxyuridine (BrdU) incorporation and Hoechst 33342 staining was performed. Newly synthesized strands were incorporated with BrdU during each cell division in the presence of BrdU in medium. After staining with Hoechst 33342, the cells that passed one division was much dimer than the cells that did not pass one division due to the incorporated BrdU in newly synthesized strands. Human MSCs were plated on sterile glass slides and incubated for 2 days in growth medium. BrdU was added to a final concentration 10 μ g/ml and cells allowed to incorporate the nucleotide analog for 0h, 24 h and 48 h under standard growth conditions. The slides were washed with PBS twice after removing the medium. Hoechst 33342 solution (10 mg/ml) was added to cover the slides for 5 min. In the dark the slides were washed 3 times for 15min in PBS. Under UV illumination, cells with BrdU incorporation (i.e. cells that went through a round of DNA replication) exhibited a dim blue color while the cells without BrdU incorporation showed a much brighter blue color. At least 200 cells per slide were counted for this feature using the Keyence BZ-9000 fluorescence microscope at 10x fluorescence lens. The number of cells with dim color or with bright blue color was recognized by eye by two people and the average value was calculated. The dim cell percentage was calculated as follows:

$$\text{Dim Percentage} = \frac{\text{Dim cell number}}{\text{Total cell number}}$$

Significance was calculated by one-way ANOVA test and multiple T-test corrected by Bonferroni method. MSCs from three donors were used for experiments. For each experiment at least 50 cells were counted for MSCs from each donor.

4 Results

4.1 Extended *in-vitro* culture of primary human mesenchymal stem cells downregulates Brca1-related genes and impairs recognition of DNA breaks

MSCs are multi-lineage stem cells that have possible uses in cell-based therapeutic applications. The required *in vitro* expansion required for medical uses may alter their cellular and epigenetic properties, including possible changes in genome stability and DNA damage response (207). To further understand the possible aging effect on DNA repair and chromosomal stability in mesenchymal stem cells (MSCs), we performed a transcriptome analysis of *in vitro* expanded hBM-MSCs and experimental assays to analysis the gene profile changes and related DNA repair pathway changes in long-term cultured MSCs.

4.1.1 Transcriptome analysis for young and *in vitro* aged human MSCs

The mRNA expression profiles from passage 4 (young) and passage 13 (aging) human MSCs. Each biological replicate involved young and old samples from one donor. The FASTQ files were downloaded from GEO database (GSE59966). The detailed data processing was described in method section and appendix. Briefly, the data was stored in FASTS files. After quality check by FASTQC, the sequencing data was mapped to a reference genome hg19. Gene matrix was obtained to perform the differently expressed gene (DEG) analysis between young and *ex vivo* aging MSCs with DESeq2. The DEGs were used to perform the pathway analysis and downstream GO analysis. Each of 3 human MSCs were used for comparison of the differently expressed genes (DEGs) between young and *ex vivo* aging MSCs. A Principal component analysis (PCA) plot indicated separation of the expression profiles of the passage 4 MSCs and passage 13 counterparts (Figure 4.1). PCA analysis orders the samples in a plane defined by 2 axes (PC1 and PC2) according to their continuous variable values (here high-dimensional transcriptome data). PC dimension 1 and PC 2 explained 58% and 18% of the variance of the dataset, respectively (Figure 4.2A). The individual profiles of the young and the *in vitro* aged human MSCs were each clustered closely together, especially in PC1 dimension, showing homogeneity between the replicates of each cell population.

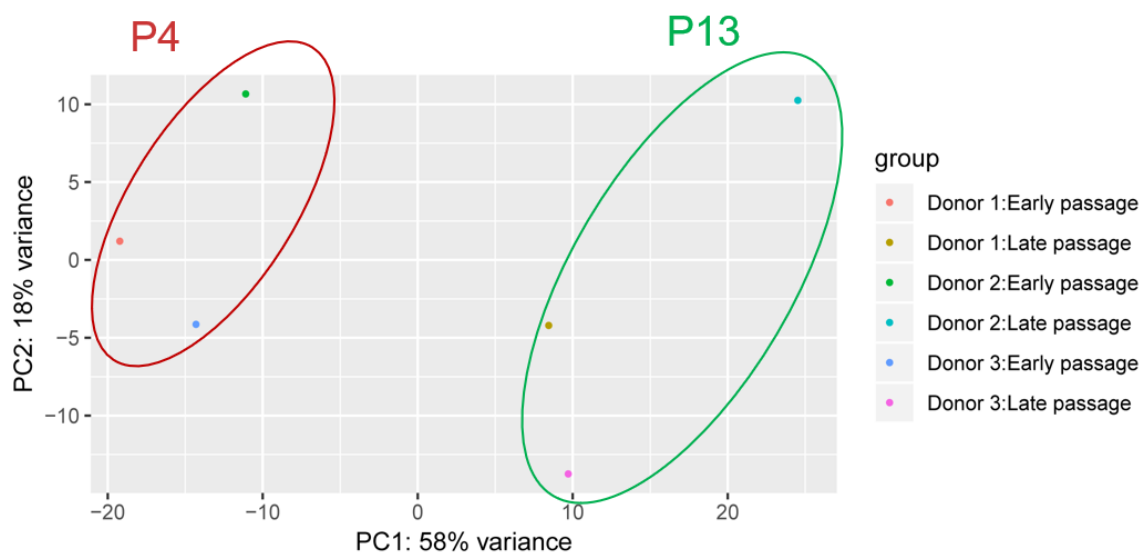


Figure 4.1: PCA analysis for the transcriptome matrix from young and *in vitro* aged samples.

The differentially expressed genes were defined as:

$$\left| \log_2 \left(\frac{\text{Expression of target gene in p13 samples}}{\text{Expression of target gene in P4 samples}} \right) \right| > 1 \text{ \& adjusted } p \text{ value} < 0.05$$

A volcano plot was used to depict the differentially expressed genes between young and *in vitro* aged samples (Figure 4.2). This plot indicated that 1308 individual genes showed a change in expression during the *ex vivo* aging. Among the most significantly altered, 583 genes were upregulated ($\log_2(\text{change}) > 1$ & *adjusted p value* < 0.05) while 725 genes were downregulated ($\log_2(\text{change}) < -1$ & *adjusted p value* < 0.05).

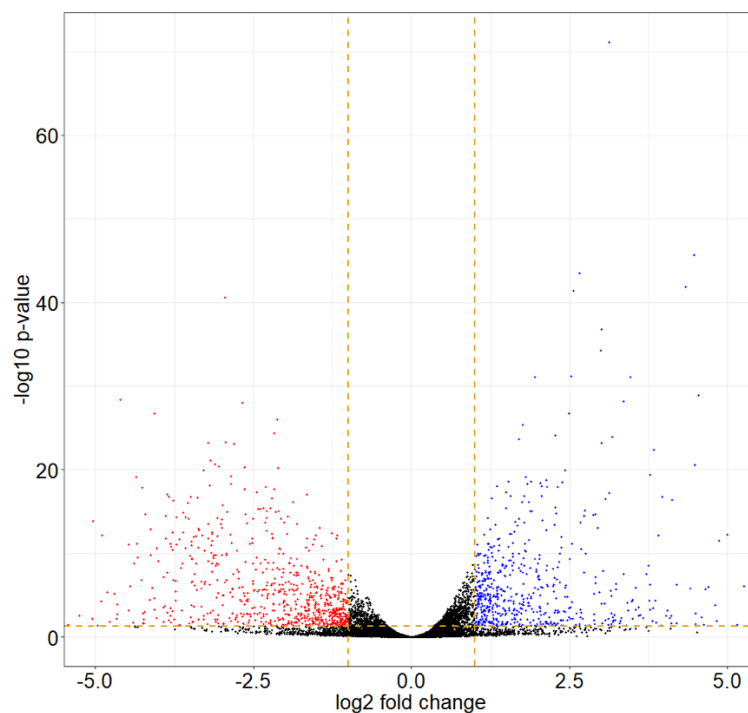


Figure 4.2: The volcano plot for the DEGs between young and *in vitro* aged human MSCs. The x-axis represents the \log_2 (fold change) and the y-axis represents the $-\log_{10}$ (adjusted-p value) of the DEGs.

A heatmap of the differentially regulated genes was plotted to show the most significantly DEGs between non-aged and *in vitro* aged human MSCs (Figure 4.3). The unsupervised clustering of the genes in the heatmap showed changes of expression in the human MSCs were clustered by length of time in culture (aged versus non-aged) rather than by donor (Figure 4.3). This is a strong indication that the source of the changes in gene expression mainly originates from the ageing process rather than from any donor-to-donor variability.

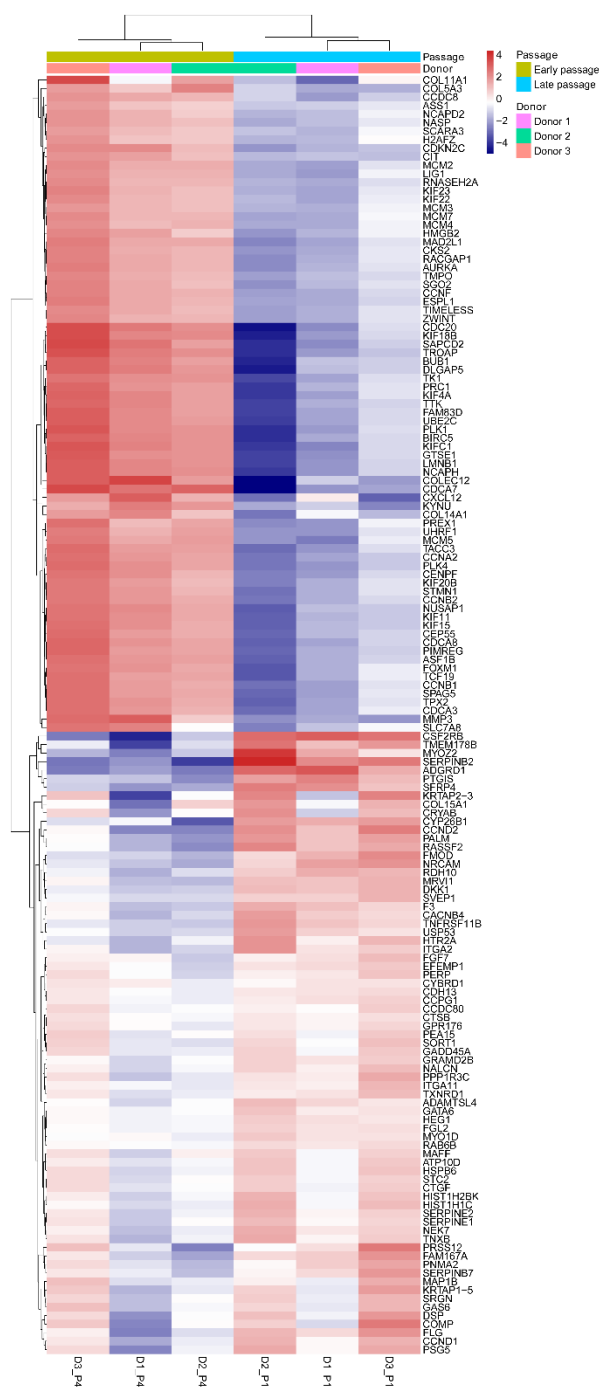


Figure 4.3: The heatmap for the DEGs between young and *in vitro* aged human MSCs.

4.1.2 Gene ontology analysis

Gene Ontology analysis (GO) was performed to identify biological characteristics of the DEGs. The results are shown in below (Figure 4.4A-4.4C). Bubble plots reveal enrichments in biological process (BP), molecular function (MF), and cellular component (CC) categories. Several DNA repair-related enrichments: nuclear

chromosome segregation, DNA conformation change, organelle fission was enriched upon *in vitro* aged process.

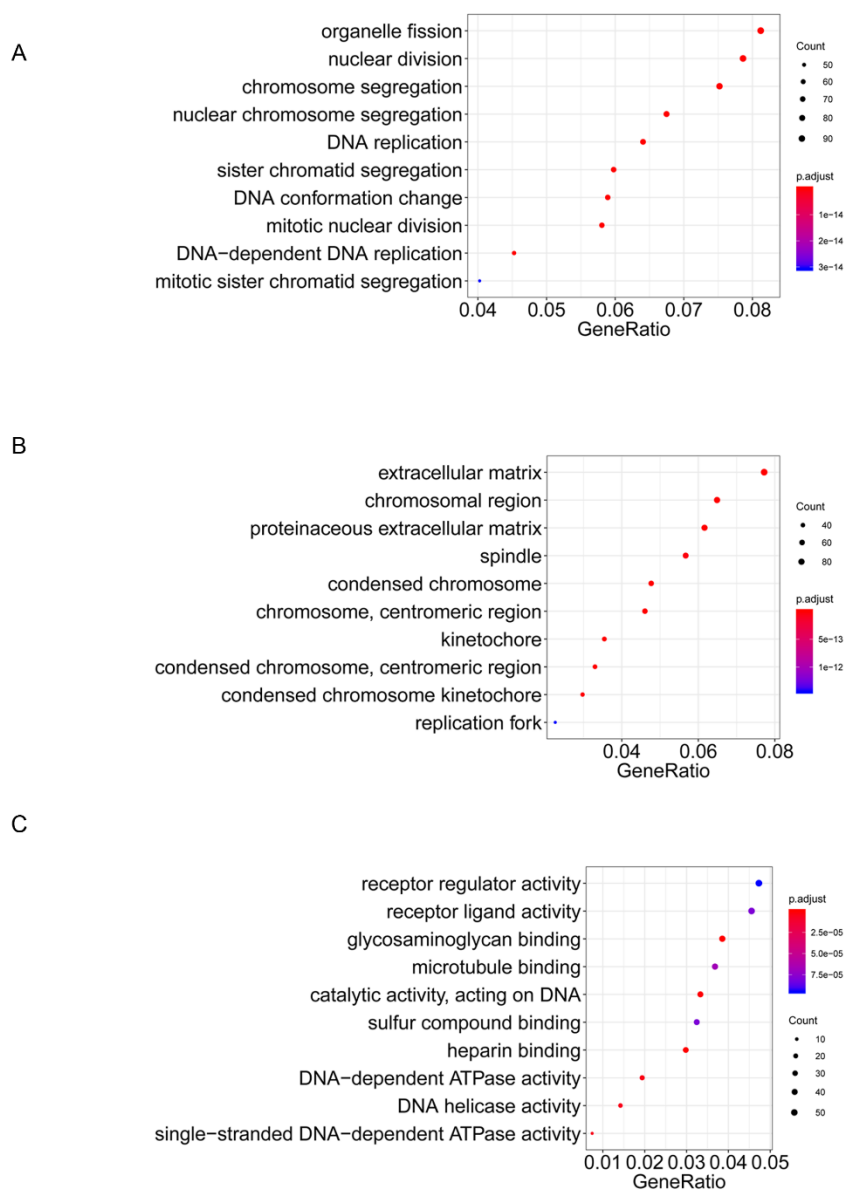


Figure 4.4: The GO analysis. (A) Enriched biological process (BP). (B) Enriched cellular component (CC). (C) Enriched molecular function (MF). The GO analysis was performed with the differential mRNA expression from passage 4 (young) and passage 13 (aging) human MSCs. q-value (adjusted p-value) <0.01 was considered as significance.

4.1.3 KEGG pathway analysis

KEGG (Kyoto Encyclopedia of Genes and Genomes) pathway analysis was performed to determine if the differentially regulated genes were involved in specific functional pathways. The results revealed alterations in expression involved mRNA species implicated in cell cycle control, regulation of DNA replication, ECM-receptor interaction, p53 signaling pathway, Fanconi anemia pathway and homologous recombination (KEGG pathway selection criteria: $q\text{-value} < 0.01$) (Figure 4.5-4.6). Other pathways without an obvious link to stem cell function were also altered, such as axon guidance, viral carcinogenesis or oocyte meiosis. This probably reflects the pleiotropic function of several of the dysregulated genes (Figure 4.5-4.6).

```
> head(summary(kk),20)
```

ID	Description	GeneRatio	BgRatio	pvalue	p.adjust
hsa04110 hsa04110	Cell cycle	43/516	124/7383	8.271871e-20	2.324396e-17
hsa03030 hsa03030	DNA replication	22/516	36/7383	3.711681e-17	5.214913e-15
hsa04512 hsa04512	ECM-receptor interaction	21/516	82/7383	1.184603e-07	1.109579e-05
hsa04115 hsa04115	p53 signaling pathway	18/516	68/7383	5.608031e-07	3.340412e-05
hsa03460 hsa03460	Fanconi anemia pathway	16/516	55/7383	5.943793e-07	3.340412e-05
hsa03440 hsa03440	Homologous recombination	13/516	41/7383	2.335776e-06	1.093922e-04
hsa04218 hsa04218	Cellular senescence	28/516	160/7383	4.786434e-06	1.921411e-04
hsa03430 hsa03430	Mismatch repair	9/516	23/7383	1.249792e-05	4.389894e-04
hsa05222 hsa05222	Small cell lung cancer	19/516	93/7383	1.751061e-05	5.467200e-04
hsa04151 hsa04151	PI3K-Akt signaling pathway	45/516	352/7383	4.702662e-05	1.321448e-03
hsa03420 hsa03420	Nucleotide excision repair	11/516	47/7383	3.016847e-04	7.346401e-03
hsa03410 hsa03410	Base excision repair	9/516	33/7383	3.137253e-04	7.346401e-03
hsa05218 hsa05218	Melanoma	14/516	72/7383	3.817256e-04	8.251146e-03
hsa04360 hsa04360	Axon guidance	25/516	175/7383	4.538299e-04	9.109015e-03
hsa05203 hsa05203	Viral carcinogenesis	27/516	201/7383	7.311306e-04	1.369651e-02
hsa05166 hsa05166	HTLV-I infection	32/516	255/7383	8.166618e-04	1.434262e-02
hsa04114 hsa04114	Oocyte meiosis	19/516	124/7383	9.124795e-04	1.508275e-02
hsa04390 hsa04390	Hippo signaling pathway	22/516	154/7383	9.815928e-04	1.532375e-02
hsa04914 hsa04914	Progesterone-mediated oocyte maturation	16/516	99/7383	1.277565e-03	1.889451e-02
hsa05226 hsa05226	Gastric cancer	21/516	149/7383	1.511097e-03	2.123091e-02

Figure 4.5: The KEGG analysis based on the DEGs. The ranked list of top 20 KEGG enrichments based on the DEG analysis.

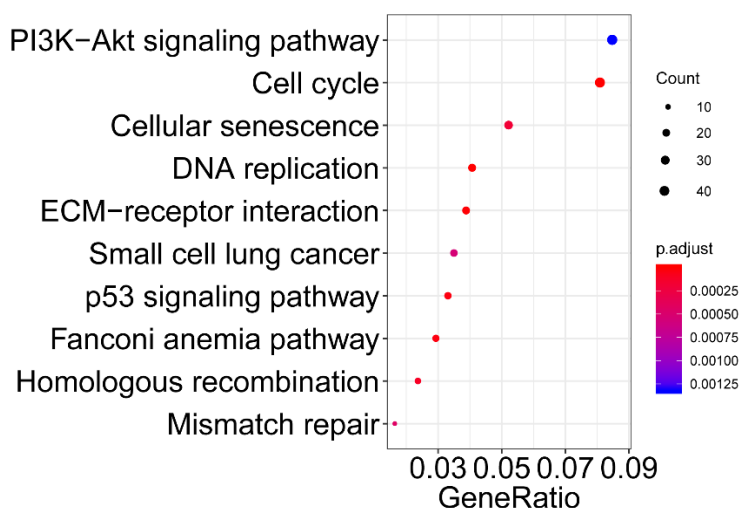


Figure 4.6: Visualization of KEGG result by the bubble plot. The KEGG analysis was performed with the differential mRNA expression from passage 4 (young) and passage 13 (aging) human MSCs. q-value (adjusted p-value) < 0.01 was considered as significance.

4.1.4 GSEA analysis

Gene Set Enrichment Analysis (GSEA) is a computational method that determines whether an a priori defined set of genes shows statistically significant, concordant differences between two biological states (e.g. phenotypes). GSEA indicated downregulation of c-MYC targets, DNA repair, E2F targets, G2M checkpoints, and oxidative phosphorylation in the aged MSCs (adjusted p-value < 0.0001) (Figure 4.7). In our previous study, we have found Long-term culture of mesenchymal stem cells impairs ATM-dependent recognition of DNA breaks and increases genetic instability.

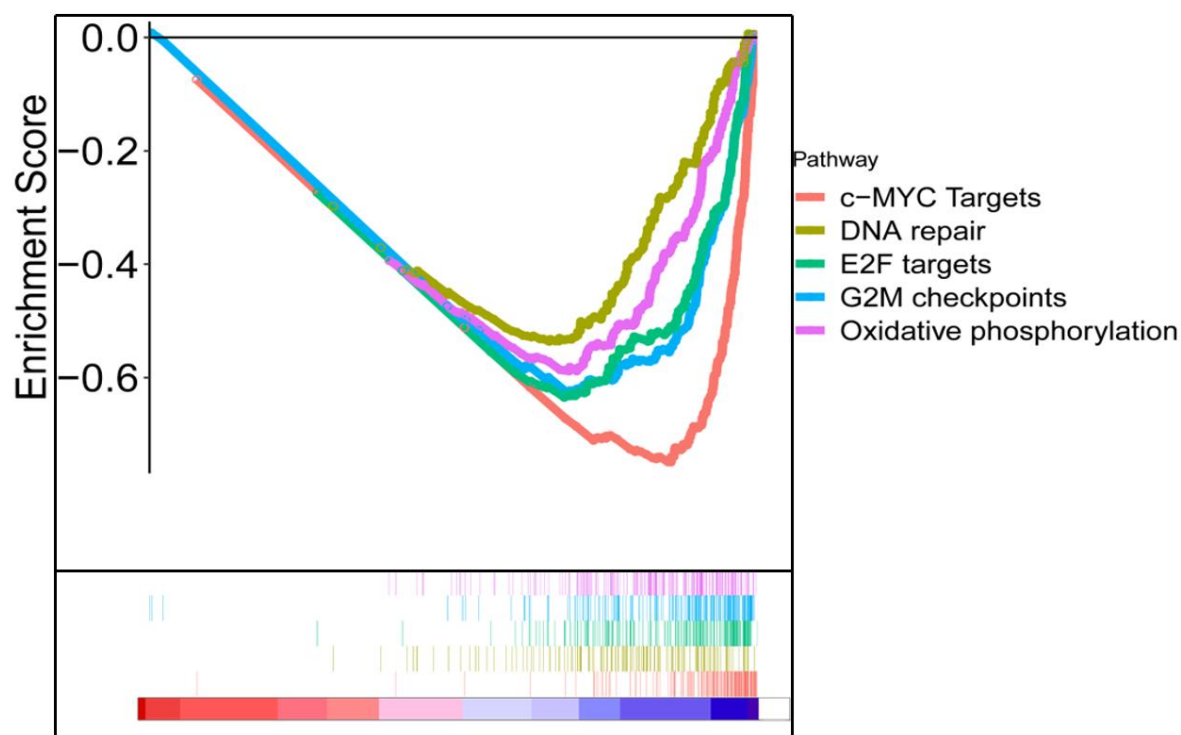


Figure 4.7: GSEA analysis based on the whole transcriptome profile of young and *in vitro* aged human MSCs. The negative enrichment score indicates the downregulation of hallmarks in ex vivo aging human MSCs. The GSEA analysis was performed with the whole transcriptome data from passage 4 (young) and passage 13 (aging) human MSCs.

4.1.5 Altered DNA repair-related profile

To further analysis the downregulated DNA repair pathway, we analyzed only mRNA species implicated in DNA repair (Figure 4.8). This revealed that 76 genes were significantly altered with the criteria $\text{adjust-}p < 0.05$ and the absolute value of \log_2 fold change > 1 . 5 genes were upregulated (\log_2 fold change > 1) while 71 genes were downregulated (\log_2 fold change < 1) during ex vivo aging process. The detailed list of DNA repair-related dysregulated genes and the fold change can be found in chapter 7.4.

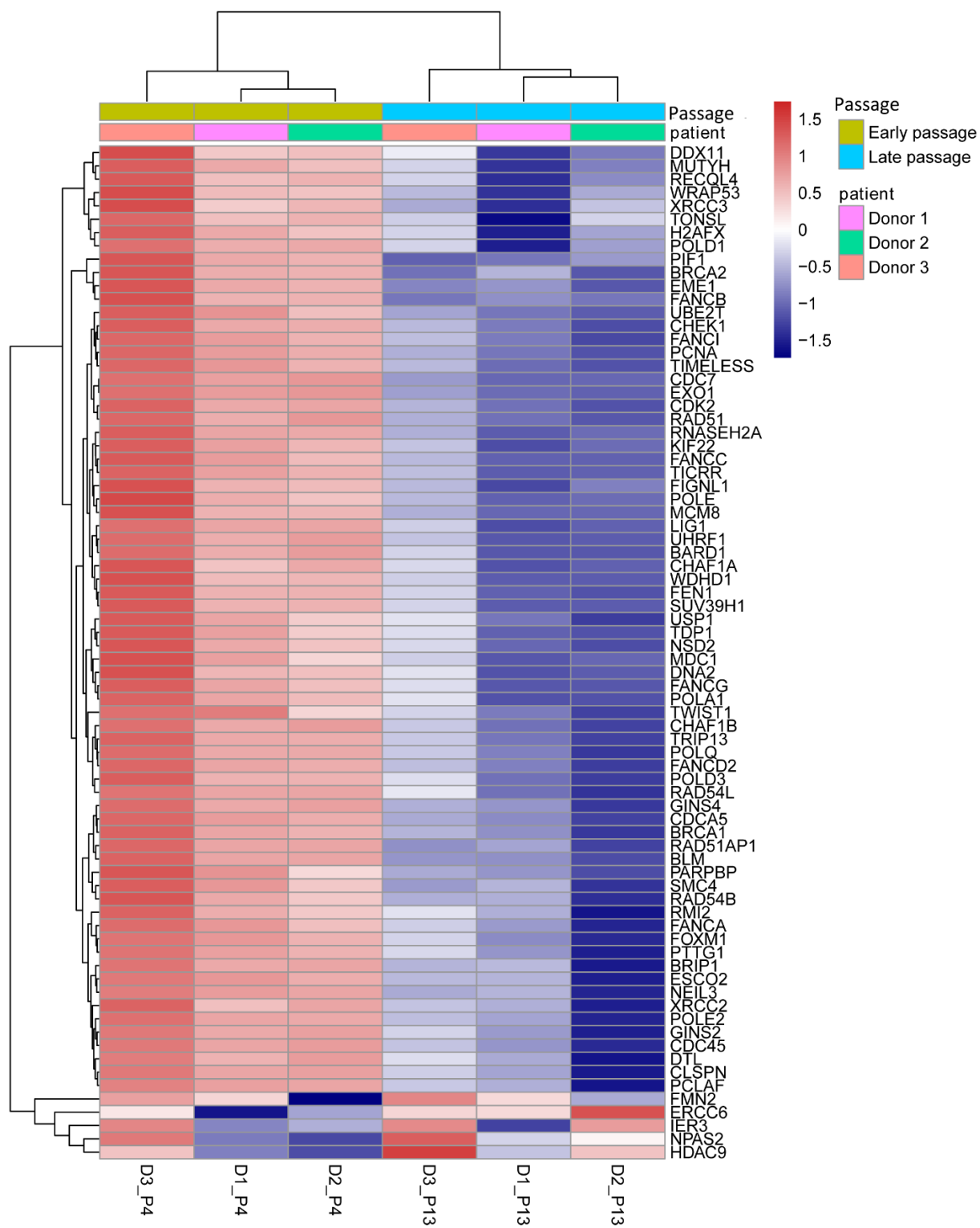


Figure 4.8: DNA repair-related gene expression alterations showing by heatmap.

4.1.6 IPA analysis revealed altered DNA replication, recombination and repair coupled with change in cellular assembly and organization

In our previous study, we have found extended *in vitro* culture of murine bone-marrow-derived MSCs gradually impairs the ability to recognize endogenous and radiation-induced DSBs. Reduced ATM dependent foci formation leads to fewer γ H2AX/53BP1 DSB repair foci after IR. Moreover, a slower DNA repair kinetics resulted in more residual DSBs in aged MSCs 7 hours post irradiation. Thus, to further understand the detailed mechanism of aging effect on DNA repair and chromosomal stability in MSCs, we here focus on the DNA repair-related pathway alterations that identified from transcriptome data.

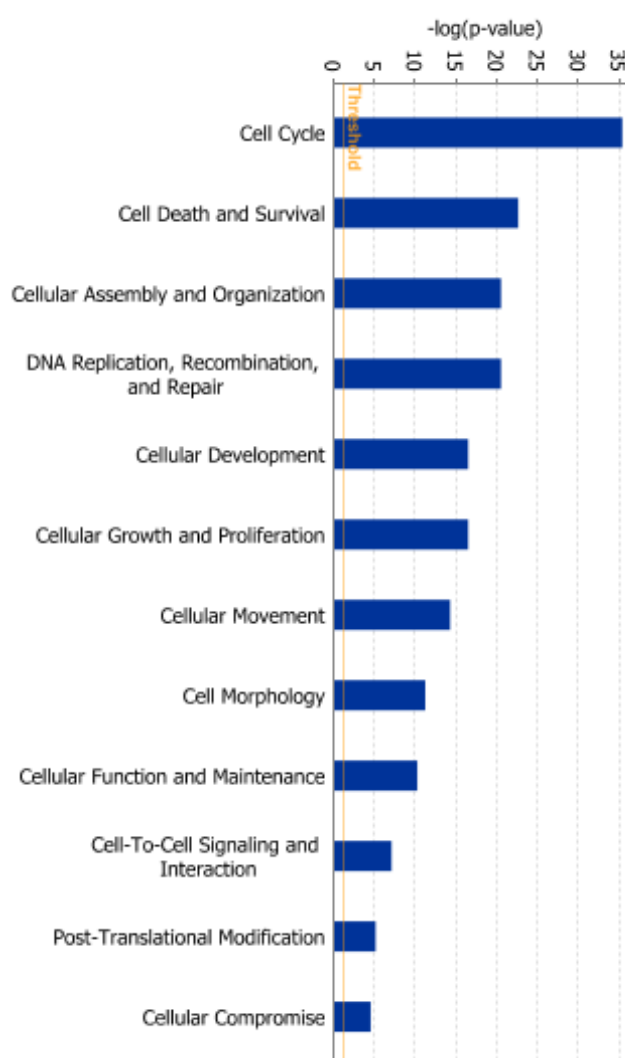


Figure 4.9: IPA functional analysis. The IPA analysis and network analysis were performed with the differential mRNA expression from passage 4 (young) and passage 13 (aging) human MSCs.

Ingenuity® Pathway Analysis (IPA) was performed to identify potential regulatory processes involved in the changes in gene expression. By identifying common regulatory nodes for selected pathways, the underlying regulatory molecules may be predicted. The IPA analysis revealed that altered DNA replication, recombination and repair coupled with change in cellular assembly and organization (Figure 4.9). This is consistent with the results from GO and KEGG analysis. Significantly, the IPA analysis identified BRCA1 and ATM as key participants in the processes influenced by the altered mRNA expression profiles (Figure 4.10).

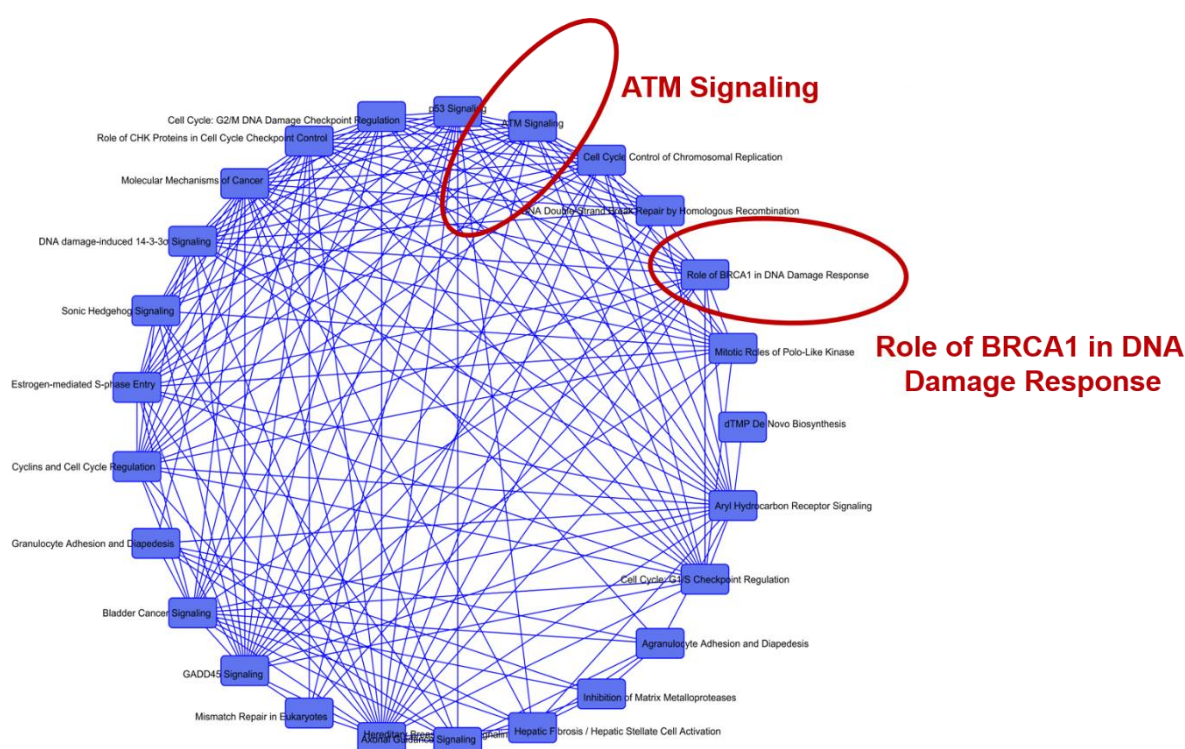


Figure 4.10: IPA network regulation of canonical pathways. The IPA analysis and network analysis were performed with the differential mRNA expression from passage 4 (young) and passage 13 (aging) human MSCs. The role of BRCA1 in DNA response and ATM signaling were magnified and labeled with red.

4.1.7 Downregulation of genes involved in homologous recombination repair

In GSEA we found that mRNAs participating in DNA repair to be dysregulated during aging and KEGG analysis suggested that the functional process of homologous recombination (HR) was implicated (Figure 4.11).

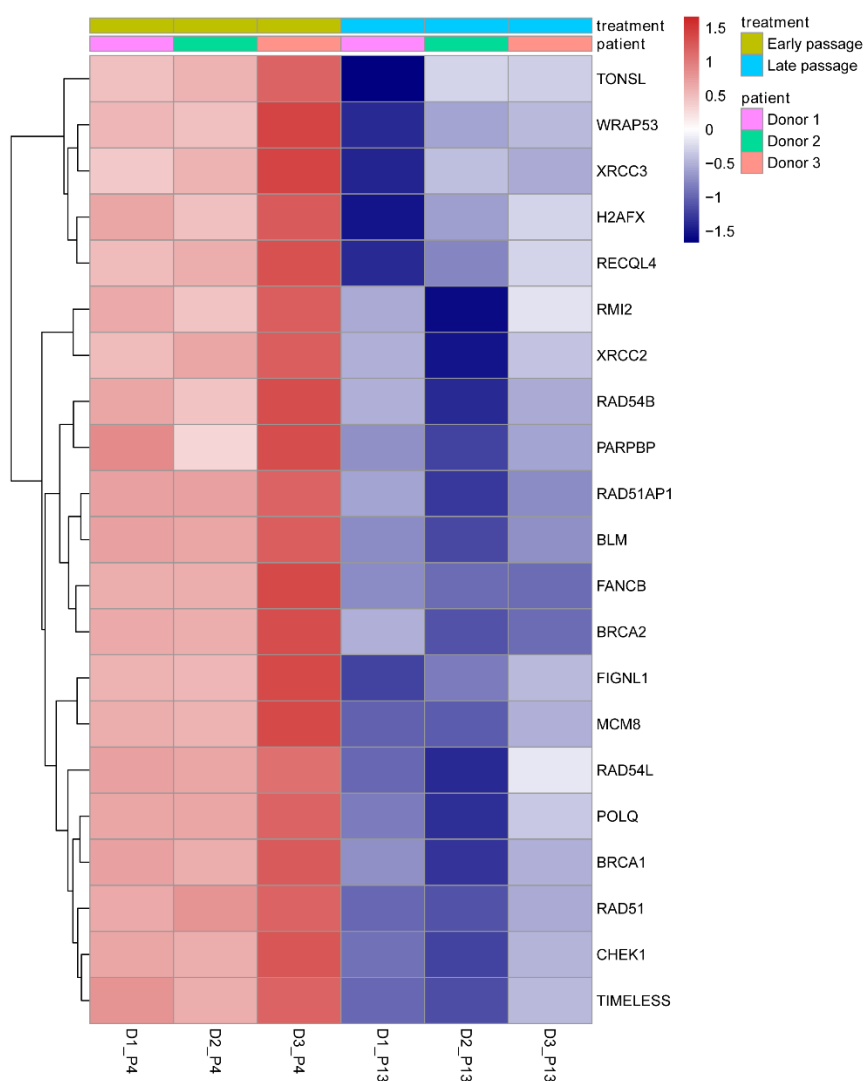


Figure 4.12: The most significantly changed homologous recombination-related genes between young and *ex vivo* aging hMSCs from RNA-seq data showing by heatmap.

4.1.8 Validation of downregulation of key components in homologous recombination

Several key components (RAD51, RAD54B, RAD54L and BRCA1) that are involved in homologous recombination repair were found to be significantly downregulated. We then performed RT-PCR analysis on young and *ex vivo* aging human MSCs. Data confirmed a downregulation between 2.3-fold (RAD54L) and 4-fold (RAD54B) of these genes during their *in vitro* expansion between week 2 and week 10 (Figure 4.13).

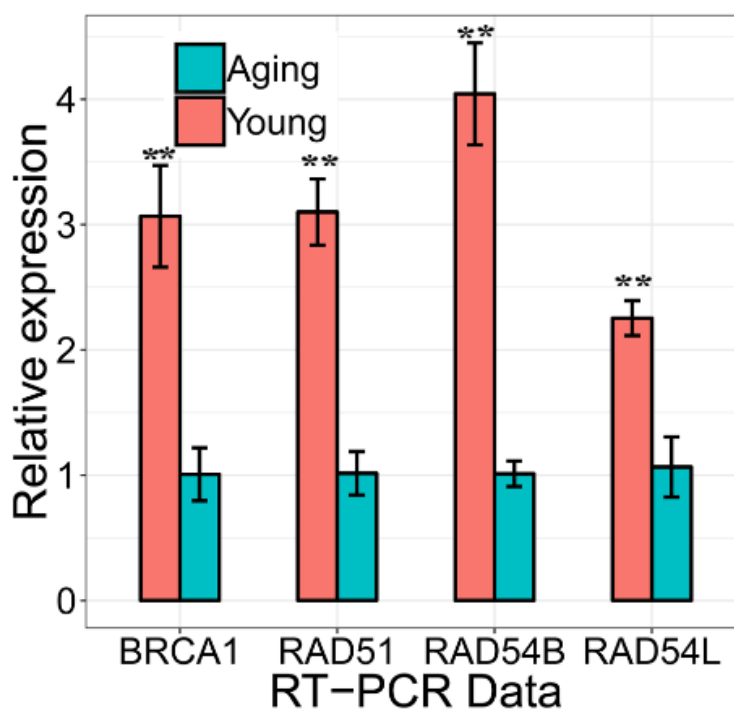


Figure 4.13: Decreased expression of homologous recombination-related genes in *ex vivo* aging hMSCs. The expression level change of BRCA1, RAD51, RAD54L, and RAD54B between young and *ex vivo* aging hMSCs by RT-PCR. The expression of target genes in aging MSCs were set arbitrary to 1 (mean values \pm SEM, $n = 3$, *: $p < 0.05$, **: $p < 0.01$).

4.1.9 Gene network and IPA analysis confirmed the alteration in BRCA-mediated DNA damage response

String network analysis indicated RAD51 and BRCA1 as the central node of gene regulation network in homologous recombination (Figure 4.14), which implies the potential important roles of BRCA1 in the dysregulated gene network during *ex vivo* aging of human MSCs.

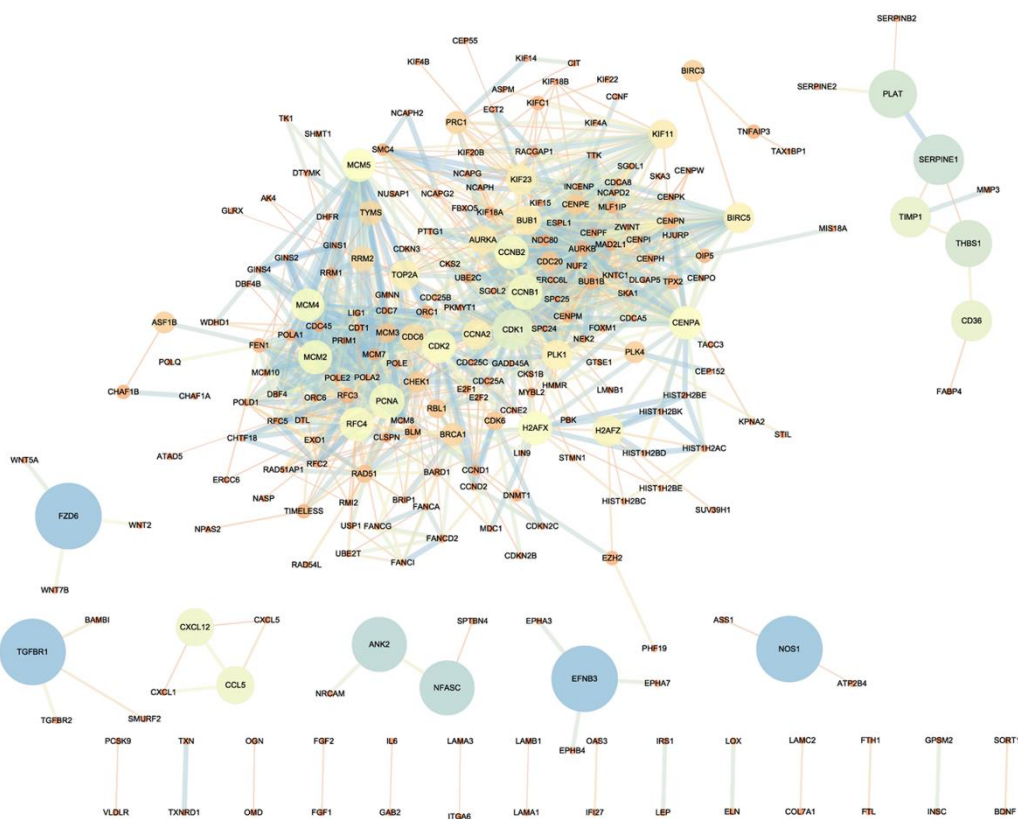


Figure 4.14: Gene network of the most significant genes affected by an *ex vivo* aging process in hMSCs.

“Cell cycle control of chromosomal replication” and “BRCA1-mediated DNA damage response” were identified as the most significantly changed pathways during *in vitro* aging of hMSCs by IPA canonical pathway analysis (Figure 4.15), which indicated the altered gene expression during *ex vivo* aging of human MSCs affect BRCA1-mediated DNA damage response.

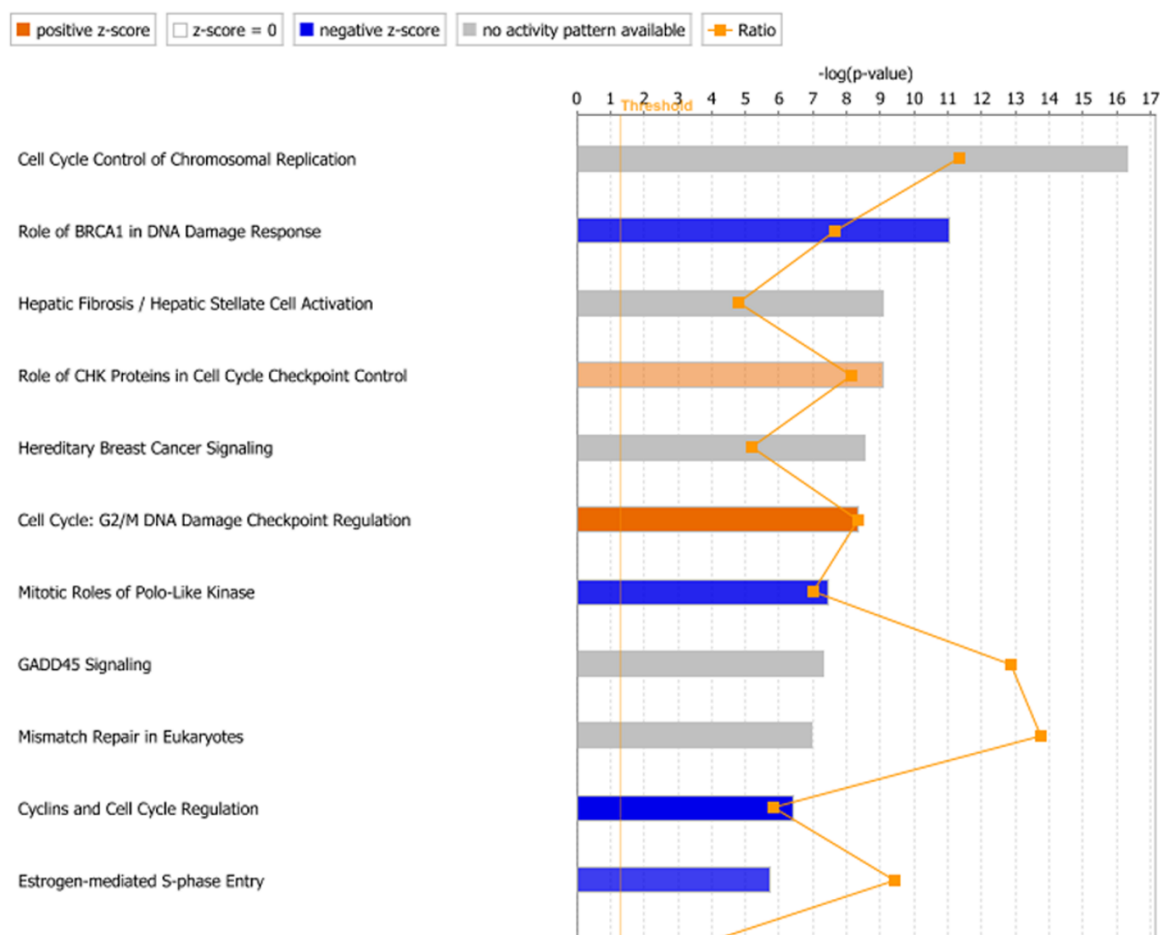


Figure 4.15: IPA analysis for the changed gene in *ex vivo* aging process in hMSCs. IPA analysis mapping the gene expression changes during *ex vivo* aging of hMSCs to “Cell Cycle Control of Chromosomal Replication” and to “BRCA1 mediated DNA Damage Response”.

4.1.10 Cell cycle analysis for young and aged human MSCs

In vitro long-term culture model of human MSC was established to validate the results from bioinformatic analysis. As we have found in the previous study that long-term culture of mesenchymal stem cells impairs ATM-dependent recognition of DNA breaks and increases genetic instability. And in the bioinformatic analysis impaired HR was identified during *ex vivo* aging of human MSCs. Thus, we focus on the dysregulation of HR during *ex vivo* aging and the related change in HR-guided DNA DSB recognition in human MSCs.

The HR pathway is predominantly active in dividing or S-phase cells. This warrants a question if downregulation of BRCA1 or HR pathway is due to reduction in S-phase

cells in *ex vivo* aged cells. Cells proliferation activity decreases and cells undergo senescence with increasing the passage numbers. Hence it is important to check if there are any cell cycle differences in young (P4) and aged (P13) MSCs, especially in the percent of S-phase cells. The cell cycle distribution in young (P4) and aged (P13) human MSCs was analysed using PI-staining of the nuclear DNA of the cells followed by flow cytometry (Figure 4.16).

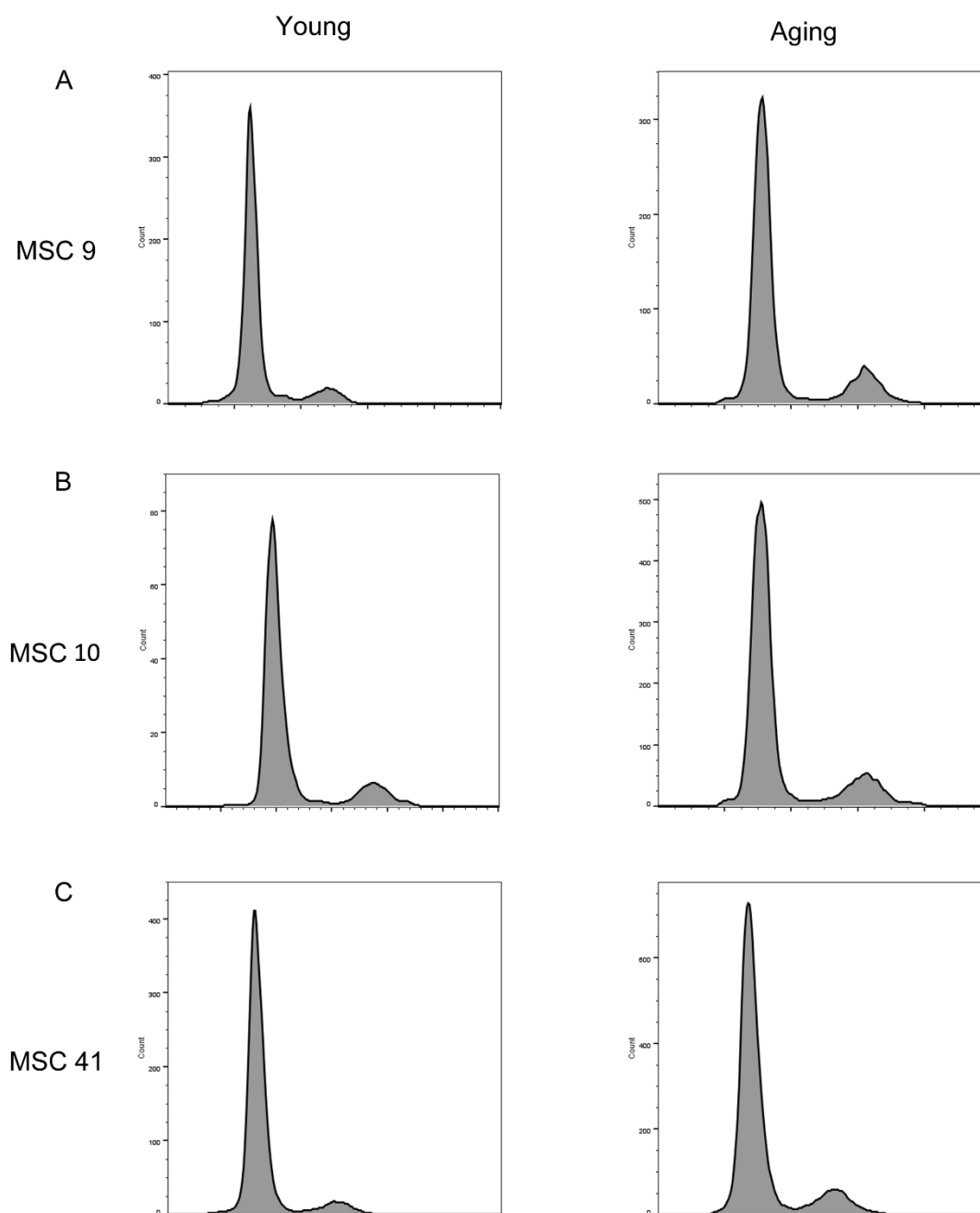


Figure 4.16: Distribution of DNA content in P3 and P11 MSCs from three donors. Each pair (Figure 4.16A, 4.16B and 4.16C) consisted of MSCs from a different donor. The Y-axis shows the count number of cells and the X-axis indicates the DNA content.

Results indicated no big difference between young (P4) and aging (P13) MSCs in terms of cell cycle distribution in our culture (Figure 4.17).

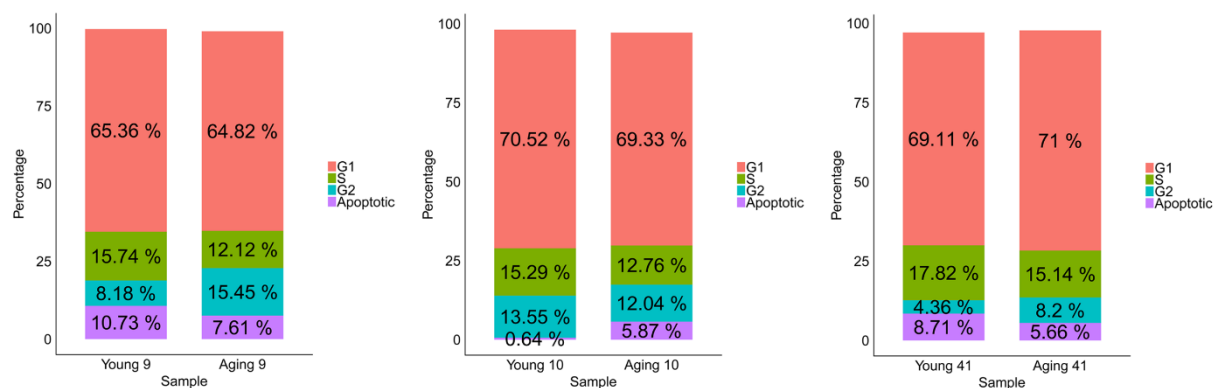


Figure 4.17: Results of the cell cycle analysis in young versus old (P3 and P11) MSCs in exponential growth phase. Each data set (young versus old) consisted of MSCs from a different donor.

The active DNA synthesis in S-phase was analysed using BrdU incorporation and Hoechst33342 staining, which revealed that within 24 hours, (20.8 +/- 2.1) % of early passage MSCs and (17.8 +/- 1.5) % of late passage MSCs had completed S-phase. After 48 h the percentage of DNA synthesizing cells increased to (37.1 +/- 2.2) % and (35.6 +/- 4.8) % in the early and late passages, respectively (difference not significant by T-test) (Figure 4.18A-4.18B). The comparison shows that neither the cell cycle distribution nor the cycle kinetics was changed by the increasing in vitro passaging of the MSCs.

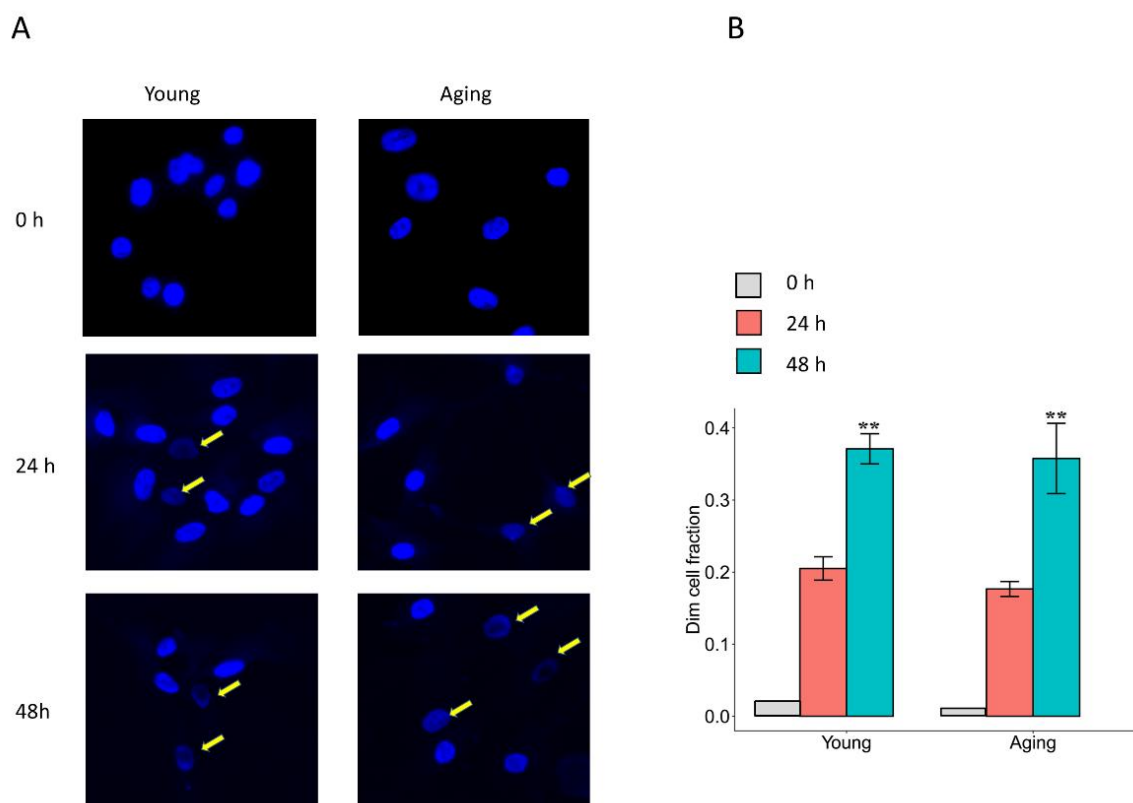


Figure 4.18 BrdU incorporation for one and two days. (A) The representative plots for BrdU incorporation followed by Hoechst 33342 staining. The yellow arrow indicates the dim cells. (B) The fraction of dim cells 0 h, 24 h, 48 h after BrdU incubation. (mean values \pm SEM, $n = 3$, MSCs from three donors were used for experiments. For each experiment at least 50 cells were counted for MSCs from each donor).

4.1.11 Impaired DNA damage response during hMSC aging *ex vivo*

To test whether the observed reduction in the DNA repair-related gene expression had a functional effect the γ -H2AX/53BP1 double-strand break repair foci were analysed in x-ray irradiated human MSCs from different passage numbers (Figure 4.19-4.20).

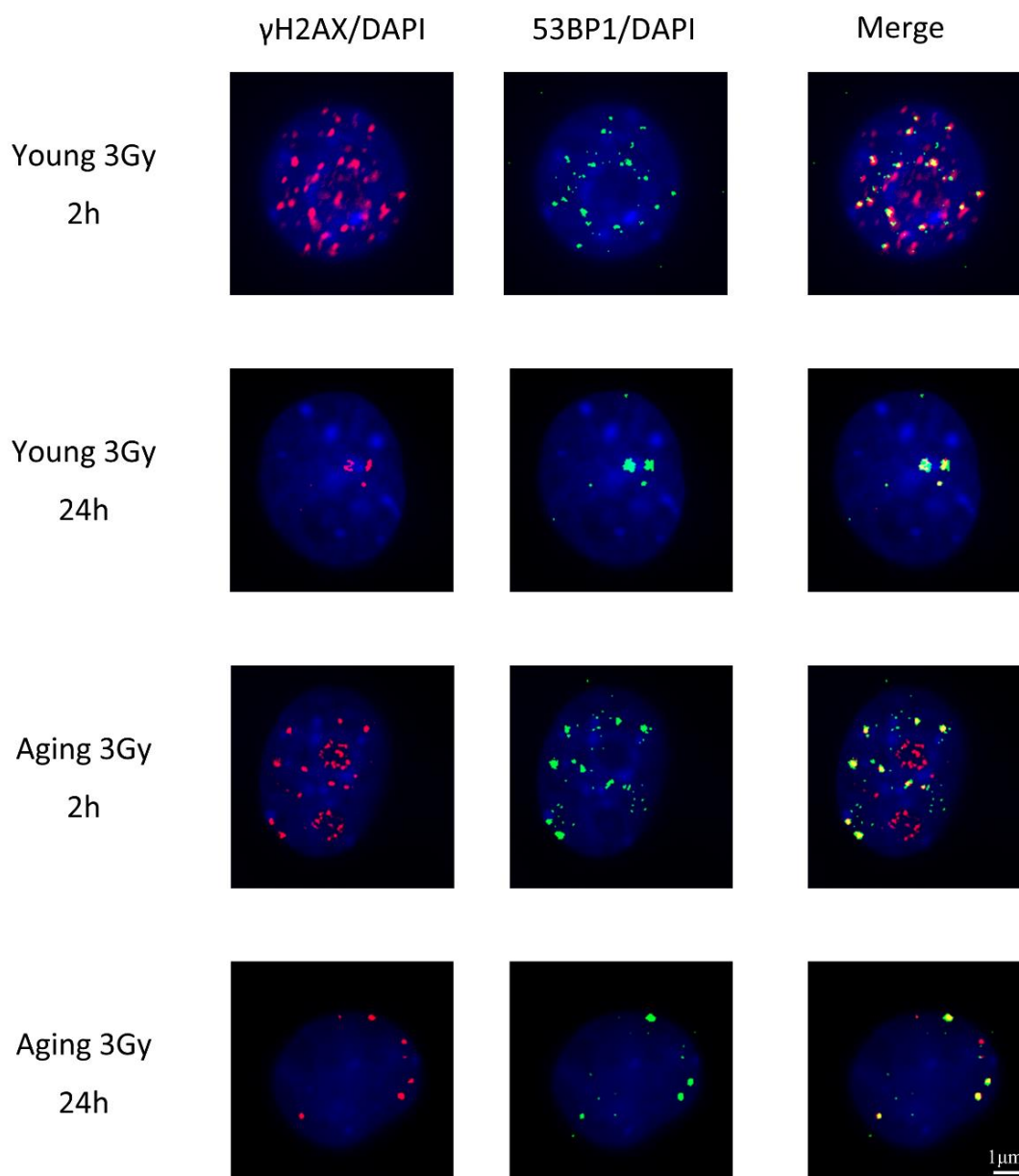


Figure 4.19: DSB damage foci (γH2AX, red; 53BP1, green) formation shown in young and ex vivo aging MSCs in control, 2 hours and 24 hours after a 3 Gy of X-irradiation groups. Nuclear counterstaining by DAPI. Merged foci containing both markers are assayed as these indicate sites of DSB repair

The mean number of γ-H2AX/53BP1 foci 2h after 3 Gy irradiation was 16.5 (CI 15.8-17.2) in young and 12.3 (CI 11.4-13.2) in aged cells ($p < 0.01$) (Figure 4.21). The baseline of γ-H2AX/53BP1 foci for sham-irradiated cells did not exhibit a significant difference between young and aged cells (Figure 4.21).

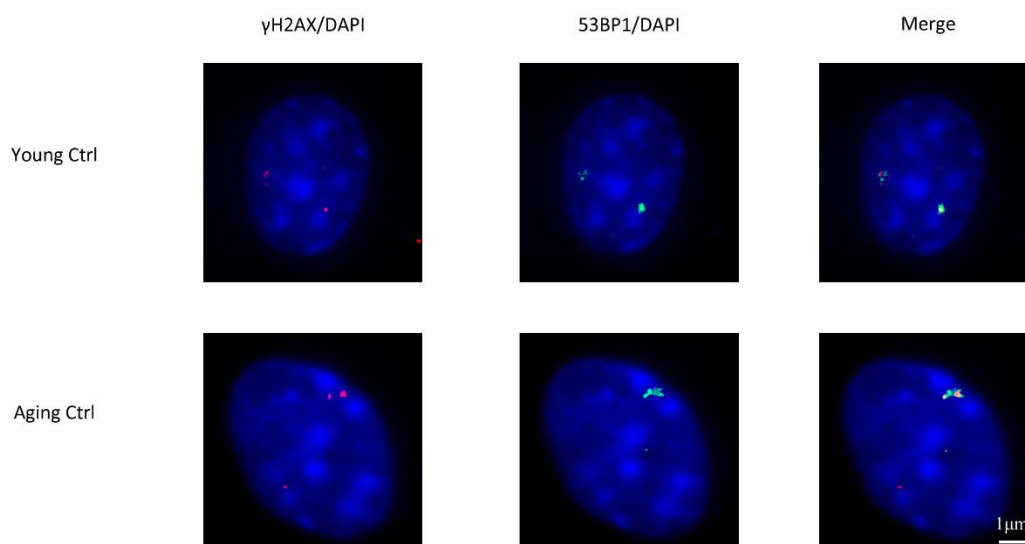


Figure 4.20: The baseline of γ -H2AX/53BP1 foci for sham-irradiated cells. Nuclear counterstaining by DAPI. Merged foci containing both markers are assayed as these indicate sites of DSB repair.

The decrease in repair foci at the early time point coincides with the onset of damage repair. The lower number indicate that the recognition of the damages sites is lower in aged cells. In contrast, the higher fraction of foci seen after 24h in the aged cells indicates that either the recognition of foci is delayed or that the repair of foci once they have been recognized is reduced (Figure 4.21B). It is unlikely that the variation in the number of residual foci detected is due to differences in the complexity of the damage as the foci size is comparable in both aged and young cells.

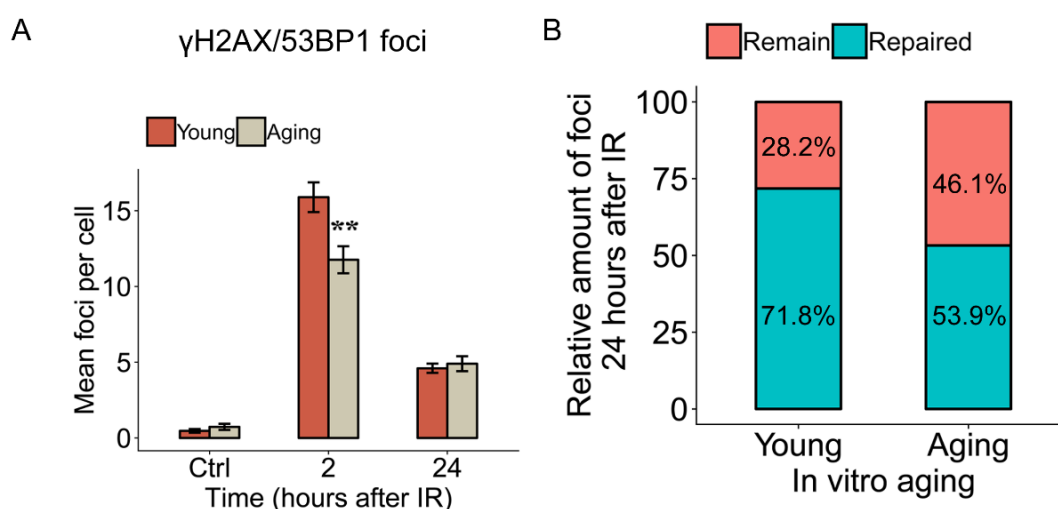


Figure 4.21: Impaired DNA repair recognition in *ex vivo* aging hMSCs. (A) Quantification of γ H2AX+53BP1 DSB-foci in MSCs 2 hours and 24 hours after 3Gy X-

irradiation. (B) The percentage of colocalized γ H2AX+53BP1 foci 24 hours post irradiation relative to the values at 2 hours post irradiation in young and *ex vivo* aging MSCs (mean values \pm SEM, $n = 3$, *: $p < 0.05$, significance by paired, one-sided T-test. MSCs from three donors were used for experiments. For each experiment at least 50 cells were counted for MSCs from each donor).

4.1.12 Changes in DNA repair foci involved in homologous recombination in human MSCs

As the bioinformatics study revealed involvement of down-regulated HR repair in aged MSCs we next investigated the HR capacity. To measure HR-guided DNA repair the formation of pBRCA1 foci (alone or in colocalization with γ -H2AX) was compared in young and in *ex vivo* aged hBM-MSCs (Figure 4.22-4.23).

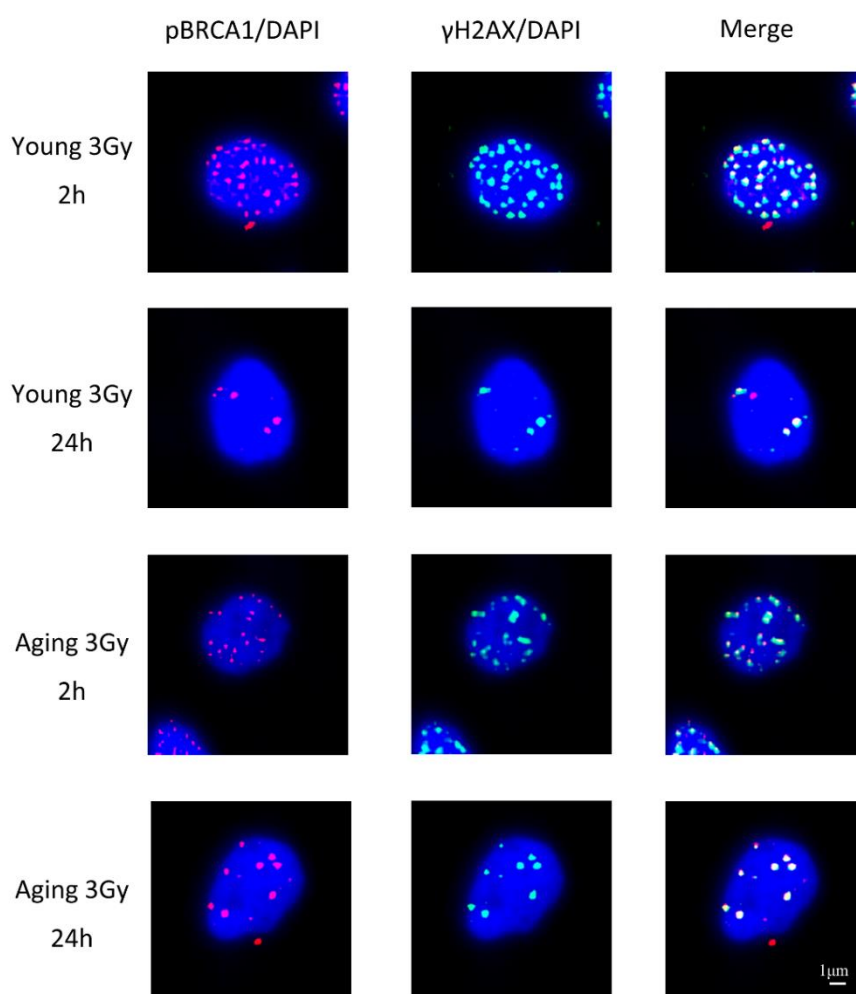


Figure 4.22: Repair foci formation is shown in young and *ex vivo* aging hMSCs 2 hours and 24 hours after 3 Gy of γ -irradiation by immunofluorescence staining for pBRCA1 (red) and γ H2AX (green). Nuclear counterstaining by DAPI.

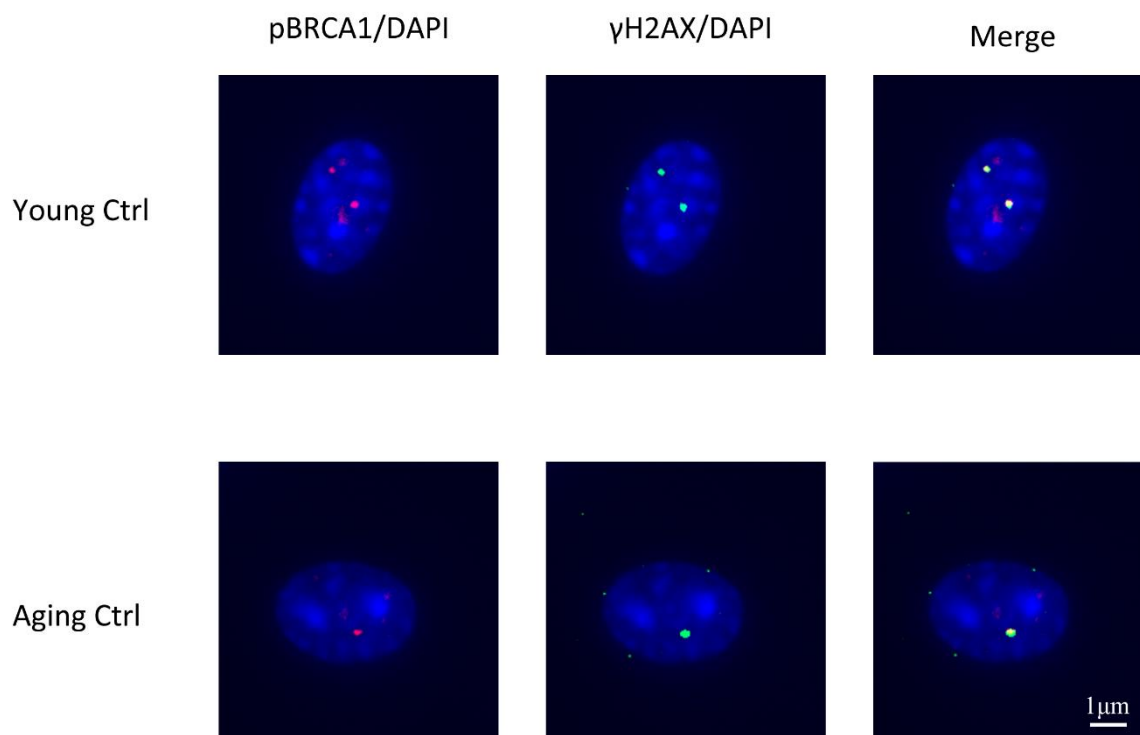


Figure 4.23: The baseline of pBRCA1/γ-H2AX foci for sham-irradiated cells. Nuclear counterstaining by DAPI. Merged foci containing both markers are assayed as these indicate sites of DSB repair.

The mean foci number of pBRCA1+γ-H2AX foci 2h after 3 Gy irradiation was 15.89 (CI 13.77 – 18.01) in young and 11.76 (CI 9.98 – 13.54) in aged cells ($p < 0.01$) (Figure 4.24A). Sham-irradiated cells of the same passage did not exhibit a significant difference in the background level of pBRCA1+γ-H2AX foci. A higher proportion of unrepaired foci were seen to be retained in *in vitro* aged hBM-MSCs (40.79%) compared to young cells (28.15%) 24h after irradiation. A similar reduction with *in vitro* age was also seen for pBRCA1 and γ-H2AX foci counted separately (Figure 4.24C, 4.24E). The effective repair efficiency of DNA DSBs can be tested by the disappearance of the DNA repair foci over a period of 24 hours after IR. It has been found that a larger portion of DNA DSBs remained unrepaired or delayed repaired in *ex vivo* aged versus the young counterpart (28.15% vs 40.79%; 25.38% vs 35.77%; 22.06% vs 31.22%, all $p < 0.05$) (Figure 4.24B, 4.24D, 4.24F), which indicated either the recognition of foci is delayed or that the repair of foci once they have been recognized is reduced

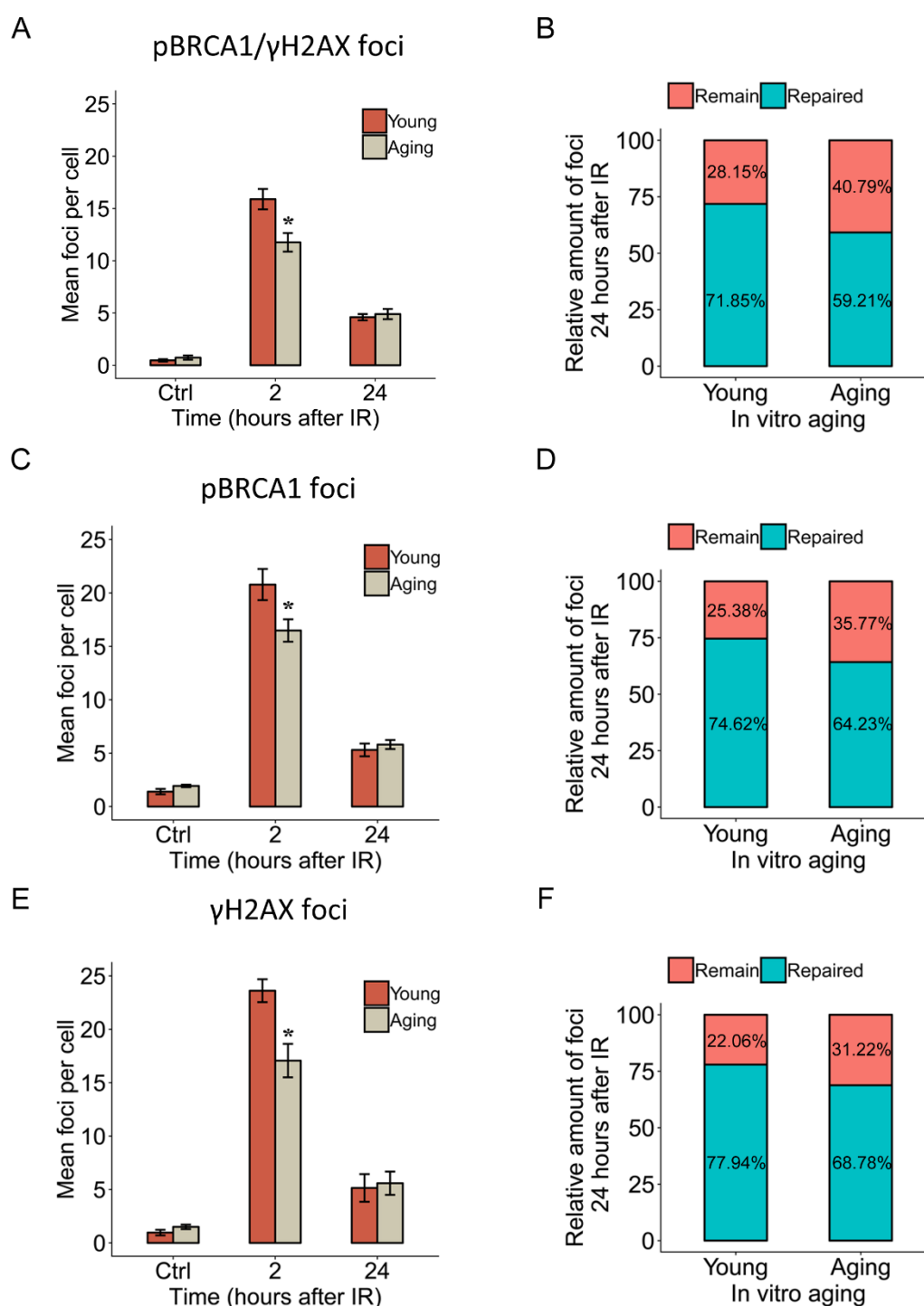


Figure 4.24: Impaired homologous recombination repair capacity in *ex vivo* aging hMSCs. (A) Quantification of pBRCA1+ γH2AX -foci formation in hMSCs 2 hours and 24 hours after 3Gy γ-irradiation. (B) The proportion of individual pBRCA1+γH2AX colocalizing foci in young and *ex vivo* aging MSCs 24 hours after γ-irradiation. (C) Quantification of pBRCA1 foci formation in hMSCs 2 hours and 24 hours after γ-irradiation. (D) The proportion of pBRCA1 foci in young and *ex vivo* aging MSCs 24 hours after γ-irradiation. (E) Quantification of γH2AX foci in hMSCs 2 hours and 24 hours after γ-irradiation. (F) The proportion of individual γH2AX foci in young and *ex vivo* aging MSCs 24 hours after γ-irradiation.

in vivo aging MSCs 24 hours after γ -irradiation. (mean values \pm SEM, $n = 3$, *: $p < 0.05$, significance by paired, one-sided T-test. MSCs from three donors were used for experiments. For each experiment at least 50 cells were counted for MSCs from each donor).

The distribution of the initial DNA repair foci in single cells was also analysed. A subset of individual cells which count for approximate 16.5% irradiated-MSCs have less foci than other irradiated-cells after 9 weeks (Figure 4.25A-4.25B), which indicates a sub-population of MSCs with a reduced DNA damage response arises during *ex vivo* expansion and aging of hBM-MSCs.

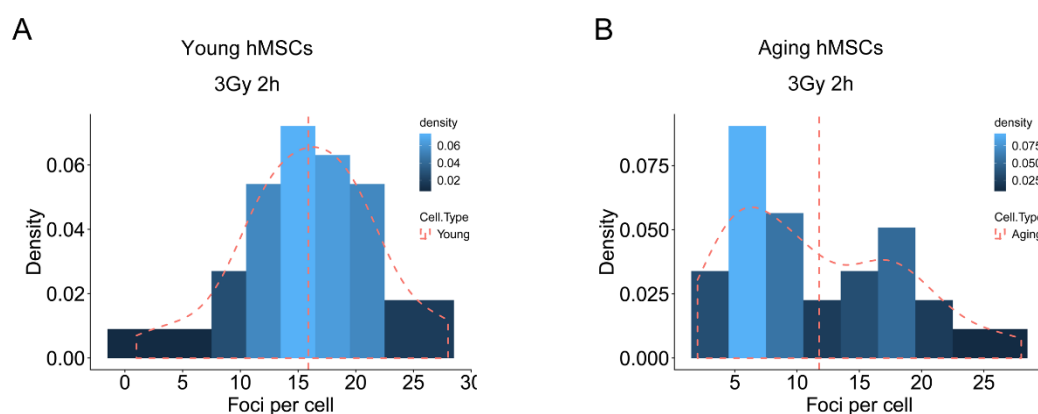


Figure 4.25: Distribution of the initial DNA repair foci in single cells. (A) Dispersion analysis of DNA repair foci in single cell from young hMSCs. (B) Dispersion analysis of DNA repair foci in single cells from *in vitro* aging hMSCs. (MSCs from three donors were used for experiments. For each experiment at least 50 cells were counted for MSCs from each donor).

4.2 Characterizing of the stemness and autologous differentiation of mouse MSC

In vitro long-term culture model of murine MSC was established as described above. The phenotypic changes in these cells during extended passage was observed. In the P0 passage, the murine MSCs exhibited the expected MSC colony formation ability (Figure 4.26A). The MSCs have heterogeneous shape in a single colony (Figure 4.26B). The shape of murine MSCs became homogeneous after the first passage by accutase. Spontaneous differentiation is only observed when single colonies were maintained for 2-3 weeks.

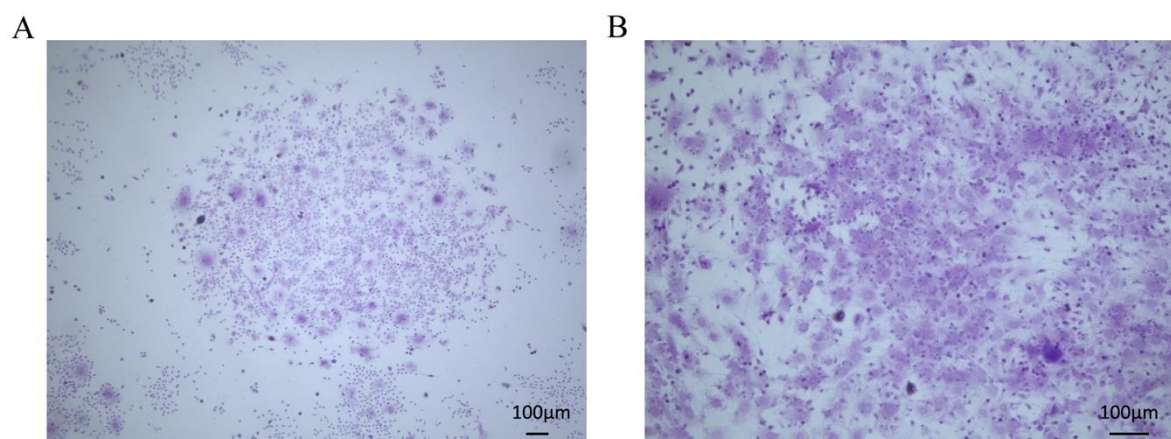


Figure 4.26: The colony formation after seeding in P0 murine MSCs. (A) A typical colony 7 days after seeding of murine MSCs from bone marrow by Giemsa staining. (B) The precursor cells for different lineage differentiation existed in one single colony as showed by the different shapes of MSCs in a single colony.

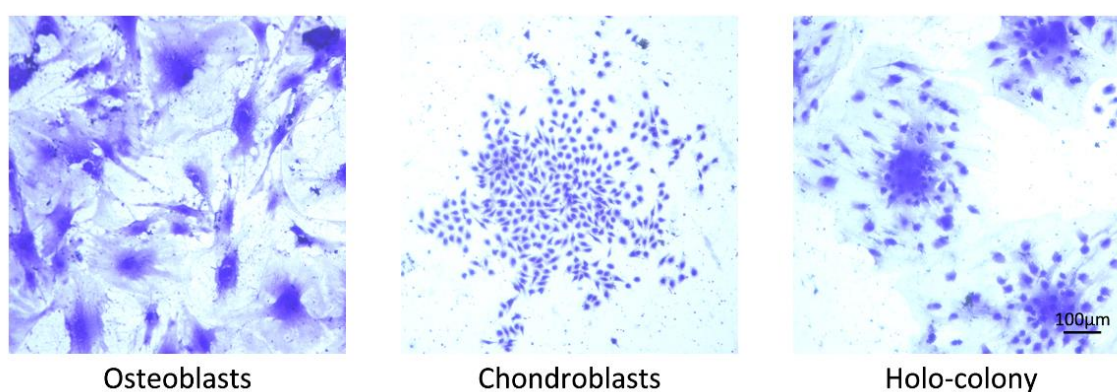


Figure 4.27: Different types of colonies existed in P0 MSCs.

We found different types of colonies existed in the P0 passage (Figure 4.27A). Some only contained osteoblasts or chondroblasts whereas others are so called holo-colonies that contains MSCs with different lineage differentiation. Limited dilution method was used to obtain colonies each derived from a single precursor cell. After colony growth the RNA was extracted and RT-PCR phenotyping was performed using stem cell markers: Klf4, Bmi1, Oct3-4 and Nestin. Results revealed the holo-colony (osteoblasts and chondroblasts exist in a single colony) had the highest expression level of Klf4, Bmi1, Oct3-4 while lowest level of Nestin compared to the other two

colony types (osteoblast colony and chondroblast colony) (Figure 4.27B). The results above confirmed the stemness of holo-colonies.

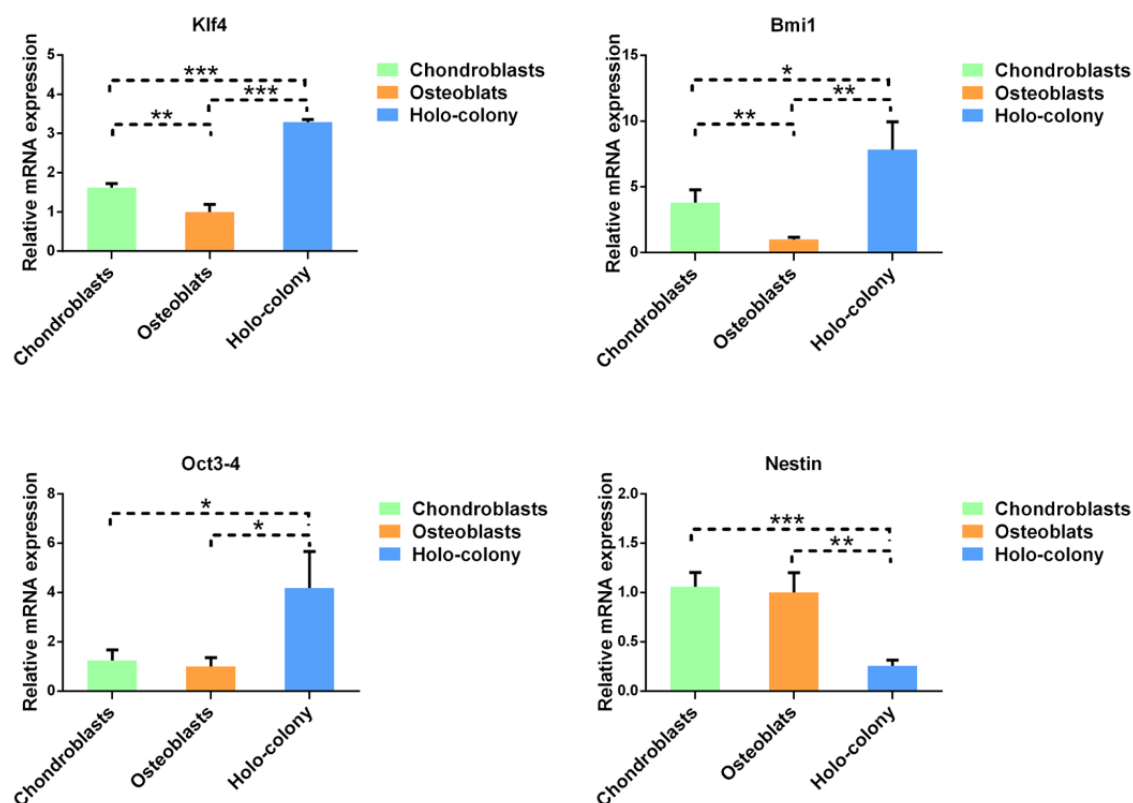


Figure 4.28: RT-PCR demonstrated the gene expression of stem cell markers in different type of colonies. (mean values \pm SEM, $n = 3$, *: $p < 0.05$, significance by Bonferroni T-test and one-way ANOVA test).

To characterize the differentiation properties of *in vitro* cultured mMSCs, ALP-Oil red double staining was performed in the holo-colony. Results show that there is indeed a spontaneous differentiation of mMSCs into osteoblasts and adipocytes in a single-colony 21 days after seeding, which confirmed the lineage differentiation abilities of MSCs from a single cell (Figure 4.29).

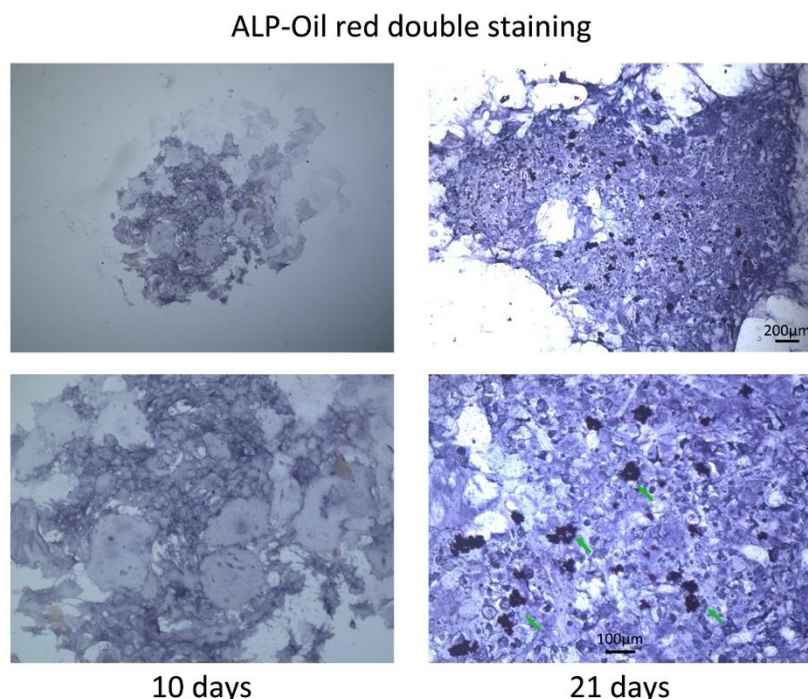


Figure 4.29: Spontaneous differentiation of mMSCs into different lineages in a single colony. The holo-colony exhibited spontaneous differentiation into osteoblasts and adipocytes by ALP-oil red double staining. The green arrow indicated the stained-red fat droplets in a single colony 21 days post seeding. The deep blue color indicates the ALP activities of osteoblasts.

4.3 Telomere instability post IR in murine MSCs

4.3.1 Q-FISH quantifies the telomere length in MSCs

Quantitative telomere FISH analysis in interphase nuclei of MSCs from young and aging mice, with or without a preceding γ -irradiation was done to estimate changes in the average telomere length. A marginal but significant reduction in telomere length (from 445 AU to 430 AU, relative change -3.4 %) was seen during 18-month aging ($p=6.1 \times 10^{-4}$) (Figure 4.30-4.31). There was also a comparable reduction of signal intensities seen after *in vitro* γ -irradiation. Thus, in young donor derived MSCs, the average telomere signal intensity reduced from 445 AU (unirradiated controls) to 434 AU (following 2 Gy irradiation), a relative reduction of -2.5% ($p < 3 \times 10^{-4}$). The same tendency was also found in old donor derived MSCs with the reduction from 430 to 426 AU.

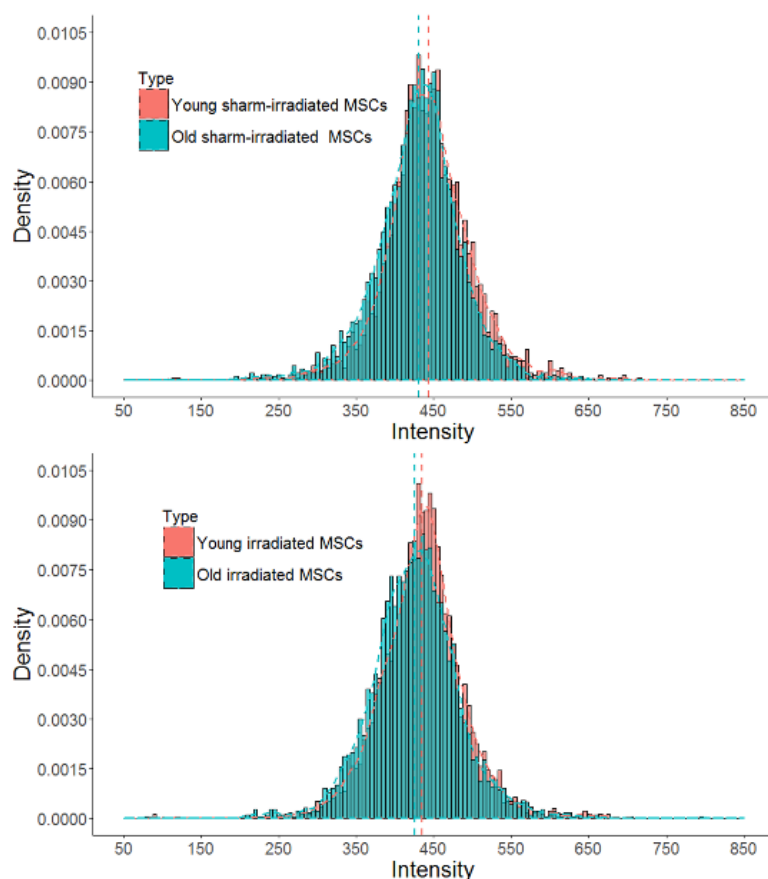


Figure 4.30: Reduction in telomere length in MSCs obtained from older mice. Q-FISH analysis of interphase spreads of MSCs which came from young and old mice with or without IR. Distribution of telomere length as analysed by Q-FISH in interphase nuclei of MSCs from young (2 month of age) and old (18 month of age) mice with or without 2Gy γ -irradiation *in vitro*. The histograms of telomere signal intensities are based on at least 2750 scored telomeres from >17 nuclei in each group. Two-way ANOVA Test was applied for detecting the significance between aging and irradiation factors.

Young sham-irradiated	445
Old sham-irradiated	430
Young 2Gy gamma-irradiated	434
Old 2Gy gamma-irradiated	426

Figure 4.31: The average Q-FISH intensity value of MSCs which came from young and old mice with or without IR

4.3.2 Telomere losses and signal interruptions associate with greater donor age and with exposure to γ -irradiation

The occurrence of interrupted or split telomere signals (multiplicity of telomere signals, MTS) is believed to result from errors during telomere replication (208), but a link to radiation-induced DNA damages has not yet been investigated. We demonstrated that IR and higher donor age can increase the frequency of MTS in MSCs independently (Figure 4.32-4.32). The basal level of MTS sites in the chromosomes of unirradiated MSCs was significantly increased in those cells obtained from older mice, with frequencies of 0.18% (CI 0.14%-0.22%) and 0.48 % (CI 0.43-0.53, $p=0.006$), respectively. A 2 Gy γ -irradiation increased the MTS frequency from 0.18% to 0.52% (CI 0.48%-0.68%) in cells derived from young animals, whilst it increased from 0.48% to 0.87 % (CI 0.81-0.93%) in aged animals. Both the effects of donor age ($p=6*10^{-4}$) and of radiation-dose ($p=3*10^{-4}$) were significant by ANOVA, but the absolute effects of radiation was similar in MSCs from young (plus 0.34%) and from old donors (plus 0.39%), the similar gap value (0.34% vs 0.39%) between radiation and non-IR MSCs from young and old donor suggesting an additive interaction rather than an age-related sensitization for radiation induced genotoxic stress.

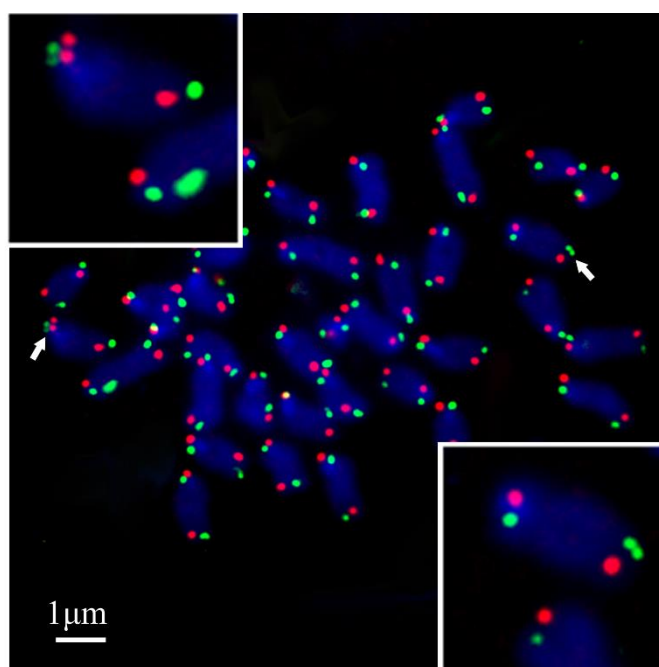


Figure 4.32: Representative metaphase spreads from irradiated MSCs, showing chromosome ends with multiple telomere signals (MTS, arrow).

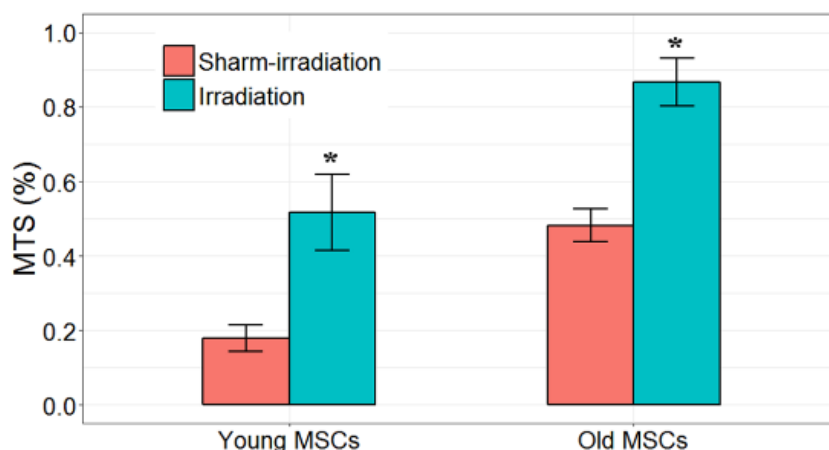


Figure 4.33: The frequency of Multiple telomere signals (MTS) increased after IR. Percentage of fragile telomeres in primary MSCs from young and old mice. At least 60 metaphases/sample are counted. (MTS, arrow; mean values \pm SEM, $n = 3$, *: $p < 0.05$, significance by one-sided T-test).

Complete loss of telomeres can only be detected reliably on metaphase chromosomes. In non-irradiated cells the number of telomere signal-free chromosome ends were unchanged. MSCs obtained from aged mice compared to those from young mice with frequencies of 0.96 % (CI 0.83%-1.09%), as opposed to 0.75% (CI 0.81%-0.99%) ($p=0.27$) respectively (Figure 4.34-4.35). Whereas the donor-age had no effect, *in vitro* γ -irradiation resulted in a significant increase of telomere signal losses in cells from both young and old animals. Thus, the irradiation produced loss of telomere signals of 2.3 % (CI 2.1% - 2.5%) in older cells compared to 1.54% (CI 1.43%-1.65%) in the cells from younger mice ($p<0.05$). Irradiation increased the frequency of telomere loss in MSCs obtained from both young and old animals. Considering both young and old animal-derived cells together the difference due to irradiation was highly significant ($p<9*10^{-5}$, ANOVA). Both the absolute increase (plus 1.34%) as well as the relative change (1.7-fold) was higher in old donor derived MSCs than in cells from young mice.

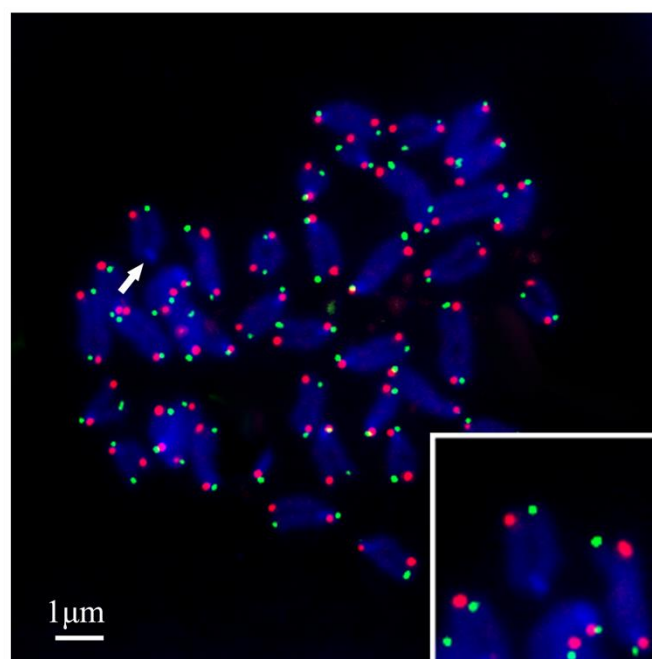


Figure 4.34: Representative metaphase spreads from irradiated MSCs, showing chromosome ends without telomere signals (SFE, arrow).

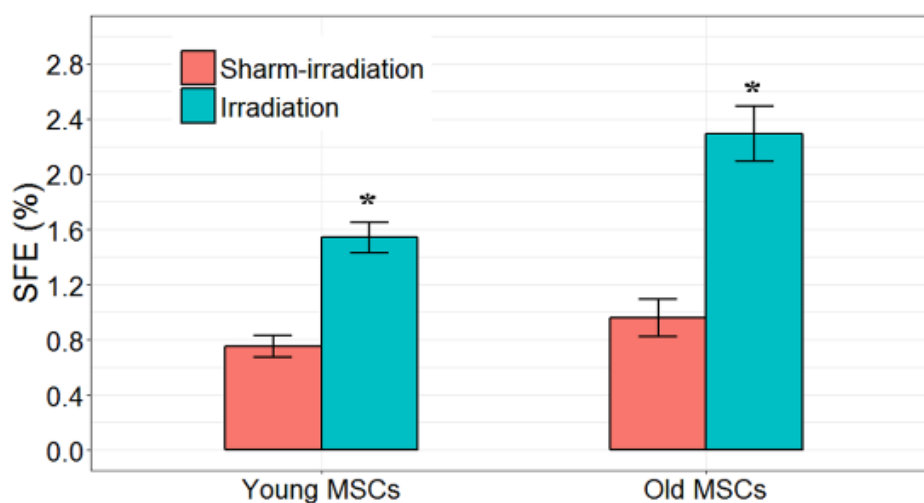


Figure 4.35: The frequency of chromosome ends without telomere signals (SFE) increased after IR. Percentage of fragile telomeres in primary MSCs from young and old mice. At least 60 metaphases/sample are counted. Error bars indicate standard error of the mean (Telomere signal free end, arrow; mean values \pm SEM, $n = 3$, *: $p < 0.05$, significance by one-sided T-test).

4.3.3 Higher donor age of MSCs increases level of T-SCE after exposure to γ -irradiation

Our results show that this form of telomere alteration is very rare in MSCs from young donors, both with or without exposure to γ -radiation (Figure 4.36-4.37). In MSCs derived from aged donor mice, however, T-SCEs were induced by 2Gy γ -irradiation, occurring in 6.7% of all metaphases analysed. This difference indicates a significant synergism between donor age and radiation-exposure (ANOVAR, $p=6 \times 10^{-4}$).

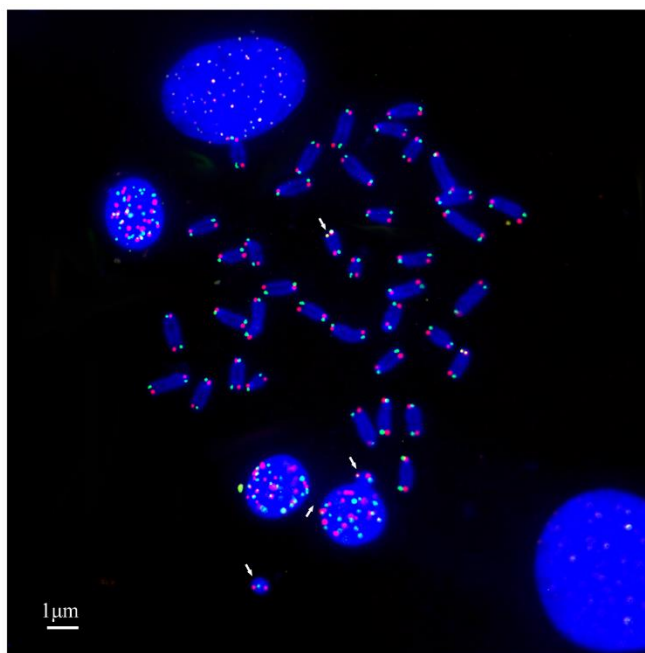


Figure 4.36: Representative metaphase spreads of aged irradiated-MSCs showing DAPI staining (blue), leading strand telomere fluorescence signals (red) and lagging strand telomere fluorescence signals (green). Arrow: chromosomal instability (T-SCE, anaphase bridge and micronuclei).

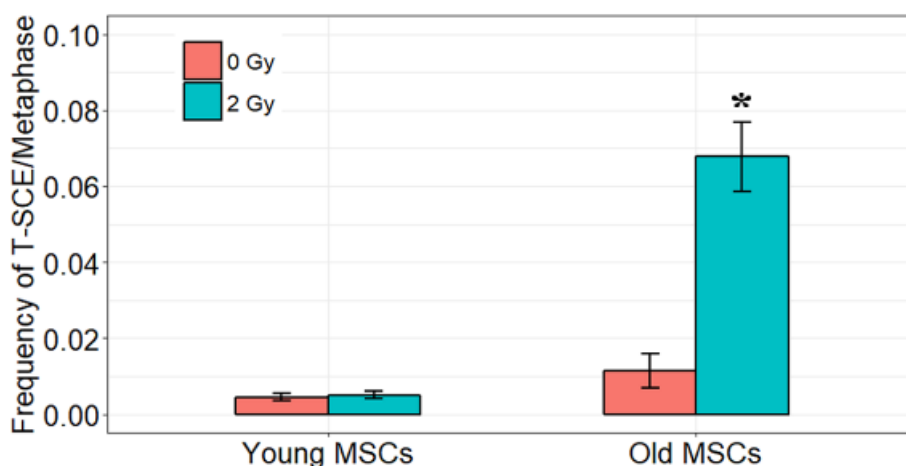


Figure 4.37: T-SCE frequency alters in irradiated MSCs from aged mice. The frequencies of T-SCEs in MSCs from young (2 month of age) and aged (18 month of age) donor mice (mean values \pm SEM, $n = 3$, *: $p < 0.05$, significance by one-sided T-test).

A high level of heterogeneity in the length of telomeres is characteristic of cells with activated ALT (209). We therefore determined the range of telomere signal intensities in individual metaphases, and compared them with the T-SCE status of the MSCs. The $\Delta range$ in one single metaphase was defined as: $\Delta range = Highest\ intensity\ value - lowest\ intensity\ value$. The histogram shows that individual MSCs that display T-SCE also have a broader range of telomere signals (Figure 4.38).

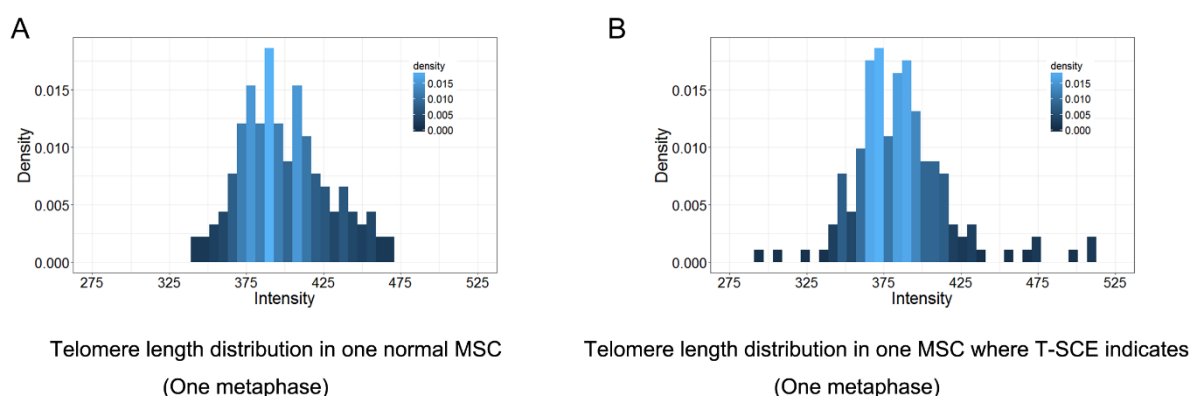


Figure 4.38: Telomere length distribution in a single metaphase. (A) Representative histogram of dynamic range of telomeric DNA signal intensity at individual chromosome ends in one normal MSC. (B) Representative histogram of

typical dynamic range of telomeric DNA signal intensity at individual chromosome ends in one MSC which T-SCE occurs.

The difference in length between the longest and shortest telomere (range) in single metaphases has a tendency to higher values in MSCs that show T-SCE as compared with MSCs without T-SCE (Mann-Whitney test $P=3.8e^{-5}$) (Fig 4.39).

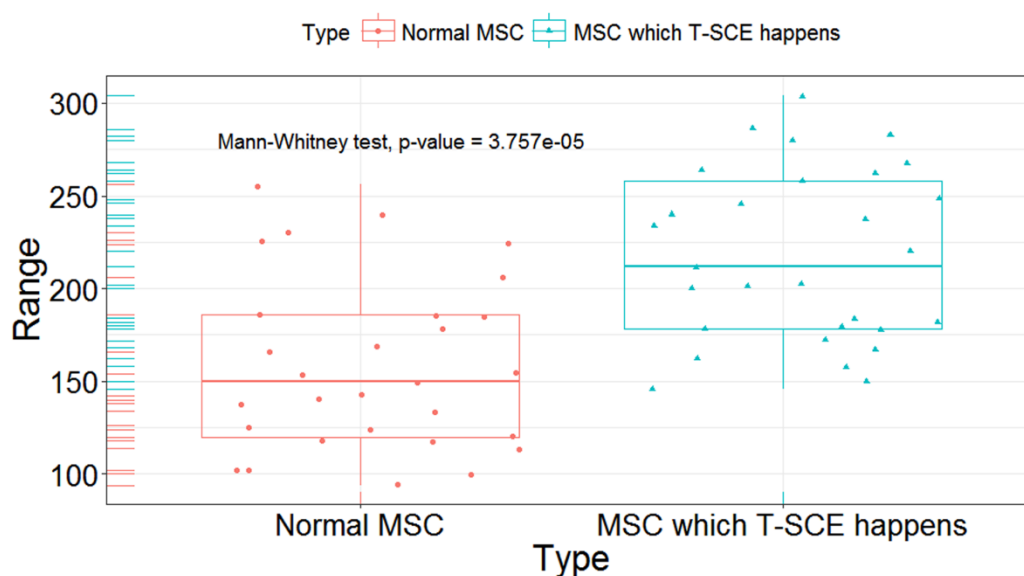


Figure 4.39: Boxplot of delta range value in normal MSCs and T-SCE MSCs.

Boxplot of delta range value in normal MSCs and T-SCE MSCs. T-SCE MSCs show a significant increase in signal range. Each dot or triangle represents the spread between the most intense and the least intense telomere signal in an individual metaphase. A Mann-Whitney test was used to calculate the statistical significance of the observed differences in delta range value (mean values \pm SEM, $n = 3$, *: $p < 0.05$, significance by Mann-Whitney test).

4.3.4 ALT associated PML bodies are not found in mMSCs after IR

ALT associated PML Bodies (APBs) are large donut-shaped nuclear structures containing PML protein, telomeric DNA, and the Shelterin proteins TRF1/2 (209). Immunofluorescence staining of a human (U2OS) and a murine osteosarcoma cell line (199) was able to detect APBs and validate the sensitivity of the assay. We then checked if APBs were detectable in irradiated MSCs derived from aged donor mice (Figure 4.40). In irradiated MSCs from old donor, despite the presence of $\sim 6.7\%$ cells with T-SCEs (see above), PML staining was only seen outside of the nucleus (Figure

4.40, upper panel). Because only PMLs in nucleus qualify as ALT-associated PML bodies, it is clear that MSCs don't present APBs.

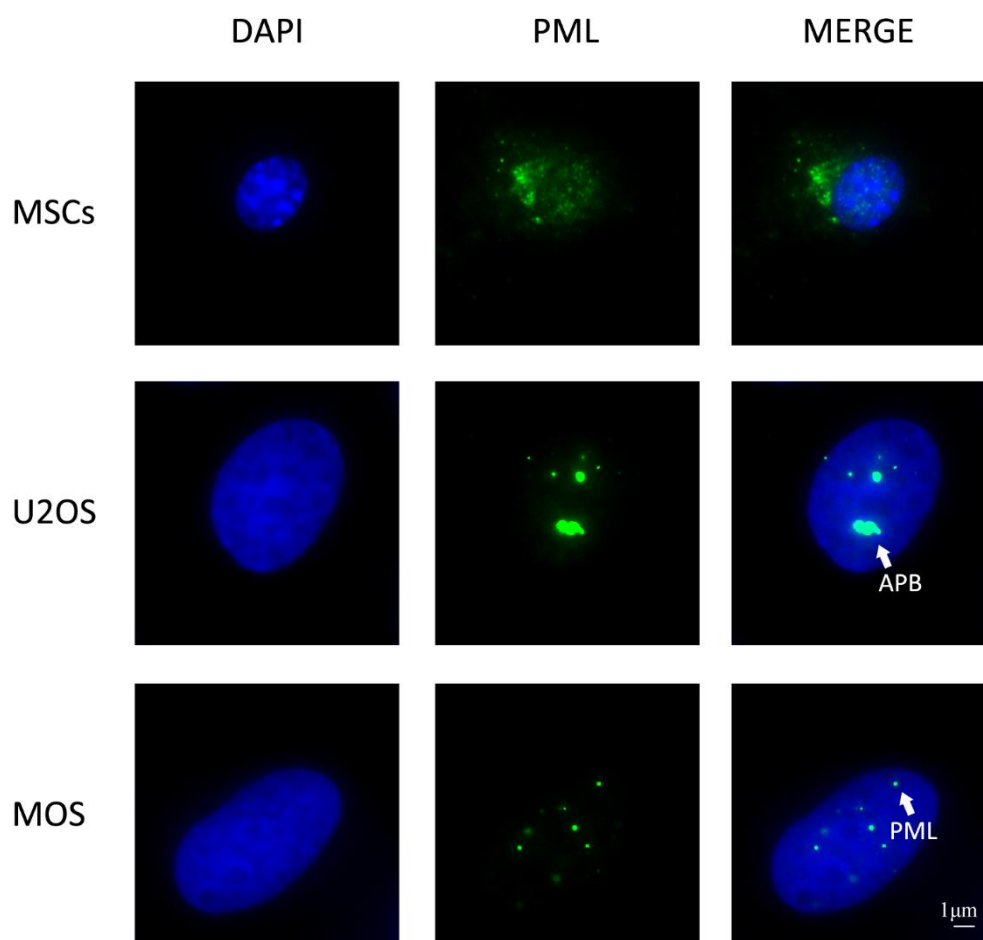


Figure 4.40: Immunofluorescence staining for ALT associated PML bodies. In cells of the human osteosarcoma U2OS cell line and of a murine osteosarcoma cell line MOS, PML bodies can be found in nuclei (green signal dots in nucleus). In irradiated MSCs, PML signals are not detectable in the cell nucleus. Green: PML immunofluorescence staining; blue: DAPI staining.

4.3.5 Irreparable DNA repair/telomere foci are existed in irradiated MSCs

To compare the effects of irradiation on the telomeres from young and aging mice we stained 2Gy-irradiated cells for the presence of repair foci (γ H2AX) and for telomeres by Tel-FISH 90 min, 8 hours, 24 hours post IR. At 90 min post-IR, a number of the γ H2AX DNA damage foci were observed to partially overlap with the telomere FISH signals, forming telomere dysfunction-induced foci (TIF). When the number of TIF signals was compared between cells obtained from young and old mice 90 min, 8

hours and 24 hours post-IR, a large fraction of γ H2AX DNA repair foci disappeared 8 hours after IR in MSCs from both young and old donor, whereas the TIFs existed for an extended time period (Figure 4.41-4.42). The proportion of telomeres with overlapping γ H2AX foci increased significantly in 8 hours (MSCs from young donor: 14.58%, $P < 0.01$, MSCs from old donor: 12.11%, $P < 0.01$) and 24 hours (MSCs from young donor: 15.64%, $P < 0.01$, MSCs from old donor: 13.64%, $P < 0.01$) post IR, compared with the fraction of overlapping telomere/ γ H2AX signals 90 min post IR (MSCs from young donor: 9.2%, MSCs from old donor: 9.0%). The above data confirmed the IR induced DNA damage on telomeres in MSCs.

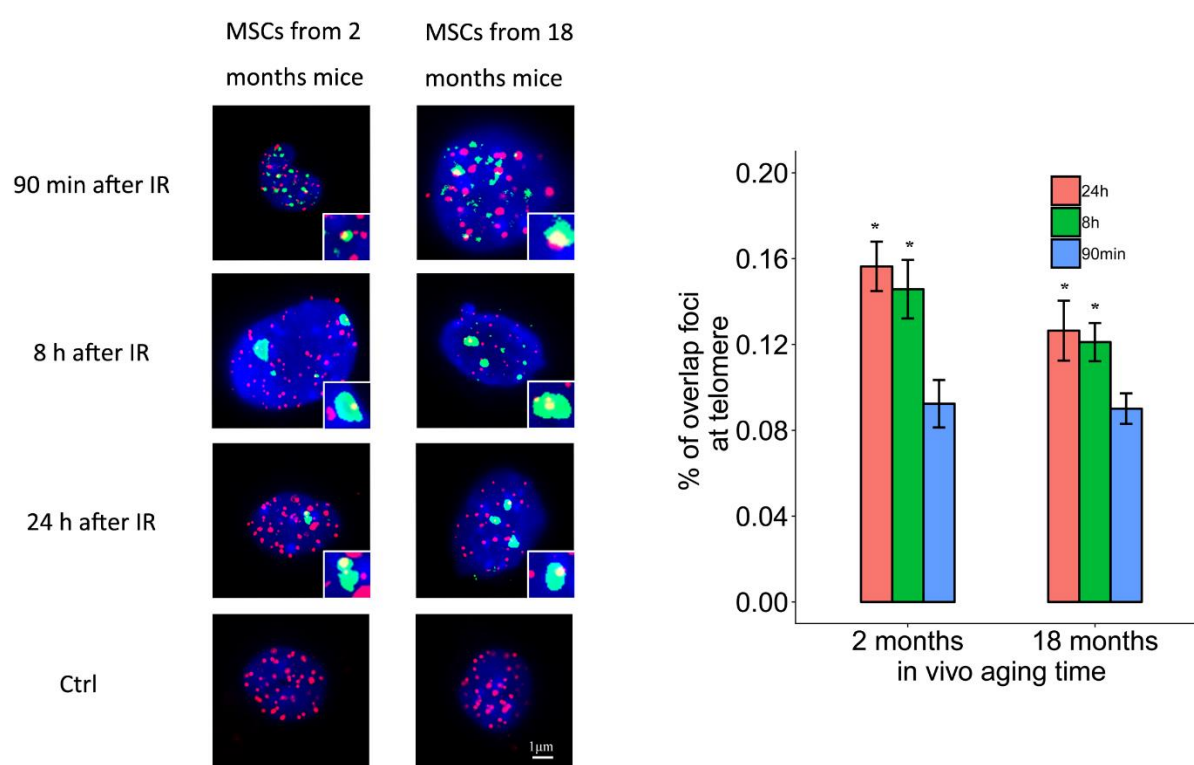


Figure 4.41: Telomeres and DSB damage foci at MSCs from 2 months, 12 months, 18 months mice after radiation. (A) Representative images from irradiated MSCs from 2 months, 12 months, 18 months mice showing co-localization of γ H2AX foci at telomeres. (B) Percentages of γ H2AX foci that overlap with telomere signals for 90 minutes, 8 hours, 24 hours after IR (mean values \pm SEM, $n = 3$, *: $p < 0.05$, significance by two-sided T-test.). There is no γ H2AX foci overlapped with telomere signal in the control group.

5 Discussion

5.1 ATM-dependent recognition of DNA breaks and chromosomal instability in *ex vivo* aging human MSCs

The cellular status of MSCs can be affected by the extended period of *in vitro* culture that is usually required for expansion of the population prior to transplantation. Their potency for lineage differentiation, telomere maintenance mechanism and growth potential may all be negatively influenced (35). In contrast, stem cell potential upon long-term *in vitro* culture have been found in embryonic stem cells (1). In our previous study and the basis of this thesis we have found that *in vitro* expanded mouse MSCs gradually lost their capacity to recognize DSBs and to form or resolve DNA repair foci. The number of background γ H2AX/53BP1 DSB repair foci in the murine MSC cells did not change over an 8-week *in vitro* culture. This indicates that the capacity for the detection and repair of the low level of spontaneous DNA DSBs remains adequate during MSC ageing. However, when exposure to ionizing radiation occurs the greatly increased number of DSBs is not fully recognized and/or repaired in older MSCs. Thus, the number of DSB repair foci was lower in older MSCs, compared to younger cells at the 2h time of damage response. Thereafter the DNA DSB repair kinetics in the older MSCs further revealed a n alteration in the repair process, leading to a higher number of residual breaks in aged MSCs after 24h. This may be interpreted as evidence for a limited capacity for DNA DSB recognition, a slower rate of damage site recognition, or a slower rate of repair. As the repair of DSBs requires phosphorylation, binding, and ultimately removal of the H2AX protein to preserve chromosomal integrity and avoid genome stability (210) the persistence of higher levels of γ H2AX/53BP1 foci we detected after irradiation of the aged MSCs indicates that they may have a greater potential for DNA misrepair and genomic instability, which leads to senescence and loss of repopulation capacity of MSCs.

Chromosomal DNA defects can be recovered by the activation of ATM pathway, indicating the important roles of ATM pathway in normal segregation of sister chromatids after mitosis (211). The phosphatidylinositol 3-kinase ATM plays the central role in DNA damage signaling (212). In the previous project we have found increased age *in vitro* associated with a reduction of ATM-dependent foci, indicating impairment of ATM signaling during *in vitro* extended culture.

5.2 Downregulated Brca1-related homologues recombination and impaired DNA double-strand break recognition in aging MSCs

In the previous section we discussed the aging process of MSCs impairs the handling of γ H2AX/53BP1 DNA foci. We argue that it would be important to identify any change of gene expression profile during aging of MSCs, as this may inform on the causes of the defects in the DSB response. Two mechanisms have been proposed for the cellular aging process in general, which may also affect MSCs. Firstly aging may be a program controlled by changes in gene expression. Secondly, this program may be subjected to a series of stochastically accidental events. The interplay of the two mechanisms characterizes aging at various levels (213, 214). Telomere shortening and telomeric structure modification also occur during the aging process, although this may be both a cause or an effect of the ageing phenomenon (215). Previous studies have revealed altered gene expression pattern during long-term culture of MSCs (216). The major changes of the gene expression profile described during long-term cell growth were associated with cell differentiation, apoptosis, cell death, mitosis and proliferation. These were deemed to be independent of isolation and expansion methods used, although the passaging method and cell seeding density may have been a significant influence on changes in the gene expression pattern (216).

One potential role of aging is to protect the tissues and organs from an increased risk of tumorigenesis due to the accumulated DNA mutations during long-term cell division (213). The aging program is related to changes in gene expression profile (217). Through our analysis of the changes between young and aging human MSCs derived from the same donors we were able to identify many changes in gene profiles, with the potential to influence various pathways associated with ageing, stemness and cell function. Consistent with the previous study by Schallmoser et al (216), we have established that mitosis, cell cycle and proliferation are key downregulated pathways during the *in vitro* MSC aging. Besides these, we also found the dysregulation in many mRNA species involved in DNA repair-related pathways. Importantly, given our observation of reduced damage recognition and/or repair we note that most of the genes that are involved in DNA repair pathway were down-regulated. Interestingly, unsupervised clustering revealed the downregulation pattern is homogeneous among different donors, therefore indicating that the impaired DNA repair capacity upon long-term culture of MSCs is independent of donor. Among the DNA repair pathways

predicted to be involved, homologous recombination (HR) was one of the most significant affected pathways. Examination of just those genes involved in the HR pathway indicated the down-regulation of several key HR-related regulators such as BRCA1, RAD51 and RAD54. If HR capacity were to be reduced during ageing then the capacity to eliminate any accumulated cytogenetic damage would also be impaired. In turn this would affect the genomic stability of MSCs. Consequently aged MSCs would be more likely to sustain permanent genetic damage if exposure to ionizing radiation, including cells *in vivo* prior to harvesting for transplantation.

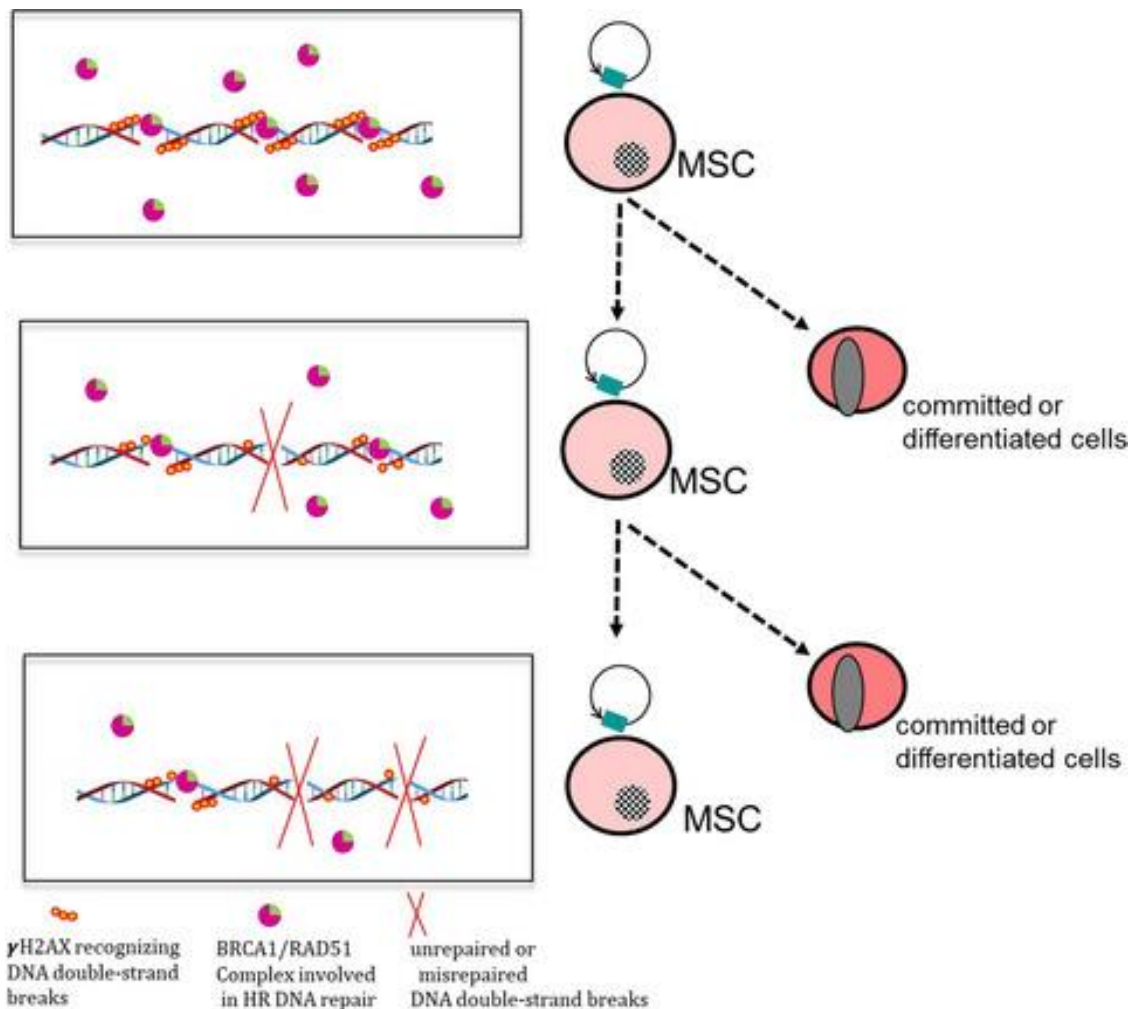


Figure 5.1: During the process of their *in vitro* expansion, primary human BM-MSCs experience in pairment of their ability to recognize DNA double-strand breaks. A slower DNA damage response (fewer γ -H2AX + 53BP1 foci) after 2h was associated with a downregulation of BRCA1-related DNA repair by homologous recombination and chromosomal replication pathways, suggesting that *in vitro* aged hMSCs could be affected by reduced genetic stability.

Consistent with the idea that impaired DNA repair increases the long-term risk for gene mutations leading to tumorigenesis (218) it has recently been found that cells derived from ex-vivo expanded rodent MSCs can undergo malignant transformation more frequently after reinjection into *scid* mice (219). However, MSCs of human origin are more resistant to transformation (220). Then it is of great interest to determine if the DNA repair potential is higher in human than mouse and can help to prevent malignant transformation of human MSCs, and if so, how long-term *in vitro* aging influence the DNA repair potential. The mechanism of DDR and DNA repair in human MSCs has not been clearly addressed.

To validate the analysis from transcriptomic data we performed RT-PCR and analysis of DNA damage repair processes. Decreased γ -H2AX/53BP1 foci may imply a reduction of initial DDR in aged human MSCs than the young counterparts, which indicated impairment of DDR pathway rather than reflects less DNA breaks in aged human MSCs (207) (Figure 5.1).

Through bioinformatic analysis by transcriptome data, BRCA1-mediated HR dysregulation and cell cycle control of chromosomal replication were identified as downregulated in aged MSCs. Applying an integration analysis of CNV, transcriptome data and clonal expansion of hMSCs, a subgroup of MSCs with greater number of CNVs and aneuploidy was found to cause strongly downregulation of BRCA1-related DDR, ATM signaling pathway and cell cycle control (220).

γ H2AX + pBRCA1 foci represents a marker of recognition of DSB. We found the reduction of pBRCA1 and γ -H2AX foci in irradiated aging hMSCs after 2h in compared to their similarly irradiated young counterparts. Furthermore, a relatively higher percentage of unrepaired DSBs (indicated by more foci) after 24 hours excluded the possibility of faster repair in aged MSCs. HR has been found to be related to the radio-resistant phenotype of MSCs in some previous studies (221, 222). Multiple DDR mechanisms contribute to the radio-resistance propriety of MSCs: rapid γ H2AX formation-induced robust DDR activation, activation of effective S and G2/M checkpoints, and efficient repair of IR-induced DSBs. Rad51 and γ H2AX foci were detected in MSCs following IR treatment and persisted in MSCs at 24 hours post 10 Gy irradiation, indicating DNA DSB repair by homologous recombination (223). Furthermore, another study demonstrated hypoxia induced DNA DSB repair in MSCs after IR, accelerating the resolution of DNA DSBs (224). HIF-1 α was found to

contribute to this upregulated DSB repair by Rad51 foci formation in response to DNA DSBs in hypoxic MSCs, which indicated the enhanced HR-guided DNA DSB recognition and improved radio-resistance of MSCs (224). One publication demonstrated that MSCs deficient for the Fanconi anemia protein FANCD2 (*Fancd2*^{-/-} MSC) involved in HR had higher DNA damage by comet tail intensity assay and slower DNA damage recovery between 1 h and 24 h after γ -IR, indicating the crucial roles of HR in DSB repair of MSCs (225). While, there was no detectable alteration of radiation-induced cell cycle arrest with *Fancd2*^{-/-} stromal cells, which indicates the slower DNA damage recovery was not due to the cell cycle change. Consistent with these studies we revealed the dysregulation of components of HR take place during *in vitro* extended culture. The relatively higher percentage of unrepaired DSBs after 24 hours in aged hMSCs indicates that *in vitro* aging not only impairs the recognition of DSBs, but may also reduce the efficiency of HR-mediated repair.

5.3 Telomere instability is increased following IR in MSCs from aging donors

We have demonstrated that the aging process affect the DNA repair capacity associated with homologous recombination. The alternate lengthening of telomere pathway (ALT) is an HR-dependent replication pathway that utilizes homology sister chromatid for synthesis. The ALT process is essential for maintenance of telomeres lost during ageing in a number of cell types, including some of those in the mesenchymal lineage (226). Consequently we argue that the dysregulation of HR during aging might affect the ALT pathway, leading to disruption of maintenance mechanism as MSCs progressively age. This would result in several features such as increased frequency of T-SCE, the occurrence of APBs and heterogeneous telomere lengths (227) Moreover, *in vitro* IR transformed human MSCs display accelerated telomere shortening, higher frequencies of anaphase bridges and an increase of unbalanced chromosomal translocations (228). This suggests that a radiation-induced DNA damage would destabilizes the telomeres of aged MSCs, resulting in deprotection of telomeres and initiation of bridge-fusion-breakage cycles and persistent chromosomal instability (229). MSCs are relatively radio-resistant and refractory to apoptosis, this may be affected by such a radiation-induced chronic destabilization of the chromosomal structure (230). Consequently we compared the response to low-dose ionizing radiation of *in-vitro* aged murine MSCs obtained from old (18 month)

donor mice with that of MSCs from young (2 month). This study focused on T-SCEs and other markers (telomere length heterogeneity and APB signals) of ALT.

We show that IR impairs telomere integrity (more telomere loss events and increased telomere fragility) in aged mMSC. Exogenous DNA damage can trigger telomere signal free ends and multiple telomere signals (152, 231). Telomere loss (showed by SFE) is thought to result from fork collapse into DSBs and failed telomere replication, and fragile telomeres (showed by MTS) are thought to arise from uncondensed regions at un-replicated ssDNA (232). In a manner consistent with previous research (226, 233), we observed the events of SFE and MTS after IR. One explanation is the variable replication stress between old and young MSCs. Replication stress is defined as the slowing or stalling of replication fork progression due to obstacles or decreased DNA synthesis arising due to exposure to stress. The high endogenous replication stress in MSCs from old donors (234) may affect synergistically with replication stress caused by IR and impair telomere integrity.

Sarcoma is the common 2nd tumor after radiation therapy and the immortality links tightly with ALT mechanism (235). MSCs are potentially relevant to target sarcoma and ALT mechanism may play an important way during malignant transformation. One study showed infused ex vivo cultured MSCs caused increased mortality and tumors in lungs and extremities (236). The donor-derived transformed cells were aneuploid, and were identified as sarcomas which when infused into secondary recipients produced similar tumors (236). Multipotent differentiation was found in high-grade osteosarcomas and one study has confirmed human MSCs are the cell of origin (237). Malignant fibrous histiocytoma (MFH), which also named high-grade undifferentiated pleomorphic sarcoma, is a common tumor with mesenchymal properties (238). One study presented evidence demonstrating that human MSCs are the progenitors of MFH (238). Taking together, there may be a potential link between tumours of the mesenchymal origin and MSCs. Although the overall prevalence of ALT activation in tumours is relatively low, a high frequency of ALT activation was found in tumours of mesenchymal origin. About 47–66% of osteosarcomas (239) and 77% of MFH (240) were shown to be ALT positive. One study presented a gene expression signature classifying telomerase and ALT immortalization (226). The gene expression profiles of telomerase-positive and ALT cell lines and liposarcoma tissue samples was investigated and results suggested a mesenchymal stem cell origin for ALT (226). Thus,

we consider it is important to explore the potential link between MSCs, ALT and radiation.

Werner syndrome, which is characterized by a congenital syndrome of premature cellular aging in various tissues and a dramatically increased risk for soft-tissue sarcomas and osteosarcomas, showed a link between ALT activity and aging (241). The common defects in the RecQ helicases has been found to associated with increased frequency of T-SCE in fibroblasts from Werner patients (242). This is also confirmed by the high frequency of anaphase bridges, T-SCE, and telomere length heterogeneity in embryonic fibroblasts from *Wrn*^{-/-} *mTerc*^{-/-} mice, which frequently undergo spontaneous malignant transformation into undifferentiated pleomorphic sarcoma after xenotransplantation in SCID-mice (243). IR is the only known exogenic risk factor to induce osteosarcoma. Till today, only a few studies have addressed the potential of IR to trigger ALT in normal cells of the mesenchymal lineage. One study demonstrated the malignant transformation of xenotransplanted immortalized human MSCs was triggered by gamma-irradiation (228). Another study showed an increased frequency of T-SCE and APBs in primary human fibroblasts following proton irradiation by Berardinelli et al (115). Recently activation of the ALT pathway was also shown in primary human fibroblasts irradiated with 4 Gy X-rays using a telomere FISH assay (120). Nevertheless, it's still not clear whether the activation of ALT in fibroblast is from an interaction of radiation-induced DSBs at eroded, unprotected telomeres, or if it is the result of a genome-wide upregulation of DNA damage surveillance and repair after chromosomal damage.

In our results, a significantly increased T-SCE frequency was found in gamma-irradiated MSCs from older donors. This was accompanied by an increase of the variation of telomere length in single cells. Although both features are important implications of ALT-activation, the full activation of ALT mechanism does not appear to have been reached due to the absence of APBs in irradiated *in-vitro* aging MSCs. There are two unusual ALT⁺ cell lines that do not have APBs. AG11395 (198), still has aggregates of telomeric DNA and HR proteins-but without PML protein while the second ALT cell line without APBs also lacks long heterogeneous telomeres (103). In our case, the lack of APBs indicates not full-spectrum activation of ALT mechanism after IR in MSCs. The high frequency of T-SCE, together with SFE (244) and MTS (208) in irradiated MSCs from aging donor, implies the early stage of telomeric instability. Telomeres of MSCs are shortened gradually during donor aging (234),

which was confirmed by the Q-FISH-based observation of telomere length intensity signal in our results. Furthermore, TRF2, one key component required to maintain the stability of the shelterin complex and the telomere region, is also downregulated during aging of human fibroblasts (245). The early indication of telomere instability may associate with the dysregulation of telomere maintenance mechanism in aging donor. A dominant negative Werner RecQL2 helicase (246), as well as by a NBS1 point-mutation that impairs the phosphorylation by ATM (247) can induce telomere instability in a B3-WrnDN1 model with and without expression of K577M-WRN. This suggests that both accelerated ageing as well as impaired DNA damage response can lead to telomere instability.

We have shown that Rad51C, which is required for the resolution of Holliday junctions during HR and at telomeres (248), is expressed at a lower level in *in-vitro* aged human MSCs and parallels the impairment of HR DNA repair. The inappropriate expression of RAD51 (together with XRCC3) can develop an ALT+ tumour model (249). Reduced activity of HR leads to the improper DNA DSB repair at telomere regions in a Rad51C mutant Chinese hamster cell line (250). RAD51D, another protein of this family, has the function for the protection of telomeres from shortening or fusion (251). In the previous study, we have observed a gradual reduction of the ATM-dependent recognition of DNA damages during aging of MSCs, whereas the DNA-PK dependent path was not altered (207). A general increase of spontaneous HR was triggered by ATM mutations in fibroblast cell lines from patients, affecting both intra- but also extra-chromosomal DNA independent of the chromatin structure (250). This suggests that ATM is essential not only to mark DNA with DSBs and involves in DNA repair, but also to suppress unwanted HR anywhere in the genome, including in the telomere regions. This idea is further supported by a study in *S.cerevisiae*, showing that TEL1, the yeast homologue of human ATM, has the ability to suppress genomic hyper-recombination and telomere shortening (252). The increased frequency of T-SCE as shown in the present study might therefore result from reduced phosphorylated ATM levels in MSCs from old donor and the genotoxic stress imposed by ionizing irradiation.

6 Conclusion

Since the discovery of mesenchymal stem cells, changes in their biological properties and their regenerative potential became obvious when they were expanded *in vitro* for a prolonged time and by repeated passaging. In this work, it was demonstrated that ageing of these cells both *in vivo* as well as *in vitro* also impairs the ATM-dependent recognition of DNA breaks and BRCA1-mediated homologous recombination. Our findings suggest long-term culture of MSCs gradually lose their ability to recognize endogenous and radiation-induced DNA double-strand breaks. Decreased number of γ H2AX/53BP1 DSB repair foci indicates the impaired DNA damage response in murine MSCs and is associated with reduced ATM-dependent DNA repair process. The slower kinetics and an increased number of residual DNA double-strand breaks post irradiation further confirmed the changes in DNA repair efficiency during aging of MSCs. Starting from an earlier observation in our institute that was made in MSCs derived from laboratory mice, I extended these studies on cells of healthy human donors and found by mapping the transcriptome changes during *in-vitro* ageing that signaling pathways involved in DNA repair by homologues recombination was downregulated, which was confirmed by experimental studies showing less efficient repair of DNA double strand breaks. Such features infer a genome instability to the long-term cultured MSCs and may increase the risk of a malignant transformation.

Bioinformatic analysis performed on transcriptome data inferred the down-regulation of BRCA1 mediated homologous recombination in human MSCs upon long-term culture. Analysis of pBRCA1+ γ H2AX foci after X-irradiation revealed that with increasing duration of *ex-vivo* growth, a subpopulation of cells develop that have a distinct lower capacity of damage recognition. It can therefore be concluded that human MSCs *in-vitro* show a similar age-related impairment of the DNA damage response as found previously in murine cells, and that the higher resistance hMSC against malignant transformation *in-vitro* must be due to other cellular processes.

Based on the findings above, we further investigated the influence of advanced donor age on the response of telomere stability in MSCs following an *in vitro* γ -irradiation. For this, MSCs from donor mice of 3 or 18 month of age were extracted

and quantified alterations in their telomere structure using CO-FISH and Q-FISH hybridization. It has been found that 18 month of *in vivo* ageing and 2 Gy of γ -irradiation independent from each other increased the frequency of telomere instability including MTS and SFE. T-SCE, a process involving illegitimate recombination, however, was induced in a synergistic manner by γ -rays mainly in MSCs of old donor mice. An increase of non-uniform telomere length in individual cells with T-SCE, but an absence of concomitant PML-body staining suggest that ionizing radiation can trigger an incomplete ALT mechanism in aged donor MSCs.

Overall, this study demonstrates that MSCs derived from donors of higher age most likely are impaired in their DNA repair capacity and telomere stability after IR. But also MSCs of younger donors can be negatively affected in terms of DNA repair and genomic stability, as soon as they are subjected to a massive *in vitro* expansion, leading to cellular ageing *ex vivo*. This work shows how *ex vivo* aging process altered the homologous recombination-related gene profile and the change in DNA repair pathway during *ex vivo* aging. Moreover, we show here that murine MSCs from aged donor mice are affected by an increased rate of telomere instability after cells are γ -irradiated *in vitro*. These findings could have implications for the choice of mesenchymal stem cells for cell-based therapies in patients. Although their therapeutic benefit has been shown in more than a thousand clinical trials worldwide, personalized medicine requires individual decisions regarding the source of autologous or allogenic stem cells, donor age, and the risk of an unavoidable radiation-exposure during or after therapy.

7 Appendix

Declaration

Some part of the result and discussion section is modified from the paper “Extended in vitro culture of primary human mesenchymal stem cells downregulates Brca1-related genes and impairs DNA double-strand break recognition”. I am the first author of this paper.

7.1 Abbreviations

°C	Degree Celsius
ALT	Alternative lengthening of the telomeres
ASC	Adult stem cell
Bmi1	Bmi1 polycomb ring finger oncogene
cDNA	Complementary DNA
CFU-F	Colony-forming unit-fibroblastic
CT	Threshold cycle
Ct	Cycle threshold
DAPI	4',6-diamidino-2-phenylindole
DDR	DNA damage response
DMEM	Dulbecco's Modified Eagle's Medium
DNA	Deoxyribonucleic acid
ESC	Embryonic stem cell
FBS	Fetal bovine serum
g	Gram
Gy	Gray
h	Hour
hMSC	Human mesenchymal stem cell
Klf4	Kruppel-like factor 4
L	Litre
M	Molar
min	minute

mL	Millilitre
mM	Millimolar
mMSC	Murine mesenchymal stem cell
MN	Micronuclei
MOS cell lines	Mouse osteosarcoma cell lines
MSC	Mesenchymal stem cell
Nanog	Nanog homeobox
Nes	Nestin
ng	Nanogram
PCR	Polymerase chain reaction
PI	Propidium Iodide
PML-NBs	Promyelocytic Leukemia nuclear bodies
PNA	Peptide nucleic acid
Real-Time PCR	Real-time polymerase chain reaction
RT	Room temperature
SA- β -gal	Senescent associated- β -galactosidase
SC	Stem cell
sec	Second
TBP	TATA box binding protein
TERT	Telomerase reverse transcriptase
T-SCE	Telomere-sister chromatid exchange
γ -rays	Gamma rays
μ g	Microgram
μ L	Microliter

7.2 Bioinformatics for transcriptome data analysis

7.2.1 RNA-seq quality check by FASTQC

The FASTQ files were subjected to FASTQC software to check the sequencing quality before all the analysis. FASTQC is a quality control tool for high throughput sequence data. The detailed code is shown below:

```

for id in `seq 1 12`
do
Fastqc -o hMSC study file_ $id (253)
done

```

The results show the library as prepared with 50 bp. The quality of the library was good enough for subsequent analysis (Figure 7.1).

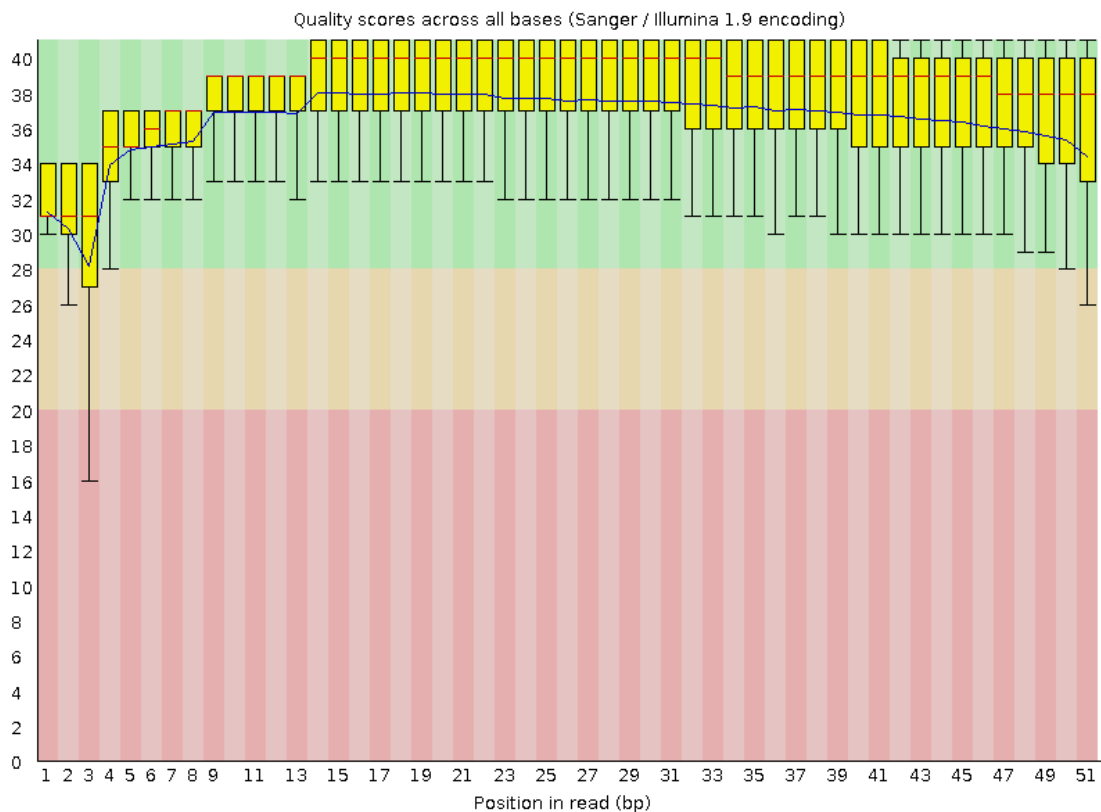


Figure 7.1: Typical output from FASTQC file. Green bar means the bp position pass through the quality while red bar represents the bp position does not pass through the quality check. Yellow means the intermediate potential between pass and not pass.

7.2.2 Aligning reads to a reference

The FASTQ files contain millions of short reads with the nucleotide sequence information and a quality score at each nucleotide sequence position. A reference genome (here we applied hg19 human genome) was used to align these reads. Both FASTQ files were used to perform tophat2 alignment for paired-ed FASTQ files. BAM

files were obtained after the alignment step. The detailed code for FASTQ file alignment by hisat2 software is shown below:

```
for id in `seq 1 6`
do
Hisat2 -o file-MSC_aging_analysis -p 8 hg19_human_genome
MSC_No_1__$id(253).fastq MSC_No_2__$id(253).fastq
done
```

The BAM files were then used to generate count matrix. The “Rsamtools” package was used to check the naming style of the sequences in the input BAM files by *Seqinfo* function:

```
seqinfo(BamFile(bamFiles[1]))
```

This function provided the information of sequence lengths of reads that mapped to each chromosome.

7.2.3 Counting reads in genes

Transcript annotation was needed to count how many reads were mapped to each gene. The GTF file with human gene annotation was downloaded from website https://www.encodegenes.org/human/release_19.html. The “GenomicFeatures” package was used to import GTF files into R software. The code is listed below:

```
gtf <- makeTxDbFromGFF ("/genomFile file/annotation.GTF", format="gtf")
exonsByGene <- exonsBy(gtf, by="gene" )
```

exonsBy function was applied to create a *Grangelist* of all gene information in the genome, which is shown below (Figure 7.2).

```

GRangesList object of length 23459:
$1
GRanges object with 15 ranges and 2 metadata columns:
      seqnames      ranges strand | exon_id exon_name
      <Rle>        <IRanges> <Rle> | <integer> <character>
 [1] chr19 58858172-58858395 - | 250809 <NA>
 [2] chr19 58858719-58859006 - | 250810 <NA>
 [3] chr19 58859832-58860494 - | 250811 <NA>
 [4] chr19 58860934-58862017 - | 250812 <NA>
 [5] chr19 58861736-58862017 - | 250813 <NA>
 ...      ...      ...      ...      ...
 [11] chr19 58868951-58869015 - | 250821 <NA>
 [12] chr19 58869318-58869652 - | 250822 <NA>
 [13] chr19 58869855-58869951 - | 250823 <NA>
 [14] chr19 58870563-58870689 - | 250824 <NA>
 [15] chr19 58874043-58874214 - | 250825 <NA>

```

Figure 7.2: *GRangesList* structure for the information of genes and exons of the genes through the genome. Each element in the *GRangesList* represents one gene and the information of this gene is included in the element (exon number, exon ID, chromosome location).

In the next step, we applied the function *summarizeOverlaps* from the “GenomicAlignments” package to obtain the actual counting:

```

se <- summarizeOverlaps(exonsByGene, BamFileList(bamFiles), mode =
“Union”, singleEnd = FALSE, ignore.strand = TRUE, fragments = TRUE)

```

Counting model ‘*Union*’ was chosen as the parameter in the function to indicate those reads which overlap any portion of exactly one feature are counted. *singleEnd = FALSE* was chosen as the FASTQ files we used were paired-end reads. The data is not strand-specific so *ignore.strand* was set as *TRUE*. Unmapped pairs were counted also as *Fragments* was set as *TRUE*, which is only used for paired-end experiments. A *summarizedExperiment* class was created after running the code. The detailed information of counting matrix was stored in *assay(se)* and is listed below, with the row names indicate the gene ID (Entrez ID) and the column names represent the sample information (Figure 7.3).

	D1_P4	D2_P4	D3_P4	D1_P13	D2_P13	D3_P13
1	163	146	435	44	166	195
10	6	9	11	4	4	0
100	192	117	274	40	48	159
1000	2280	2558	6024	2316	2695	7688
10000	1532	1158	2425	799	982	1434
100008586	0	0	0	0	0	0

Figure 7.3: Counting matrix of the P3 and P14 human MSCs that stored in `assay(se)`. `se` is a `SummarizedExperiment` class that stored the experimental design and counting matrix of the transcriptome files.

The `rowData` slot is a `GRangesList` that contains all the information about the exons for each gene. The `colData` slot is assigned with our sample table (Figure 7.4):

```
> colData(se)
DataFrame with 6 rows and 4 columns
  sampleName      fileName      Passage      patient
  <factor>        <factor>      <character> <factor>
1      D1_P4 SRR1533801.bam Early passage Donor 1
2      D2_P4 SRR1533802.bam Early passage Donor 2
3      D3_P4 SRR1533803.bam Early passage Donor 3
4      D1_P13 SRR1533804.bam Late passage Donor 1
5      D2_P13 SRR1533805.bam Late passage Donor 2
6      D3_P13 SRR1533806.bam Late passage Donor 3
```

Figure 7.4: `colData` slot contains all information about the experimental design in `DataFrame` class.

7.2.4 Deseq2 for differently expressed gene analysis

Firstly, the expression matrix was loaded into `DESeqDataSet` class, which is built on top of the `SummarizedExperiment` class as shown below (Figure 7.5):



Figure 7.5: The structure of DESeqDataSet. Red part contains the gene matrix of expression values. The purple block contains the information of experiment design and the blue block contains genomic features such as gene symbols and gene IDs.

7.2.5 Design formula to perform DEG analysis.

DESeqDataSet class has an associated “*design formula*” to perform DEG analysis. The *design formula* was specified at the beginning of the analysis and contained information which variables in the column metadata table specify the experimental design and how these factors should be assessed in the pipeline.

The simplest *design formula* for DEG assay is “*~condition*”, where *condition* is a column in column metadata table that illustrate which groups the samples belong to. For our project, we specified “*~Donor + Passage*”, which means that the test was applied for the effect of “*Passage*”, controlling for the effect of “*Donor*”:

```
dataset <- DESeqDataSet( se, design = ~Donor + Passage )
```

7.2.6 Relevel of experimental condition

Firstly, we made sure that “*early passage*” was the base level in the “*Passage*” factor, so that the calculation of fold change was set as “*Late passage*” over “*Early passage*” and not opposite. The *revel* function achieves this:

```
dataset$sampleName <- droplevels(dataset$sampleName )
dataset$treatment <- relevel( dataset $Passage, "Early passage" )
```

The genes with zero values for all samples are removed to speed up the annotation steps below:

```
dataset <- dataset[ rowSums( counts(dataset) ) > 0 , ]
```

7.2.7 Pipeline running

The DESeq2 analysis analysing counts with patient and passage effects can be performed with the function *DESeq*:

```
dataset <- DESseq(dataset)
res <- results(dataset)
```

The estimation of size factor that control for differences in the library size of each files, the estimation of dispersion of each gene and a generalized linear model are shown during the analysis. A *DESeqDataSet* that contains the results and information of the analysis is returned after the running.

7.2.8 Inspection of the result from DESeq2 analysis

Calling results without any parameters will obtain the fold change between late passage (P13) and early passage (P4) and the adjusted p value (Benjamini-Hochberg adjusting) for the last variable in the design formula (Here “*Passage*”) (Figure 7.6):

```

> res
log2 fold change (MLE): Passage Late.passage vs Early.passage
Wald test p-value: Passage Late.passage vs Early.passage
DataFrame with 18992 rows and 6 columns
  baseMean      log2FoldChange      lfcSE      stat
  <numeric>    <numeric>          <numeric>  <numeric>
1    165.550757986999 -0.00294890211910943 0.388211754200098 -0.0075961175497779
10   5.290680409106  -1.15588974126658   1.5504448735185  -0.745521341009345
100  116.286174971008 -0.488940993252109 0.408084974793049 -1.19813524989511
1000 3801.36742393746  1.0874349804725 0.196583199731532  5.5316780984213
10000 1299.61902924177  0.291599272396844 0.167843198069953  1.73733148408738
...
9991 1542.68611386719  0.306026604364945 0.205229969310535  1.49113994117444
9992 3.50664900328573 -0.117450435034539 1.50701659684309 -0.0779357276360295
9993 1984.19603748427 -0.00247300208710179 0.184790148251714 -0.013382759365143
9994 362.304776524517 -0.463880547599638 0.234299863919007 -1.97985837396813
9997 12.7680165232387 -0.439921863942254 0.925103484978143 -0.475538003137722

```

Figure 7.6: Result contains a *DataFrame* with genes (ENTREZID from hg19 genome) as rows and statistics in columns.

Calling *mccols* function resulted a *DataFrame* object that contains metadata of column information of *res* (Figure 7.7):

```

> mcols(res, use.names=TRUE)
DataFrame with 6 rows and 2 columns
  type      description
  <character> <character>
baseMean    intermediate mean of normalized counts for all samples
log2FoldChange results log2 fold change (MLE): Passage Late.passage vs Early.passage
lfcSE       results standard error: Passage Late.passage vs Early.passage
stat        results Wald statistic: Passage Late.passage vs Early.passage
pvalue      results Wald test p-value: Passage Late.passage vs Early.passage
padj        results BH adjusted p-values

```

Figure 7.7: The information of metadata is stored in a *DataFrame* structure. The *DataFrame* contains 6 rows and 2 columns for illustrating the description of the column in result.

BaseMean is the average of the normalized count values, which is divided by size factors and taken over all samples. The next four columns refer to a specific contrast, namely the comparison of the levels *Late passage* versus *Early passage* of the factor variable *Passage*.

The column *log2FoldChange* is the effect size estimate. It reveals the level of gene expression change due to passage change as late passage in comparison to early passage. Log2 scaling was used on the fold change.

The column lfcSE tells the standard error estimate for the log2 fold change estimate. Each gene was performed with a hypothesis test in DESeq2 to see whether evidence is enough to decide against the null hypothesis that there is no difference between early passage and late passage on the exact gene and that the observed difference between passage was merely caused by experimental variability.

The results of the test are shown as a p value. Padj column represents the Benjamini-Hochberg adjusted p-value from pvalue column.

7.2.9 Gene symbol annotation

The result table uses “ENTREZID” gene ID in res. org.Hs.eg.db was applied to convert “ENTREZID” gene ID to gene symbol:

```
Ann<-
org.Hs.eg.db::select(org.Hs.eg.db,keys=rownames(res),columns=c("ENTREZID",
"SYMBOL","GENENAME"))
table(ann$ENTREZID==rownames(res))
results.annotated <- cbind(res, ann)
COmRNA<-assay(se)
annforCOmRNA<-
org.Hs.eg.db::select(org.Hs.eg.db,keys=rownames(COmRNA),columns=c("SYMBOL"))
row.names(COmRNA)<-annforCOmRNA$SYMBOL
```

7.2.10 Diagnostic plots

MA plot provides an overview for the comparison between early passage and late passage:

```
plotMA( res, ylim = c(-3, 3) )
```

Each dot represents a gene in the results (Figure 7.8). The x-axis shows average expression of the gene over all samples. The y-axis represents the log2 fold change

between early passage and late passage. The genes with an adjusted p value lower than 0.05 are shown in red.

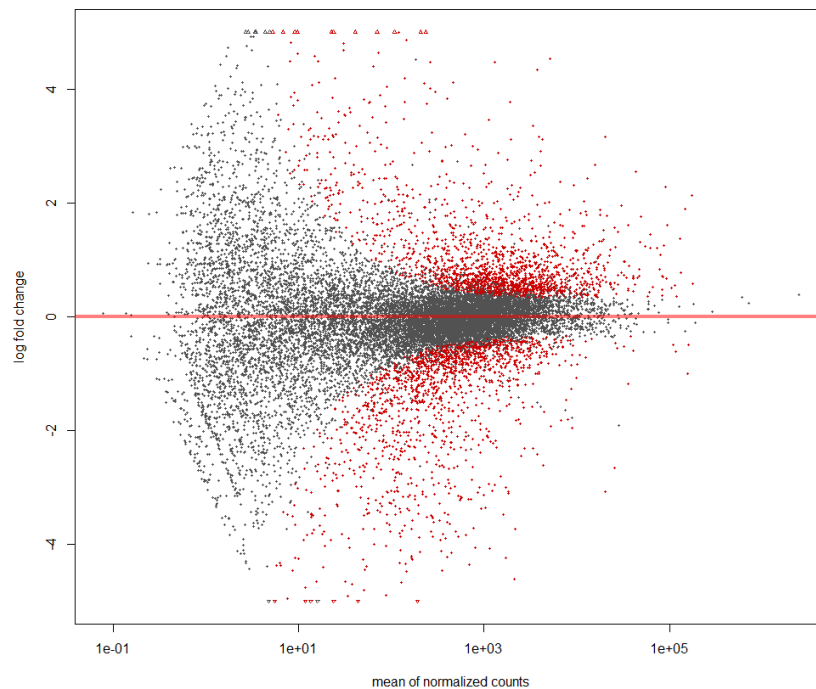


Figure 7.8 MAplot of comparison between samples from early passage and late passage. The MA plot shows the log₂ fold changes from the passage average expression of the gene over all samples. The analysis process assesses a prior on log₂ fold changes, resulting in moderated estimation from genes with low counts and highly variable counts. The narrowing spread of points on the right side of the figure reveals the estimation process.

Shrinkage estimation of log fold changes was also applied in our analysis by DESeq2. When the expression values were too low to obtain an accurate calculation of the fold change, the result is shrunken towards zero to avoid that these values dominate the top-ranked fold change on the list. Moreover, the significance of fold change of a target gene is not only depending on the fold change in two groups but also on its within-group variability. The within-group variability was quantified as the dispersion. The dispersion is a squared coefficient of variation for highly expressed genes: 10% dispersion value indicates the genes tend to differ by typically 10% between samples of the same group. The passion noise is added as an additional source for the weakly expressed genes:

```
plotDispEsts( dds, ylim = c(1e-6, 1e1) )
```

Every point represents one gene with the mean of normalized counts and the dispersion value from the experiment (Figure 7.9). The red fitted trend line indicates the mean dispersion's dependence, and then each gene's estimate is shrunk towards the red fitted trend line to obtain the final estimate value (blue points) that are then used in the hypothesis test. High gene-wise dispersed genes are the blue circle points above the fitted trend line, which are labelled as dispersion outliers. These estimates are therefore not shrunk toward the fitted trend line.

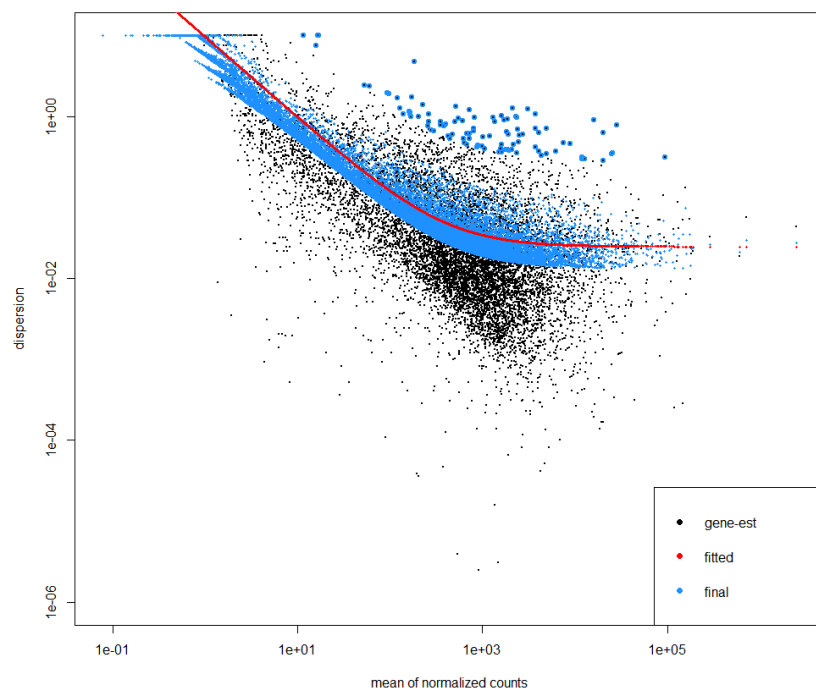


Figure 7.9: Shrinkage estimation plot of comparison between samples from early passage and late passage. The Shrinkage estimation plot shows the shrinkage of each gene towards the red fitted trend line that represents mean dispersion's dependence. Every point represents one gene with the mean of normalized values. High gene-wise dispersed genes are the blue circle points above the fitted trend line, which are labelled as dispersion outliers.

7.2.11 Sample distances and Principal components analysis (PCA)

Clustering and ordination (e.g. principal components analysis) methods are common methods to handle high-dimensional data, which work best for homoscedastic data. Homoscedastic data are data that the variance of gene expression level does not

rely on the expression level. In transcriptome and single cell transcriptome data, the variance increases with the mean value of gene expression. Therefore, the PCA analysis which based on a normalized gene expression matrix will only depends on the most highly expressed genes due to the largest variance among groups. One simple and useful strategy is to take the logarithm of the normalized count values plus a small pseudo-count; however, now the genes with low counts tend to dominate the results due to the strong Poisson noise inherent to small count values, they show the strongest relative differences between samples.

In this study, we applied regularized-logarithm transformation which inherited from DESeq2 to handle this problem. The strong expressed genes will be applied with log2 transformation, whereas values from low expressed genes are shrunken towards the average value of the gene across all samples. A ridge penalty as an empirical Bayesian was applied to help the gene expression matrix become more homoscedastic (Figure 7.10).

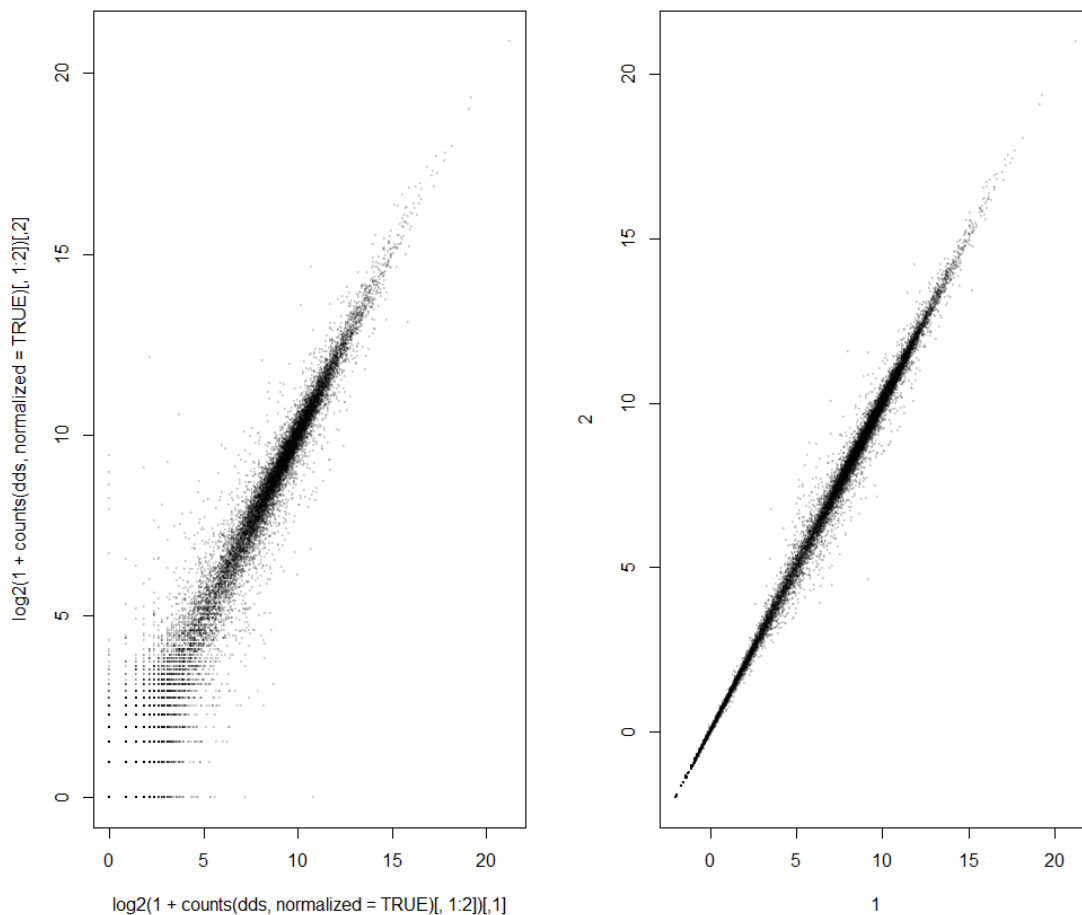


Figure 7.10: Scatter plot of P3 MSC sample 1 vs P3 MSC sample 2. Left: using an ordinary log2 transformation. Right: Using the rlog transformation. Each dot represents one gene. The gene with lower expression value still showed higher variance after log transformation, which may dominate the results from PCA analysis. After rlog transformation (A ridge penalty as an empirical Bayesian), the genes with high and low expression level become more homoscedastic, which leads to more accuracy in PCA analysis.

After rlog transformation, we applied Euclidean distance method to check the distance between samples. The gene matrix was transpose to help calculate the distance between samples rather than calculating distance between genes. The distances are visualized in a heatmap (Figure 7.11). The code is listed below:

```
library("gplots")
library("RColorBrewer")
rld <- rlog(dds)
```

```
colData(se)
Distance <- dist(t(assay(rld)))
MatrixDistance <- as.matrix(Distance)
rownames(MatrixDistance) <- paste( rld$Passage,rld$patient, sep="-" )
colnames(MatrixDistance) <- NULL
colours = colorRampPalette( rev(brewer.pal(9, "Blues")) )(255)
heatmap.2(MatrixDistance, trace="none", col=colours, margins=c(13, 15))
```

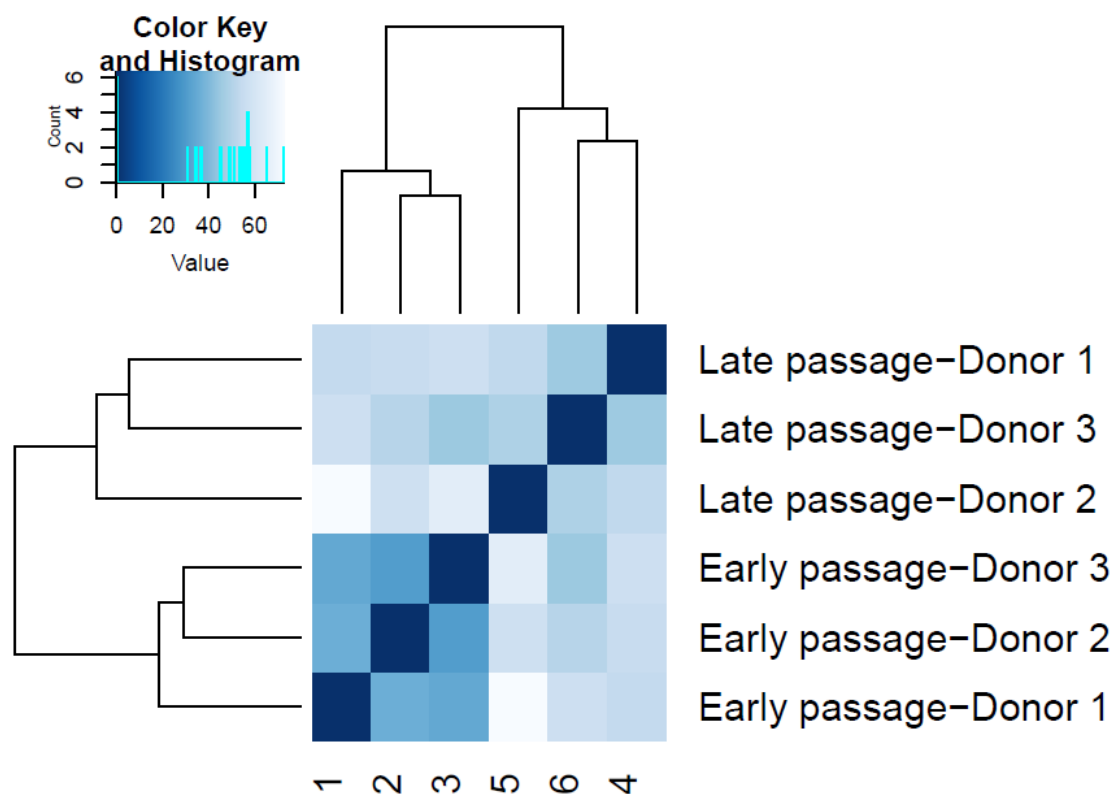


Figure 7.11: Euclidean distance heatmap showing the distance between samples by gene matrix values. The plot indicated the samples within the same passage cluster together.

7.2.12 Heatmap of Euclidean distance among samples.

Principal-components analysis (PCA) is a commonly used dimensional reducing method, which was also applied to estimate the distance by unsupervised clustering. PCA projects high-dimensional samples into 2D plane to visualize the distance between samples (Figure 7.12).

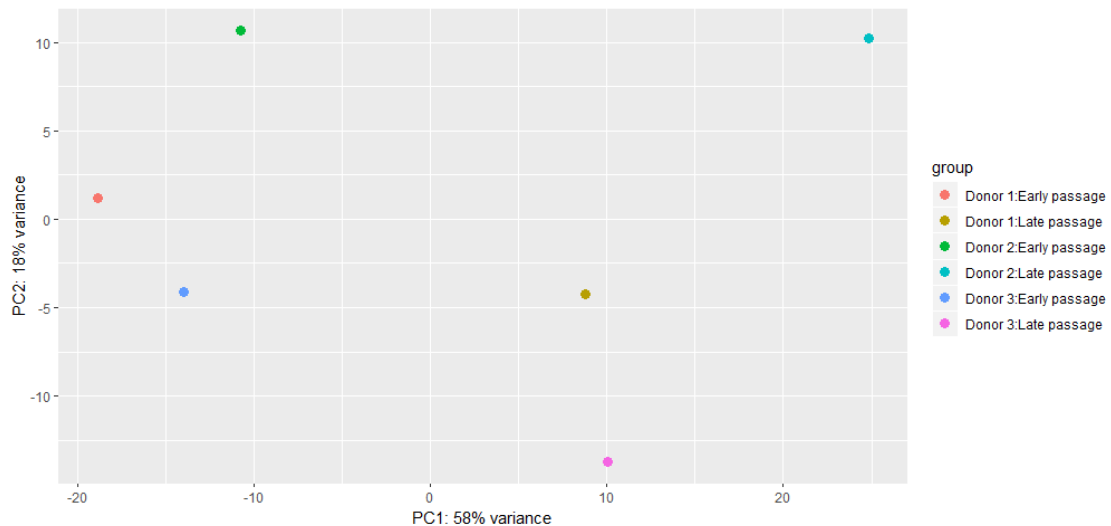


Figure 7.12: Principal-components analysis (PCA) reveals the samples within the same passage clustered together. PC1 explained 58% variance in the gene matrix and PC2 explained 18% variance in the gene matrix. In PC1 dimension the samples within the same passage had closer distance.

7.2.13 Gene ontology analysis and KEGG analysis

Functional pathway analysis included several kinds of methods such as Gene ontology (GO) analysis, KEGG (Kyoto Encyclopedia of Genes and Genomes) pathway analysis, Gene set enrichment analysis (GSEA) and others. Some typical ways to perform functional pathway analysis is shown in below (Figure 7.13):

Name	Availability	Reference
ORA tools		
Onto-Express	Web (http://vortex.cs.wayne.edu)	[4,5]
GenMAPP	Standalone (http://www.genmapp.org)	[11,71]
GoMiner	Standalone, Web (http://discover.nci.nih.gov/gominer)	[72,73]
FatiGO	Web (http://babelomics.bioinfo.cipf.es)	[74]
GOstat	Web (http://gostat.wehi.edu.au)	[7]
FuncAssociate	Web (http://llama.mshri.on.ca/funcassociate/)	[6]
GOToolBox	Web (http://genome.crg.es/GOToolBox/)	[10]
GeneMerge	Standalone, Web (http://genemerge.cbc.umd.edu/)	[9]
GOEAST	Web (http://omicslab.genetics.ac.cn/GOEAST/)	[75]
ClueGO	Standalone (http://www.ici.upmc.fr/cluego/)	[76]
FunSpec	Web (http://funspec.med.utoronto.ca/)	[77]
GARBAN	Web	[78]
GO:TermFinder	Standalone (http://search.cpan.org/dist/GO-TermFinder/)	[8]
WebGestalt	Web (http://bioinfo.vanderbilt.edu/webgestalt/)	[79]
agriGO	Web (http://bioinfo.cau.edu.cn/agriGO/)	[80]
GOFFA	Standalone, Web (http://edkb.fda.gov/webstart/arraytrack/)	[81]
WEGO	Web (http://wego.genomics.org.cn/cgi-bin/wego/index.pl)	[82]
FCS tools		
GSEA	Standalone (http://www.broadinstitute.org/gsea/)	[21,29]
sigPathway	Standalone (BioConductor)	[22]
Category	Standalone (BioConductor)	[24]
SAFE	Standalone (BioConductor)	[30]
GlobalTest	Standalone (BioConductor)	[15]
PCOT2	Standalone (BioConductor)	[17]
SAM-GS	Standalone (http://www.ualberta.ca/~yyasui/software.html)	[83]
Catmap	Standalone (http://bioinfo.thep.lu.se/catmap.html)	[84]
T-profiler	Web (http://www.t-profiler.org)	[85]
FunCluster	Standalone (http://corneliu.henegar.info/FunCluster.htm)	[86]
GeneTrail	Web (http://genetrail.bioinf.uni-sb.de)	[87]
GAzer	Web	[88]
PT-based tools		
ScorePAGE	No implementation available	[37]
Pathway-Express	Web (http://vortex.cs.wayne.edu)	[38,39]
SPIA	Standalone (BioConductor)	[40]
NetGSA	No implementation available	[43]

doi:10.1371/journal.pcbi.1002375.t001

Figure 7.13: The list of commonly used functional pathway analysis (from Khatri P et al (254)).

The steps of functional pathway analysis include over-representation analysis, functional class scoring and pathway topology analysis. Finally, the pathway significance is assessed (Figure 7.14).

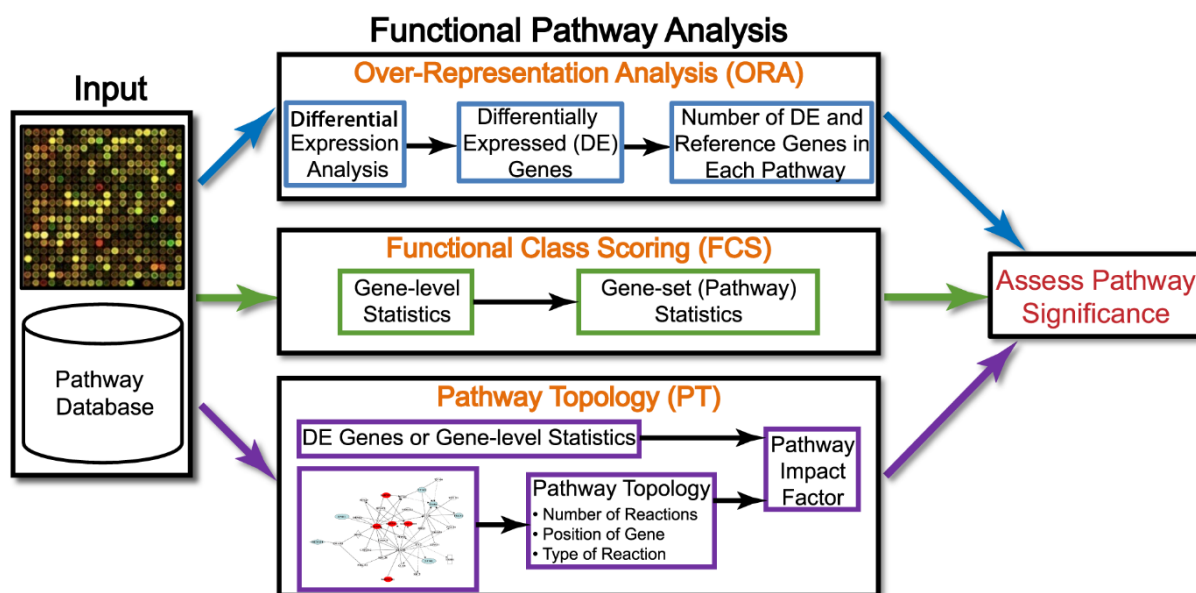


Figure 7.14: The steps of functional pathway analysis (from Khatri P et al (254))

GO analysis is to perform enrichment analysis on gene sets and detect the molecular mechanism behind the gene sets. In our project, the DEGs (adjust p-value < 0.05, $\text{abs}(\log\text{FC}) > 1.5$) were subjected to GO analysis by package “clusterProfiler”. The GO aspect is divided into three categories: molecular function, biological process, cellular component. All three categories were selected to perform the analysis. P-value is the probability of seeing at least x number of genes out of the total y genes in the list annotated to a particular GO term, given the proportion of genes in the whole genome that are annotated to that GO Term. The closer the p-value is to zero, the more significant the particular GO term associated with the group of genes is. The detailed code is listed below:

```
library(clusterProfiler)
ego_BP <- enrichGO(
  gene = row.names(results.annotated.sig),
  universe = row.names(results.annotated),
  'org.Hs.eg.db',
  ont = "BP",
  readable = TRUE)
ego_BP2 <- simplify(ego_BP) ##simplf GO term
summary(ego_BP2)
dotplot(ego_BP)
```

```

goplot(ego_BP)
cnetplot(ego_BP, foldChange=genelist, circular = TRUE, colorEdge = TRUE)
heatplot(ego_BP2, foldChange=genelist)
emapplot(ego_BP)

```

KEGG pathway analysis was performed to find the pathways that associated with the aging of hMSCs. The same DEG gene list was subjected to KEGG analysis. The code is listed below:

```

library(clusterProfiler)
kk <- enrichKEGG(rownames(results.annotated.sig), organism="hsa",
keyType = "ncbi-geneid",
pvalueCutoff = 0.05,
pAdjustMethod = "BH",
qvalueCutoff = 0.1)
keggresult<-data.frame(kk)
dotplot(kk)
cnetplot(kk, foldChange=genelist, circular = TRUE, colorEdge = TRUE)

```

Pathwayveiw package was applied to plot the significant genes in a target KEGG pathway, the code is listed below:

```

hsa04110 <- pathview(gene.data = allgenelist,
pathway.id = "hsa04110",
species = "hsa",
limit = list(gene=max(abs(allgenelist)), cpd=1))

```

A typical pathwayview plot with significant genes in the DNA replication pathway is shown below (Figure 7.15):

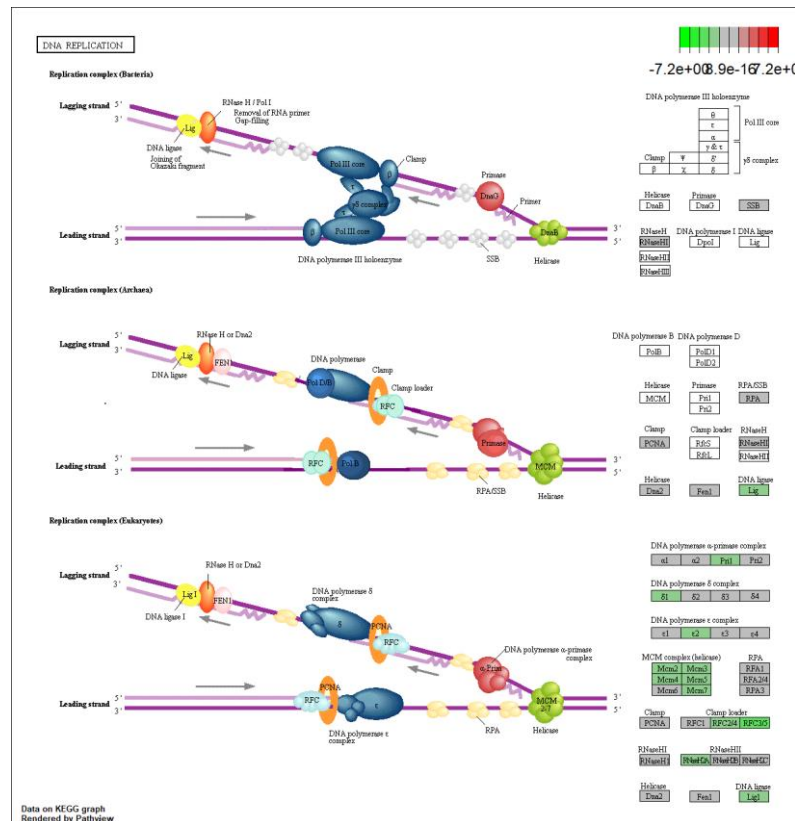


Figure 7.15: Pathway view for significantly dysregulated genes in DNA replication pathway. Downregulated genes are labeled with green color and upregulated genes are indicated with red color.

7.2.14 Gene set enrichment analysis (GSEA)

GSEA is a computational method to determine whether a defined gene set shows statistically significant difference between two groups (late passage MSC versus early passage MSC). In our analysis, *h.all.v6.2.symbols.gmt* from Broad institute (<https://www.gsea-msigdb.org/gsea/index.jsp>) was applied as the defined gene set. The default parameters were selected to perform the analysis. P-value was adjusted by BH method. P-value less than 0.05 was considered as significant for the identified hallmark. NES score greater than 0 was identified as up-regulation for the identified pathway in the late passage MSC.

7.3 List of significant genes in transcriptome analysis

Significant genes with $\log_2(\text{FC}) > 2$ and adjusted -p value < 0.05 . The significant genes in transcriptome analysis are listed in Table 7.1.

Table 7.1: List of significant genes in transcriptome analysis

Symbol	LFC	padj	Gene name
TMPO-AS1	-2.78	0.00469	TMPO antisense RNA 1
VPS9D1-AS1	-2.38	0.01449	VPS9D1 antisense RNA 1
LOC100132111	2.29	0.03692	uncharacterized LOC100132111
HECTD2-AS1	3.17	0.02998	HECTD2 antisense RNA 1
TROAP	-4.22	0.00000	trophinin associated protein
LOC100288181	-2.88	0.00567	uncharacterized LOC100288181
LOC100288637	-3.17	0.00000	OTU deubiquitinase 7A pseudogene
TMEM225B	2.27	0.03935	transmembrane protein 225B
CDH6	2.25	0.02512	cadherin 6
LINC01013	3.12	0.00629	long intergenic non-protein coding RNA 1013
TMEM178B	4.48	0.00000	transmembrane protein 178B
CDH10	4.08	0.00533	cadherin 10
KIF20A	-4.07	0.00059	kinesin family member 20A
NA	2.26	0.00000	NA
FRY	2.06	0.00000	FRY microtubule binding protein
CDK2	-2.20	0.00000	cyclin dependent kinase 2
RCAN2	-2.44	0.00209	regulator of calcineurin 2
CDKN2C	-2.68	0.00000	cyclin dependent kinase inhibitor 2C
CDKN3	-3.13	0.00000	cyclin dependent kinase inhibitor 3
MRV11	3.06	0.00000	murine retrovirus integration site 1 homolog
ABCA9	2.10	0.00176	ATP binding cassette subfamily A member 9
NDC80	-3.51	0.00000	NDC80, kinetochore complex component
SPON2	-2.08	0.00814	spondin 2
SPON1	2.04	0.00089	spondin 1
TACC3	-3.22	0.00000	transforming acidic coiled-coil containing protein 3
FST	2.00	0.00000	folliculin
SEMA6B	-3.75	0.00887	semaphorin 6B
RNAHEH2A	-2.07	0.00000	ribonuclease H2 subunit A
CENPA	-3.22	0.00000	centromere protein A
SPAG5	-3.01	0.00000	sperm associated antigen 5
CENPE	-3.15	0.00000	centromere protein E
CENPF	-2.96	0.00000	centromere protein F
POSTN	-2.66	0.00173	periostin
RAD51AP1	-2.35	0.00000	RAD51 associated protein 1
PNMA2	2.28	0.00000	PNMA family member 2
POLQ	-3.08	0.00000	DNA polymerase theta
PLK4	-3.38	0.00000	polo like kinase 4
DBF4	-2.16	0.00000	DBF4 zinc finger
KIF2C	-4.47	0.00070	kinesin family member 2C
ADAP1	2.54	0.00007	ArfGAP with dual PH domains 1
UBE2C	-3.62	0.00000	ubiquitin conjugating enzyme E2 C
ADAMTS8	-4.24	0.00750	ADAM metalloproteinase with thrombospondin type 1 motif 8
CIT	-2.12	0.00000	citron rho-interacting serine/threonine kinase
ZWINT	-2.24	0.00000	ZW10 interacting kinetochore protein
CORO1A	-3.78	0.00083	coronin 1A

LZTS1	-3.67	0.00000	leucine zipper tumor suppressor 1
ANXA10	2.11	0.04796	annexin A10
GALNT6	-2.73	0.00000	polypeptide N-acetylgalactosaminyltransferase 6
PADI2	3.20	0.00975	peptidyl arginine deiminase 2
NXPH3	2.41	0.00086	neurexophilin 3
MTFR2	-2.52	0.00038	mitochondrial fission regulator 2
CDCA5	-2.55	0.00000	cell division cycle associated 5
OIP5	-2.19	0.00011	Opa interacting protein 5
FHAD1	-2.79	0.00508	forkhead associated phosphopeptide binding domain 1
OSBPL7	-2.68	0.00000	oxysterol binding protein like 7
C1QTNF2	-3.09	0.01470	C1q and TNF related 2
DDIT4L	-2.37	0.00025	DNA damage inducible transcript 4 like
FAM46B	-2.02	0.00004	family with sequence similarity 46 member B
RMI2	-2.49	0.00027	RecQ mediated genome instability 2
OSR2	-2.02	0.00001	odd-skipped related transcription factor 2
CKS2	-2.34	0.00000	CDC28 protein kinase regulatory subunit 2
SFXN2	-2.09	0.00000	sideroflexin 2
BTBD11	-2.39	0.00000	BTB domain containing 11
PAQR4	-3.06	0.00001	progesterin and adipoQ receptor family member 4
CNGA3	2.67	0.00473	cyclic nucleotide gated channel alpha 3
TNFAIP8L1	-2.42	0.00000	TNF alpha induced protein 8 like 1
KLF17	-2.04	0.03754	Kruppel like factor 17
IQGAP3	-4.15	0.00004	IQ motif containing GTPase activating protein 3
COL11A1	-2.30	0.00000	collagen type XI alpha 1 chain
COL13A1	2.91	0.00000	collagen type XIII alpha 1 chain
LYPD6B	2.22	0.03980	LY6/PLAUR domain containing 6B
COL15A1	2.67	0.00000	collagen type XV alpha 1 chain
COMP	2.31	0.00000	cartilage oligomeric matrix protein
IL31RA	-4.07	0.00002	interleukin 31 receptor A
CLDN23	-2.01	0.03409	claudin 23
ASB5	3.32	0.00536	ankyrin repeat and SOCS box containing 5
NEK7	2.43	0.00000	NIMA related kinase 7
RIMS4	3.55	0.00000	regulating synaptic membrane exocytosis 4
CRYAB	2.26	0.00000	crystallin alpha B
CSF2RA	6.34	0.00688	colony stimulating factor 2 receptor alpha subunit
CSF2RB	6.71	0.00000	colony stimulating factor 2 receptor beta common subunit
LACC1	2.53	0.00000	laccase domain containing 1
KIF18B	-4.13	0.00000	kinesin family member 18B
EME1	-2.17	0.00064	essential meiotic structure-specific endonuclease 1
CSTA	2.14	0.00000	cystatin A
SPC24	-4.27	0.00000	SPC24, NDC80 kinetochore complex component
CKAP2L	-2.93	0.00000	cytoskeleton associated protein 2 like
ZNF385B	-3.40	0.00000	zinc finger protein 385B
SGO2	-2.30	0.00000	shugoshin 2
SGO1	-3.49	0.00000	shugoshin 1
MBOAT1	-3.82	0.00301	membrane bound O-acyltransferase domain containing 1
AMOT	-2.76	0.00250	angiomin
RDH10	3.13	0.00000	retinol dehydrogenase 10

ESCO2	-3.33	0.00000	establishment of sister chromatid cohesion N-acetyltransferase 2
TMEM229B	2.03	0.00001	transmembrane protein 229B
BRINP1	-2.55	0.00333	BMP/retinoic acid inducible neural specific 1
NAGS	-2.14	0.04614	N-acetylglutamate synthase
C18orf54	-2.04	0.00000	chromosome 18 open reading frame 54
DAW1	2.44	0.00000	dynein assembly factor with WD repeats 1
LONRF2	3.85	0.00005	LON peptidase N-terminal domain and ring finger 2
ADAMTS15	-2.26	0.02098	ADAM metallopeptidase with thrombospondin type 1 motif 15
ADAMTS16	-2.23	0.01974	ADAM metallopeptidase with thrombospondin type 1 motif 16
DNM1	-2.63	0.00000	dynamain 1
DSP	2.48	0.00000	desmoplakin
E2F1	-2.19	0.00001	E2F transcription factor 1
E2F2	-4.70	0.00001	E2F transcription factor 2
EDN1	2.51	0.00030	endothelin 1
EFNB3	-4.45	0.00000	ephrin B3
ZNF367	-2.49	0.00144	zinc finger protein 367
LCTL	-2.38	0.00523	lactase like
APOBEC3A	-3.84	0.01079	apolipoprotein B mRNA editing enzyme catalytic subunit 3A
LIPH	5.15	0.03630	lipase H
EPHA3	-3.90	0.00020	EPH receptor A3
EPHA5	3.95	0.04657	EPH receptor A5
EPHA7	-4.81	0.00000	EPH receptor A7
AK4	2.13	0.00000	adenylate kinase 4
EPOR	-2.56	0.00189	erythropoietin receptor
EZH2	-2.29	0.00000	enhancer of zeste 2 polycomb repressive complex 2 subunit
F2RL1	-2.70	0.00162	F2R like trypsin receptor 1
F3	2.90	0.00000	coagulation factor III, tissue factor
FABP4	-4.91	0.00006	fatty acid binding protein 4
FANCA	-2.82	0.00000	Fanconi anemia complementation group A
FANCD2	-2.51	0.00000	Fanconi anemia complementation group D2
DDIAS	-2.33	0.00000	DNA damage induced apoptosis suppressor
SKA1	-3.80	0.00000	spindle and kinetochore associated complex subunit 1
SKA3	-3.16	0.00000	spindle and kinetochore associated complex subunit 3
FES	-2.02	0.00005	FES proto-oncogene, tyrosine kinase
FGFR2	-4.77	0.01389	fibroblast growth factor receptor 2
COBLL1	2.05	0.00000	cordon-bleu WH2 repeat protein like 1
NTNG1	-2.34	0.02614	netrin G1
ANKRD6	2.73	0.00000	ankyrin repeat domain 6
DKK1	3.13	0.00000	dickkopf WNT signaling pathway inhibitor 1
TPX2	-3.06	0.00000	TPX2, microtubule nucleation factor
CEP152	-2.04	0.00000	centrosomal protein 152
FOXM1	-3.01	0.00000	forkhead box M1
NMNAT2	2.46	0.00002	nicotinamide nucleotide adenylyltransferase 2
FLG	3.36	0.00000	filaggrin
STAB1	-3.45	0.00022	stabilin 1

PASK	-2.34	0.00034	PAS domain containing serine/threonine kinase
SYNE2	-2.02	0.00061	spectrin repeat containing nuclear envelope protein 2
ARC	-2.27	0.00001	activity regulated cytoskeleton associated protein
FMOD	3.46	0.00000	fibromodulin
NCAPH	-3.89	0.00000	non-SMC condensin I complex subunit H
SLC7A8	-2.16	0.00000	solute carrier family 7 member 8
TTC9	2.88	0.00183	tetratricopeptide repeat domain 9
FOLR3	4.49	0.00147	folate receptor 3
TSPAN15	-3.50	0.00467	tetraspanin 15
CLDN14	2.90	0.02891	claudin 14
SH3BP1	-3.63	0.00000	SH3 domain binding protein 1
CADM1	3.20	0.00250	cell adhesion molecule 1
KIF4A	-3.58	0.00000	kinesin family member 4A
FRZB	-3.46	0.01617	frizzled related protein
CENPI	-2.37	0.00001	centromere protein I
CALHM5	2.01	0.00000	calcium homeostasis modulator family member 5
PHYHD1	-2.03	0.03433	phytanoyl-CoA dioxygenase domain containing 1
LINC01018	4.41	0.00000	long intergenic non-protein coding RNA 1018
PCSK9	3.42	0.00008	proprotein convertase subtilisin/kexin type 9
TMEM151A	2.51	0.00710	transmembrane protein 151A
MAMDC2	-2.02	0.00023	MAM domain containing 2
GAD1	2.80	0.04453	glutamate decarboxylase 1
BAMBI	2.15	0.00000	BMP and activin membrane bound inhibitor
PART1	-3.73	0.00000	prostate androgen-regulated transcript 1 (non-protein coding)
OLFML2B	-3.10	0.00880	olfactomedin like 2B
NALCN	2.07	0.00000	sodium leak channel, non-selective
ASPM	-3.22	0.00000	abnormal spindle microtubule assembly
CHD5	3.59	0.00317	chromodomain helicase DNA binding protein 5
ARHGEF26	-2.79	0.00826	Rho guanine nucleotide exchange factor 26
FBXO5	-2.03	0.00000	F-box protein 5
SEZ6L2	-3.28	0.00000	seizure related 6 homolog like 2
RGS17	-2.12	0.00501	regulator of G protein signaling 17
SNORD52	-3.68	0.03544	small nucleolar RNA, C/D box 52
ANKRD1	2.67	0.00049	ankyrin repeat domain 1
GPR162	-2.34	0.00174	G protein-coupled receptor 162
GPM6B	-2.04	0.00838	glycoprotein M6B
ADGRD1	6.20	0.00000	adhesion G protein-coupled receptor D1
GAS2L3	-3.33	0.00000	growth arrest specific 2 like 3
LYPD5	2.26	0.02560	LY6/PLAUR domain containing 5
MAMSTR	-2.20	0.00062	MEF2 activating motif and SAP domain containing transcriptional regulator
WDR62	-2.76	0.00000	WD repeat domain 62
CCDC150	-2.86	0.01323	coiled-coil domain containing 150
KIF4B	-2.99	0.00001	kinesin family member 4B
FBXO43	-3.47	0.01636	F-box protein 43
GRIA1	-2.22	0.03472	glutamate ionotropic receptor AMPA type subunit 1
RACGAP1	-2.39	0.00000	Rac GTPase activating protein 1
UHRF1	-2.64	0.00000	ubiquitin like with PHD and ring finger domains 1
PKN3	-3.49	0.00000	protein kinase N3

PADI1	3.54	0.00055	peptidyl arginine deiminase 1
HIST1H1C	2.27	0.00000	histone cluster 1 H1 family member c
SLC40A1	-3.19	0.00131	solute carrier family 40 member 1
HELLS	-2.94	0.00000	helicase, lymphoid specific
HGF	-2.67	0.02365	hepatocyte growth factor
HLA-DPB1	-4.04	0.00000	major histocompatibility complex, class II, DP beta 1
HMGB2	-2.11	0.00000	high mobility group box 2
HMMR	-3.82	0.00000	hyaluronan mediated motility receptor
HSD11B1	3.36	0.00000	hydroxysteroid 11-beta dehydrogenase 1
BIRC5	-3.72	0.00000	baculoviral IAP repeat containing 5
HTR2A	3.01	0.00000	5-hydroxytryptamine receptor 2A
TNC	-3.08	0.00803	tenascin C
IBSP	4.10	0.02222	integrin binding sialoprotein
ICA1	-4.41	0.01837	islet cell autoantigen 1
NLRP10	2.11	0.00121	NLR family pyrin domain containing 10
TMEM119	-2.61	0.00138	transmembrane protein 119
CCDC190	5.25	0.00000	coiled-coil domain containing 190
CCDC36	-2.05	0.04809	coiled-coil domain containing 36
ARSI	-2.29	0.00001	arylsulfatase family member I
RSPO2	-2.10	0.01073	R-spondin 2
SLC35F4	-3.93	0.01588	solute carrier family 35 member F4
IFI27	-2.21	0.00000	interferon alpha inducible protein 27
NCKAP5	2.37	0.00983	NCK associated protein 5
OSTN	6.18	0.00001	osteocrin
IGFBP1	2.60	0.03184	insulin like growth factor binding protein 1
IGFBP5	2.04	0.01552	insulin like growth factor binding protein 5
IL1A	2.70	0.00688	interleukin 1 alpha
IL6	2.25	0.00000	interleukin 6
SHROOM2	-3.47	0.00000	shroom family member 2
ITGA2	2.88	0.00000	integrin subunit alpha 2
ANOS1	-2.69	0.00006	anosmin 1
FAM111B	-3.77	0.00000	family with sequence similarity 111 member B
KCNB1	3.76	0.00004	potassium voltage-gated channel subfamily B member 1
LHFPL4	2.22	0.03844	LHFPL tetraspan subfamily member 4
KCNJ12	2.89	0.00001	potassium voltage-gated channel subfamily J member 12
KIF11	-3.18	0.00000	kinesin family member 11
KIFC1	-4.07	0.00000	kinesin family member C1
KRT14	4.02	0.00277	keratin 14
KRT15	2.27	0.00068	keratin 15
KRT16	2.04	0.00253	keratin 16
CENPW	-2.27	0.00000	centromere protein W
INSC	-2.99	0.00015	INSC, spindle orientation adaptor protein
KRT19	3.24	0.00000	keratin 19
KRT31	4.04	0.00064	keratin 31
KRT32	4.49	0.02976	keratin 32
KRT33A	3.48	0.00005	keratin 33A
KRT33B	3.75	0.00000	keratin 33B
KRT34	3.77	0.00056	keratin 34

TRABD2B	3.60	0.00026	TraB domain containing 2B
ARHGEF37	2.18	0.00446	Rho guanine nucleotide exchange factor 37
XKR5	-5.43	0.03442	XK related 5
L1CAM	2.43	0.00105	L1 cell adhesion molecule
STMN1	-2.81	0.00000	stathmin 1
LCN1	3.81	0.01116	lipocalin 1
LEP	4.80	0.00016	leptin
LIG1	-2.21	0.00000	DNA ligase 1
LMNB1	-3.87	0.00000	lamin B1
KRT16P2	3.31	0.01214	keratin 16 pseudogene 2
MIR137HG	2.02	0.00024	MIR137 host gene
LSAMP	2.97	0.00000	limbic system associated membrane protein
MAD2L1	-2.64	0.00000	mitotic arrest deficient 2 like 1
MATN2	-2.01	0.00019	matrilin 2
MCM2	-2.30	0.00000	minichromosome maintenance complex component 2
MCM5	-2.86	0.00000	minichromosome maintenance complex component 5
MCM7	-2.02	0.00000	minichromosome maintenance complex component 7
MDK	-2.50	0.00000	midkine
MKI67	-4.25	0.00162	marker of proliferation Ki-67
MMP1	-2.98	0.02645	matrix metalloproteinase 1
MMP3	-3.49	0.00000	matrix metalloproteinase 3
MMP17	-2.34	0.00374	matrix metalloproteinase 17
PSG8	2.61	0.00147	pregnancy specific beta-1-glycoprotein 8
AARD	6.79	0.00001	alanine and arginine rich domain containing protein
MT1A	-2.17	0.01136	metallothionein 1A
MT1F	-2.68	0.00346	metallothionein 1F
MT1M	-3.22	0.00156	metallothionein 1M
MYBL2	-3.89	0.00000	MYB proto-oncogene like 2
MYBPH	-2.09	0.00000	myosin binding protein H
MYH2	4.63	0.03604	myosin heavy chain 2
NAP1L2	3.18	0.00460	nucleosome assembly protein 1 like 2
NCAM1	-3.29	0.00838	neural cell adhesion molecule 1
NEB	3.05	0.00011	nebulin
NEDD9	2.24	0.00000	neural precursor cell expressed, developmentally down-regulated 9
NEK2	-3.73	0.00000	NIMA related kinase 2
NOS1	-5.74	0.00010	nitric oxide synthase 1
NOV	2.42	0.00002	nephroblastoma overexpressed
NPTX1	-2.43	0.00000	neuronal pentraxin 1
NRCAM	3.77	0.00000	neuronal cell adhesion molecule
NRGN	-3.92	0.00028	neurogranin
OMD	-2.19	0.00010	osteomodulin
OGN	-2.18	0.00001	osteoglycin
TNFRSF11B	3.17	0.00000	TNF receptor superfamily member 11b
ORC1	-3.41	0.00000	origin recognition complex subunit 1
OXTR	3.90	0.00000	oxytocin receptor
PCSK6	2.20	0.01420	proprotein convertase subtilisin/kexin type 6
PAFAH1B3	-2.88	0.00000	platelet activating factor acetylhydrolase 1b catalytic subunit 3
COL5A3	-2.30	0.00000	collagen type V alpha 3 chain

SERPINB2	7.21	0.00000	serpin family B member 2
PALM	3.83	0.00000	paralemmin
PAPPA	2.02	0.00000	pappalysin 1
PDE11A	3.01	0.00010	phosphodiesterase 11A
PI15	-6.05	0.00000	peptidase inhibitor 15
GMNN	-2.36	0.00000	geminin, DNA replication inhibitor
NUSAP1	-3.19	0.00000	nucleolar and spindle associated protein 1
NRN1	-3.23	0.03143	neuritin 1
GTSE1	-3.77	0.00000	G2 and S-phase expressed 1
DTL	-2.98	0.00001	denticleless E3 ubiquitin protein ligase homolog
ACKR4	2.50	0.00000	atypical chemokine receptor 4
PDGFRL	-3.06	0.00000	platelet derived growth factor receptor like
GINS2	-2.83	0.00000	GINS complex subunit 2
GPRC5B	3.42	0.00060	G protein-coupled receptor class C group 5 member B
MYOZ2	5.00	0.00000	myozenin 2
PENK	-2.45	0.00000	proenkephalin
VIT	-2.59	0.00003	vitrin
PGF	-4.89	0.00000	placental growth factor
SERPINE2	2.13	0.00000	serpin family E member 2
PKP2	3.39	0.04255	plakophilin 2
PLA2G2A	4.65	0.00000	phospholipase A2 group IIA
PLAT	3.16	0.00001	plasminogen activator, tissue type
PLK1	-3.84	0.00000	polo like kinase 1
PODXL	2.75	0.04708	podocalyxin like
POLD1	-2.18	0.00000	DNA polymerase delta 1, catalytic subunit
POLE2	-2.59	0.00005	DNA polymerase epsilon 2, accessory subunit
SH3TC1	-2.74	0.00000	SH3 domain and tetratricopeptide repeats 1
ANLN	-3.48	0.00017	anillin actin binding protein
PIMREG	-3.22	0.00000	PICALM interacting mitotic regulator
NEURL1B	-3.79	0.00000	neuralized E3 ubiquitin protein ligase 1B
ADAMTSL4	2.12	0.00000	ADAMTS like 4
USP53	2.74	0.00000	ubiquitin specific peptidase 53
LY6K	-3.37	0.00000	lymphocyte antigen 6 family member K
EPDR1	2.31	0.00000	ependymin related 1
ZNF853	-2.60	0.04395	zinc finger protein 853
ERCC6L	-3.66	0.00000	ERCC excision repair 6 like, spindle assembly checkpoint helicase
ASPN	2.34	0.00000	asporin
NCAPG2	-2.04	0.00000	non-SMC condensin II complex subunit G2
PPP1R3C	2.14	0.00000	protein phosphatase 1 regulatory subunit 3C
CDCA8	-3.28	0.00000	cell division cycle associated 8
CEP55	-2.99	0.00000	centrosomal protein 55
FANCI	-2.20	0.00000	Fanconi anemia complementation group I
PPP2R2C	3.01	0.02456	protein phosphatase 2 regulatory subunit Bgamma
NEIL3	-3.44	0.00000	nei like DNA glycosylase 3
SPTLC3	-2.06	0.00000	serine palmitoyltransferase long chain base subunit 3
HJURP	-3.16	0.00000	Holliday junction recognition protein
MCM10	-3.86	0.00000	minichromosome maintenance 10 replication initiation factor
PRELP	2.37	0.04266	proline and arginine rich end leucine

			rich repeat protein
TNFRSF19	-2.10	0.00000	TNF receptor superfamily member 19
PRIM1	-2.30	0.00000	DNA primase subunit 1
PPP1R9A	3.61	0.00218	protein phosphatase 1 regulatory subunit 9A
DEPDC1	-3.64	0.00070	DEP domain containing 1
ASF1B	-3.15	0.00000	anti-silencing function 1B histone chaperone
PRR11	-3.14	0.00066	proline rich 11
DEPDC1B	-3.47	0.00000	DEP domain containing 1B
PBK	-3.44	0.00000	PDZ binding kinase
LMO3	-2.30	0.01379	LIM domain only 3
MAP2K6	-3.66	0.04529	mitogen-activated protein kinase kinase 6
SUSD2	-3.19	0.00000	sushi domain containing 2
CYP26B1	4.12	0.00000	cytochrome P450 family 26 subfamily B member 1
PSG1	2.49	0.00036	pregnancy specific beta-1-glycoprotein 1
PSG3	2.27	0.00122	pregnancy specific beta-1-glycoprotein 3
PSG4	2.24	0.00000	pregnancy specific beta-1-glycoprotein 4
PSG5	2.73	0.00000	pregnancy specific beta-1-glycoprotein 5
PSG7	2.40	0.00935	pregnancy specific beta-1-glycoprotein 7 (gene/pseudogene)
PSG9	2.09	0.02988	pregnancy specific beta-1-glycoprotein 9
NDUFA4L2	2.37	0.00000	NDUFA4, mitochondrial complex associated like 2
RGMA	-3.00	0.00000	repulsive guidance molecule BMP co-receptor a
KIF15	-3.16	0.00000	kinesin family member 15
KNL1	-3.87	0.00113	kinetochore scaffold 1
ARFGEF3	2.91	0.00000	ARFGEF family member 3
PTGER4	-2.10	0.00000	prostaglandin E receptor 4
RHOJ	2.30	0.00000	ras homolog family member J
PTGIS	4.34	0.00000	prostaglandin I2 synthase
SPC25	-3.28	0.00000	SPC25, NDC80 kinetochore complex component
RNF150	2.14	0.02133	ring finger protein 150
MTUS1	-3.37	0.00852	microtubule associated scaffold protein 1
4-Mar	2.36	0.00000	membrane associated ring-CH-type finger 4
PREX1	-2.61	0.00000	phosphatidylinositol-3,4,5-trisphosphate dependent Rac exchange factor 1
ISLR2	2.16	0.03032	immunoglobulin superfamily containing leucine rich repeat 2
PTN	-4.67	0.00614	pleiotrophin
PTPRB	3.50	0.00004	protein tyrosine phosphatase, receptor type B
PTPRC	2.88	0.00959	protein tyrosine phosphatase, receptor type C
BARD1	-2.71	0.00004	BRCA1 associated RING domain 1
PTPRR	3.18	0.01484	protein tyrosine phosphatase, receptor type R
RRAGD	4.83	0.01208	Ras related GTP binding D
RAD51	-2.07	0.00000	RAD51 recombinase
CCND1	2.56	0.00000	cyclin D1
TGIF2	-2.16	0.00000	TGFB induced factor homeobox 2
RPS6KA1	-3.33	0.00021	ribosomal protein S6 kinase A1
RRAD	2.01	0.00684	RRAD, Ras related glycolysis inhibitor and calcium channel regulator
RRM2	-3.10	0.00000	ribonucleotide reductase regulatory subunit M2
CCL5	3.71	0.00000	C-C motif chemokine ligand 5

CCL20	2.81	0.04377	C-C motif chemokine ligand 20
CXCL5	-2.23	0.00000	C-X-C motif chemokine ligand 5
CXCL12	-3.08	0.00000	C-X-C motif chemokine ligand 12
CHTF18	-2.29	0.00000	chromosome transmission fidelity factor 18
CLSPN	-3.08	0.00000	claspin
BLM	-2.83	0.00002	Bloom syndrome RecQ like helicase
CENPK	-2.10	0.00000	centromere protein K
NCAPG	-3.93	0.00000	non-SMC condensin I complex subunit G
SFRP1	3.67	0.00581	secreted frizzled related protein 1
SFRP4	4.53	0.00000	secreted frizzled related protein 4
PURPL	5.64	0.00273	p53 upregulated regulator of p53 levels
LINC00842	2.31	0.00062	long intergenic non-protein coding RNA 842
LYPLAL1-DT	2.36	0.01110	LYPLAL1 divergent transcript
HHIP	-3.80	0.01775	hedgehog interacting protein
KRT16P3	3.21	0.00967	keratin 16 pseudogene 3
SHOX	-3.06	0.00213	short stature homeobox
DEPTOR	2.33	0.00000	DEP domain containing MTOR interacting protein
MARCKSL1	-3.13	0.00000	MARCKS like 1
SLC6A4	3.82	0.00033	solute carrier family 6 member 4
PSG10P	3.16	0.00152	pregnancy specific beta-1-glycoprotein 10, pseudogene
FAM72B	-2.00	0.00000	family with sequence similarity 72 member B
BMP6	2.04	0.00033	bone morphogenetic protein 6
SLC7A2	-4.97	0.04051	solute carrier family 7 member 2
SLPI	3.29	0.02088	secretory leukocyte peptidase inhibitor
GRAMD2B	2.06	0.00000	GRAM domain containing 2B
SOX5	-3.09	0.00000	SRY-box 5
SOX11	-4.66	0.00013	SRY-box 11
AURKA	-2.42	0.00000	aurora kinase A
BST1	2.02	0.00000	bone marrow stromal cell antigen 1
BST2	-3.06	0.02087	bone marrow stromal cell antigen 2
SYT1	2.20	0.02368	synaptotagmin 1
TCF19	-3.00	0.00000	transcription factor 19
BUB1	-3.61	0.00000	BUB1 mitotic checkpoint serine/threonine kinase
BUB1B	-4.12	0.00000	BUB1 mitotic checkpoint serine/threonine kinase B
TEK	2.76	0.00000	TEK receptor tyrosine kinase
THBS4	-2.12	0.00000	thrombospondin 4
TK1	-3.38	0.00000	thymidine kinase 1
TLL1	-4.01	0.00000	tolloid like 1
TLL2	3.15	0.00000	tolloid like 2
TM4SF4	2.49	0.00418	transmembrane 4 L six family member 4
TMPO	-2.17	0.00000	thymopoietin
TNNT1	-4.25	0.02261	troponin T1, slow skeletal type
TNXB	2.28	0.00000	tenascin XB
TOP2A	-3.74	0.00005	DNA topoisomerase II alpha
ACTG2	-2.62	0.00004	actin, gamma 2, smooth muscle, enteric
TRPC4	-4.24	0.02312	transient receptor potential cation channel subfamily C member 4
TTK	-3.53	0.00000	TTK protein kinase
KRTAP2-2	2.13	0.01559	keratin associated protein 2-2

CNTNAP3B	2.28	0.00003	contactin associated protein like 3B
KRT16P1	3.12	0.03172	keratin 16 pseudogene 1
TYMS	-2.60	0.00001	thymidylate synthetase
KRTAP2-3	3.00	0.00000	keratin associated protein 2-3
UCP2	-2.40	0.00129	uncoupling protein 2
COL14A1	-2.32	0.00000	collagen type XIV alpha 1 chain
VTN	2.68	0.00125	vitronectin
WNT2	4.19	0.00000	Wnt family member 2
WNT7B	-4.34	0.00000	Wnt family member 7B
XRCC2	-2.24	0.01099	X-ray repair cross complementing 2
CA2	-4.10	0.00000	carbonic anhydrase 2
CA11	-3.82	0.00038	carbonic anhydrase 11
CACNB4	2.94	0.00000	calcium voltage-gated channel auxiliary subunit beta 4
CENPM	-3.49	0.00000	centromere protein M
MLPH	-2.03	0.00009	melanophilin
CENPU	-2.29	0.00002	centromere protein U
GALNT12	2.31	0.02331	polypeptide N-acetylgalactosaminyltransferase 12
E2F8	-4.39	0.00000	E2F transcription factor 8
IQCA1	2.54	0.00602	IQ motif containing with AAA domain 1
TFPI2	2.00	0.00000	tissue factor pathway inhibitor 2
SHCBP1	-3.17	0.00000	SHC binding and spindle associated 1
HHIPL2	-4.66	0.00180	HHIP like 2
TM4SF20	2.46	0.01110	transmembrane 4 L six family member 20
ATAD5	-2.64	0.00001	ATPase family, AAA domain containing 5
WDR76	-2.48	0.00000	WD repeat domain 76
SVEP1	2.65	0.00000	sushi, von Willebrand factor type A, EGF and pentraxin domain containing 1
DBF4B	-2.32	0.00000	DBF4 zinc finger B
MYCT1	3.06	0.00903	MYC target 1
MFAP5	2.68	0.00000	microfibril associated protein 5
ITIH5	4.69	0.00000	inter-alpha-trypsin inhibitor heavy chain family member 5
LIMD2	-2.98	0.02441	LIM domain containing 2
COLEC12	-4.61	0.00000	collectin subfamily member 12
CAMK4	-2.84	0.00144	calcium/calmodulin dependent protein kinase IV
FAM83D	-3.55	0.00000	family with sequence similarity 83 member D
CDT1	-3.41	0.00000	chromatin licensing and DNA replication factor 1
NETO2	-2.10	0.00000	neuropilin and tolloid like 2
KRTAP1-1	2.13	0.02266	keratin associated protein 1-1
KRTAP2-1	2.11	0.01587	keratin associated protein 2-1
KIF18A	-2.30	0.00000	kinesin family member 18A
CHAF1B	-2.77	0.00000	chromatin assembly factor 1 subunit B
CDC7	-2.03	0.00000	cell division cycle 7
CDC45	-3.44	0.00000	cell division cycle 45
CDCA3	-2.87	0.00000	cell division cycle associated 3
MXD3	-2.51	0.00000	MAX dimerization protein 3
HIST1H3D	2.40	0.04019	histone cluster 1 H3 family member d
NUF2	-3.58	0.00000	NUF2, NDC80 kinetochore complex component
CCDC3	2.05	0.02644	coiled-coil domain containing 3
FAM167A	2.99	0.00000	family with sequence similarity 167 member A

HIST1H4H	2.34	0.00108	histone cluster 1 H4 family member h
CDC47	-5.04	0.00000	cell division cycle associated 7
KRTAP1-5	2.06	0.00000	keratin associated protein 1-5
HASPIN	-2.64	0.00012	histone H3 associated protein kinase
RACGAP1P	-2.05	0.00566	Rac GTPase activating protein 1 pseudogene
CCDC8	-2.11	0.00000	coiled-coil domain containing 8
BRIP1	-3.08	0.00002	BRCA1 interacting protein C-terminal helicase 1
CTTNBP2	-2.09	0.00014	cortactin binding protein 2
MND1	-3.29	0.00312	meiotic nuclear divisions 1
GINS4	-2.18	0.00000	GINS complex subunit 4
RAD54L	-3.27	0.00000	RAD54 like
FNDC1	2.03	0.00000	fibronectin type III domain containing 1
TEAD2	-2.17	0.00000	TEA domain transcription factor 2
PSRC1	-2.52	0.00000	proline and serine rich coiled-coil 1
CBX2	-2.48	0.01099	chromobox 2
ARHGEF39	-2.60	0.00176	Rho guanine nucleotide exchange factor 39
PRSS12	2.53	0.00000	serine protease 12
HIST1H2BK	2.04	0.00000	histone cluster 1 H2B family member k
KRTAP2-4	2.31	0.00138	keratin associated protein 2-4
CPZ	2.34	0.00000	carboxypeptidase Z
UNC5C	-5.25	0.00283	unc-5 netrin receptor C
KRT38	3.86	0.01998	keratin 38
SERPINB7	2.38	0.00000	serpin family B member 7
ADAM19	-2.20	0.00000	ADAM metallopeptidase domain 19
FGF18	-2.57	0.00971	fibroblast growth factor 18
FCGBP	2.24	0.00000	Fc fragment of IgG binding protein
CCKAR	-4.22	0.00104	cholecystokinin A receptor
VNN1	6.81	0.00000	vanin 1
CCNA2	-3.11	0.00000	cyclin A2
CCNB1	-2.94	0.00000	cyclin B1
TIMELESS	-2.21	0.00000	timeless circadian regulator
CCND2	4.47	0.00000	cyclin D2
KYNU	-2.92	0.00000	kynureninase
ARHGAP11B	-2.46	0.00000	Rho GTPase activating protein 11B
CCNF	-2.46	0.00000	cyclin F
SAPCD2	-4.27	0.00000	suppressor APC domain containing 2
UNC5A	-3.52	0.02161	unc-5 netrin receptor A
BMF	-2.66	0.02988	Bcl2 modifying factor
PRC1	-3.36	0.00000	protein regulator of cytokinesis 1
IL33	3.77	0.00000	interleukin 33
PKMYT1	-4.33	0.00000	protein kinase, membrane associated tyrosine/threonine 1
INA	2.66	0.02780	internexin neuronal intermediate filament protein alpha
CCNB2	-2.86	0.00000	cyclin B2
CCNE2	-2.83	0.00000	cyclin E2
SYNGR1	2.43	0.00000	synaptogyrin 1
EXO1	-3.08	0.00000	exonuclease 1
DGKI	2.14	0.00000	diacylglycerol kinase iota
IL1RL1	4.11	0.00277	interleukin 1 receptor like 1

AURKB	-4.48	0.00000	aurora kinase B
DLGAP1	4.86	0.00000	DLG associated protein 1
PTTG1	-2.92	0.00000	pituitary tumor-transforming 1
TRIP13	-2.10	0.00000	thyroid hormone receptor interactor 13
TGM5	4.58	0.00400	transglutaminase 5
LHX2	-5.05	0.00613	LIM homeobox 2
MYOCD	4.19	0.02321	myocardin
RECQL4	-2.08	0.00000	RecQ like helicase 4
FOXQ1	-4.03	0.00535	forkhead box Q1
CD36	3.23	0.00000	CD36 molecule
KIF23	-2.17	0.00000	kinesin family member 23
NRG2	-2.75	0.01475	neuregulin 2
GABBR2	3.03	0.00000	gamma-aminobutyric acid type B receptor subunit 2
APOBEC3B	-3.14	0.00000	apolipoprotein B mRNA editing enzyme catalytic subunit 3B
KIF20B	-2.64	0.00000	kinesin family member 20B
GDA	5.48	0.00248	guanine deaminase
GNA14	2.15	0.00010	G protein subunit alpha 14
ESPL1	-2.51	0.00000	extra spindle pole bodies like 1, separase
HDAC9	2.01	0.00000	histone deacetylase 9
PCLAF	-2.96	0.00000	PCNA clamp associated factor
RASSF2	3.96	0.00000	Ras association domain family member 2
DLGAP5	-3.79	0.00000	DLG associated protein 5
ARHGAP11A	-2.52	0.00000	Rho GTPase activating protein 11A
CDK1	-3.48	0.00000	cyclin dependent kinase 1
MELK	-2.53	0.00000	maternal embryonic leucine zipper kinase
GINS1	-2.74	0.00000	GINS complex subunit 1
TRIL	-2.59	0.01826	TLR4 interactor with leucine rich repeats
SV2A	-2.84	0.00000	synaptic vesicle glycoprotein 2A
CDC20	-4.36	0.00000	cell division cycle 20
KIF14	-3.31	0.00000	kinesin family member 14
CDC25A	-2.65	0.00001	cell division cycle 25A
MAFB	-2.29	0.00191	MAF bZIP transcription factor B
CDC25C	-3.73	0.00000	cell division cycle 25C
CDH1	3.50	0.00713	cadherin 1

7.4 List of DNA repair-related DEGs

Table 7.2: List of significant genes in transcriptome analysis

Symbol	ENTREZ ID	log2 Fold Change	padj
CHAF1A	10036	-1.52844	3.65E-07
SMC4	10051	-1.56668	1.45E-07
CDK2	1017	-2.20441	1.53E-12
RNASEH2A	10535	-2.06795	7.81E-15
RAD51AP1	10635	-2.35394	2.49E-06
POLD3	10714	-1.16163	0.001388

POLQ	10721	-3.08199	1.60E-09
CHEK1	1111	-1.43386	1.80E-06
WDHD1	11169	-1.34586	2.53E-06
CDCA5	113130	-2.55379	6.46E-12
RMI2	116028	-2.48802	0.000266
EME1	146956	-2.17109	0.000637
ESCO2	157570	-3.33015	2.45E-07
DDX11	1663	-1.25695	2.04E-06
DNA2	1763	-1.18752	0.023112
ERCC6	2074	1.992698	1.48E-09
FANCA	2175	-2.82211	2.91E-08
FANCC	2176	-1.08033	0.001372
FANCD2	2177	-2.51192	1.48E-09
FANCB	2187	-1.93884	0.023648
FANCG	2189	-1.58407	5.45E-07
FEN1	2237	-1.4229	2.16E-07
FOXM1	2305	-3.00783	9.64E-15
RAD54B	25788	-1.27084	0.038156
UBE2T	29089	-1.63851	6.75E-08
UHRF1	29128	-2.6412	4.76E-21
H2AFX	3014	-1.59762	1.11E-06
KIF22	3835	-1.96337	4.10E-15
LIG1	3978	-2.21216	4.38E-13
MUTYH	4595	-1.26081	0.006965
TONSL	4796	-1.50016	0.00062
NPAS2	4862	1.3667	2.13E-12
PCNA	5111	-1.31251	1.41E-08
DTL	51514	-2.97914	1.02E-05
GINS2	51659	-2.8331	2.04E-06
POLA1	5422	-1.34287	2.71E-05
POLD1	5424	-2.18247	1.43E-09
POLE	5426	-1.15098	1.05E-06
POLE2	5427	-2.58958	5.06E-05
PARPBP	55010	-1.30325	0.002608
WRAP53	55135	-1.1507	0.004102
FANCI	55215	-2.19907	1.31E-12
NEIL3	55247	-3.43979	7.30E-07
TDP1	55775	-1.14863	0.000367
FMN2	56776	1.767884	7.01E-05
BARD1	580	-2.71276	3.55E-05
RAD51	5888	-2.07283	1.84E-06
CLSPN	63967	-3.08013	1.59E-07
FIGNL1	63979	-1.02666	0.002209
BLM	641	-2.82921	1.70E-05
BRCA1	672	-1.73406	4.10E-07
BRCA2	675	-1.11428	0.018006
SUV39H1	6839	-1.61547	1.97E-05
TWIST1	7291	-1.6637	3.33E-09
USP1	7398	-1.01898	8.86E-05
NSD2	7468	-1.41979	1.26E-11
XRCC2	7516	-2.23788	0.010992

XRCC3	7517	-1.032	0.012888
PIF1	80119	-1.12832	0.017682
CHAF1B	8208	-2.76702	7.83E-09
CDC7	8317	-2.02885	1.85E-08
CDC45	8318	-3.43507	2.72E-08
BRIP1	83990	-3.08103	1.77E-05
GINS4	84296	-2.17872	3.94E-07
RAD54L	8438	-3.26707	2.42E-07
MCM8	84515	-1.49369	1.23E-06
IER3	8870	1.121993	5.64E-07
TIMELESS	8914	-2.20722	2.85E-17
TICRR	90381	-1.52538	0.000355
EXO1	9156	-3.07548	8.11E-13
PTTG1	9232	-2.9248	1.75E-10
TRIP13	9319	-2.10396	1.02E-10
RECQL4	9401	-2.07876	3.06E-11
MDC1	9656	-1.17559	7.45E-13
HDAC9	9734	2.012294	4.74E-08
PCLAF	9768	-2.95768	3.04E-07

7.5 List of Figures

- 1 Figure 1.1: Stem cell division.** Whether stem cells divide symmetrically or asymmetrically determines their self-renewal dynamics and their fate as committed precursors or differentiated cells (modified from Michael Rosemann (1)). The decision of stem cells to undergo symmetric cell division (only self-renewal and generation of two identical ASCs) or asymmetric cell division (either self-renewal or the generation of a committed precursor cell) depends on external triggers such as the presence of growth factors or their contact to neighbouring cells. LTRP: Long term repopulating potential. 4
- 2 Figure 1.2: The differential potential of mesenchymal stem cells.** Mesenchymal stem cells are self-renewing cells that can differentiate into several cell lineages, e.g. chondrocytes, adipocytes, osteocytes, fibroblasts, and other lineages. (modified from Michael Rosemann (1)) 6
- 3 Figure 1.3: Current MSC-based clinical trials.** The pie chart shows the proportion of MSC-based clinical trials classified by disease category (from Najjar et al (73)). 13
- 4 Figure 1.4: Bridge-fusion-bridge cycle.** A bridge will be formed by the sister chromatids during anaphase. The fusion breaks apart from each other by pulling in

opposite directions, which results in the two daughter cells receiving an uneven chromatid. The BFB cycle will continue in every subsequent cell division since the lack of telomeres on the two resulting chromatids, and stop until those chromatids receive a telomere, usually from a different chromatid through the process of translocation.	15
5 Figure 3.1: Real-Time PCR melting curve.	41
6 Figure 3.2: Real-Time PCR amplification plot. A graph showing a set threshold, background fluorescence and a baseline start for the sample after the Real-Time PCR reaction.	43
7 Figure 3.3: Experimental design for transcriptome analysis. Human MSCs from passage 4 (young) and passage 13 (aging) were used to analyze differential mRNA expression by NGS transcriptome profiling.	43
8 Figure 3.4: The pipeline of RNA-seq for our project.	45
9 Figure 3.5: An output plot from FASTQC software showing the quality of the FASTQ file used in the project. Green bar means the bp position pass through the quality while red bar represents the bp position does not pass through the quality check. Yellow means the intermediate potential between pass and not pass.	45
10 Figure 3.6: Quantification of γH2AX and 53BP1 co-localized foci. Single nuclei were defined and DNA repair foci were automatically scored by a threshold (Extraction setting by brightness) with the Keyence counting software. Left: The original plot. Right: The co-localized γ H2AX and 53BP1 signals were scored automatically by Keyence analyzer software.	48
11 Figure 3.7: Typical picture of metaphase. Representative metaphase spreads of primary mouse MSCs showing DAPI counterstaining (blue), leading strand (G-rich) telomere fluorescence signals (red) and lagging strand (C-rich) telomere fluorescence signals (green).....	51
12 Figure 3.8: Dysfunctional telomeric phenotype in MSCs after IR. Examples of chromosomal abnormalities observed after 2Gy γ -irradiation <i>in vitro</i> . Metaphase spreads were stained with orientation dependent CO-FISH. (a) normal telomere; (b-h) aberrant chromosomes from MSCs after IR; (b) telomeric signal missing from chromatid; (c) multiple telomeric signal in one chromatid end; (d) Sister telomere fusion in one end of a chromatid pair; (e) fragment of chromosome without a	

telomeric signal; (f) fragment with a telomeric signal; (g) chromosome fusion; (h) T-SCE in sister chromatids. 52

13 Figure 3.9: T-SCE and sister chromatid exchange after IR in MSCs. (A) A schematic presentation of CO-FISH. (A) A schematic presentation of CO-FISH. In brief, BrdU incorporated strands are removed, leaving parental strands of the telomeres to be detected by Cy5-(TTAGGG)₃ PNA probe (red color) and Alexa488-(CCCTAA)₃ PNA probe (green color). In an event of T-SCE, one chromatid end shows telomere signals in both green and red. (B) Representative metaphase spreads of normal telomere, sister chromatid exchange and T-SCE event showing DAPI staining (blue) and telomere fluorescence signals (red for leading strand, green for lagging strand)..... 53

14 Figure 4.1: PCA analysis for the transcriptome matrix from young and *in vitro* aged samples...... 59

15 Figure 4.2: The volcano plot for the DEGs between young and *in vitro* aged human MSCs. The x-axis represents the log₂ (fold change) and the y-axis represents the -log₁₀ (adjusted-p value) of the DEGs. 60

16 Figure 4.3: The heatmap for the DEGs between young and *in vitro* aged human MSCs...... 61

17 Figure 4.4: The GO analysis. (A) Enriched biological process (BP). (B) Enriched cellular component (CC). (C) Enriched molecular function (MF). The GO analysis was performed with the differential mRNA expression from passage 4 (young) and passage 13 (aging) human MSCs. q-value (adjusted p-value) <0.01 was considered as significance. 62

18 Figure 4.5: The KEGG analysis based on the DEGs. The ranked list of top 20 KEGG enrichments based on the DEG analysis. 63

19 Figure 4.6: Visualization of KEGG result by the bubble plot. The KEGG analysis was performed with the differential mRNA expression from passage 4 (young) and passage 13 (aging) human MSCs. q-value (adjusted p-value) <0.01 was considered as significance..... 64

20 Figure 4.7: GSEA analysis based on the whole transcriptome profile of young and *in vitro* aged human MSCs. The negative enrichment score indicates the downregulation of hallmarks in ex vivo aging human MSCs. The GSEA analysis

was performed with the whole transcriptome data from passage 4 (young) and passage 13 (aging) human MSCs.	65
21 Figure 4.8: DNA repair-related gene expression alterations showing by heatmap.	66
22 Figure 4.9: IPA functional analysis. The IPA analysis and network analysis were performed with the differential mRNA expression from passage 4 (young) and passage 13 (aging) human MSCs.	67
23 Figure 4.10: IPA network regulation of canonical pathways. The IPA analysis and network analysis were performed with the differential mRNA expression from passage 4 (young) and passage 13 (aging) human MSCs. The role of BRCA1 in DNA response and ATM signaling were magnified and labeled with red.	68
24 Figure 4.11: Decreased expression of homologous recombination-related genes in <i>ex vivo</i> aging hMSCs. The decreased homologous recombination-related gene expression in <i>ex vivo</i> aging hMSCs showing by KEGG plot from RNA-seq data. RAD54, RAD51, and BRCA were significantly downregulated. The KEGG analysis was performed with the differential mRNA expression from passage 4 (young) and passage 13 (aging) human MSCs.	69
25 Figure 4.12: The most significantly changed homologous recombination-related genes between young and <i>ex vivo</i> aging hMSCs from RNA-seq data showing by heatmap.	70
26 Figure 4.13: Decreased expression of homologous recombination-related genes in <i>ex vivo</i> aging hMSCs. The expression level change of BRCA1, RAD51, RAD54L, and RAD54B between young and <i>ex vivo</i> aging hMSCs by RT-PCR. The expression of target genes in aging MSCs were set arbitrary to 1 (mean values \pm SEM, n = 3, *: p < 0.05, **: p < 0.01).	71
27 Figure 4.14: Gene network of the most significant genes affected by an <i>ex vivo</i> aging process in hMSCs.	72
28 Figure 4.15: IPA analysis for the changed gene in <i>ex vivo</i> aging process in hMSCs. IPA analysis mapping the gene expression changes during <i>ex vivo</i> aging of hMSCs to “Cell Cycle Control of Chromosomal Replication” and to “BRCA1 mediated DNA Damage Response”.	73

29 Figure 4.16: Distribution of DNA content in P3 and P11 MSCs from three donors. Each pair (Figure 4.16A, 4.16B and 4.16C) consisted of MSCs from a different donor. The Y-axis shows the count number of cells and the X-axis indicates the DNA content.	74
30 Figure 4.17: Results of the cell cycle analysis in young versus old (P3 and P11) MSCs in exponential growth phase. Each data set (young versus old) consisted of MSCs from a different donor.....	75
31 Figure 4.18 BrdU incorporation for one and two days. (A) The representative plots for BrdU incorporation followed by Hoechst 33342 staining. The yellow arrow indicates the dim cells. (B) The fraction of dim cells 0 h, 24 h, 48 h after BrdU incubation. (mean values \pm SEM, n = 3, MSCs from three donors were used for experiments. For each experiment at least 50 cells were counted for MSCs from each donor).	76
32 Figure 4.19: DSB damage foci (γH2AX, red; 53BP1, green) formation shown in young and <i>ex vivo</i> aging MSCs in control, 2 hours and 24 hours after a 3 Gy of X-irradiation groups. Nuclear counterstaining by DAPI. Merged foci containing both markers are assayed as these indicate sites of DSB repair.....	77
33 Figure 4.20: The baseline of γ-H2AX/53BP1 foci for sham-irradiated cells. Nuclear counterstaining by DAPI. Merged foci containing both markers are assayed as these indicate sites of DSB repair.....	78
34 Figure 4.21: Impaired DNA repair recognition in <i>ex vivo</i> aging hMSCs. (A) Quantification of γ H2AX+53BP1 DSB-foci in MSCs 2 hours and 24 hours after 3Gy X-irradiation. (B) The percentage of colocalized γ H2AX+53BP1 foci 24 hours post irradiation relative to the values at 2 hours post irradiation in young and <i>ex vivo</i> aging MSCs (mean values \pm SEM, n = 3, *: p < 0.05, significance by paired, one-sided T-test. MSCs from three donors were used for experiments. For each experiment at least 50 cells were counted for MSCs from each donor).	78
35 Figure 4.22: Repair foci formation is shown in young and <i>ex vivo</i> aging hMSCs 2 hours and 24 hours after 3 Gy of γ-irradiation by immunofluorescence staining for pBRCA1 (red) and γH2AX (green). Nuclear counterstaining by DAPI.	79

36 Figure 4.23: The baseline of pBRCA1/γ-H2AX foci for sham-irradiated cells.	
Nuclear counterstaining by DAPI. Merged foci containing both markers are assayed as these indicate sites of DSB repair.....	80
37 Figure 4.24: Impaired homologous recombination repair capacity in <i>ex vivo</i> aging hMSCs.	
(A) Quantification of pBRCA1+ γ H2AX -foci formation in hMSCs 2 hours and 24 hours after 3Gy γ -irradiation. (B) The proportion of individual pBRCA1+ γ H2AX colocalizing foci in young and <i>ex vivo</i> aging MSCs 24 hours after γ -irradiation. (C) Quantification of pBRCA1 foci formation in hMSCs 2 hours and 24 hours after γ -irradiation. (D) The proportion of pBRCA1 foci in young and <i>ex vivo</i> aging MSCs 24 hours after γ -irradiation. (E) Quantification of γ H2AX foci in hMSCs 2 hours and 24 hours after γ -irradiation. (F) The proportion of individual γ H2AX foci in young and <i>ex vivo</i> aging MSCs 24 hours after γ -irradiation. (mean values \pm SEM, n = 3, *: p < 0.05, significance by paired, one-sided T-test. MSCs from three donors were used for experiments. For each experiment at least 50 cells were counted for MSCs from each donor).	81
38 Figure 4.25: Distribution of the initial DNA repair foci in single cells.	
(A) Dispersion analysis of DNA repair foci in single cell from young hMSCs. (B) Dispersion analysis of DNA repair foci in single cells from <i>in vitro</i> aging hMSCs. (MSCs from three donors were used for experiments. For each experiment at least 50 cells were counted for MSCs from each donor).....	82
39 Figure 4.26: The colony formation after seeding in P0 murine MSCs.	
(A) A typical colony 7 days after seeding of murine MSCs from bone marrow by Giemsa staining. (B) The precursor cells for different lineage differentiation existed in one single colony as showed by the different shapes of MSCs in a single colony.....	83
40 Figure 4.27: Different types of colonies existed in P0 MSCs.	83
41 Figure 4.28: RT-PCR demonstrated the gene expression of stem cell markers in different type of colonies. (mean values \pm SEM, n = 3, *: p < 0.05, significance by Bonferroni T-test and one-way ANOVA test).....	84
42 Figure 4.29: Spontaneous differentiation of mMSCs into different lineages in a single colony.	
The holo-colony exhibited spontaneous differentiation into osteoblasts and adipocytes by ALP-oil red double staining. The green arrow indicated the stained-red fat droplets in a single colony 21 days post seeding. The deep blue color indicates the ALP activities of osteoblasts.....	85

43 Figure 4.30: Reduction in telomere length in MSCs obtained from older mice. Q-FISH analysis of interphase spreads of MSCs which came from young and old mice with or without IR. Distribution of telomere length as analysed by Q-FISH in interphase nuclei of MSCs from young (2 month of age) and old (18 month of age) mice with or without 2Gy γ -irradiation <i>in vitro</i> . The histograms of telomere signal intensities are based on at least 2750 scored telomeres from >17 nuclei in each group. Two-way ANOVA Test was applied for detecting the significance between aging and irradiation factors.	86
44 Figure 4.31: The average Q-FISH intensity value of MSCs which came from young and old mice with or without IR	86
45 Figure 4.32: Representative metaphase spreads from irradiated MSCs, showing chromosome ends with multiple telomere signals (MTS, arrow)	87
46 Figure 4.33: The frequency of Multiple telomere signals (MTS) increased after IR. Percentage of fragile telomeres in primary MSCs from young and old mice. At least 60 metaphases/sample are counted. (MTS, arrow; mean values \pm SEM, n = 3, *: p < 0.05, significance by one-sided T-test).....	88
47 Figure 4.34: Representative metaphase spreads from irradiated MSCs, showing chromosome ends without telomere signals (SFE, arrow).	89
48 Figure 4.35: The frequency of chromosome ends without telomere signals (SFE) increased after IR. Percentage of fragile telomeres in primary MSCs from young and old mice. At least 60 metaphases/sample are counted. Error bars indicate standard error of the mean (Telomere signal free end, arrow; mean values \pm SEM, n = 3, *: p < 0.05, significance by one-sided T-test).....	89
49 Figure 4.36: Representative metaphase spreads of aged irradiated-MSCs showing DAPI staining (blue), leading strand telomere fluorescence signals (red) and lagging strand telomere fluorescence signals (green). Arrow: chromosomal instability (T-SCE, anaphase bridge and micronuclei).....	90
50 Figure 4.37: T-SCE frequency alters in irradiated MSCs from aged mice. The frequencies of T-SCEs in MSCs from young (2 month of age) and aged (18 month of age) donor mice (mean values \pm SEM, n = 3, *: p < 0.05, significance by one-sided T-test).....	91

- 51 Figure 4.38: Telomere length distribution in a single metaphase.** (A) Representative histogram of dynamic range of telomeric DNA signal intensity at individual chromosome ends in one normal MSC. (B) Representative histogram of typical dynamic range of telomeric DNA signal intensity at individual chromosome ends in one MSC which T-SCE occurs..... 91
- 52 Figure 4.39: Boxplot of delta range value in normal MSCs and T-SCE MSCs.** Boxplot of delta range value in normal MSCs and T-SCE MSCs. T-SCE MSCs show a significant increase in signal range. Each dot or triangle represents the spread between the most intense and the least intense telomere signal in an individual metaphase. A Mann-Whitney test was used to calculate the statistical significance of the observed differences in delta range value (mean values \pm SEM, $n = 3$, *: $p < 0.05$, significance by Mann-Whitney test). 92
- 53 Figure 4.40: Immunofluorescence staining for ALT associated PML bodies.** In cells of the human osteosarcoma U2OS cell line and of a murine osteosarcoma cell line MOS, PML bodies can be found in nuclei (green signal dots in nucleus). In irradiated MSCs, PML signals are not detectable in the cell nucleus. Green: PML immunofluorescence staining; blue: DAPI staining..... 93
- 54 Figure 4.41: Telomeres and DSB damage foci at MSCs from 2 months, 12 months, 18 months mice after radiation.** (A) Representative images from irradiated MSCs from 2 months, 12 months, 18 months mice showing co-localization of γ H2AX foci at telomeres. (B) Percentages of γ H2AX foci that overlap with telomere signals for 90 minutes, 8 hours, 24 hours after IR (mean values \pm SEM, $n = 3$, *: $p < 0.05$, significance by two-sided T-test.). There is no γ H2AX foci overlapped with telomere signal in the control group..... 94
- 55 Figure 5.1: During the process of their *in vitro* expansion, primary human BM - MSCs experience impairment of their ability to recognize DNA double - strand breaks.** A slower DNA damage response (fewer γ -H2AX + 53BP1 foci) after 2h was associated with a downregulation of BRCA1-related DNA repair by homologous recombination and chromosomal replication pathways, suggesting that *in vitro* aged hMSCs could be affected by reduced genetic stability. 97
- 56 Figure 7.1: Typical output from FASTQC file.** Green bar means the bp position pass through the quality while red bar represents the bp position does not pass

through the quality check. Yellow means the intermediate potential between pass and not pass.	107
57 Figure 7.2: <i>GRangesList</i> structure for the information of genes and exons of the genes through the genome. Each element in the <i>GRangesList</i> represents one gene and the information of this gene is included in the element (exon number, exon ID, chromosome location).....	109
58 Figure 7.3: Counting matrix of the P3 and P14 human MSCs that stored in <i>assay(se)</i>. <i>se</i> is a <i>summarizedExperiment</i> class that stored the experimental design and counting matrix of the transcriptome files.	110
59 Figure 7.4: <i>colData</i> slot contains all information about the experimental design in <i>DataFrame</i> class.	110
60 Figure 7.5: The structure of <i>DESeqDataSet</i>. Red part contains the gene matrix of expression values. The purple block contains the information of experiment design and the blue block contains genomic features such as gene symbols and gene IDs.	111
61 Figure 7.6: Result contains a <i>DataFrame</i> with genes (ENTREZID from hg19 genome) as rows and statistics in columns.	113
62 Figure 7.7: The information of metadata is stored in a <i>DataFrame</i> structure. The <i>DataFrame</i> contains 6 rows and 2 columns for illustrating the description of the column in result.	113
63 Figure 7.8 MAplot of comparison between samples from early passage and late passage. The MA plot shows the log ₂ fold changes from the passage average expression of the gene over all samples. The analysis process assesses a prior on log ₂ fold changes, resulting in moderated estimation from genes with low counts and highly variable counts. The narrowing spread of points on the right side of the figure reveals the estimation process.	115
64 Figure 7.9: Shrinkage estimation plot of comparison between samples from early passage and late passage. The Shrinkage estimation plot shows the shrinkage of each gene towards the red fitted trend line that represents mean dispersion's dependence. Every point represents one gene with the mean of normalized values. High gene-wise dispersed genes are the blue circle points above the fitted trend line, which are labelled as dispersion outliers.	116

65 Figure 7.10: Scatter plot of P3 MSC sample 1 vs P3 MSC sample 2. Left: using an ordinary log ₂ transformation. Right: Using the rlog transformation. Each dot represents one gene. The gene with lower expression value still showed higher variance after log transformation, which may dominate the results from PCA analysis. After rlog transformation (A ridge penalty as an empirical Bayesian), the genes with high and low expression level become more homoscedastic, which leads to more accuracy in PCA analysis.	118
66 Figure 7.11: Euclidean distance heatmap showing the distance between samples by gene matrix values. The plot indicated the samples within the same passage cluster together.	119
67 Figure 7.12: Principal-components analysis (PCA) reveals the samples within the same passage clustered together. PC1 explained 58% variance in the gene matrix and PC2 explained 18% variance in the gene matrix. In PC1 dimension the samples within the same passage had closer distance.	120
68 Figure 7.13: The list of commonly used functional pathway analysis (from Khatri P et al (254)).	121
69 Figure 7.14: The steps of functional pathway analysis (from Khatri P et al (254))	122
70 Figure 7.15: Pathway view for significantly dysregulated genes in DNA replication pathway. Downregulated genes are labeled with green color and upregulated genes are indicated with red color.	124

7.6 List of Tables

1 Table 2.1: Medium for cell culture	27
2 Table 2.2: Enzyme	27
3 Table 2.3: Enzyme	28
4 Table 2.4: Solutions and buffers	28
5 Table 2.5: Chemicals	29
6 Table 2.6: Consumables	31

7	Table 2.7: Technical equipment	32
8	Table 2.8: Software	33
9	Table 2.9: Primer sequences	33
10	Table 3.1: Reverse transcription reaction mixture	39
11	Table 3.2: RT-PCR reaction mixture	40
12	Table 3.3: RT-PCR reaction program	41
13	Table 7.1: List of significant genes in transcriptome analysis	125
14	Table 7.2: List of significant genes in transcriptome analysis	136

8 Reference

1. Rosemann M. Radiation-induced aging and genetic instability of mesenchymal stem cells: an issue for late health effects? *Genetics, evolution and radiation*: Springer; 2016. p. 385-96.
2. Pera MF, Reubinoff B, Trounson A. Human embryonic stem cells. *J Cell Sci*. 2000;113(1):5-10.
3. Minguell JJ, Erices A, Conget P. Mesenchymal stem cells. *Experimental biology and medicine*. 2001;226(6):507-20.
4. Friedenstein A, Kuralesova AI. Osteogenic precursor cells of bone marrow in radiation chimeras. *Transplantation*. 1971;12(2):99-108.
5. Friedenstein A, Latzinik N, Gorskaya YF, Luria E, Moskvina I. Bone marrow stromal colony formation requires stimulation by haemopoietic cells. *Bone and mineral*. 1992;18(3):199-213.
6. Friedenstein A, Chailakhyan R, Gerasimov U. Bone marrow osteogenic stem cells: in vitro cultivation and transplantation in diffusion chambers. *Cell proliferation*. 1987;20(3):263-72.
7. Caplan AI. Mesenchymal stem cells. *Journal of orthopaedic research*. 1991;9(5):641-50.
8. Pittenger MF, Mackay AM, Beck SC, Jaiswal RK, Douglas R, Mosca JD, et al. Multilineage potential of adult human mesenchymal stem cells. *science*. 1999;284(5411):143-7.
9. Musina R, Bekchanova E, Belyavskii A, Sukhikh G. Differentiation potential of mesenchymal stem cells of different origin. *Bulletin of experimental biology and medicine*. 2006;141(1):147-51.
10. Bianco P, Robey PG, Simmons PJ. Mesenchymal stem cells: revisiting history, concepts, and assays. *Cell stem cell*. 2008;2(4):313-9.
11. Battula VL, Treml S, Bareiss PM, Gieseke F, Roelofs H, De Zwart P, et al. Isolation of functionally distinct mesenchymal stem cell subsets using antibodies against CD56, CD271, and mesenchymal stem cell antigen-1. *Haematologica*. 2009;94(2):173-84.
12. Watson JT, Foo T, Wu J, Moed BR, Thorpe M, Schon L, et al. CD271 as a marker for mesenchymal stem cells in bone marrow versus umbilical cord blood. *Cells Tissues Organs*. 2013;197(6):496-504.
13. Ho A, Wagner W, Franke W. Heterogeneity of mesenchymal stromal cell preparations. *Cytotherapy*. 2008;10(4):320-30.
14. Horwitz E, Le Blanc K, Dominici M, Mueller I, Slaper-Cortenbach I, Marini FC, et al. Clarification of the nomenclature for MSC: The International Society for Cellular Therapy position statement. *Cytotherapy*. 2005;7(5):393-5.
15. Dominici M, Le Blanc K, Mueller I, Slaper-Cortenbach I, Marini F, Krause D, et al. Minimal criteria for defining multipotent mesenchymal stromal cells. The International Society for Cellular Therapy position statement. *Cytotherapy*.

2006;8(4):315-7.

16. Lv F-J, Tuan RS, Cheung KM, Leung VY. Concise review: the surface markers and identity of human mesenchymal stem cells. *Stem cells*. 2014;32(6):1408-19.
17. De Ugarte DA, Alfonso Z, Zuk PA, Elbarbary A, Zhu M, Ashjian P, et al. Differential expression of stem cell mobilization-associated molecules on multi-lineage cells from adipose tissue and bone marrow. *Immunology letters*. 2003;89(2-3):267-70.
18. Pelekanos RA, Li J, Gongora M, Chandrakanthan V, Scown J, Suhaimi N, et al. Comprehensive transcriptome and immunophenotype analysis of renal and cardiac MSC-like populations supports strong congruence with bone marrow MSC despite maintenance of distinct identities. *Stem cell research*. 2012;8(1):58-73.
19. Hong J-H, Hwang ES, McManus MT, Amsterdam A, Tian Y, Kalmukova R, et al. TAZ, a transcriptional modulator of mesenchymal stem cell differentiation. *Science*. 2005;309(5737):1074-8.
20. James AW. Review of signaling pathways governing MSC osteogenic and adipogenic differentiation. *Scientifica*. 2013;2013.
21. Gargett CE. Uterine stem cells: what is the evidence? *Human reproduction update*. 2006;13(1):87-101.
22. Haynesworth S, Goshima J, Goldberg V, Caplan A. Characterization of cells with osteogenic potential from human marrow. *Bone*. 1992;13(1):81-8.
23. Solchaga LA, Penick KJ, Welter JF. Chondrogenic differentiation of bone marrow-derived mesenchymal stem cells: tips and tricks. *Mesenchymal stem cell assays and applications*: Springer; 2011. p. 253-78.
24. Wagner W, Horn P, Castoldi M, Diehlmann A, Bork S, Saffrich R, et al. Replicative senescence of mesenchymal stem cells: a continuous and organized process. *PloS one*. 2008;3(5).
25. Lu T, Finkel T. Free radicals and senescence. *Experimental cell research*. 2008;314(9):1918-22.
26. Ben-Porath I, Weinberg RA. The signals and pathways activating cellular senescence. *The international journal of biochemistry & cell biology*. 2005;37(5):961-76.
27. Turinetto V, Vitale E, Giachino C. Senescence in human mesenchymal stem cells: functional changes and implications in stem cell-based therapy. *International journal of molecular sciences*. 2016;17(7):1164.
28. Platas J, Guillén MI, del Caz MDP, Gomar F, Castejón MA, Mirabet V, et al. Paracrine effects of human adipose-derived mesenchymal stem cells in inflammatory stress-induced senescence features of osteoarthritic chondrocytes. *Aging (Albany NY)*. 2016;8(8):1703.
29. Raggi C, Berardi AC. Mesenchymal stem cells, aging and regenerative medicine. *Muscles, ligaments and tendons journal*. 2012;2(3):239.
30. Acosta JC, O'Loghlen A, Banito A, Guijarro MV, Augert A, Raguz S, et al. Chemokine signaling via the CXCR2 receptor reinforces senescence. *Cell*. 2008;133(6):1006-18.
31. Freund A, Orjalo AV, Desprez P-Y, Campisi J. Inflammatory networks during cellular senescence: causes and consequences. *Trends in molecular medicine*.

2010;16(5):238-46.

32. Campisi J, Andersen JK, Kapahi P, Melov S, editors. Cellular senescence: a link between cancer and age-related degenerative disease? *Seminars in cancer biology*; 2011: Elsevier.
33. Stenderup K, Justesen J, Clausen C, Kassem M. Aging is associated with decreased maximal life span and accelerated senescence of bone marrow stromal cells. *Bone*. 2003;33(6):919-26.
34. Alessio N, Del Gaudio S, Capasso S, Di Bernardo G, Cappabianca S, Cipollaro M, et al. Low dose radiation induced senescence of human mesenchymal stromal cells and impaired the autophagy process. *Oncotarget*. 2015;6(10):8155.
35. Höfig I, Ingawale Y, Atkinson MJ, Hertlein H, Nelson PJ, Rosemann M. p53-dependent senescence in mesenchymal stem cells under chronic normoxia is potentiated by low-dose γ -irradiation. *Stem cells international*. 2016;2016.
36. Wagner W, Bork S, Lepperdinger G, Jousen S, Ma N, Strunk D, et al. How to track cellular aging of mesenchymal stromal cells? *Aging (Albany NY)*. 2010;2(4):224.
37. Jarvinen L, Badri L, Wettlaufer S, Ohtsuka T, Standiford TJ, Toews GB, et al. Lung resident mesenchymal stem cells isolated from human lung allografts inhibit T cell proliferation via a soluble mediator. *The Journal of Immunology*. 2008;181(6):4389-96.
38. Sheng H, Wang Y, Jin Y, Zhang Q, Zhang Y, Wang L, et al. A critical role of IFN γ in priming MSC-mediated suppression of T cell proliferation through up-regulation of B7-H1. *Cell research*. 2008;18(8):846-57.
39. Aggarwal S, Pittenger MF. Human mesenchymal stem cells modulate allogeneic immune cell responses. *Blood*. 2005;105(4):1815-22.
40. Beyth S, Borovsky Z, Mevorach D, Liebergall M, Gazit Z, Aslan H, et al. Human mesenchymal stem cells alter antigen-presenting cell maturation and induce T-cell unresponsiveness. *Blood*. 2005;105(5):2214-9.
41. Jiang X-X, Zhang Y, Liu B, Zhang S-X, Wu Y, Yu X-D, et al. Human mesenchymal stem cells inhibit differentiation and function of monocyte-derived dendritic cells. *Blood*. 2005;105(10):4120-6.
42. Kim H-S, Choi D-Y, Yun SJ, Choi S-M, Kang JW, Jung JW, et al. Proteomic analysis of microvesicles derived from human mesenchymal stem cells. *Journal of proteome research*. 2012;11(2):839-49.
43. Özcan S, Alessio N, Acar MB, Mert E, Omerli F, Peluso G, et al. Unbiased analysis of senescence associated secretory phenotype (SASP) to identify common components following different genotoxic stresses. *Aging (Albany NY)*. 2016;8(7):1316.
44. Spaeth E, Klopp A, Dembinski J, Andreeff M, Marini F. Inflammation and tumor microenvironments: defining the migratory itinerary of mesenchymal stem cells. *Gene therapy*. 2008;15(10):730-8.
45. Kidd S, Spaeth E, Dembinski JL, Dietrich M, Watson K, Klopp A, et al. Direct evidence of mesenchymal stem cell tropism for tumor and wounding microenvironments using in vivo bioluminescent imaging. *Stem cells*. 2009;27(10):2614-23.
46. Roorda BD, ter Elst A, Kamps WA, de Bont ES. Bone marrow-derived cells and tumor growth: contribution of bone marrow-derived cells to tumor micro-environments

with special focus on mesenchymal stem cells. *Critical reviews in oncology/hematology*. 2009;69(3):187-98.

47. Lourenco S, Teixeira VH, Kalber T, Jose RJ, Floto RA, Janes SM. Macrophage migration inhibitory factor–CXCR4 is the dominant chemotactic axis in human mesenchymal stem cell recruitment to tumors. *The Journal of Immunology*. 2015;194(7):3463-74.
48. Crisan M, Chen CW, Corselli M, Andriolo G, Lazzari L, Péault B. Perivascular multipotent progenitor cells in human organs. *Annals of the New York Academy of Sciences*. 2009;1176(1):118-23.
49. Le Blanc K, Samuelsson H, Gustafsson B, Remberger M, Sundberg B, Arvidson J, et al. Transplantation of mesenchymal stem cells to enhance engraftment of hematopoietic stem cells. *Leukemia*. 2007;21(8):1733-8.
50. Torrente Y, Polli E. Mesenchymal stem cell transplantation for neurodegenerative diseases. *Cell transplantation*. 2008;17(10-11):1103-13.
51. Wang F, Yasuhara T, Shingo T, Kameda M, Tajiri N, Yuan WJ, et al. Intravenous administration of mesenchymal stem cells exerts therapeutic effects on parkinsonian model of rats: focusing on neuroprotective effects of stromal cell-derived factor-1 α . *BMC neuroscience*. 2010;11(1):52.
52. Wilkins A, Kemp K, Ginty M, Hares K, Mallam E, Scolding N. Human bone marrow-derived mesenchymal stem cells secrete brain-derived neurotrophic factor which promotes neuronal survival in vitro. *Stem cell research*. 2009;3(1):63-70.
53. Danielyan L, Beer-Hammer S, Stolzing A, Schäfer R, Siegel G, Fabian C, et al. Intranasal delivery of bone marrow-derived mesenchymal stem cells, macrophages, and microglia to the brain in mouse models of Alzheimer's and Parkinson's disease. *Cell transplantation*. 2014;23(1_suppl):123-39.
54. Borlongan CV. Recent preclinical evidence advancing cell therapy for Alzheimer's disease. *Experimental neurology*. 2012;237(1):142-6.
55. Ma T, Gong K, Ao Q, Yan Y, Song B, Huang H, et al. Intracerebral transplantation of adipose-derived mesenchymal stem cells alternatively activates microglia and ameliorates neuropathological deficits in Alzheimer's disease mice. *Cell transplantation*. 2013;22(1_suppl):113-26.
56. Saresella M, Calabrese E, Marventano I, Piancone F, Gatti A, Calvo MG, et al. PD1 negative and PD1 positive CD4+ T regulatory cells in mild cognitive impairment and Alzheimer's disease. *Journal of Alzheimer's disease*. 2010;21(3):927-38.
57. Yang H, Yang H, Xie Z, Wei L, Bi J. Systemic transplantation of human umbilical cord derived mesenchymal stem cells-educated T regulatory cells improved the impaired cognition in A β PPswe/PS1dE9 transgenic mice. *PloS one*. 2013;8(7).
58. Firestein GS. Evolving concepts of rheumatoid arthritis. *Nature*. 2003;423(6937):356.
59. Wehrens EJ, Prakken BJ, Van Wijk F. T cells out of control—impaired immune regulation in the inflamed joint. *Nature Reviews Rheumatology*. 2013;9(1):34.
60. González MA, Gonzalez-Rey E, Rico L, Büscher D, Delgado M. Treatment of experimental arthritis by inducing immune tolerance with human adipose-derived mesenchymal stem cells. *Arthritis & Rheumatism: Official Journal of the American College of Rheumatology*. 2009;60(4):1006-19.

61. Tang D-Q, Wang Q, Burkhardt BR, Litherland SA, Atkinson MA, Yang L-J. In vitro generation of functional insulin-producing cells from human bone marrow-derived stem cells, but long-term culture running risk of malignant transformation. *American journal of stem cells*. 2012;1(2):114.
62. Phadnis SM, Joglekar MV, Dalvi MP, Muthyala S, Nair PD, Ghaskadbi SM, et al. Human bone marrow-derived mesenchymal cells differentiate and mature into endocrine pancreatic lineage in vivo. *Cytotherapy*. 2011;13(3):279-93.
63. Prabakar KR, Dominguez-Bendala J, Molano RD, Pileggi A, Villate S, Ricordi C, et al. Generation of glucose-responsive, insulin-producing cells from human umbilical cord blood-derived mesenchymal stem cells. *Cell transplantation*. 2012;21(6):1321-39.
64. Unsal IO, Ginis Z, Pinarli FA, Albayrak A, Cakal E, Sahin M, et al. Comparison of therapeutic characteristics of islet cell transplantation simultaneous with pancreatic mesenchymal stem cell transplantation in rats with type 1 diabetes mellitus. *Stem Cell Reviews and Reports*. 2015;11(3):526-32.
65. Noort W, Feye D, Van Den Akker F, Stecher D, Chamuleau S, Sluijter J, et al. Mesenchymal stromal cells to treat cardiovascular disease: strategies to improve survival and therapeutic results. *Panminerva medica*. 2010;52(1):27.
66. Ramkisoensing AA, Pijnappels DA, Askar SF, Passier R, Swildens J, Goumans MJ, et al. Human embryonic and fetal mesenchymal stem cells differentiate toward three different cardiac lineages in contrast to their adult counterparts. *PLoS One*. 2011;6(9):e24164.
67. Xu W, Zhang X, Qian H, Zhu W, Sun X, Hu J, et al. Mesenchymal stem cells from adult human bone marrow differentiate into a cardiomyocyte phenotype in vitro. *Experimental biology and medicine*. 2004;229(7):623-31.
68. Shake JG, Gruber PJ, Baumgartner WA, Senechal G, Meyers J, Redmond JM, et al. Mesenchymal stem cell implantation in a swine myocardial infarct model: engraftment and functional effects. *The Annals of thoracic surgery*. 2002;73(6):1919-26.
69. Ohnishi S, Yanagawa B, Tanaka K, Miyahara Y, Obata H, Kataoka M, et al. Transplantation of mesenchymal stem cells attenuates myocardial injury and dysfunction in a rat model of acute myocarditis. *Journal of molecular and cellular cardiology*. 2007;42(1):88-97.
70. Roura S, Bagó JR, Soler-Botija C, Pujal JM, Gálvez-Montón C, Prat-Vidal C, et al. Human umbilical cord blood-derived mesenchymal stem cells promote vascular growth in vivo. *PloS one*. 2012;7(11):e49447.
71. Kang B-J, Kim H, Lee SK, Kim J, Shen Y, Jung S, et al. Umbilical-cord-blood-derived mesenchymal stem cells seeded onto fibronectin-immobilized polycaprolactone nanofiber improve cardiac function. *Acta biomaterialia*. 2014;10(7):3007-17.
72. Ullah I, Subbarao RB, Rho GJ. Human mesenchymal stem cells-current trends and future prospective. *Bioscience reports*. 2015;35(2).
73. Najar M, Krayem M, Meuleman N, Bron D, Hélène B, Lagneaux L. Immunohematology Mesenchymal Stromal Cell-based Therapy: From Research to Clinic. *Applied Immunohistochemistry & Molecular Morphology*. 2018;26(3):e26-e43.
74. Serakinci N, Christensen R, Graakjaer J, Cairney CJ, Keith WN, Alsner J, et al. Ectopically hTERT expressing adult human mesenchymal stem cells are less

radiosensitive than their telomerase negative counterpart. *Experimental cell research*. 2007;313(5):1056-67.

75. Baxter MA, Wynn RF, Jowitt SN, Wraith JE, Fairbairn LJ, Bellantuono I. Study of telomere length reveals rapid aging of human marrow stromal cells following in vitro expansion. *Stem cells*. 2004;22(5):675-82.

76. Smogorzewska A, van Steensel B, Bianchi A, Oelmann S, Schaefer MR, Schnapp G, et al. Control of human telomere length by TRF1 and TRF2. *Molecular and cellular biology*. 2000;20(5):1659-68.

77. De Lange T. Shelterin: the protein complex that shapes and safeguards human telomeres. *Genes & development*. 2005;19(18):2100-10.

78. Wang RC, Smogorzewska A, De Lange T. Homologous recombination generates T-loop-sized deletions at human telomeres. *Cell*. 2004;119(3):355-68.

79. Greider CW. Telomeres do D-loop–T-loop. *Cell*. 1999;97(4):419-22.

80. Hemann MT, Strong MA, Hao L-Y, Greider CW. The shortest telomere, not average telomere length, is critical for cell viability and chromosome stability. *Cell*. 2001;107(1):67-77.

81. Akincilar SC, Unal B, Tergaonkar V. Reactivation of telomerase in cancer. *Cellular and Molecular Life Sciences*. 2016;73(8):1659-70.

82. Aubert G, Lansdorp PM. Telomeres and aging. *Physiological reviews*. 2008;88(2):557-79.

83. Stolzing A, Jones E, Mcgonagle D, Scutt A. Age-related changes in human bone marrow-derived mesenchymal stem cells: consequences for cell therapies. *Mechanisms of ageing and development*. 2008;129(3):163-73.

84. Reddel RR. Alternative lengthening of telomeres, telomerase, and cancer. *Cancer letters*. 2003;194(2):155-62.

85. Shay JW, Reddel RR, Wright WE. Cancer and telomeres—an ALternative to telomerase. *Science*. 2012;336(6087):1388-90.

86. Collins K, Greider CW. Tetrahymena telomerase catalyzes nucleolytic cleavage and nonprocessive elongation. *Genes & development*. 1993;7(7b):1364-76.

87. Morin GB. Recognition of a chromosome truncation site associated with α -thalassaemia by human telomerase. *Nature*. 1991;353(6343):454-6.

88. Cohn M, Blackburn EH. Telomerase in yeast. *Science*. 1995;269(5222):396-400.

89. Scheel C, Schaefer K-L, Jauch A, Keller M, Wai D, Brinkschmidt C, et al. Alternative lengthening of telomeres is associated with chromosomal instability in osteosarcomas. *Oncogene*. 2001;20(29):3835.

90. Henson JD, Hannay JA, McCarthy SW, Royds JA, Yeager TR, Robinson RA, et al. A robust assay for alternative lengthening of telomeres in tumors shows the significance of alternative lengthening of telomeres in sarcomas and astrocytomas. *Clinical Cancer Research*. 2005;11(1):217-25.

91. Chen Y-J, Hakin-Smith V, Teo M, Xinarianos GE, Jellinek DA, Carroll T, et al. Association of mutant TP53 with alternative lengthening of telomeres and favorable prognosis in glioma. *Cancer research*. 2006;66(13):6473-6.

92. Heaphy CM, Subhawong AP, Hong S-M, Goggins MG, Montgomery EA,

Gabrielson E, et al. Prevalence of the alternative lengthening of telomeres telomere maintenance mechanism in human cancer subtypes. *The American journal of pathology*. 2011;179(4):1608-15.

93. Londoño-Vallejo JA, Der-Sarkissian H, Cazes L, Bacchetti S, Reddel RR. Alternative lengthening of telomeres is characterized by high rates of telomeric exchange. *Cancer research*. 2004;64(7):2324-7.

94. Cesare AJ, Reddel RR. Alternative lengthening of telomeres: models, mechanisms and implications. *Nature reviews genetics*. 2010;11(5):319.

95. Cerone MA, Autexier C, Londoño-Vallejo JA, Bacchetti S. A human cell line that maintains telomeres in the absence of telomerase and of key markers of ALT. *Oncogene*. 2005;24(53):7893.

96. Chung I, Osterwald S, Deeg KI, Rippe K. PML body meets telomere: the beginning of an ALTernate ending? *Nucleus*. 2012;3(3):263-75.

97. Eskiw CH, Bazett-Jones DP. The promyelocytic leukemia nuclear body: sites of activity? *Biochemistry and cell biology*. 2002;80(3):301-10.

98. Bernardi R, Pandolfi PP. Structure, dynamics and functions of promyelocytic leukaemia nuclear bodies. *Nature reviews Molecular cell biology*. 2007;8(12):1006.

99. Hofmann TG, Will H. Body language: the function of PML nuclear bodies in apoptosis regulation. *Cell Death & Differentiation*. 2003;10(12):1290-9.

100. Xue Y, Gibbons R, Yan Z, Yang D, McDowell TL, Sechi S, et al. The ATRX syndrome protein forms a chromatin-remodeling complex with Daxx and localizes in promyelocytic leukemia nuclear bodies. *Proceedings of the National Academy of Sciences*. 2003;100(19):10635-40.

101. Giorgi C, Ito K, Lin H-K, Santangelo C, Wieckowski MR, Lebiedzinska M, et al. PML regulates apoptosis at endoplasmic reticulum by modulating calcium release. *Science*. 2010;330(6008):1247-51.

102. Missiroli S, Bonora M, Patergnani S, Poletti F, Perrone M, Gafà R, et al. PML at mitochondria-associated membranes is critical for the repression of autophagy and cancer development. *Cell reports*. 2016;16(9):2415-27.

103. Grobelny JV, Godwin AK, Broccoli D. ALT-associated PML bodies are present in viable cells and are enriched in cells in the G (2)/M phase of the cell cycle. *Journal of cell science*. 2000;113(24):4577-85.

104. Pickett HA, Reddel RR. Molecular mechanisms of activity and derepression of alternative lengthening of telomeres. *Nature structural & molecular biology*. 2015;22(11):875-80.

105. Potts PR, Yu H. The SMC5/6 complex maintains telomere length in ALT cancer cells through SUMOylation of telomere-binding proteins. *Nature structural & molecular biology*. 2007;14(7):581-90.

106. Draskovic I, Arnoult N, Steiner V, Bacchetti S, Lomonte P, Londoño-Vallejo A. Probing PML body function in ALT cells reveals spatiotemporal requirements for telomere recombination. *Proceedings of the National Academy of Sciences*. 2009;106(37):15726-31.

107. Porreca RM, Herrera-Moyano E, Skourti E, Law PP, Franco RG, Montoya A, et al. TRF1 averts chromatin remodelling, recombination and replication dependent-break induced replication at mouse telomeres. *Elife*. 2020;9.

108. Lillard-Wetherell K, Machwe A, Llangland GT, Combs KA, Behbehani GK, Schonberg SA, et al. Association and regulation of the BLM helicase by the telomere proteins TRF1 and TRF2. *Human molecular genetics*. 2004;13(17):1919-32.
109. Nabetani A, Yokoyama O, Ishikawa F. Localization of hRad9, hHus1, hRad1, and hRad17 and caffeine-sensitive DNA replication at the alternative lengthening of telomeres-associated promyelocytic leukemia body. *Journal of Biological Chemistry*. 2004;279(24):25849-57.
110. Zhang J-M, Yadav T, Ouyang J, Lan L, Zou L. Alternative lengthening of telomeres through two distinct break-induced replication pathways. *Cell reports*. 2019;26(4):955-68. e3.
111. Henson JD, Reddel RR. Assaying and investigating Alternative Lengthening of Telomeres activity in human cells and cancers. *FEBS letters*. 2010;584(17):3800-11.
112. Jiang W-Q, Zhong Z-H, Henson JD, Neumann AA, Chang AC-M, Reddel RR. Suppression of alternative lengthening of telomeres by Sp100-mediated sequestration of the MRE11/RAD50/NBS1 complex. *Molecular and cellular biology*. 2005;25(7):2708-21.
113. Potts PR, Yu H. The SMC5/6 complex maintains telomere length in ALT cancer cells through SUMOylation of telomere-binding proteins. *Nature structural & molecular biology*. 2007;14(7):581.
114. Fasching CL, Bower K, Reddel RR. Telomerase-independent telomere length maintenance in the absence of alternative lengthening of telomeres-associated promyelocytic leukemia bodies. *Cancer Research*. 2005;65(7):2722-9.
115. Berardinelli F, Antoccia A, Cherubini R, De Nadal V, Gerardi S, Cirrone G, et al. Transient activation of the ALT pathway in human primary fibroblasts exposed to high-LET radiation. *Radiation research*. 2010;174(5):539-49.
116. Morrish TA, Greider CW. Short telomeres initiate telomere recombination in primary and tumor cells. *PLoS Genet*. 2009;5(1):e1000357.
117. Neumann AA, Watson CM, Noble JR, Pickett HA, Tam PP, Reddel RR. Alternative lengthening of telomeres in normal mammalian somatic cells. *Genes & development*. 2013;27(1):18-23.
118. McEachern MJ, Haber JE. Break-induced replication and recombinational telomere elongation in yeast. *Annu Rev Biochem*. 2006;75:111-35.
119. Mao P, Liu J, Zhang Z, Zhang H, Liu H, Gao S, et al. Homologous recombination-dependent repair of telomeric DSBs in proliferating human cells. *Nature communications*. 2016;7(1):1-11.
120. De Vitis M, Berardinelli F, Coluzzi E, Marinaccio J, O'Sullivan RJ, Sgura A. X-rays Activate Telomeric Homologous Recombination Mediated Repair in Primary Cells. *Cells*. 2019;8(7):708.
121. Golden E, Pellicciotta I, Demaria S, Barcellos-Hoff MH, Formenti SC. The convergence of radiation and immunogenic cell death signaling pathways. *Frontiers in oncology*. 2012;2:88.
122. Russell WL, Russell LB, Kelly EM. Radiation Dose Rate and Mutation Frequency: The frequency of radiation-induced mutations is not, as the classical view holds, independent of dose rate. *Science*. 1958;128(3338):1546-50.
123. Dahle J, Kvam E, Stokke T. Bystander effects in UV-induced genomic instability:

antioxidants inhibit delayed mutagenesis induced by ultraviolet A and B radiation. *Journal of carcinogenesis*. 2005;4:11.

124. Momčilović O, Choi S, Varum S, Bakkenist C, Schatten G, Navara C. Ionizing Radiation Induces Ataxia Telangiectasia Mutated-Dependent Checkpoint Signaling and G2 But Not G1 Cell Cycle Arrest in Pluripotent Human Embryonic Stem Cells. *Stem Cells*. 2009;27(8):1822-35.

125. Olive PL, Banánth JP. Induction and rejoining of radiation-induced DNA single-strand breaks: "tail moment" as a function of position in the cell cycle. *Mutation Research/DNA Repair*. 1993;294(3):275-83.

126. Aykin-Burns N, Slane BG, Liu AT, Owens KM, O'Malley MS, Smith BJ, et al. Sensitivity to low-dose/low-LET ionizing radiation in mammalian cells harboring mutations in succinate dehydrogenase subunit C is governed by mitochondria-derived reactive oxygen species. *Radiation research*. 2010;175(2):150-8.

127. Cucinotta F, Nikjoo H, Goodhead D. Model for radial dependence of frequency distributions for energy imparted in nanometer volumes from HZE particles. *Radiation research*. 2000;153(4):459-68.

128. Karagiannis T, Kn H, El-Osta A. Disparity of histone deacetylase inhibition on repair of radiation-induced DNA damage on euchromatin and constitutive heterochromatin compartments. *Oncogene*. 2007;26(27):3963-71.

129. Prendergast AM, Cruet-Hennequart S, Shaw G, Barry FP, Carty MP. Activation of DNA damage response pathways in human mesenchymal stem cells exposed to cisplatin or γ -irradiation. *Cell cycle*. 2011;10(21):3768-77.

130. Wu L-J, Randers-Pehrson G, Xu A, Waldren CA, Geard CR, Yu Z, et al. Targeted cytoplasmic irradiation with alpha particles induces mutations in mammalian cells. *Proceedings of the National Academy of Sciences*. 1999;96(9):4959-64.

131. Yentrapalli R, Azimzadeh O, Barjaktarovic Z, Sarioglu H, Wojcik A, Harms-Ringdahl M, et al. Quantitative proteomic analysis reveals induction of premature senescence in human umbilical vein endothelial cells exposed to chronic low-dose rate gamma radiation. *Proteomics*. 2013;13(7):1096-107.

132. Philipp J, Sievert W, Azimzadeh O, von Toerne C, Metzger F, Posch A, et al. Data independent acquisition mass spectrometry of irradiated mouse lung endothelial cells reveals a STAT-associated inflammatory response. *International Journal of Radiation Biology*. 2020;96(5):642-50.

133. Chen H, Zhang B, Yao Y, Chen N, Chen X, Tian H, et al. NADPH oxidase-derived reactive oxygen species are involved in the HL-60 cell monocytic differentiation induced by isoliquritigenin. *Molecules*. 2012;17(11):13424-38.

134. Dianov GL, Parsons JL. Co-ordination of DNA single strand break repair. *DNA repair*. 2007;6(4):454-60.

135. Corre I, Niaudet C, Paris F. Plasma membrane signaling induced by ionizing radiation. *Mutation Research/Reviews in Mutation Research*. 2010;704(1-3):61-7.

136. Suzuki K, Mori I, Nakayama Y, Miyakoda M, Kodama S, Watanabe M. Radiation-induced senescence-like growth arrest requires TP53 function but not telomere shortening. *Radiation research*. 2001;155(1):248-53.

137. Zahnreich S, Melnikova L, Winter M, Nasonova E, Durante M, Ritter S, et al. Radiation-induced premature senescence is associated with specific cytogenetic

changes. *Mutation Research/Genetic Toxicology and Environmental Mutagenesis*. 2010;701(1):60-6.

138. Lehmann BD, McCubrey JA, Jefferson HS, Paine MS, Chappell WH, Terrian DM. A dominant role for p53-dependent cellular senescence in radiosensitization of human prostate cancer cells. *Cell cycle*. 2007;6(5):595-605.

139. Shrivastav M, De Haro LP, Nickoloff JA. Regulation of DNA double-strand break repair pathway choice. *Cell research*. 2008;18(1):134.

140. Weterings E, Chen DJ. The endless tale of non-homologous end-joining. *Cell research*. 2008;18(1):114.

141. San Filippo J, Sung P, Klein H. Mechanism of eukaryotic homologous recombination. *Annu Rev Biochem*. 2008;77:229-57.

142. Ayouaz A, Raynaud C, Heride C, Revaud D, Sabatier L. Telomeres: hallmarks of radiosensitivity. *Biochimie*. 2008;90(1):60-72.

143. Fumagalli M, Rossiello F, Clerici M, Barozzi S, Cittaro D, Kaplunov JM, et al. Telomeric DNA damage is irreparable and causes persistent DNA-damage-response activation. *Nature cell biology*. 2012;14(4):355.

144. Henle ES, Han Z, Tang N, Rai P, Luo Y, Linn S. Sequence-specific DNA cleavage by Fe²⁺-mediated fenton reactions has possible biological implications. *Journal of Biological Chemistry*. 1999;274(2):962-71.

145. Opresko PL, Fan J, Danzy S, Wilson III DM, Bohr VA. Oxidative damage in telomeric DNA disrupts recognition by TRF1 and TRF2. *Nucleic acids research*. 2005;33(4):1230-9.

146. Tchirkov A, Lansdorp PM. Role of oxidative stress in telomere shortening in cultured fibroblasts from normal individuals and patients with ataxia-telangiectasia. *Human molecular genetics*. 2003;12(3):227-32.

147. von Zglinicki T. Oxidative stress shortens telomeres. *Trends in biochemical sciences*. 2002;27(7):339-44.

148. Serra V, von Zglinicki T, Lorenz M, Saretzki G. Extracellular superoxide dismutase is a major antioxidant in human fibroblasts and slows telomere shortening. *Journal of Biological Chemistry*. 2003;278(9):6824-30.

149. Chan SW, Blackburn EH. New ways not to make ends meet: telomerase, DNA damage proteins and heterochromatin. *Oncogene*. 2002;21(4):553-63.

150. Smogorzewska A, Karlseder J, Holtgreve-Grez H, Jauch A, de Lange T. DNA ligase IV-dependent NHEJ of deprotected mammalian telomeres in G1 and G2. *Current Biology*. 2002;12(19):1635-44.

151. Sun L, Tan R, Xu J, LaFace J, Gao Y, Xiao Y, et al. Targeted DNA damage at individual telomeres disrupts their integrity and triggers cell death. *Nucleic acids research*. 2015;43(13):6334-47.

152. Berardinelli F, Antoccia A, Buonsante R, Gerardi S, Cherubini R, Nadal VD, et al. The role of telomere length modulation in delayed chromosome instability induced by ionizing radiation in human primary fibroblasts. *Environmental and molecular mutagenesis*. 2013;54(3):172-9.

153. Nieri D, Berardinelli F, Sgura A, Cherubini R, De Nadal V, Gerardi S, et al. Cytogenetics effects in AG01522 human primary fibroblasts exposed to low doses of

radiations with different quality. *International journal of radiation biology*. 2013;89(9):698-707.

154. Li P, Hou M, Lou F, Björkholm M, Xu D. Telomere dysfunction induced by chemotherapeutic agents and radiation in normal human cells. *The international journal of biochemistry & cell biology*. 2012;44(9):1531-40.

155. Maeda T, Nakamura K, Atsumi K, Hirakawa M, Ueda Y, Makino N. Radiation-associated changes in the length of telomeres in peripheral leukocytes from inpatients with cancer. *International journal of radiation biology*. 2013;89(2):106-9.

156. Berardinelli F, Antoccia A, Cherubini R, De Nadal V, Gerardi S, Tanzarella C, et al. Telomere alterations and genomic instability in long-term cultures of normal human fibroblasts irradiated with X rays and protons. *Radiation protection dosimetry*. 2010;143(2-4):274-8.

157. Rubio MA, Davalos AR, Campisi J. Telomere length mediates the effects of telomerase on the cellular response to genotoxic stress. *Experimental cell research*. 2004;298(1):17-27.

158. Ram R, Uziel O, Eldan O, Fenig E, Beery E, Lichtenberg S, et al. Ionizing radiation up-regulates telomerase activity in cancer cell lines by post-translational mechanism via ras/phosphatidylinositol 3-kinase/Akt pathway. *Clinical Cancer Research*. 2009;15(3):914-23.

159. Shay J, Bacchetti S. A survey of telomerase activity in human cancer. *European journal of cancer*. 1997;33(5):787-91.

160. Mao P, Liu J, Zhang Z, Zhang H, Liu H, Gao S, et al. Homologous recombination-dependent repair of telomeric DSBs in proliferating human cells. *Nature communications*. 2016;7:12154.

161. Coluzzi E, Leone S, Sgura A. Oxidative Stress Induces Telomere Dysfunction and Senescence by Replication Fork Arrest. *Cells*. 2019;8(1):19.

162. von Zglinicki T, Pilger R, Sitte N. Accumulation of single-strand breaks is the major cause of telomere shortening in human fibroblasts. *Free Radical Biology and Medicine*. 2000;28(1):64-74.

163. Coluzzi E, Colamartino M, Cozzi R, Leone S, Meneghini C, O'Callaghan N, et al. Oxidative stress induces persistent telomeric DNA damage responsible for nuclear morphology change in mammalian cells. *PloS one*. 2014;9(10):e110963.

164. Hu Y, Shi G, Zhang L, Li F, Jiang Y, Jiang S, et al. Switch telomerase to ALT mechanism by inducing telomeric DNA damages and dysfunction of ATRX and DAXX. *Scientific reports*. 2016;6:32280.

165. Liu H, Xie Y, Zhang Z, Mao P, Liu J, Ma W, et al. Telomeric recombination induced by DNA damage results in telomere extension and length heterogeneity. *Neoplasia*. 2018;20(9):905-16.

166. Tanaka H, Mendonca MS, Bradshaw PS, Hoelz DJ, Malkas LH, Meyn MS, et al. DNA damage-induced phosphorylation of the human telomere-associated protein TRF2. *Proceedings of the National Academy of Sciences*. 2005;102(43):15539-44.

167. Huda N, Tanaka H, Mendonca MS, Gilley D. DNA damage-induced phosphorylation of TRF2 is required for the fast pathway of DNA double-strand break repair. *Molecular and cellular biology*. 2009;29(13):3597-604.

168. Bo H, Ghazizadeh M, Shimizu H, Kurihara Y, Egawa S, Moriyama Y, et al. Effect

- of ionizing irradiation on human esophageal cancer cell lines by cDNA microarray gene expression analysis. *Journal of Nippon Medical School*. 2004;71(3):172-80.
169. Bérubé NG. ATRX in chromatin assembly and genome architecture during development and disease. *Biochemistry and Cell Biology*. 2011;89(5):435-44.
170. Heaphy CM, De Wilde RF, Jiao Y, Klein AP, Edil BH, Shi C, et al. Altered telomeres in tumors with ATRX and DAXX mutations. *Science*. 2011;333(6041):425-.
171. Napier CE, Huschtscha LI, Harvey A, Bower K, Noble JR, Hendrickson EA, et al. ATRX represses alternative lengthening of telomeres. *Oncotarget*. 2015;6(18):16543.
172. Conomos D, Pickett H, Reddel R. Alternative lengthening of telomeres: remodeling the telomere architecture. *Frontiers in oncology*. 2013;3:27.
173. Clynes D, Jelinska C, Xella B, Ayyub H, Scott C, Mitson M, et al. Suppression of the alternative lengthening of telomere pathway by the chromatin remodelling factor ATRX. *Nature communications*. 2015;6(1):1-11.
174. Baker N, Boyette LB, Tuan RS. Characterization of bone marrow-derived mesenchymal stem cells in aging. *Bone*. 2015;70:37-47.
175. Sethe S, Scutt A, Stolzing A. Aging of mesenchymal stem cells. *Ageing research reviews*. 2006;5(1):91-116.
176. Turgeman G, Zilberman Y, Zhou S, Kelly P, Moutsatsos IK, Kharode YP, et al. Systemically administered rhBMP-2 promotes MSC activity and reverses bone and cartilage loss in osteopenic mice. *Journal of cellular biochemistry*. 2002;86(3):461-74.
177. Chen Q, Liu K, Robinson AR, Clauson CL, Blair HC, Robbins PD, et al. DNA damage drives accelerated bone aging via an NF- κ B-dependent mechanism. *Journal of Bone and Mineral Research*. 2013;28(5):1214-28.
178. Garg A. Lipodystrophies. *Genetic Diagnosis of Endocrine Disorders: Elsevier*; 2016. p. 325-39.
179. Mansilla E, Díaz Aquino V, Zambón D, Marin GH, Mártire K, Roque G, et al. Could metabolic syndrome, lipodystrophy, and aging be mesenchymal stem cell exhaustion syndromes? *Stem cells international*. 2011;2011.
180. Nardi NB, da Silva Meirelles L. Mesenchymal stem cells: isolation, in vitro expansion and characterization. *Stem cells: Springer*; 2008. p. 249-82.
181. Tan J, Wu W, Xu X, Liao L, Zheng F, Messinger S, et al. Induction therapy with autologous mesenchymal stem cells in living-related kidney transplants: a randomized controlled trial. *Jama*. 2012;307(11):1169-77.
182. Li H, Fan X, Kovi RC, Jo Y, Moquin B, Konz R, et al. Spontaneous expression of embryonic factors and p53 point mutations in aged mesenchymal stem cells: a model of age-related tumorigenesis in mice. *Cancer research*. 2007;67(22):10889-98.
183. Yang Y-HK. Aging of mesenchymal stem cells: Implication in regenerative medicine. *Regenerative therapy*. 2018;9:120-2.
184. Brandl A, Meyer M, Bechmann V, Nerlich M, Angele P. Oxidative stress induces senescence in human mesenchymal stem cells. *Experimental cell research*. 2011;317(11):1541-7.
185. Geißler S, Textor M, Kühnisch J, Könnig D, Klein O, Ode A, et al. Functional comparison of chronological and in vitro aging: differential role of the cytoskeleton and

- mitochondria in mesenchymal stromal cells. *PloS one*. 2012;7(12):e52700.
186. Kasper G, Mao L, Geissler S, Draycheva A, Trippens J, Kühnisch J, et al. Insights into mesenchymal stem cell aging: involvement of antioxidant defense and actin cytoskeleton. *Stem cells*. 2009;27(6):1288-97.
187. Li Z, Liu C, Xie Z, Song P, Zhao RC, Guo L, et al. Epigenetic dysregulation in mesenchymal stem cell aging and spontaneous differentiation. *PloS one*. 2011;6(6):e20526.
188. Jung J-W, Lee S, Seo M-S, Park S-B, Kurtz A, Kang S-K, et al. Histone deacetylase controls adult stem cell aging by balancing the expression of polycomb genes and jumonji domain containing 3. *Cellular and Molecular Life Sciences*. 2010;67(7):1165-76.
189. Bork S, Pfister S, Witt H, Horn P, Korn B, Ho AD, et al. DNA methylation pattern changes upon long-term culture and aging of human mesenchymal stromal cells. *Aging cell*. 2010;9(1):54-63.
190. Eom YW, Oh J-E, Lee JI, Baik SK, Rhee K-J, Shin HC, et al. The role of growth factors in maintenance of stemness in bone marrow-derived mesenchymal stem cells. *Biochemical and biophysical research communications*. 2014;445(1):16-22.
191. Izadpanah R, Kaushal D, Kriedt C, Tsien F, Patel B, Dufour J, et al. Long-term in vitro expansion alters the biology of adult mesenchymal stem cells. *Cancer research*. 2008;68(11):4229-38.
192. Torgovnick A, Schumacher B. DNA repair mechanisms in cancer development and therapy. *Frontiers in genetics*. 2015;6:157.
193. Xiao W, Mohseny AB, Hogendoorn PC, Cleton-Jansen A-M. Mesenchymal stem cell transformation and sarcoma genesis. *Clinical sarcoma research*. 2013;3(1):10.
194. Song B, Kim B, Choi S-H, Song KY, Chung Y-G, Lee Y-S, et al. Mesenchymal stromal cells promote tumor progression in fibrosarcoma and gastric cancer cells. *Korean journal of pathology*. 2014;48(3):217.
195. Josse C, Schoemans R, Niessen N-A, Delgaudine M, Hellin A-C, Herens C, et al. Systematic chromosomal aberrations found in murine bone marrow-derived mesenchymal stem cells. *Stem cells and development*. 2010;19(8):1167-73.
196. Bernardo ME, Zaffaroni N, Novara F, Cometa AM, Avanzini MA, Moretta A, et al. Human bone marrow-derived mesenchymal stem cells do not undergo transformation after long-term in vitro culture and do not exhibit telomere maintenance mechanisms. *Cancer research*. 2007;67(19):9142-9.
197. Ingawale Y. Characterisation of murine mesenchymal stem cells during ageing and radiation exposure: Technische Universität München; 2016.
198. Yeager TR, Neumann AA, Englezou A, Huschtscha LI, Noble JR, Reddel RR. Telomerase-negative immortalized human cells contain a novel type of promyelocytic leukemia (PML) body. *Cancer research*. 1999;59(17):4175-9.
199. Gottschalk S, Estrada H, Degtyaruk O, Rebling J, Klymenko O, Rosemann M, et al. Short and long-term phototoxicity in cells expressing genetic reporters under nanosecond laser exposure. *Biomaterials*. 2015;69:38-44.
200. Andrews S. FastQC: a quality control tool for high throughput sequence data. Babraham Bioinformatics, Babraham Institute, Cambridge, United Kingdom; 2010.

201. Pertea M, Kim D, Pertea GM, Leek JT, Salzberg SL. Transcript-level expression analysis of RNA-seq experiments with HISAT, StringTie and Ballgown. *Nature protocols*. 2016;11(9):1650.
202. Lawrence M, Huber W, Pages H, Aboyoun P, Carlson M, Gentleman R, et al. Software for computing and annotating genomic ranges. *PLoS Comput Biol*. 2013;9(8):e1003118.
203. Love MI, Huber W, Anders S. Moderated estimation of fold change and dispersion for RNA-seq data with DESeq2. *Genome biology*. 2014;15(12):550.
204. Yu G, Wang L-G, Han Y, He Q-Y. clusterProfiler: an R package for comparing biological themes among gene clusters. *OmicS: a journal of integrative biology*. 2012;16(5):284-7.
205. Genet MD, Cartwright IM, Kato TA. Direct DNA and PNA probe binding to telomeric regions without classical in situ hybridization. *Molecular Cytogenetics*. 2013;6(1):42.
206. Paulasova P, Pellestor F, editors. The peptide nucleic acids (PNAs): a new generation of probes for genetic and cytogenetic analyses. *Annales de genetique*; 2004: Elsevier.
207. Hladik D, Höfig I, Oestreicher U, Beckers J, Matjanovski M, Bao X, et al. Long-term culture of mesenchymal stem cells impairs ATM-dependent recognition of DNA breaks and increases genetic instability. *Stem cell research & therapy*. 2019;10(1):218.
208. Vallabhaneni H, O'Callaghan N, Sidorova J, Liu Y. Defective repair of oxidative base lesions by the DNA glycosylase Nth1 associates with multiple telomere defects. *PLoS Genet*. 2013;9(7):e1003639.
209. Hakin-Smith V, Jellinek D, Levy D, Carroll T, Teo M, Timperley W, et al. Alternative lengthening of telomeres and survival in patients with glioblastoma multiforme. *The Lancet*. 2003;361(9360):836-8.
210. Helmink BA, Tubbs AT, Dorsett Y, Bednarski JJ, Walker LM, Feng Z, et al. H2AX prevents CtIP-mediated DNA end resection and aberrant repair in G1-phase lymphocytes. *Nature*. 2011;469(7329):245-9.
211. Kanu N, Zhang T, Burrell RA, Chakraborty A, Cronshaw J, DaCosta C, et al. RAD18, WRNIP1 and ATMIN promote ATM signalling in response to replication stress. *Oncogene*. 2016;35(30):4009-19.
212. Lee J, Paull TT. Activation and regulation of ATM kinase activity in response to DNA double-strand breaks. *Oncogene*. 2007;26(56):7741-8.
213. Wagner W, Bork S, Horn P, Krunic D, Walenda T, Diehlmann A, et al. Aging and replicative senescence have related effects on human stem and progenitor cells. *PLoS one*. 2009;4(6).
214. Hayflick L. Biological aging is no longer an unsolved problem. *Annals of the New York academy of Sciences*. 2007;1100(1):1-13.
215. O'Hare MJ, Bond J, Clarke C, Takeuchi Y, Atherton AJ, Berry C, et al. Conditional immortalization of freshly isolated human mammary fibroblasts and endothelial cells. *Proceedings of the National Academy of Sciences*. 2001;98(2):646-51.
216. Schallmoser K, Bartmann C, Rohde E, Bork S, Guelly C, Obenauf AC, et al. Replicative senescence-associated gene expression changes in mesenchymal

stromal cells are similar under different culture conditions. *Haematologica*. 2010;95(6):867-74.

217. Yu K-R, Kang K-S. Aging-related genes in mesenchymal stem cells: a mini-review. *Gerontology*. 2013;59(6):557-63.

218. Kinzler KW, Vogelstein B. Cancer-susceptibility genes. Gatekeepers and caretakers. *Nature*. 1997;386(6627):761, 3.

219. Zhou YF, Bosch-Marce M, Okuyama H, Krishnamachary B, Kimura H, Zhang L, et al. Spontaneous transformation of cultured mouse bone marrow–derived stromal cells. *Cancer research*. 2006;66(22):10849-54.

220. Wang Y, Zhang Z, Chi Y, Zhang Q, Xu F, Yang Z, et al. Long-term cultured mesenchymal stem cells frequently develop genomic mutations but do not undergo malignant transformation. *Cell death & disease*. 2013;4(12):e950-e.

221. Cmielova J, Havelek R, Soukup T, Jiroutová A, Visek B, Suchánek J, et al. Gamma radiation induces senescence in human adult mesenchymal stem cells from bone marrow and periodontal ligaments. *International journal of radiation biology*. 2012;88(5):393-404.

222. Nicolay NH, Perez RL, Saffrich R, Huber PE. Radio-resistant mesenchymal stem cells: mechanisms of resistance and potential implications for the clinic. *Oncotarget*. 2015;6(23):19366.

223. Sugrue T, Brown JA, Lowndes NF, Ceredig R. Multiple facets of the DNA damage response contribute to the radioresistance of mouse mesenchymal stromal cell lines. *Stem cells*. 2013;31(1):137-45.

224. Sugrue T, Lowndes NF, Ceredig R. Hypoxia enhances the radioresistance of mouse mesenchymal stromal cells. *Stem Cells*. 2014;32(8):2188-200.

225. Berhane H, Epperly MW, Goff J, Kalash R, Cao S, Franicola D, et al. Radiologic differences between bone marrow stromal and hematopoietic progenitor cell lines from Fanconi anemia (*Fancc2*–/–) mice. *Radiation research*. 2014;181(1):76-89.

226. Lafferty-Whyte K, Cairney CJ, Will MB, Serakinci N, Daidone M-G, Zaffaroni N, et al. A gene expression signature classifying telomerase and ALT immortalization reveals an hTERT regulatory network and suggests a mesenchymal stem cell origin for ALT. *Oncogene*. 2009;28(43):3765-74.

227. Cesare AJ, Reddel RR. Alternative lengthening of telomeres: models, mechanisms and implications. *Nature reviews genetics*. 2010;11(5):319-30.

228. Christensen R, Alsner J, Brandt Sorensen F, Dagnaes-Hansen F, Kolvraa S, Serakinci N. Transformation of human mesenchymal stem cells in radiation carcinogenesis: long-term effect of ionizing radiation. 2008.

229. Murnane JP. Telomere dysfunction and chromosome instability. *Mutation research/Fundamental and molecular mechanisms of mutagenesis*. 2012;730(1-2):28-36.

230. Nicolay NH, Sommer E, Lopez R, Wirkner U, Trinh T, Sisombath S, et al. Mesenchymal stem cells retain their defining stem cell characteristics after exposure to ionizing radiation. *International Journal of Radiation Oncology* Biology* Physics*. 2013;87(5):1171-8.

231. Pope-Varsalona H, Liu F-J, Guzik L, Opresko PL. Polymerase η suppresses telomere defects induced by DNA damaging agents. *Nucleic acids research*.

2014;42(21):13096-109.

232. Zimmermann M, Kibe T, Kabir S, de Lange T. TRF1 negotiates TTAGGG repeat-associated replication problems by recruiting the BLM helicase and the TPP1/POT1 repressor of ATR signaling. *Genes & development*. 2014;28(22):2477-91.

233. Stout GJ, Blasco MA. Telomere length and telomerase activity impact the UV sensitivity syndrome xeroderma pigmentosum C. *Cancer research*. 2013;73(6):1844-54.

234. Bellantuono I, Aldahmash A, Kassem M. Aging of marrow stromal (skeletal) stem cells and their contribution to age-related bone loss. *Biochimica et Biophysica Acta (BBA)-Molecular Basis of Disease*. 2009;1792(4):364-70.

235. Kuttesch Jr JF, Wexler LH, Marcus RB, Fairclough D, Weaver-McClure L, White M, et al. Second malignancies after Ewing's sarcoma: radiation dose-dependency of secondary sarcomas. *Journal of Clinical Oncology*. 1996;14(10):2818-25.

236. Tolar J, Nauta AJ, Osborn MJ, Panoskaltsis Mortari A, McElmurry RT, Bell S, et al. Sarcoma derived from cultured mesenchymal stem cells. *Stem cells*. 2007;25(2):371-9.

237. Li N, Yang R, Zhang W, Dorfman H, Rao P, Gorlick R. Genetically transforming human mesenchymal stem cells to sarcomas: changes in cellular phenotype and multilineage differentiation potential. *Cancer*. 2009;115(20):4795-806.

238. Matushansky I, Hernando E, Socci ND, Mills JE, Matos TA, Edgar MA, et al. Derivation of sarcomas from mesenchymal stem cells via inactivation of the Wnt pathway. *The Journal of clinical investigation*. 2007;117(11):3248-57.

239. Ulaner GA, Huang H-Y, Otero J, Zhao Z, Ben-Porat L, Satagopan JM, et al. Absence of a telomere maintenance mechanism as a favorable prognostic factor in patients with osteosarcoma. *Cancer Research*. 2003;63(8):1759-63.

240. Henson JD, Neumann AA, Yeager TR, Reddel RR. Alternative lengthening of telomeres in mammalian cells. *oncogene*. 2002;21(4):598-610.

241. Goto M, Miller RW, Ishikawa Y, Sugano H. Excess of rare cancers in Werner syndrome (adult progeria). *Cancer Epidemiology and Prevention Biomarkers*. 1996;5(4):239-46.

242. Hagelstrom RT, Blagoev KB, Niedernhofer LJ, Goodwin EH, Bailey SM. Hyper telomere recombination accelerates replicative senescence and may promote premature aging. *Proceedings of the National Academy of Sciences*. 2010;107(36):15768-73.

243. Laud PR, Multani AS, Bailey SM, Wu L, Ma J, Kingsley C, et al. Elevated telomere-telomere recombination in WRN-deficient, telomere dysfunctional cells promotes escape from senescence and engagement of the ALT pathway. *Genes & development*. 2005;19(21):2560-70.

244. Fouquerel E, Barnes RP, Uttam S, Watkins SC, Bruchez MP, Opresko PL. Targeted and persistent 8-oxoguanine base damage at telomeres promotes telomere loss and crisis. *Molecular cell*. 2019;75(1):117-30. e6.

245. Fujita K, Horikawa I, Mondal AM, Jenkins LMM, Appella E, Vojtesek B, et al. Positive feedback between p53 and TRF2 during telomere-damage signalling and cellular senescence. *Nature cell biology*. 2010;12(12):1205.

246. Bai Y, Murnane JP. Telomere instability in a human tumor cell line expressing a

- dominant-negative WRN protein. *Human genetics*. 2003;113(4):337-47.
247. Bai Y, Murnane JP. Telomere Instability in a Human Tumor Cell Line Expressing NBS1 With Mutations at Sites Phosphorylated by ATM1 1 RO1 CA69044 from the National Cancer Institute. *Molecular cancer research*. 2003;1(14):1058-69.
248. Liu Y, Masson J-Y, Shah R, O'Regan P, West SC. RAD51C is required for Holliday junction processing in mammalian cells. *Science*. 2004;303(5655):243-6.
249. Muntoni A, Reddel RR. The first molecular details of ALT in human tumor cells. *Human molecular genetics*. 2005;14(suppl_2):R191-R6.
250. Drexler GA, Wilde S, Beisker W, Ellwart J, Eckardt-Schupp F, Fritz E. The rate of extrachromosomal homologous recombination within a novel reporter plasmid is elevated in cells lacking functional ATM protein. *DNA repair*. 2004;3(10):1345-53.
251. Tarsounas M, Muñoz Po, Claas A, Smiraldo PG, Pittman DL, Blasco MaA, et al. Telomere maintenance requires the RAD51D recombination/repair protein. *Cell*. 2004;117(3):337-47.
252. Fritz E, Friedl AA, Zwacka RM, Eckardt-Schupp F, Meyn MS. The yeast TEL1 gene partially substitutes for human ATM in suppressing hyperrecombination, radiation-induced apoptosis and telomere shortening in AT cells. *Molecular biology of the cell*. 2000;11(8):2605-16.
253. Adams D, Gonzalez-Duarte A, O'Riordan WD, Yang C-C, Ueda M, Kristen AV, et al. Patisiran, an RNAi Therapeutic, for Hereditary Transthyretin Amyloidosis. 2018;379(1):11-21.
254. Khatri P, Sirota M, Butte AJ. Ten years of pathway analysis: current approaches and outstanding challenges. *PLoS computational biology*. 2012;8(2).

9 Bibliography

Personal Details

Address: Franz-Metzner-Straße 17

Telephone: +4915773543071

E-mail: baoxuanwen@gmail.com;

Date of Birth: 13th September 1991

xuanwen.bao@tum.de

Nationality: Chinese

Employment & Work Experience

2016-2020: Institute of Radiation Biology, **Helmholtz Zentrum München**

2015-2016: Dalian physics and chemical institute, **Chinese Academy of Science**

Education

Since 2016-Present: **Technical university (TU) München** PhD work.

Radiation Biology Institute (ISB), **Helmholtz Zentrum München**.

2009-2016 **Dalian Medical University** 7-Year Clinical Medicine Program

Languages

Native tongue: Chinese

Fluent written and spoken English

Fellowships, Awards, and Honors

CSC Scholarship

Posters and Talks

EMBL Conference Mammalian Genetics and Genomics: From Molecular Mechanisms to Translational Applications, 24 - 27 October 2017

Skills

1. Bioinformatic analysis and computational biology skills based on R/Bioconductor and Python (Bulk RNA-seq analysis, single-cell RNA-seq

analysis, DNA methylation analysis, Proteomics, and clinical analysis).

2. Data analysis (e.g. data cleaning, random forest, naive Bayes, SVM, logistic regression, decision tree, machine learning and deep learning [based on Pytorch framework]). Experience in R and Python coding (e.g. Pandas, Numpy, Pytorch, Tidyverse).
3. Biochemical experiment skills (e.g. RT-PCR, cell culture, western blot, immunofluorescence staining, CO-FISH, Q-FISH, TIF staining, and flow cytometry).

Publication List:

1. Yang, L., Kraft, V.A., Pfeiffer, S., Merl-Pham, J., **Bao, X.**, An, Y., Hauck, S.M. and Schick, J.A. (2020), **Nonsense-mediated decay factor SMG7 sensitizes cells to TNF α -induced apoptosis via CYLD tumor suppressor and the noncoding oncogene Pvt1.** *Molecular Oncology*. 2020
2. Sun, J., Zhao, T., Zhao, D., Qi, X., **Bao, X.**, Shi, R., & Su, C. (2020). **Development and validation of a hypoxia-related gene signature to predict overall survival in early-stage lung adenocarcinoma patients.** *Therapeutic Advances in Medical Oncology*. 2020
3. **Bao, X.**, Shi, R., Zhao T, Wang, Y., Anastasov, N., Rosemann, M., Fang WJ. **Integrated analysis of single-cell RNA-seq and bulk RNA-seq unravels tumour heterogeneity plus M2-like tumour-associated macrophage infiltration and aggressiveness in TNBC.** *Cancer immunology, immunotherapy* 2020
4. Shi, R.; **Bao, X.**; Rogowski, P.; Schäfer, C.; Schmidt-Hegemann, N.-S.; Unger, K.; Lu, S.; Sun, J.; Buchner, A.; Stief, C.; Belka, C.; Li, M. **Establishment and Validation of an Individualized Cell Cycle Process-Related Gene Signature to Predict Cancer-Specific Survival in Patients with Bladder Cancer.** *Cancers* 2020, 12, 1146. (Co-first author)
5. **Bao, X.**, Wang, J., Zhou, G., Aszodi, A., Schönitzer, V., Scherthan, H., ... & Rosemann, M. (2020). **Extended *in vitro* culture of primary human mesenchymal stem cells downregulates Brca1-related genes and impairs DNA double-strand break recognition.** *FEBS Open Bio*.

6. **Bao X**, Shi R, Zhao T, et al. **Immune landscape and a novel immunotherapy-related gene signature associated with clinical outcome in early-stage lung adenocarcinoma**[J]. *Journal of Molecular Medicine*, 1-14.
7. **Bao, X.**, Shi, R., Zhao, T., & Wang, Y. (2020). **Mast cell-based molecular subtypes and signature associated with clinical outcome in early-stage lung adenocarcinoma.** *Molecular Oncology*.
8. Tong, Z., Liu, Y., Ma, H., Zhang, J., Lin, B., **Bao, X.**, ... & Fang, W. (2020). **Development, Validation and Comparison of Artificial Neural Network Models and Logistic Regression Models Predicting Survival of Unresectable Pancreatic Cancer.** *Frontiers in Bioengineering and Biotechnology*, 8, 196.
9. Kraft, V. A., Bezjian, C. T., Pfeiffer, S., Ringelstetter, L., Müller, C., Zandkarimi, F., **Bao, X.**, ... & Brandner, S. (2019). **GTP Cyclohydrolase 1/Tetrahydrobiopterin Counteract Ferroptosis through Lipid Remodeling.** *ACS Central Science*, 2019.
10. Shi, R., **Bao, X.**, Weischenfeldt, J., Schaefer, C., Rogowski, P., Schmidt-Hegemann, N. S., ... & Stief, C. (2020). **A Novel Gene Signature-Based Model Predicts Biochemical Recurrence-Free Survival in Prostate Cancer Patients after Radical Prostatectomy.** *Cancers*, 12(1), 1. (Co-first author)
11. **Bao, X.**, Anastasov, N., Wang, Y., & Rosemann, M. (2019). **A novel epigenetic signature for overall survival prediction in patients with breast cancer.** *Journal of translational medicine*, 17(1), 380.
12. **Bao, X.**, Shi, R., Zhang, K., Xin, S., Li, X., Zhao, Y., & Wang, Y. (2019). **Immune Landscape of Invasive Ductal Carcinoma Tumour Microenvironment Identifies a Prognostic and Immunotherapeutically Relevant Gene Signature.** *Frontiers in oncology*, 2019.
13. Bao, M., Shi, R., Zhang, K., Zhao, Y., Wang, Y., & **Bao, X.** (2019). **Development of a membrane lipid metabolism–based signature to predict overall survival for personalized medicine in ccRCC patients.** *EPMA Journal*, 1-11.
14. Wang, Y., Zhang, Q., Gao, Z., Xin, S., Zhao, Y., Zhang, K., ... & **Bao, X.** (2019). **A novel 4-gene signature for overall survival prediction in lung adenocarcinoma patients with lymph node metastasis.** *Cancer cell international*, 19(1), 100.

-
15. Wang, Y., Deng, H., Xin, S., Zhang, K., Shi, R., & **Bao, X.** (2019). **Prognostic and predictive value of three DNA methylation signatures in lung adenocarcinoma.** *Frontiers in genetics*, 10, 349.
 16. Hladik, D., Höfig, I., Oestreicher, U., Beckers, J., Matjanovski, M., **Bao, X.**, ... & Rosemann, M. (2019). **Long-term culture of mesenchymal stem cells impairs ATM-dependent recognition of DNA breaks and increases genetic instability.** *Stem cell research & therapy*, 10(1), 218.
 17. Wang, Y., Xin, S., Zhang, K., Shi, R., & **Bao, X.** (2019). **Low GAS5 Levels as a Predictor of Poor Survival in Patients with Lower-Grade Gliomas.** *Journal of oncology*, 2019.
 18. Wang, J., Wang, J., Zhang, K., Wang, Y., & **Bao, X.** (2018). **Bayesian Network Meta-Analysis of the Effectiveness of Various Interventions for Nontraumatic Osteonecrosis of the Femoral Head.** *BioMed research international*, 2018.

10 Acknowledgement

I would like to thank Prof Michael Atkinson, my doctor father, for giving me the chance to do my PhD in the institute of radiation biology. His guidance throughout my whole PhD period let me know how to make a presentation, to do research work, and to work as a scientist. I appreciate his help to improve my scientific presentation, my thesis, and all the helpful discussions throughout my PhD study. Without his help I would not finish my PhD.

I would like to thank Dr. Michael Rosemann. He supported me not only in academia but also in my life. He taught me lots of the lab experience and biology knowledge, as well as great, helpful, and interesting discussions. He always supports me to explore the border of knowledge and learn the technologies that I am interested in. During the PhD period, I got great interests in cancer research and bioinformatics, he supported my interests and helped me to find the opportunity for collaboration with other labs. I really appreciate his help during my study.

I would like to thank Prof. Harry Scherthan, who is a great scientist in DNA repair and telomere biology. He shared my important antibodies and his helpful suggestions give me the opportunity to finish my thesis. Without the antibodies he shared and the important information he gave, I may not publish one paper that involved in my thesis. Every time I learned a lot from him in the thesis committee meeting.

To Natasa Anastasov and Omid Azimzadeh, for all the helpful discussions about breast cancer and proteomics, though not appear in this thesis, I enjoyed a lot!

I would like to share my personal thanks to all my colleagues in ISB. I sincerely appreciate Silvia and Solvejg for their help in supporting office works. My sincere thanks to Bahar for arranging all lab meetings, seminars, thesis committee meetings.

I am pleased to thank MLST PhD program managing directors Bettina and Raphaela, who helped me a lot during the whole PhD period and especially during the preparation of my thesis.

Special thanks to Yanfang Wang, my wife, for being with me during all the happy and tough time. Without her I cannot manage to finish my study in Germany. To Haowen

Deng, my friend, for teaching me a lot in informatics and all the happy time we had. I would like to thank my parents for lots of love and great support during my PhD.